# DENSITY FUNCTIONAL THEORY INVESTIGATIONS OF ZEOLITE AND INTERMETALLIC ALLOY ACTIVE SITE STRUCTURES FOR KINETICS OF HETEROGENEOUS CATALYSIS

by

**Brandon Christopher Bukowski**

**A Dissertation**

*Submitted to the Faculty of Purdue University*

*In Partial Fulfillment of the Requirements for the degree of*

**Doctor of Philosophy**
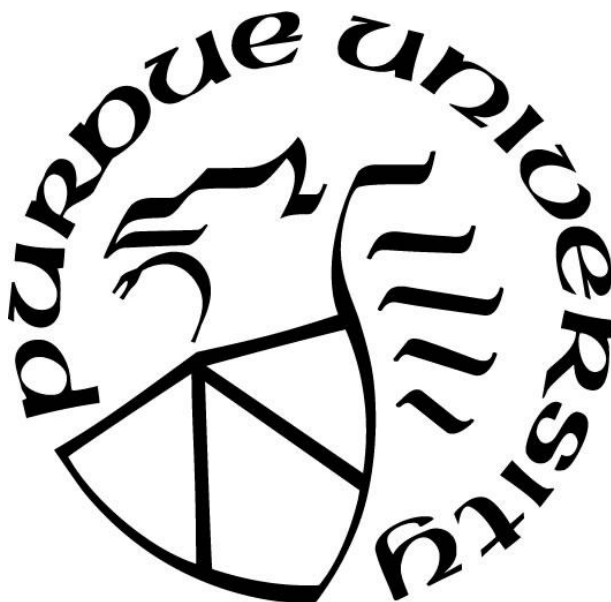


Davidson School of Chemical Engineering

West Lafayette, Indiana

August 2019

# THE PURDUE UNIVERSITY GRADUATE SCHOOL
# STATEMENT OF COMMITTEE APPROVAL

Dr. Jeffrey P. Greeley, Chair

> Davidson School of Chemical Engineering

Dr. Rajamani Gounder

> Davidson School of Chemical Engineering

Dr. Fabio H. Ribeiro

> Davidson School of Chemical Engineering

Dr. Alejandro Strachan

> Add or Delete Department

**Approved by:**

> Dr. John Morgan
>
> > Head of the Graduate Program

*Dedicated to my wife, my parents, my brother*

# ACKNOWLEDGMENTS

I am forever grateful to my adviser, Dr. Jeffrey Greeley for his guidance throughout my time in graduate school. He was a role model in every sense, beyond advising technical growth and development, he taught me how to balance my time and efforts to achieve goals that I never thought would be possible. I am forever grateful to Dr. Rajamani Gounder for his guidance throughout graduate school, both in advancing my technical understanding and ability to communicate my work to others. I am forever grateful to Dr. Fabio Ribeiro for showing me how to dream and have a vision for the future. I am forever grateful to Dr. William Nicholas Delgass for showing me the creativity and joy that can come from pursuing your scientific passion.

Many other great scientists and professors have had great influences on my development. These include Dr. Alejandro Strachan for his advice and tutelage, Dr. David Corti, Dr. Lyudmila Slipchenko, Dr. Stephen Beaudoin, Dr. Sangtae Kim, Dr. Jeremy Kropf, Dr. Peilin Liao, Dr. Brett Savoie, and Dr. Jeffrey Miller. Many graduate students and postdocs, both present and future have touched my life, including Jason Bates, Robert Warburton, Dr. Evan Wegener, Dr. Zhenwei Wu, Dr. Viktor Cybulskis, Dr. Stephen Purdy, Dr. Tej Choksi, Dr. Hee-Joon Chun, Dr. Paulami Majundar, Dr. Zhenhua Zeng, Dr. Jeffrey Lowe, Dr. Michael Cordon, Dr. James Harris, Dr. John DiIorio, Juan Carlos Vega-Vila, Jeremy Arvay, Garrett Mitchell, Joseph Kubal, Siddarth Despande, Pushkar Ghanekar, Ranga Rohit Seemakurthi, and of course Yinan Xu. This is far from an exhaustive list, as there are too many who have crossed paths with me in a meaningful way these last five years.

I thank the collaborators I have worked with throughout my dissertation. These include Dr. Rajamani Gounder and Jason Bates for my work in Sn-Beta; Dr. Jeffrey Miller, Evan Wegener, Viktor Cybulskis, Zhenwei Wu, Stephen Purdy for my work on modeling the RIXS process; Dr. William Nicholas Delgass, Jeremy Arvay, Garrett Mitchel for my work modeling the TS-1 catalyst. Dr. David Flaherty and Daniel Bregante for my work predicting adsorption of acetonitrile in Ti-Beta. I thank Tristan Maxson for his work on MYCROSOLVE and his general computer science techniques.I thank the funding and computing clusters that have supported me along the way

# TABLE OF CONTENTS

# LIST OF TABLES

# LIST OF FIGURES

# ABSTRACT

Author: Bukowski, Brandon, C. PhD
Institution: Purdue University
Degree Received: August 2019
Title: Density Functional Theory Investigations of Zeolite and Intermetallic Alloy Active Site Structures for Kinetics of Heterogeneous Catalysis
Committee Chair: Jeffrey Greeley

Catalysis has a responsibility to provide solutions to the growing grand challenge of sustainability in the fuels and chemical industry to help combat climate change. These changes; however, cannot be realized without a more fundamental understanding of the active sites that catalyze chemical reactions, and how they can be tuned to control rates and selectivities. Four specific examples of active site modification will be considered in this work: the speciation of isolated metals in zeolite frameworks, solvent thermodynamics and structure at defects in zeolite frameworks, the electronic modification of platinum through alloying in well-defined intermetallic nanoparticles, and the mobility and shape of gold nanoparticles in zeolite channels. Each will highlight how quantum chemistry calculations can provide a fundamental understanding of how these active site modifications influence the kinetics of chemical reactions, and how they can be controlled to pursue solutions to the reduction of carbon through sustainable utilization of shale gas as well as renewable chemicals production through biomass upgrading.

Zeolites exchanged with metal heteroatoms can behave as solid Lewis or Brønsted acids depending on heteroatom identity. Lewis acid heteroatoms can adsorb water and hydrolyze to speciate into "open sites" which have been shown to differ in their ability to catalyze reactions such as glucose isomerization as compared to "closed sites" which are fully coordinated to the zeolite framework. The structure and catalytic properties of these sites are interrogated by a gas phase reaction, ethanol dehydration, in Sn-Beta by a combined Density Functional Theory (DFT) and experimental study. DFT is used to map the possible reaction mechanisms for ethanol dehydration, including the speciation of Sn sites into hydrolyzed configurations from water or ethanol. A microkinetic model for ethanol dehydration including unselective and inhibitory intermediates is constructed. This microkinetic model predicts the population of reactants and products on the catalyst surface as well as the sensitivity of individual elementary steps to the total rates. Powerful anharmonic entropy methods using *ab-initio* molecular dynamics (AIMD) is used

to capture the entropy of confined reactive intermediates, which is shown to be necessary to compare with experiment. Results on closed and hydrolyzed open zeolite sites can then be compared with ethanol dehydration on "defect open" sites which were shown experimentally to occur at material stacking faults. A grain boundary model is constructed of zeolite Beta, where unique sites have similar ligand identity as hydrolyzed open sites. These defect open sites are found to not contribute to the observed reaction rate as they cannot stabilize the same transition state structures that were observed in internal Beta sites.

Intuition about the ethanol dehydration reaction in Sn-Beta was then used to map a more expansive and diverse chemical network, the synthesis of butadiene from acetaldehyde and ethanol. For elementary reactions in this mechanism, which included aldol condensation, MPV reduction, and crotyl alcohol dehydration in addition to ethanol dehydration, the hydrolyzed open sites were found to be crucial reactive intermediates. Hydrolyzed sites were necessary to stabilize favorable transition states, which requires reconstruction of the local framework environment. Methods to preferentially stabilize hydrolyzed sites were then explored, using a screening algorithm developed to consider all possible sites in each zeolite framework. It was found that the stability of these hydrolyzed sites could be correlated to the local strain exerted by the surrounding silica matrix. This provides a new descriptor that stabilizes intermediates relevant to the synthesis of butadiene and ethanol dehydration.

Next, the structure and thermodynamic stability of water networks around Sn-Beta defects and heteroatom active sites was considered using AIMD. As many biomass reactions occur in the presence of water, the interactions of water with hydrophobic and hydrophilic functionalized defects dictate how the stability of reactive intermediates and transition states is affected by a solvating environment. Locally stable and strongly nucleated clusters of water were observed to form at Sn defects, with less densely packed water structures stable at hydrophilic defects. This is in comparison to defect-free siliceous Beta, where significantly less water uptake is observed. These local clusters are in equilibrium with the less dense liquid-like phase that extends between defects. These results motivate localized cluster models around active sites in Lewis acids, as well as advance the fundamental understanding of hydrophobic/hydrophilic interactions in microporous materials. The local cluster models are then applied to the ethanol dehydration reaction in protonated aluminum Beta zeolites where experimentally observed non-unity coefficient ratios are

rationalized by quantifying a different degree of solvation for the ethanol reactant state as opposed to the transition state, validated by a thermodynamic phase diagram.

Changes in the electronic energy levels of *d* electrons upon alloying was studied in conjunction with a new spectroscopic technique being performed at Argonne National Laboratory to develop new descriptors to predict the degree of coking for different alloys. Resonant Inelastic X-ray Scattering (RIXS) simultaneously probes the occupied and unoccupied valence states of platinum in nanoparticles at ambient conditions. The specific excitation process of this spectroscopy is particularly amendable to DFT modeling, which was used to provide richer chemical insight into how changes in observed RIXS signature related to the electronic structure changes of platinum upon alloying. From a suite of multiple 3d alloy promoter catalysts synthesized, a quantitative comparison with DFT modeled spectroscopy was developed. The stability of DFT calculated coke precursors, relevant to dehydrogenation catalysts to convert light alkanes into olefins, was then correlated to DFT modeled RIXS spectra, which is a better descriptor for adsorption of unsaturated chemical intermediates that used previously, as well as being a descriptor accessible to direct experimental usage.

Finally, the diffusion of gold nanoparticles in the TS-1 catalyst was studied using AIMD to help understand what structural motifs of gold are present under reaction conditions and how the shape and binding sites of gold is strongly influenced by deformation by the zeolite framework. This is used to help predict new zeolites for use in direct propylene epoxidation using molecular oxygen and hydrogen. The optimization of this catalyst is environmentally relevant to reduce the usage of inorganics and reduce the cost associated with production of hydrogen peroxide. Following these discussions, the role of computation in the prediction of active site structures and kinetics in conjunction with experiment was included. The broader impact of these findings will also be considered, which span beyond these specific reactions and materials.

# 1. INTRODUCTION

## 1.1 Catalysis in a modern world

It has been just over 100 years since Fritz Haber won the Nobel prize for performing alchemy on the industrial scale, by taking nitrogen and hydrogen gas and producing ammonia. This discovery in many ways still reflects the ideas present in the field of catalysis. In fact, literature on the ammonia synthesis reaction is still popular[1], [2], reflecting the universal concepts which remain to this day. Haber began to experiment with hydrogenation at increasingly severe conditions, to operating conditions of 200 atmospheres and temperatures of 400-500C, requiring new developments in the construction of reactors and a direct application of thermodynamic principles to ensure safety and reliability of the process[3]. Haber's studies reflected his knowledge of chemistry, engineering, and materials science to commercialize the ammonia synthesis reaction. This combined approach proved successful, and towards the end of 1918 Germany could meet the demand of ammonia for fertilizer despite trade blockades. This confluence of skills would be further epitomized by Vladimir Ipatieff and Hermann Pines from whom many of the refinery operations to produce high octane gasoline were born[4]. While at Universal Oil Products, Pines and Ipatieff performed fundamental research on alkanes, at the time considered uninteresting to many academic chemists of their time due to their generally inert nature. Pines used his chemistry background to show how strong acids could perform alkylation reactions which lead to the beginning of oil refining into commercial gasoline.

These successes came out of necessity, either food shortages in Germany or the rising demand for high quality gasoline in the United States, which were only realized through work spanning diverse scientific fields. Little has changed in the 100 years since Haber, and still catalysis science is sought as a tool to solve the rising energy crisis and combat greenhouse gas emissions. In other respects; however, catalysis has changed dramatically by the techniques available to understand and design catalyst active sites that are responsible for chemical transformations. Among these techniques is the use of quantum chemistry, perhaps first envisioned by Enrico Fermi, and realized by the pioneering work of John Pople, Walter Kohn, and Lu Jeu Sham.

With the advent of computers during the second world war, quantum mechanical theories from modern physics could finally be applied to practical systems with many interacting electrons. The development of electron-electron interactions solved in the limit of an arbitrary number of particles (in theory) postulated that it would only be a matter of time until computing power was plentiful enough to explicitly capture the energy of chemical bonds. Pioneers in the field of modern applied physics immediately began work applying computational theory to manipulate individual atoms. While the simulation of molecular species was made accessible through the contributions of John Pople, the simulation of extended solids ubiquitous to heterogeneous catalysis remained a difficult problem that will be discussed in section 1.3.1 of this dissertation. It was not until the work of Kohn and Sham that calculations of extended surfaces became possible, which through many other important contributions allowed for theoretical adsorption onto catalyst surfaces. For their contributions to the field of chemistry; Pople and Kohn received the 1998 Nobel Prize in chemistry.

The development of theory in catalysis has driven interest towards ideas of rapidly screening materials for favorable properties; yet, the fundamental understanding of the kinetics of heterogeneous catalysis remains unable to provide an encompassing theory of how to choose a catalyst *a priori*, without the guidance of experiment. It would be impossible to imagine researchers now or in the future to stop trying to push the limits of computation as a means to both predict new materials and also as a tool to explain the mechanism of chemical transformations. This thesis will straddle both perspectives, which at this time I believe is the most fruitful approach: primarily to use theory in close conjunction with experiment in order to gain fundamental insights into what chemical and structural motifs are desirable for a given process, and then to use these insights to develop structure-property relationships which provide feedback to experimentalists for their ability to tailor new materials to the properties required in new catalysts.

I view the modern field of catalysis as still having the potential for tremendous growth, as the integration of theoretical calculations and experimental studies have not reached full maturity; as evidenced by the tremendous opportunity to increase the involvement of the petrochemical industry in computational catalysis. The role of theory in conjunction with experiment to provide fundamental insight is critical in addressing the energy and environmental needs as evidenced in the body of this dissertation.

## 1.2 Catalysis science for sustainable fuels and chemicals

It is now without a doubt that human sources have contributed to the rise in temperature across the globe, and $CO_2$ emissions continue to rise despite policy change beginning to make an impact. While policy change can help drive a reduction in $CO_2$, there is currently no roadmap to broad sustainability in the fuel and chemical industry. Recent reports such as that by Nolan and coworkers shows the extent to which terrestrial changes to ecosystems throughout the planet are intimately linked to the changes we have wrought by rising greenhouse gas emissions.[5] The effects of climate change are far-reaching and it's likely that the true scope of these changes are not well understood. Recent work by Swinburn and coworkers have discussed how climate change is synergistic with the obesity and undernutrition epidemics, and malnutrition will only become more difficult to address as the effects of climate change become more severe[6]. Tremendous research is being done across the globe to address sustainability for energy and fuels, which remains a pressing issue, yet key technologies also need to be enabled to reduce the carbon burden of the fuels and chemicals industries as long-term sustainable solutions are developed. In this thesis, the transformation of shale gas into fuels, and the transformation of biomass into fuels and chemicals will be explored as fundamental steps to reach sustainability. In addition, the development of catalysts which reduce harmful waste and energy inefficient separation processes will be discussed, with the epoxidation of propylene being highlighted.

Energy in the United States is changing dramatically, due primarily to the rise of shale gas. The EIA May 2019 report published by the US Department of Energy shows how for the first time since the 1980s the United States has reduced its energy imports, and since 2007 increased its share as an energy exporter[7]. Among these changes is a dramatic increase in natural gas production, which as of February 2019 has surpassed crude oil sources by 0.2 quadrillion Btus. Production of renewables continues to grow steadily yet has yet to surpass coal production. Coal production has dropped dramatically in the last 10 years; however, it remains the dominant source of electricity in the United States[7]. The fraction of electricity generated through coal resources has started to be surpassed by natural gas. As of 2016, the DoE has shown that the combined shares of wind and solar generation has continued to grow, in addition to hydrothermal, biomass, and geothermal sources.[8] Despite this growth, new investments in clean energy decreased by 9.3% in the United States, and global investment in clean energy decreased by 18%[8]. These statistics reflect the

changes that in conjunction with climate change provide opportunities for catalysis to make an impact in how renewables and shale gas are used responsibly.

Changes in the energy industry are just one factor in how shale gas has changed the chemical industry of the United States, and the shifts in the chemical industry are changing how petroleum feedstocks are being utilized. Shifts in the feedstock composition of petroleum have recently caused there to be reduced production of olefins such as propylene and butadiene[9]. These products were traditionally produced from naptha cracking at the refinery scale, and the refinery shift to ethane cracking will continue as the composition of petroleum continues to change[10]. Both propylene and butadiene are key chemicals for polymers. The rise of shale gas has provided one avenue for producing olefins, which is dehydrogenation of alkanes. The proposed Center for the Strategic Transformation of Alkane Resources (CISTAR) process involves catalytic dehydrogenation of alkenes to olefins, followed by oligomerization to liquid fuels. This thesis will directly address work done through this center to design dehydrogenation catalysts to produce propylene from propane found in shale gas. Procurement of shale resources has only become economical in the last decade due to technological advances in drilling, but the utilization of the alkanes present in shale is fundamentally a catalysis science problem. Scientific challenges in dehydrogenation which can be addressed with catalysis science include reducing the formation of unselective products and catalyst coking which must be addressed especially for smaller shale gas processing plants[11]. Butadiene can also be produced from alkane resources, such as the Houdry process which uses dehydrogenation of n-butane.[9] While pursuing shale gas conversion helps reduce dependence on petroleum reserves by the synthesis of fuels and chemical resources of a more abundant resource, it does not address the long term need for sustainable fuels and chemicals.

One proposed renewable source of chemical feedstocks is the processing of biomass. The shale revolution has made the profitability of biomass upgrading less attractive, yet for the long-term future of the chemical industry and especially regions of the world where shale gas is less economical, the production of fuels and platform chemicals through biomass will always be a relevant pursuit. Many hurdles, both scientific and practical exist which prevent the widespread use of biomass as fuels, from the level of appropriate land use and agricultural considerations, the selectivity and economics of catalysts necessary for biomass refining, and the overall carbon efficiency of biomass transformation, are all at play. One aspect of biomass conversion that is often overlooked is the genetic engineering of plants and algaes to naturally produce higher lignin and

cellulose contents, in addition to micro-organisms adept at decomposing plants and algae into sugar families that can be refined catalytically into fuels and platform chemicals[12]. Some early work in this field has been performed by Chen and Dixon who showed that regulation of lignin biosynthetic enzymes produced transgenic alfalfa with nearly twice as much sugars[13]. Recent work by Mizrachi and coworkers has used genetic networking studies to find genetic linkages that affect physical properties such as growth and wood chemistry of Eucalyptus[14]. The degree to which plant and algae resources can be tailored to produce precursors for further refining makes it difficult to perform a technoeconomic analysis on when biomass becomes economical. Biomass conversion chemistry may begin by being economical for a select number of aromatics or sugar-derivatives too difficult to synthesize from shale gas. Despite short term trends in the fuel and chemical industry, biomass catalysis is still necessary for long term sustainability.

Additional practical scientific hurdles exist even if a pure mixture of sugars and alcohols can be processed from genetically engineered plants and algae. Assuming micro-organisms can be engineered to break down cellulosic lignin to simple sugars removing the need for acid washing and de-polymerization, selective catalysis to fuels and desired chemicals remains a formidable challenge. The US Department of Energy has released a report screening promising value added chemicals to be refined from biomass, which include four carbon diacids such a Succinic, Fumaric, and Malic acids to produce tetrahydrofuran, 4-carbon diols, and butyrolactone for use as solvents and in polymers[15]. The catalysis of forming such compounds typically involves dehydration and decarboxylation chemistries, to reduce the oxygen content of feedstocks[16]. Many of these reactions will produce water as products during deoxygenation reactions, requiring catalysts that are water-tolerant at elevated temperatures[17]. Deoxygenation chemistries also are complicated by multiple unselective pathways[18], producing chemical products of no commercial value in a technology already pressed to reach efficiency by virtue of its many sequential steps from the biological scale.

Ethanol provides a more straightforward example of a biomass feedstock than can be more readily incorporated into the fuels and chemicals industry. Ethanol production in the United States has been steadily growing[19], and ethanol is likely to be a large fraction of biomass feedstocks, making it an attractive platform to use to study the types of chemistries present for other more complicated feedstocks. Some of the important chemical targets which have been proposed to be synthesized from ethanol include 1-butanol, ethylene, acetaldehyde, acetic acid, isobutylene, and

1,3-butadiene[20]. Butadiene will be discussed in detail in this thesis, and this introduction will include a historical perspective for the types of practical difficulties found in refining alcohols. The earliest chemical synthesis of butadiene from ethanol was first discovered by Vladimir Ipatieff. As early as 1903 Ipatiev and later Ostromislenskiy discovered how ethanol could be transformed into butadiene using alumina. This process, and later the Lebedev process would be attractive methods for synthetic rubber in World War 2 until petroleum refining became the dominant synthetic route due to process economics[20]. A technoeconomic analysis and life-cycle assessment (LCA) for butadiene synthesis comparing bioethanol and petroleum feedstocks has recently been performed, and while there are many unknowns in this analysis, the base case analysis indicates a decrease in greenhouse gas emission for the process as well as favorable decreases in the environmental hazards and impacts. Changes in the petroleum and ethanol industry as well as the development of new catalysts, the topic of chapter 5 of this thesis, can dramatically change how butadiene is produced, especially as refinery-based naptha cracking continues to slow down. While there are many factors which determine the profitability and feasibility of widespread biomass upgrading for fuels and/or chemicals, the fundamental design of new catalysts for water-tolerant deoxygenation chemistry is an important problem to be addressed by the catalysis community.

Thus far I have considered the design of new catalysts to help address either short-term changes in the fuels and chemical industry (through dehydrogenation of shale gas), or long-term changes including water-tolerant and selective deoxygenation catalysts for biomass upgrading; but another important topic to be addressed by catalysis science is the development of more sustainable and energy efficient methods to improve existing chemical processes. One example of this is the epoxidation of propylene to propylene oxide (PO). PO is a crucial platform chemical used for a wide range of chemicals including polymers for the textile and plastics industry. The classical method to produce PO is the chlorohydrin process which uses propylene and chlorine gas to form propene chlorohydrin[21], [22]. Propene chlorohydrin is then dehydrochlorinated using calcium hydroxide to form the product and a calcium chloride salt. A brine containing the calcium chloride salts and some alkanes has to be disposed of, in addition to any other chlorine-containing byproducts[22]. The industry has moved towards using hydrogen peroxide as a more environmentally safe oxidant which avoids the inorganic salts. Here hydrogen peroxide is fed with propylene when it is oxidized into PO. This method is still disadvantageous due to the cost and

dangers with concentrated hydrogen peroxide[21]. One solution being explored is to produce the hydrogen peroxide directly in the reactor from molecular hydrogen and oxygen. It is more economical and less dangerous to use hydrogen and oxygen, using a dual function catalyst that can make hydrogen peroxide and then epoxidize propylene. Attempts to commercialize this process have been unsuccessful as the catalyst required must be able to do both reactions selectively, but also efficiently utilize of hydrogen gas. The development of a new catalyst for direct PO production is useful as it provides an avenue for performing industrially relevant chemistry using a more economical, safer, and more sustainable oxidant.

These three examples: light alkane dehydrogenation, butadiene synthesis from ethanol, and direct epoxidation of propylene, will all be discussed in greater detail in this thesis, and they provide important case studies for how advances in catalysis can directly combat climate change and increase sustainability. These problems are not new problems. All these reactions have been studied since the beginning of the $20^{th}$ century, so what has changed since then? Is it realistic to think that they can be solved now? Several reasons exist for believing that this may be the case. For one, the integration of petroleum as a convenient chemical feedstock has displaced other processes, and focused both industrial and academic research efforts to improving petroleum-adjacent processes. The decades of experience studying petroleum have provided an enormous wealth of knowledge and practical experience that can be transferred to these new problems. One example that will be discussed in a later section, is the use of molecular sieves in Fluid Catalytic Cracking which were highly desirable due to their shape-selectivity to producing high-octane fuels, now being used for biomass upgrading where their shape-selectivity is just as relevant. Advances in computational resources and computational physics has also made calculations of realistic catalysts at the level of electronic structure relatively routine and standardized. Despite limitations to these methods, continuous improvement has allowed for the development of new physical and chemical insights into the structure and function of catalysts which were not possible previously. The spectroscopy of catalysts, including TEM synchrotron techniques such as high resolution X-ray diffraction (XRD), X-ray absorption near-edge structure (XANES), Extended X-ray absorption fine structure (EXAFS), and most recently Resonant Inelastic X-ray Scattering (RIXS) provide unprecedented detail and control for understanding catalysis. Coupled with advances in the synthesis of these materials, there are many new tools and depth of understanding to address these classical problems.

### 1.3 Theory and computation in catalysis

### 1.3.1 Density Functional Theory

Computational approaches to the solution of physics problems began in earnest with the calculation of scattering probabilities for collisions necessary in the development of atomic weapons[23]. Despite the best efforts of parameterized models, simplifications, and reformulation, the of large nuclei at the level required to design the atomic bomb proved difficult without computation. General solutions to the Schrödinger wave equation were elusive for all but the simplest models involving no more than a handful electrons, and so computation became a necessary technique for any practical quantum mechanical calculation. As a quantum system obeys the variational principle first developed in Newtonian physics, and it is possible to find the wavefunction that minimizes the total energy of a given system[24]. The variational principle guarantees the existence of a unique state for the system where the energy cannot be decreased, a ground state. We can define a basis set, preferably one that is complete and orthogonal, such as the spherical harmonics or Chebyshev polynomials, and use standard variational calculus to determine form of wavefunctions that define the ground state subject to the (time-independent) Schrodinger equation:

$$H\Psi = E\Psi \qquad (1.1)$$

where H defines the Hamiltonian of the system, analogous to the classical mechanical case, an operator for the kinetic and potential energies of the system, and the electron wavefunction $\Psi$, a nebulous quantity that can be related to the electronic density by its square.

The variational principle is necessary to solve problems in quantum mechanics where electrons and nuclei interact, and the consideration of electron-electron interactions quickly becomes untenable for any more than a few individual electrons. A general form of a many-electron Hamiltonian in the form expressed by Thijssen[24] is reproduced here:

$$H = \sum_{i=1}^{N} \frac{p_i^2}{2m} + \sum_{n=1}^{K} \frac{p_n^2}{2m_n} + \frac{1}{4\pi\varepsilon_0} \frac{1}{2} \sum_{i,j=1;i\neq j}^{N} \frac{e^2}{|r_i-r_j|} - \frac{1}{4\pi\varepsilon_0} \sum_{n=1}^{K} \sum_{i=1}^{N} \frac{Z_n e^2}{|r_i-R_n|} +$$

$$\frac{1}{4\pi\varepsilon_0} \frac{1}{2} \sum_{n,n'=1;n\neq n'}^{K} \frac{Z_n Z_{n'} e^2}{|R_n-R_{n'}|} \qquad (1.2)$$

where the first two terms relate the kinetic energies of electrons and nuclei, the third term is the electron-electron interactions, the fourth term is the favorable electron-nucleus interactions, and the final term is the nuclear-nuclear interactions. Typically, coupling between electrons and nuclei is separated, as electrons are much faster moving than nuclei, and thus from the reference frame

of the electrons, nuclei are stationary. This is the so-called Born-Oppenheimer approximation, which dramatically simplifies the Hamiltonian of a multi-electronic system. Again in the form of Thijssen[24], our simplified Hamiltonian can be expressed by the following expression

$$H_{BO} = \sum_{i=1}^{N} \frac{p_i^2}{2m} + \frac{1}{4\pi\varepsilon_0} \frac{1}{2} \sum_{i,j=1; i \neq j}^{N} \frac{e^2}{|r_i - r_j|} - \frac{1}{4\pi\varepsilon_0} \sum_{n=1}^{K} \sum_{i=1}^{N} \frac{Z_n e^2}{|r_i - R_n|} \qquad (1.3)$$

where now the total energy is defined as the energy of electrons in a spatially varying field of charge exerted by the nuclei. To account for electrons being fermions, each electronic state must be antisymmetric, which is due to each electron having a spin and orbital component. Typically, wavefunctions will be restricted to a Slater determinant which ensures each individual orbital is antisymmetric and correlation between electrons is included. As described by Thijssen, each electron is "surrounded by an 'exchange hole' in which other electrons having the same spin are hardly found"[24]. The inclusion of the Slater antisymmetry into the Hamiltonian expression gives rise to the Hartree-Fock equation, one of the earliest quantum chemistry methods capable of predicting the electronic states of a many-electron system. A particularly lucid derivation of the Hartree-Fock equations is provided by Szabo and Ostlund[25]. The foundation of the Hartree-Fock method is still relevant in modern solid-state physics and quantum chemistry despite it being entirely eclipsed by newer methods for solving the Schrodinger equation.

While the Hartree-Fock equation proved immediately applicable to studying the electronic interactions of molecules, the electronic interactions and nonlocal interaction of the Hartree potential made application to solids difficult. In metals, electronic bands due to delocalized bonding were observed, which could not be treated with direct application of the Hartree-Fock equations. This challenge motivated the development of more advanced methods, such as Density Functional Theory (DFT). Many consider DFT to have emerged in a vacuum, but here I would like to discuss in brief the other methods which were foundational to modern DFT theory. Korringa had derived expressions for early band structures in metal which satisfied Bloch's theorem that electron wavefunctions are periodic when repeating in the primitive reciprocal lattice space or so-called Brillouin zone[26]. Korringa was able to show how the electronic structure of a metal depended on the its reciprocal lattice units, which provided directions for future electronic structure methods. Studies of the homogenous electron gas (HEG) where the correlation of electronic states could be analytically solved would later be necessary for DFT exchange and correlation functionals. The text by Martin provides a particularly illuminating discussion of how computational solid state physics techniques developed[27]. While band structure methods were

successful in predicting the electronic structure of simple metals, such as the alkali earth metals, they were unable to predict metals with stronger electronic correlation and Hartree exchange, such as oxides, alloys, and surfaces of metals, where the metallic electronic states were significantly different from a bulk metal due to the undercoordinated metal atoms localizing electronic states.

Hohenburg and Kohn proved that the electron density can be variational, where a unique and universal functional of the electron density has a minimum ground state energy[28], [29]. This finding would dramatically improve the development of new electronic structure methods, as now the total energy of the system can be expressed in terms of the electron density instead of individual wavefunctions. The Kohn-Sham equation represent a fictitious system, that approaches the exact Schrödinger wave equation with the correct choice of exchange and correlation functional. The total energy can be expressed by the following expression, again taken from Thijssen[24]

$$\left[ -\frac{1}{2}\nabla^2 - \sum_n \frac{Z_n}{|\boldsymbol{r}-\boldsymbol{R}_n|} + \int d^3r' n(\boldsymbol{r}') \frac{1}{|\boldsymbol{r}-\boldsymbol{r}'|} + V_{xc}[n](\boldsymbol{r}) \right] \Psi_k(\boldsymbol{r}) = \varepsilon_k \Psi_k(\boldsymbol{r}) \tag{1.4}$$

where the electron density n(**r**) is the total electron density calculated by the expectation value of the individual wavefunctions

$$n(\boldsymbol{r}) = \sum_{k=1}^{N} |\Psi_k(\boldsymbol{r})|^2 \tag{1.5}$$

The simplification imparted by considering the electron density instead of the electron wavefunctions cannot be understated. In a multi-electron interacting system each wavefunction will exist as a 3-D scalar field, and for atoms with as many electrons as platinum, the number of independent parameters becomes unreasonably large, especially when considering the explicit Hartree exchange and correlation constraints. The Kohn-Sham equation maps this into a single 3-D scalar field, significantly reducing the complexity of electronic structure calculations. Here the first term is the kinetic energy of electrons, the second term is the electron-nuclear interactions, and the third term is the approximate electrostatic interaction of an electron with the field of surrounding electrons, and the forth term is the exchange and correlation (XC) functional. This term includes electron self-interaction as the field including all electron interactions. A correct choice of $V_{XC}$ would remediate the simplistic electron self-interaction introduced by using the electron density, however an exact form of the XC functional is not known. Limits for the exchange interaction can be taken from quantum Monte-Carlo simulations of the HEG where the exchange interactions scale with the third root of the electron density[24].

The electron-electron self-interaction is typically referred to as the Hartree potential, where the density of a single orbital is related to the field of charge exerted by the surrounding electrons. From Thijssen[24]

$$V_H(\boldsymbol{r}) = \int d^3r' n_s(\boldsymbol{r}') \frac{1}{|\boldsymbol{r}-\boldsymbol{r}'|} \tag{1.6}$$

where $n_s$ denotes the density of a specific orbital. As Thijssen shows, this is a generalized Poisson equation, which we can solve for the shape of the potential. I find this particularly satisfying as often the mechanical solution of these expressions can often be divorced from their functional expressions. The Poisson form of the Hartree equation, given by Thijssen, is written as

$$\nabla^2 V_H(\boldsymbol{r}) = -4\pi n_S(\boldsymbol{r}) \tag{1.7}$$

This form is far more familiar to engineers with a background in transport. While the derivation of the Local Density Approximation (LDA) and Generalized Gradient Approximation (GGA) for the exchange and correlation functional are exciting, they are beyond the scope of this thesis. So far the salient details I have shown are that the variational principle through choice of a basis set of orthonormal functions can be used to solve an analogue of the Schrodinger equation where the one-electron densities are varied using the Kohn Sham equation which is functionally equivalent to the Schrödinger equation in the limit of an exact choice of XC functional. The basis set of functions most amenable to periodic solids are plane wave functions which reflect the periodic wavefunctions in the expected solutions. For heavy elements, electrons closest to the core become relativistic, and poorly converge with the number of plane waves. A pseudopotential is often invoked, in which the core electrons of an element are replaced with an effective potential of known density which is assumed to be invariant to chemical bonding. This is often a good approximation for elements such as Pt, where the core electrons are shielded from interactions, and typically it is the valence electrons which participate in bonding. Still, the energy range of basis functions to treat the electron density is a necessary parameter to be provided by the researcher. As electron wavefunctions are periodic across the Brillouin zone, multiple points in the Brillouin zone must be sampled to model the realistic periodicity of electron wavefunctions in solids. These k-points in the Brillouin zone must be specified to ensure realistic periodic wavefunctions are calculated. The spin of electrons, especially for magnetic metals, radicals, and the treatment of bond-breaking/bond-formation becomes important and must be accounted for in the DFT code.

Perhaps most important is the correct choice of XC functional. GGA-level functionals which use the gradient of the electron density have been traditional used for modeling chemical bonding and transition states due to its appropriate balance of performance and predictable sources of error. Higher order methods using the Laplacian of the electron density (so-called meta-GGA) functionals have not shown significant improvement, although the SCAN functional developed by Perdew[30] looks to be the most promising implementation of a meta-GGA thus far. Specifically for the chemisorption of molecular species on metal surfaces, benchmark studies by Norskov, Campbell and coworkers have shown that among a suite of GGA level functionals, functionals which incorporate van der Waals (vdW) interactions self-consistently in the functional such as BEEF-vdW[31] are able to accurately treat the adsorption enthalpy of molecular intermediates on metal surfaces. In fact, the development of more accurate GGA functionals which include vdW interactions is what has provided avenues for the calculation of adsorption in microporous environments. GGA functionals; however, do not include rigorous non-local exchange, which is implicit in the Hartree-Fock equation. Hybrid functionals, which use a screened short-range exchange, can treat periodic systems where the localization of electrons in chemical bonds are poorly captured with typical GGA functionals[32], [33]. The calculation of even local Hartree-Fock exchange is more computationally demanding than other GGA functionals. This makes hybrid functional calculations better suited as a benchmark for GGA results, to determine how well the GGA functional can capture the dominant electronic effects in the system. For systems such as metals without a bandgap, the utility of hybrid functionals is less clear, as typically excessive localization can result in unphysical behavior in metals. In metals, it is the correlation of periodic electrons which comprise the dominant many-body interactions, and for these system quantum Monte-Carlo (QMC) methods are of interest as they can directly evaluate these many-body correlation effects not captured with GGA functionals[34]. The computational complexity of QMC calculations are so extreme at this time that they cannot realistically be used even for benchmarking purposes. The hybrid functionals and QMC techniques, however, give an indication of what future methods may become feasible. The search for a "perfect" XC functional remains a highly elusive, and likely an unreasonable goal. For computation in computational catalysis, there will always be niche systems where strong exchange or correlation is dominant; however, for many catalysts of interest, it is the size and scale of these systems that are a more formidable set of hurdles.

### 1.3.2 Catalyst models with Density Functional Theory

For a realistic supported metal catalyst, a 2 nm nanoparticle supported by the catalyst can be on the order of ~600 atoms. Zeolites, metal-organic frameworks (MOFs), and other microporous materials with distributions of active metal sites can also span hundreds to thousands of atoms. Typical techniques to address this materials gap has included modeling individual facets of metal surfaces, where the adsorption of molecules to each surface facet can be computed to provide an ensemble of possible sites that may adsorb. For bifunctional catalysts where the support/metal interface is important, a nanowire which captures the local structure at the interface can provide quantitative evidence for adsorption at the interface. For microporous materials, bulk unit cells of the pure crystal have been used as well as clusters cut from the crystal structure which capture the local chemical environment. Each of these models must be generated with careful consideration of the real system, and reflects the goal of constructing a model, to capture the details that are important to address without introducing all the additional complexities that obfuscate the key effects to be studied. It is not realistic to wait until computational methods can model a "realistic" system of a full catalyst particle with hundreds of thousand or million atoms at the level of full QMC, propagated in time using molecular dynamics for hours when it is the adsorption energy of oxygen at a single Pt(111) ensemble at equilibrium that can predict the kinetics of a chemical reaction. By constructing appropriate models that are designed to attack the fundamental questions that define the electronic structure of relevant reactive intermediates and transition states, an understanding of how to predict the properties of new catalysts emerges.

One technique for connecting models of adsorption and transition states to macroscopic experimental kinetics is through microkinetic models[35]. Microkinetic modeling refers to the use of rate and equilibrium constants, either calculated or computed, to construct a reaction network that can be used to model the catalyst under reaction conditions. Experimental microkinetic models have been used by Bhan and coworkers to understand routes for propane aromatization on H-ZSM-5[36], while Broadbelt and coworkers have used network theories to make kinetic models with computation and experimental data for vast reaction networks to predict product selectivities and reaction mechanisms for biologically derived chemical intermediates[37]. The pioneering work in combining both the reactor equation methods and DFT calculation of rate and equilibrium constants comes from the work from the Mavrikakis group, who showed how microkinetic models derived from DFT calculations could be used to connect with experimental kinetics[35]. This

thesis will draw heavily from the ideas from this group and their combination of quantum mechanics, statistical mechanics, and kinetic theory to calculate macroscopic observables. DFT-derived microkinetic models have been incorporated into a diverse space of chemical reactions and catalysts, such as the work by Hansen, Norskov, and Bligaard to understand the selectivity of non-oxidative dehydrogenation of ethane on metals where a microkinetic model is necessary to predict product selectivities[38], or recent work by Besora and Maseras in applying microkinetic modeling for homogeneous catalysis when determination of the dominant kinetic pathway cannot be derived from a free energy analysis[39]. It is worth remembering that a microkinetic model is still a model, and cannot capture every possible interaction that affects catalysis, but can provide chemical and kinetic insight that is either not directly accessible to experimental studies, or substantially easier to analyze with computation. Throughout these chapters I will discuss the importance of coupling microkinetic models with experimental studies to determine the limits of the computational models, and target what features of the catalysis are likely to be most relevant.

Models for how changes in the electronic structure of a catalyst surface (for example by changing the metal, and consequently the number of *d* electrons) affect the adsorption of intermediates is another avenue for building a physical and chemical understanding of catalysis. The most successful model for describing changes in gas phase adsorption energies on metals is the d-band model, developed by Hammer and Norskov[40]–[42]. The d-band method is itself a simplification of Newns-Anderson model of molecular adsorption[43], [44] of which a full derivation is beyond the scope of this thesis. The salient features of the Newns-Anderson model is that linear combinations of atomic orbitals are insufficient for considering the adsorption process, and that a spectrum of energy levels from the metal interact with adsorbate[43]. This result states that it is the coupling of all d-states, when properly normalized, that interact with the localized atomic adsorbate states to define the chemisorption energy. The spectrum of d-electron densities of a metal, the density of states (DOS) can be readily calculated with DFT. Hammer and Norskov showed how the chemisorption energy of adsorbates was quantitatively related to the mean of the d electron DOS, referred to as the d-band center. This d-band center was proposed as a simplified descriptor for bonding between metals and adsorbates, which reflects the Newns-Anderson result of coupling the spectrum of metal states with localized adsorbates.

One application of the d-band theory is for scaling relationships, which predict the chemisorption of similar chemical intermediates[45]. The first scaling relationships were derived

for the adsorption of methane-derived ($CH_x$) and ammonia-derived ($NH_x$) intermediates, among others, on transition metal surfaces. The adsorption energies of $CH_x$ intermediates were found to vary linearly with each other, across the range of metals, with slopes related to bond-order conservation[45]. For example, when relating the adsorption of atomic carbon (C*) to methylidine (CH*) the maximum number of bonds formed by atomic carbon is 4, an methylidine must make 3 bonds to the surface to maintain its valence structure, which results in a slope between the two intermediates of 0.75. The observed linearity was described using the d-band model, where the coupling of metal states with adsorbates is proportional to the sum of individual adsorbate states[45]. Scaling relationships can be coupled with classical Bronsted-Evans-Polanyi (BEP) relationships which relate reaction energies with transition state energies. This provides an avenue for rapidly screening catalysts based on a limited set of reactive intermediates linearly related by scaling relationships, and then connected to transition states to provide kinetic screening. Rosen, Notestein, and Snurr have used scaling relationships and BEPs to predict the kinetic barriers for methane activation across a wide and structurally diverse set of MOFs to inform experimental synthesis efforts[46]. Predictive catalysis efforts have also become more connected with the general rise of data science and machine learning to predict the energies of reaction networks using the minimum set of DFT computations. Recently Chowdhury et al. showed how important the set of adsorption descriptors and careful tuning of machine learning techniques using cross-validation to prevent overfitting is key to expanding the scope of predictive computational design[47].

So far, I have shown how quantum theory can be extended to the level of machine learning and predictive catalyst design; yet this introduces the question of what role theory has in catalysis, and how that is changing over time. Medvedev and Bushmarinov wrote a critique in which they state that DFT is straying from the path of predicting rigorous chemical properties, and most modern functionals are empirical approximations[48]. This review of functionals reflects a shifting perspective in the computational catalysis community as to whether DFT's ultimate purpose is to provide fundamental chemical and physical insight, or as a tool for efficient screening and identification of kinetically interesting catalysts. It is of my opinion, that the computational catalysis field has grown to the extent that these routes are not mutually exclusive. DFT will always find a use in fundamental physical chemistry, yet the further development of predictive screening using data science and machine learning has tremendous untapped potential to aid the synthesis and reaction network analysis of many problems in catalysis. If anything, I think both sides need

to be closely linked, as many current machine learning studies of catalysis show that the design of descriptors and parameter-spaces is still best enumerated using chemical intuition from the researcher, and then allowing neural networks to pare down the space of possible descriptors to find a minimal set that can then be screened across. Such techniques are widely used in the materials community, for example the resent work by Vieten et al to screen perovskites using Materials Project based on their redox enthalpies[49]. With precise physical descriptors derived from microkinetic models developed in close collaboration with experiment, and better-organized databases of DFT calculations and machine learning algorithms to explore those descriptors, the role of computational modeling as both an explanatory and predictive technique in catalysis can become more useful to the field.

## 1.4   Scope of this thesis

From the methods and techniques discussed in this introduction, fundamental studies of active sites in unique catalyst environments will be described in in detail. We begin with the derivation of scaling relationships in zeolites (CHAPTER 2) which include families of dissociative-adsorption reactions in both Lewis and Bronsted acid functionalized zeolite Chabazite (CHA). The hydrolysis of water to form a hydrolyzed open site is observed, which has been discussed as a potential active site for Lewis acid zeolites. The high degree of correlation in these scaling relationships reflect the isolated sites in zeolites where coadsorption effects such as those on metal surfaces are not present. The kinetic relevance of different speciations of Sn sites in zeolite Beta is considered in CHAPTER 3 where a comprehensive microkinetic model of ethanol dehydration is constructed in tandem with experimental kinetic studies, which include the anharmonicity in zeolite Beta. In CHAPTER 4 ethanol dehydration in Sn-Beta is extended to grain boundary sites, where hydrolysis is not possible, and these grain boundary sites stabilize fundamentally different transition states due to their location in the zeolite framework. In CHAPTER 5 the intuition gained from studying ethanol dehydration is applied to a substantially more demanding reaction network, the production of butadiene from ethanol in zeolite Beta. Here the hydrolysis of active sites plays a crucial role to stabilize transition states. Using a microkinetic model, and the insight that the stability of hydrolyzed sites and enolates control reactivity toward butadiene, CHAPTER 6 uses the local strain on sites in zeolites to explain differences in

hydrolyzed site stability among different zeolite frameworks, to predict better butadiene catalysts from frameworks that allow more stable hydrolyzed sites.

The structure of water both in nearly condensed and liquid phase is calculated in CHAPTER 7 to understand how defects nucleate clustering and hydrogen bond networks in Beta. These insights are used to make local solvent models which have a defined thermodynamic state. The entropy of adsorption of deuterated acetonitrile is considered in CHAPTER 8 and the importance of using different entropy approximations which include anharmonicity is compared with experimental measurements. The local solvent models are then applied to aluminum-containing H-Beta where experimentally observed activity coefficient ratios in partially condensed solvents for ethanol dehydration are explained by AIMD techniques to study the thermodynamic mixing of intermediates and transition states with well-defined water clusters. (CHAPTER 9)

A new spectroscopic technique (Resonant Inelastic X-ray Scattering, RIXS) was performed on Pt and PtZn intermetallic alloys where the electronic bands of Pt could be directly observed to shift upon alloying. DFT calculations and modeling of the RIXS process was performed to provide chemical intuition into how trends in the spectroscopy were related to shifts in the $d$ states of platinum (CHAPTER 10). $Pt_3Mn$ intermetallic alloys were then studied with differing numbers of pure-Pt and $Pt_3Mn$ to show how dehydrogenation reaction stability and adsorption can be controlled by catalyst underlayers (CHAPTER11). Experimental RIXS studies across a range of 3d promoter metals were measured, provided a large database of Pt electronic shifts which could then be compared with DFT modeling techniques, where the correlation between DFT-predicted and experimental RIXS peaks is quantitative. This is used to develop descriptors for chemical adsorption which are based on the RIXS process and are therefore accessible to validation by both theory and experiment (CHAPTER 12).

Finally, the structure of gold clusters at 200 C in the MFI zeolite framework (Au/TS-1) will be discussed where AIMD and Metadynamics were used to show facile gold diffusion based on calculated diffusion barriers at reaction conditions (CHAPTER 13). An overall perspective on the role of computation in understanding catalytic active sites is then presented in the Final Remarks (CHAPTER 14).

# 2. SITE SPECIATION AND SCALING RELATIONS IN LEWIS ACID ZEOLITES

## 2.1 Introduction

Zeolites are a class of microporous crystalline solid acid materials composed of tetrahedrally coordinated silicon oxide building blocks[50], [51]. The silicon oxide framework itself is generally inert, but a common strategy to make zeolites catalytically active is to introduce point defects via isomorphic substitution of heteroatoms for silicon[52]–[54]. Heteroatom substitutions, in turn, are classified according to their acid functionality. Metals in a $3^+$ oxidation state generate OH groups in the framework which behave as Brønsted acids, while metals in a $4^+$ oxidation state behave as Lewis acids[17]. The best known example of such an exchange is the substitution of silicon with aluminum. In order to balance charge in the framework, oxygen atoms adjacent to the aluminum are bonded to a hydrogen atom, allowing these defects to behave as Brønsted acids[55]–[57]. However, new synthesis methods are permitting an ever-expanding number of heteroatoms to be substituted into the zeolite frameworks, including various Lewis acid heteroatoms[58], [59].

First principles methods have made an increasing contribution to developing understanding of the properties of these different classes of acid sites in recent years, describing phenomena ranging from acid site strength to activity/selectivity patterns of complex reaction networks[60]–[66]. These and other studies employ a variety of first principles methods. Traditional cluster models are effective in describing localized catalytic properties of acid sites, but these models often fail to accurately describe long range dispersive interactions that are sensitive to pore sizes and shapes[67]. A variety of methods have been developed to circumvent this difficulty, including QM/MM approaches[68], [69] and hybrid MP2:DFT calculations[70]. Alternatively, some studies treat the entire material with fully periodic boundary conditions. The periodic treatment, coupled with use of hybrid functionals[32] or semi-empirical van der Waal's (vdW) corrections[71], allows for a more rigorous description of long range dispersion and exchange interactions. Such

treatments are particularly attractive for zeolites with relatively small unit cells, including chabazite (CHA), which contains 8, 6, and 4 member silicon oxide rings and a total of 108 atoms per unit cell. CHA also contains a single crystallographically distinct T-site[72], significantly limiting the number of heteroatom substitution sites that must be considered in catalysis analyses.

Previous studies have provided a great deal of insight into the properties of zeolites with a limited number of heteroatom substitutions, but there remains a need to develop a fundamental set of principles that can be used to establish trends in zeolite catalysis across a large space of such substitutions. One class of catalytic reactivity trends, which has been comprehensively developed on metal and some oxide surfaces, is that of scaling relationships[73], [74]. In creating a scaling relationship, one hopes to correlate similar properties, such as reaction enthalpies or adsorption energies[64], [65], [75], [76], across a large number of similar catalytic materials. These relationships were first developed on close-packed and stepped transition metal surfaces[45] and were later extended to metal oxide surfaces[76]. Molecules or radicals of $CH_x$, $NH_x$, $OH_x$, and $SH_x$ were adsorbed onto metal surfaces and exhibited different slopes when their adsorption energies were plotted against the adsorption energies of their saturated molecular analogs, such as $CH_4$ in the case of $CH_x$ species. These slopes were explained according to a bond counting rule and are related to the number of bonds in the adsorbate relative to that of the reference molecule. The intercepts of the scaling relationships, on the other hand, have been understood in terms of the local coordination number of the adsorbate on different surface facets, thus introducing a structure-sensitivity to the correlations[77]. One can therefore decompose the scaling relationships on simple metals and oxides in terms of a slope related to the electronic structure of the adsorbate and an intercept related to the geometric structure of the surface.

In the present contribution, we extend the domain of scaling relationships from simple metal and metal oxide surfaces to zeolite-based materials, and we demonstrate that linear scaling trends exist for a wide range of heteroatoms in the CHA framework. Motivated by the known ability of Lewis acids to dissociate organic compounds and to activate OH and CH bonds in carbonyl compounds[17], as well as the general importance of sulfur-containing species for industrial desulfurization and for $NO_x$ SCR catalysts in vehicles[78]–[80], we focus on activation of various OH, CH, and SH-containing moieties in heteroatom-based Lewis acid sites. To demonstrate the generality of the obtained relationships, we further provide a brief comparison of similar dissociative mechanisms on Brønsted acid sites. Finally, we present a simple demonstration of

how the scaling relationships may be applied to efficiently estimate trends in the catalytic properties of a range of Lewis acid-based CHA structures.

## 2.2    Methods

All calculations are performed using self-consistent, periodic Density Functional Theory (DFT), as implemented within the Vienna Ab-initio Simulation Package (VASP)[81]–[84]. The Bayesian Error Estimation Functional (BEEF-vdW)[31], which explicitly accounts for dispersion interactions within the self-consistent electronic structure cycle, is employed for most of the calculations. In addition, a subset of calculations are performed using a hybrid functional with a screened coulomb potential, (HSE06)[85]; the same convergence parameters are used for both functionals unless otherwise noted. For all calculations, the Projector Augmented Wave (PAW) core potentials[86], [87], developed from PBE[88] calculations, are used. The defect-free CHA unit cell is relaxed along all lattice vectors, and dimensions of 13.76 Å, 13.77 Å, 14.88 Å along the a, b, c unit vectors are obtained. The optimized cell volume is within 2.3% of the cell volume reported in the International Zeolite Association Database. Upon heteroatom doping, a full atomic relaxation, with fixed lattice vectors, is performed to simulate a low silicon/metal ratio. Forces on all atoms are fully converged to 50 meV/Å. A plane wave cutoff energy of 520 eV is employed for all calculations, and this value is confirmed to converge binding energies to within 0.05 eV in all cases.  The same cutoff is applied to the bulk unit cell optimization, and convergence of the Pulay stress with respect to the cutoff energy is confirmed. Single gamma point Brillouin zone sampling is found to be sufficient to converge electronic energies. All calculations are performed spin-polarized. Gas phase calculations were performed with a Fermi smearing of 0.1 eV with the same unit cell and cutoff energy. Gas phase calculations were converged to within 0.01 eV with respect to Fermi smearing width.

Reaction energies are calculated by taking the separated zeolite and gas molecules in vacuum as the thermodynamic reference states. Thus, adsorption energies are determined according to the relationship

$$\Delta E_{ads-dissoc} = E_{(A+H)*} - E_{AH} - E_*$$ (1)

where $\Delta E_{ads-dissoc}$ is an adsorption-dissociation reaction energy, * is the zeolite acid site, and AH is the gas phase molecule.  To preserve charge neutrality, A and H are always coadsorbed on the

zeolite framework. Dissociation reactions for molecules with similar bond connectivities are plotted against each other to produce scaling relationships of the form

$$\Delta E^B_{ads-dissoc} = \gamma \Delta E^C_{ads-dissoc} + \xi \qquad (2)$$

Here, the two dissociative reaction energies, $\Delta E^B_{ads-dissoc}$ and $\Delta E^C_{ads-dissoc}$, can be thought of as adsorption energies of species B and C. The slope $\gamma$ can be understood on the basis of bond counting arguments provided elsewhere[76].

During optimization of each adsorbate, a set of high symmetry configurations are initially selected based on simple physical criteria, including adsorption of hydrogen atoms on oxygen atoms adjacent to the heteroatom and placement of OH ligands in symmetrically distinct locations around the heteroatom. Due to the complex three dimensional nature of the CHA framework, however, the search for stable adsorption geometries is augmented by a set of low temperature, short timescale, ab-initio molecular dynamics (AIMD) runs which provided additional information about the potential energy surface around the acid site. To bolster the initial set of configurations, AIMD runs are carried out at 250K using a Nose-Hoover thermostat as implemented in VASP[89]. A constant stepsize of 0.75fs is used, and the simulation is run for 1ps. Geometries are then extracted from the AIMD run and individually optimized as described previously.

## 2.3   Results

The chabazite unit cell is composed of two primary building units, a hexagonal block and a block with four and eight membered rings which form a large open chamber. CHA has a single distinct T-site, and in previous literature the heteroatom exchange has been made at the eight membered ring[65], [90, p. 3]. Molecular and dissociated species, including $H_2O$, $CH_3OH$, $CH_4$, $H_2S$, $CH_3SH$, $CH_2O$, $CH_3CHO$, $CHOH$, and $CH_2$, are adsorbed at this T site. The first five species are common to a variety of petrochemically-relevant reactions, while the latter four exhibit additional complexity due to either size, as with $CH_3CHO$, or open shell character, as with $CHOH$ and $CH_2$. To ensure charge neutrality in the zeolite framework, hydrogen is always coadsorbed on the oxygen atom adjacent to the heteroatom after dissociation of the parent molecule. As mentioned above, the reported energies are, therefore, more akin to a dissociative adsorption energies than to the simple adsorption energies reported in previous scaling studies[73], [74], [76]. Detailed results are presented in the following discussion and figures, while the overall trends for all scaling relationships are summarized in Table 2.1.

Figure 2.1 shows the reaction energies for dissociative adsorption, corresponding to O-H scission, in methanol and water in Lewis acid-based CHA frameworks. Substitutions with Sn, Ti, Hf, Zr, Ge, Si, Pb, Re, and Th are considered. Using a Bader charge analysis, we confirm that these heteroatoms have a +4 oxidation state when substituted into the CHA cage, confirming that they function as Lewis acids (see APPENDIX A). Illustrative structures for O-H activation on Zr-substituted CHA are included in subplots B and C of Figure 2.1 for water and methanol dissociation, respectively. Both dissociated products bind through oxygen, producing hydroxy and methoxy ligands on the heteroatom. Dissociated hydrogen atoms, on the other hand, are bound to the adjacent oxygen, causing an elongation of approximately 0.25Å in the heteroatom-oxygen bond. For these Lewis acids, an excellent scaling relationship exists between the water and methanol dissociative adsorption energies. The slope is 1.05, and the intercept is -0.16 eV; the standard error both quantities is less than 0.04.
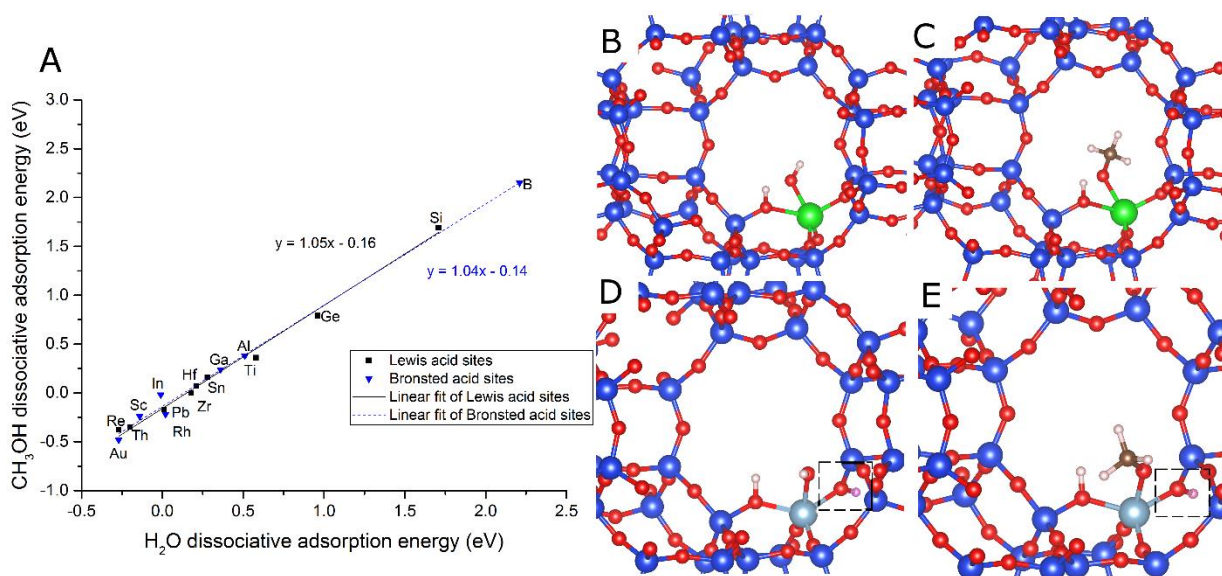


Figure 2.1 O-H bond activation for water and methanol in chabazite as calculated with BEEF-vdW. (A) Dissociative adsorption energies on Lewis acid heteroatoms (black squares) and Brønsted acid heteroatoms (blue triangles) are plotted along with separate linear regressions for each heteroatom type. (B) Water dissociation on a Zr Lewis acid site. (C) Methanol dissociation on a Zr Lewis acid site. (D) Water dissociation on an Al Brønsted acid site. (E) Methanol dissociation on an Al Brønsted acid site. The Brønsted acidic hydrogen is highlighted in pink and is inside of the dashed box in subplots (C) and (D).

For comparison, a smaller set of Brønsted acid-type heteroatoms are also included in the analysis, with representative geometries shown for water and methanol dissociation on aluminum

in panels D and E of Figure 2.1 (the acidic hydrogen is highlighted in pink and is outlined by a dashed box). We note that the oxygen atoms receiving the dissociated hydrogen are the same as with the Lewis acids, leaving three possible oxygen atoms for the acidic hydrogen atoms to reside. The energetic difference between these sites is found to be minimal (see APPENDIX A). The slope of the scaling relationship is 1.04, and the intercept is -0.14 eV, with standard errors of less than 0.04.

A slope of 1.0 is expected for both Lewis and Brønsted heteroatoms according to the bond counting arguments advanced originally by Abild-Pedersen et al[73].  In that analysis, adsorption energies of $CH_x$ species, referenced to gaseous methane and molecular hydrogen, are plotted against the adsorption energies of atomic carbon with the same reference state, resulting in a slope of $(x_{max}-x)/x_{max}$, where x is the number of bonds between carbon and hydrogen and where $x_{max}$ is four for carbon.  In the present work, both species plotted in Figure 2.1 have the same values of $x_{max}$ and x.  The maximum number of bonds formed by oxygen in methanol and water ($x_{max}$) is two, while the number of intramolecular bonds to oxygen once dissociation occurs is one for both species. This implies a slope of unity when adsorption-dissociation energies are plotted on each axis, in excellent agreement with the calculated results.

Figure 2.2 shows a scaling relationship for SH bond activation in $CH_3SH$ and $H_2S$.  The slope of the correlation for Lewis acids with different heteroatoms is again close to 1.0, as expected from bond counting arguments.  For comparison, a set of Brønsted acid heteroatoms is also included in Figure 2.2, subpanels D and E, with the acidic hydrogen atom highlighted in pink and contained within the dashed box. While the slopes of the Lewis and Brønsted acid scaling relationships are quite similar, there is a difference in the intercepts of 0.47eV. This difference may be due, in part, to the formation of a hydrogen bond between the Brønsted proton and the adsorbed thiomethoxy group; this stabilization does not exist in dissociated $H_2S$ due to the longer bond length between the Brønsted proton and the SH group.  Likewise, the proton/OH distance in dissociated methanol is larger, limiting the influence of this hydrogen bonding interaction in the methanol/water scaling relationship, and resulting in similar intercepts for the Lewis and Brønsted scaling relationships (Figure 2.1).
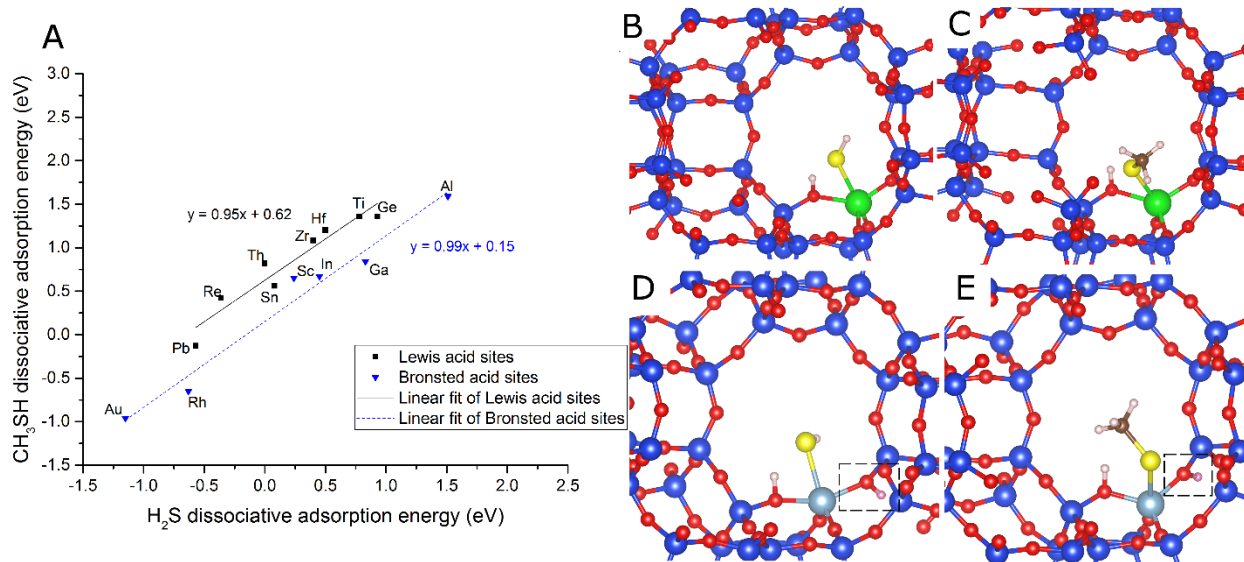
Figure 2.2 SH bond activation for hydrogen sulfide and methane thiol as calculated with BEEF-vdW. (A) Dissociative adsorption energies on Lewis acid heteroatoms (black squares) and Brønsted acid heteroatoms (blue triangles) are plotted along with separate linear regressions of each heteroatom type. (B) Hydrogen sulfide dissociation on a Zr Lewis acid site. (C) Methane thiol dissociation on a Zr Lewis acid site. (D) Hydrogen sulfide dissociation on a Al Brønsted acid site. (E) Methane thiol dissociation on a Al Brønsted acid site. The Brønsted acidic hydrogen is highlighted in pink and is inside of the dashed box for subplots D and E.

Figure 2.3 shows energetics for C-H bond activation in methane and methanol. Methane and methanol groups bind through carbon with the methanol group free to hydrogen bond with the dissociated hydrogen. An elongation of the protonated oxygen-metal bond by 0.25Å is observed. The calculated slope of the scaling relationship is 0.96, with a standard error of 0.05, in excellent agreement with the theoretical slope of unity deduced from bond counting arguments.
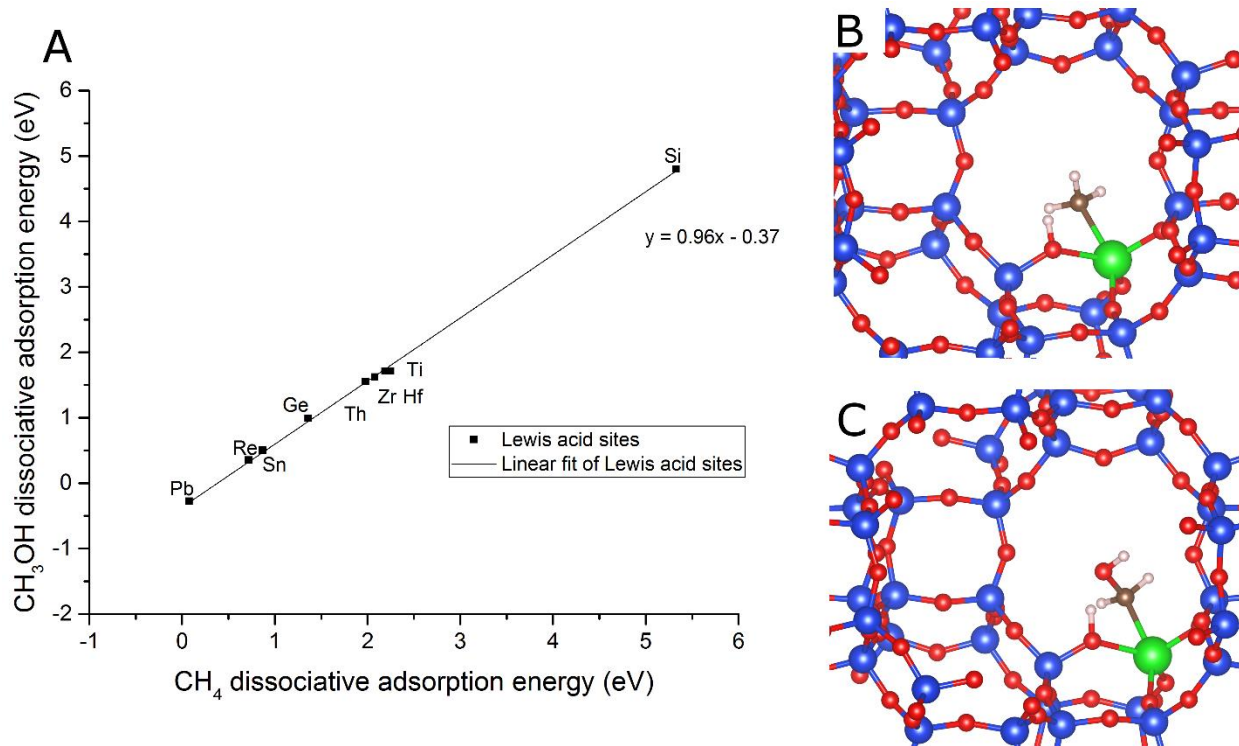
Figure 2.3 C-H bond activation for methane and methanol as calculated with BEEF-VdW. . (A) Dissociative adsorption energies on Lewis acid heteroatoms (black squares) and Brønsted acid heteroatoms (blue triangles) are plotted along with separate linear regressions of each heteroatom type. (B) Methane dissociation on a Zr Lewis acid site. (C) Methanol dissociation on a Zr Lewis acid site.

To evaluate the applicability of scaling relationships to larger adsorbates in zeolites, we have evaluated dissociative adsorption energies for formaldehyde and acetaldehyde on a series of Lewis acid-substituted chabazite structures. Both formaldehyde and acetaldehyde exhibit similar conformations when adsorbed on the heteroatom, as the methyl moiety on acetaldehyde does not sterically impact the adsorption configuration to an extensive degree. Both carbon and oxygen atoms appear to interact with the heteroatom, and for both formaldehyde and acetaldehyde, the R group (hydrogen for formaldehyde and methyl for acetaldehyde) is positioned at 90° relative to the CO bond. The quality of the scaling relationship is again very good, and the calculated slope is found to be close to the ideal value of 1.0.
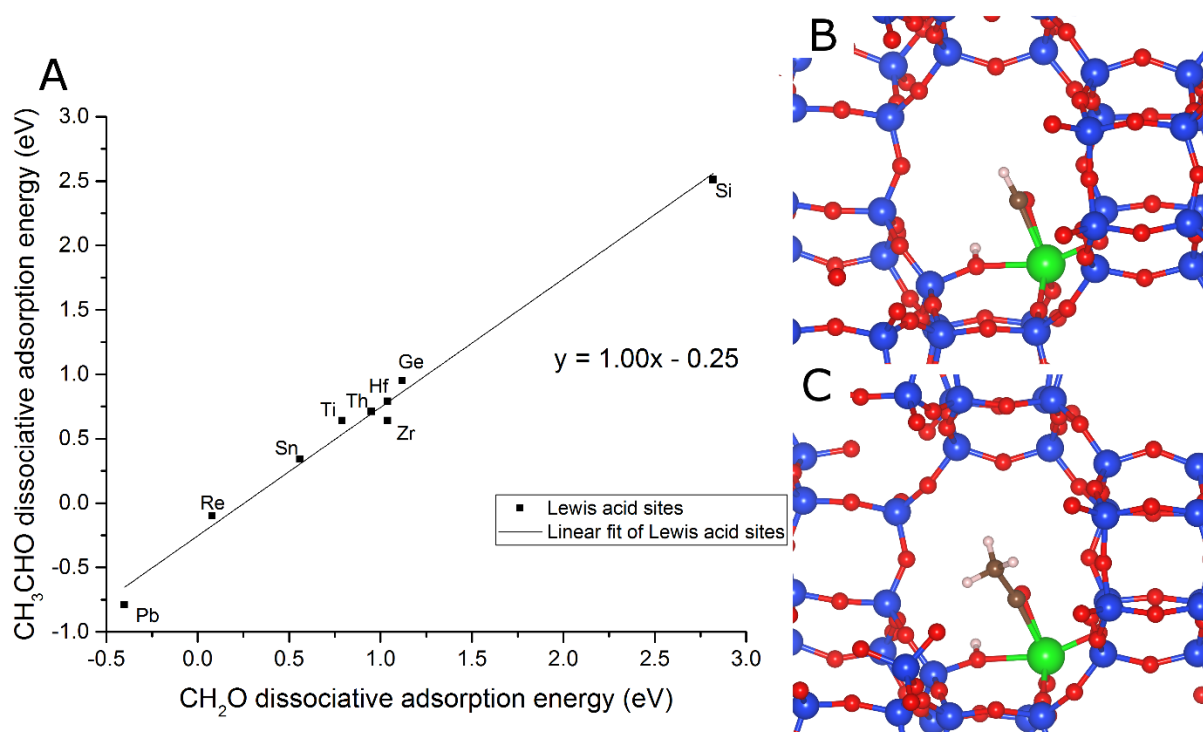
Figure 2.4 C-H bond activation for formaldehyde and acetaldehyde as calculated with BEEF-VdW. (A) Dissociative adsorption energies on Lewis acid heteroatoms. (B) Formaldehyde dissociation on a Zr Lewis acid site. (C) Acetaldehyde dissociation on a Zr Lewis acid site.

As an additional test of the applicability of scaling relationships to adsorption in Lewis acid-substituted zeolites, we consider the dissociative adsorption of $CH_2$ and $CHOH$. Although these adsorbates are open shell, charge neutrality is preserved by ensuring that the initial and final states of the adsorbate have even numbers of unbound electrons (such species could, in theory, be produced by loss of two hydrogen atoms from adsorbed methane or methanol, followed by desorption of $H_2$, although such a process would be quite endothermic). Calculations using the standard BEEF-vdW produce yield spin counts of either 0 or +2, reflecting the possibility that the two electrons available in the molecules could be either spin paired or unpaired in the adsorbed configurations. Interestingly, these adsorption energetics do not yield scaling relationships of reasonable quality. No scaling correlation is observed when the adsorbates were allowed to adopt their lowest energy spin states, and while forcing the adsorbates into a spin +2 state does produce a linear scaling correlation, the slope is approximately 1.4, which is difficult to rationalize based on any traditional bond counting arguments.

A possible explanation for the poor quality of the scaling relationships described above is that adsorbates with unpaired electrons at the Lewis acid site may experience complex exchange-related effects in the semiconducting zeolite framework that are not well described by the GGA-based BEEF-vdW functional. To test this hypothesis, test calculations using the HSE06 hybrid functional have been carried out. Lowest energy configurations, as calculated with BEEF-vdW, are used as initial guesses for the HSE06 ionic relaxation. Geometries are optimized to an energy cutoff of 0.05eV due to the computational expense of performing full ionic relaxations with screened exact exchange. The HSE06 calculations do not change any of the lowest energy spin-states and have a negligible effect on adsorption geometries. However, the change in calculated dissociative adsorption energies is more significant, and a substantially improved scaling relationship, with a slope of close to 1.0, is obtained as shown in Figure 2.5. We note that use of HSE06 for the other scaling relationships described above does not change the scaling compared to the BEEF-vdW results (see APPENDIX A); the use of HSE06 seems therefore to be important in the specific case of open shell adsorbates.
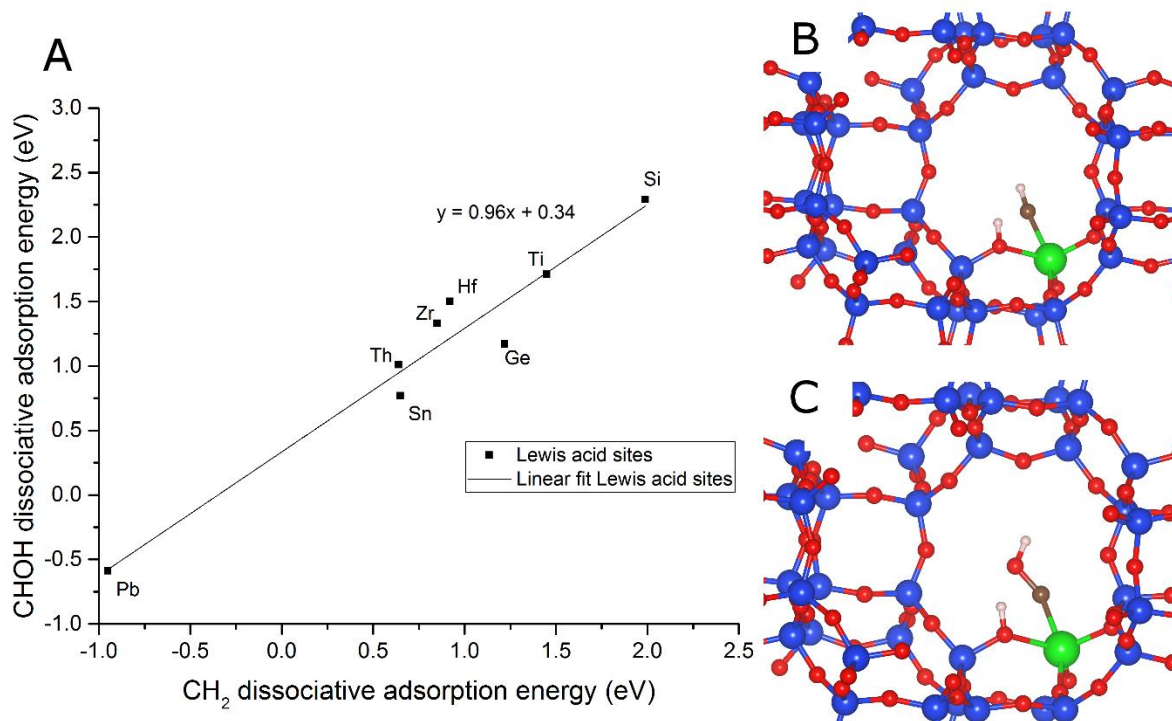


Figure 2.5 CH bond activation in open shell species, as calculated with HSE06. (A) Dissociative adsorption energies on Lewis acid heteroatoms (black squares). (B) $CH_2$ dissociation on a Zr Lewis acid site. (C) CHOH dissociation on a Zr Lewis acid site.

As mentioned above, the change in adsorption-dissociation energy, as calculated between BEEF-vdW and HSE06 on $CH_2$ and CHOH, is significant, and some energies change by as much as 1 eV. These changes can, in turn, affect the slopes of the scaling relationships. However, the energetic ordering of elements does not change when using HSE06 compared to BEEF-vdW, and for qualitative analysis or screening studies, the predicted reactivity of different heteroatoms can therefore still be assessed using less expensive BEEF-vdW calculations. Nonetheless, for rigorous microkinetic modeling of reactive intermediates, it may be important to include a small set of HSE06 calculations to determine if there is a significant energetic difference in comparison to a GGA functional.

Finally, we comment briefly on the possibility of developing scaling relationships in Lewis acid-based zeolites that exhibit non-unity slopes. To obtain physically meaningful results, all species must maintain charge neutrality, and one strategy for accomplishing this is to ensure that the framework is always appropriately charge compensated with adsorbed hydrogen. As an example, a scaling relationship between $CH_3$ with one adsorbed hydrogen atom and $CH_2$ with two adsorbed hydrogen atoms could, in principle, be developed. However, inclusion of a second dissociated hydrogen causes significant framework reconstruction that can only be avoided by imposing artificial constraints on the relaxation of the heteroatom and the surrounding Si atoms. With such constraints applied, a scaling slope of ½ is found, fully consistent with bond counting arguments (see APPENDIX A). However, the fact that the existence of multiple framework hydrogen atoms will cause reconstruction in real zeolites suggests that these scaling relationships with slopes that deviate from unity are not of physical interest.

Table 2.1 Dissociative adsorption energies for dissociative adsorption reactions in chabazite zeolites. The reference energies are the zeolite with no adsorbates and the appropriate species in the gas phase.

|     |          | Ge   | Sn   | Ti   | Zr   | Hf   | Pb    | Th    | Re    | Si    |
|-----|----------|------|------|------|------|------|-------|-------|-------|-------|
| O-H | $H_2O$   | 0.96 | 0.28 | 0.58 | 0.18 | 0.21 | 0.01  | -0.2  | -0.27 | 1.71  |
|     | $CH_3OH$ | 0.79 | 0.16 | 0.36 | 0.00 | 0.07 | -0.17 | -0.35 | -0.38 | 1.69  |
| S-H | $H_2S$   | 0.93 | 0.08 | 0.78 | 0.4  | 0.5  | -0.57 | /     | 0.00  | -0.36 |
|     | $CH_3SH$ | 1.36 | 0.56 | 1.36 | 1.08 | 1.2  | -0.13 | 2.64  | 0.82  | 0.42  |
| C-H | $CH_4$   | 1.36 | 0.87 | 2.25 | 2.08 | 2.19 | 0.08  | 1.98  | 0.72  | 5.33  |
|     | $CH_3OH$ | 0.99 | 0.5  | 1.71 | 1.62 | 1.71 | -0.28 | 1.55  | 0.35  | 4.8   |
|     | $CH_2O$  | 1.12 | 0.56 | 0.79 | 1.04 | 1.04 | -0.4  | 2.82  | 0.95  | 0.08  |
|     | $CH_3CHO$ | 0.95 | 0.34 | 0.64 | 0.64 | 0.79 | -0.79 | 2.51  | 0.71  | -0.1  |
|     | $CH_2^\dagger$ | 1.22 | 0.65 | 1.45 | 0.85 | 0.92 | -0.95 | 0.64  | /     | /     |
|     | $CHOH^\dagger$ | 1.17 | 0.77 | 1.71 | 1.33 | 1.5  | -0.59 | 1.01  | /     | /     |

†The $CH_2$ and CHOH species are reported with their HSE06 calculated value, as described in the text.

## 2.4   Discussion

Scaling relationships can be used to efficiently elucidate thermodynamic trends for different catalytic pathways, in turn forming the basis for the development of volcano plots and catalyst screening methods. Although the relationships do not directly provide kinetic information, the thermodynamics alone often provide important insights into reactivity patterns that may be subsequently refined through consideration of full kinetic data. In this section, we extend our results to a very simple and chemically intuitive model system. This example is provided to illustrate how these relationships can be used to develop reaction pathway insights. We consider methanol oxidation to formaldehyde[91]–[93] which can be performed on oxophilic metal-oxides such as molybdenum trioxide[94]. We seek to use the scaling relationships developed above to elucidate some of the potential mechanisms for this reaction over Lewis acid sites in CHA. The overall reaction is $CH_3OH \rightleftharpoons CH_2O + H_2$, and we consider a mechanism with two dehydrogenation steps to arrive at formaldehyde, together with a third step where two adsorbed hydrogen atoms

combine to produce hydrogen gas. For simplicity, we analyze only the initial hydrogen activation step although similar techniques could be used for other elementary steps. It is important to note that our goal is not to find the globally most favorable pathway for methanol reaction in Lewis acid-based zeolites. Rather, we simply seek to illustrate how scaling relationships can facilitate the analysis of reaction energetics.

The initial dehydrogenation step in methanol can proceed via either O-H or C-H bond activation. In the case of O-H activation, an adsorbed methoxy group is formed which can further react to form formaldehyde through a C-H activation step. However, one could also imagine the C-H activation taking place first, in which case a carbenium ion is formed. Following the formation of the carbenium ion, an O-H bond activation step would yield formaldehyde. As mentioned above, we analyze only the initial bond activation step in this reaction network.

We consider three of the more common Lewis acid zeolites, Sn, Ti, and Zr, and we compare O-H and C-H bond activation in these materials. For the O-H bond activation, we evaluate the water dissociation energy over each heteroatom and apply the scaling relationship which correlates water dissociation to O-H bond activation in methanol. Similarly, we use calculated methane dissociation energies to estimate the energy of C-H bond activation in methanol. As shown in Figures 2.1 and 2.3, scaling relationships with near-unity slopes exist for each of these scenarios. As seen on the left half of Figure 2.6, we find that for Sn, the dissociative adsorption energy for initial C-H bond activation in methanol is 0.34 eV greater than that for O-H bond activation. For Ti and Zr, we find the energetics of C-H bond activation to be 1.34 eV and 1.62 eV greater than those of O-H bond activation, respectively. These results, which require only a calculation of the thermodynamics of O-H and C-H activation in water and methane on the respective sites, allow us to completely exclude the possibility of C-H bond activation on Ti and Zr on closed Lewis acid sites. Although this result is chemically intuitive, we again emphasize that the purpose of Figure 2.6 is only to illustrate how, in a simple model system, scaling relationships may be applied to extract thermodynamic trends. In the case of Sn, however, it may not be as safe to completely neglect activation of C-H, given that the transition state energy could render the kinetics of C-H and O-H activation similar.

An additional benefit of employing scaling relations can be realized by performing similar estimates for the competition between C-H and O-H bond activation in ethanol. In ethanol, there exist two types of C-H bonds: methylene centered on the alpha carbon and an alkyl group

corresponding to the beta carbon. We have already demonstrated that C-H cleavage in methanol scales linearly with C-H activation in methane (Figure 2.3), and we further associate cleavage of the C-H bond in methanol with activation of the methylene bond in ethanol.  These considerations suggest that a scaling relationship can established between C-H scission in methane and methylene C-H scission in ethanol. We assume, based on previous results, that the slope will be unity, and thus only a single calculation of methylene C-H activation in ethanol on Sn-substituted CHA is needed to establish the scaling relationship.  The resulting intercept is -0.19 eV.  Using similar assumptions, a scaling relationship can also be established between C-H activation in methane and activation of the terminal methyl group in ethanol.  The slope is again assumed to be unity, and a single calculation of ethanol activation on Sn-substituted CHA yields and intercept of -0.12 eV. Finally, assumption of a unity slope between O-H activation in ethanol and water, and determination of the intercept of -0.30 eV through a single test calculation, completes the analysis. Applying these scaling relationships to ethanol activation, and taking the C-H dissociation energy to be equal to the most favorable of the energies estimated from the alpha and beta carbons, leads to predicted differences between C-H and O-H activation on Ti and Zr of 1.78 eV and 2.00 eV, respectively. Knowing only the water and methane dissociation energies in the various zeolites, this simple analysis allows one to definitively exclude the possibility of initial C-H activation in ethanol on these Lewis structures.

In addition, we comment briefly on the applicability of the provided scaling relationships to the question of whether or not Lewis acid sites will open under catalytic conditions.  In general, the dissociation of OH bonds in water on a Lewis acid site produces a hydroxyl ligand and protonated oxygen pair. In zeolite literature, this arrangement is described as an open site, and it is hypothesized to be the active site for many catalytically relevant reactions[17], [69]. Further, there has been recent work which suggests that Lewis acid sites may open and close under reaction conditions[95], and it is also conceivable that other OH- or CH-containing molecules might play a similar role in opening up Lewis sites. The data along the x-axis in Figure 2.1, corresponding to the dissociative adsorption energy of water on various Lewis sites in CHA, provides the thermodynamic driving force for such site opening by water, assuming the entropy of adsorption is similar for each heteroatom-substituted CHA cage. Thus, the dissociative adsorption energies provide a useful guide to the population of open and closed sites in the various Lewis acid-substituted CHA structures at equilibrium.  Accordingly, Sn is predicted to have a higher coverage

of open sites at equilibrium than is Ti due to their 0.30eV difference in adsorption-dissociation energies. Similarly, the coverage of Si open sites is likely to be negligible relative to Sn or Ti due to the large (1.71eV) adsorption-dissociation energy in Si. Some of the exotic heteroatoms, such Pb and Re, could have open site coverages that exceed Sn. We further note, in passing, that since the scaling relationships imply that the thermodynamics of dissociation of OH bonds in other molecules track that of water, these trends are also likely to describe the relative tendency of other molecules to open sites. The catalytic consequences of such site transformations could provide an interesting topic for future study with applications to microkinetic models and catalyst screening of new heteroatom substitutions.
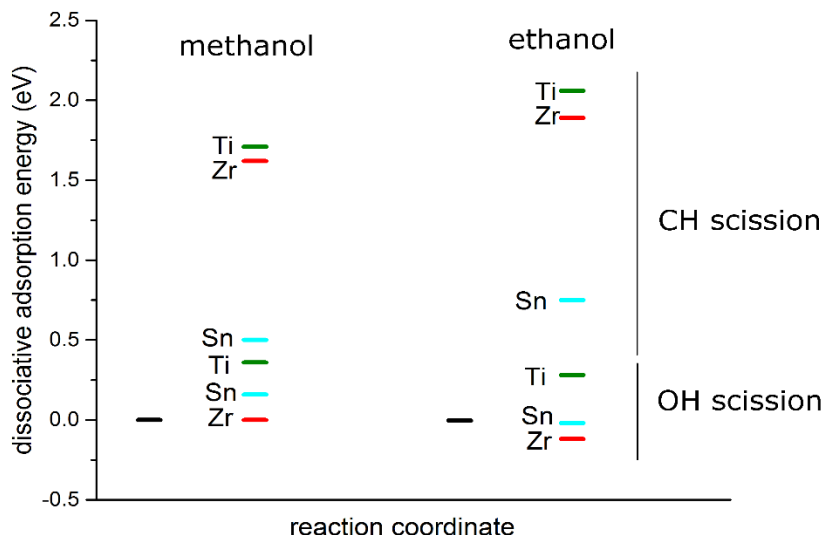


Figure 2.6 Comparison of methanol/ethanol dissociative adsorption energies in Ti, Zr, and Sn CHA zeolites via initial C-H or O-H scission estimated from scaling relationships. The gas phase reference state, corresponding to the zeolite and methanol/ethanol gas phase molecules in vacuum, is denoted in black.

## 2.5   Conclusions

Periodic Density Functional Theory calculations have been used to construct scaling relationships for the dissociative adsorption energies of small molecular species in Lewis acid-substituted chabazite zeolites. Comparison of the energetics of O-H scission in $CH_3OH$ and $H_2O$,

C-H scission in $CH_3OH$ and $CH_4$, S-H activation in $CH_3SH$ and $H_2S$, C-H cleavage in $CH_2O$ and $CH_3CHO$, and C-H activation in $CH_2$ and CHOH, leads to the identification of highly linear scaling relationships. These relationships follow rules of bond order conservation established previously in other catalytic materials, and slopes of near unity are seen in all cases. The practical benefits of these scaling relationships are illustrated by their use in rapidly estimating and comparing the energetics of initial C-H and O-H bond activation in methanol and ethanol in Lewis acid chabazite structures. The scaling relationships determined in this study are, more generally, expected to provide a useful basis for rapidly comparing the thermodynamics of different reaction networks in acid-substituted zeolite materials.

# 3. SITE SPECIATION IN ETHANOL DEHYDRATION IN LEWIS ACID ZEOLITES

## 3.1 Introduction

Microporous Lewis acids formed through isomorphous metal atom substitution into siliceous zeolite frameworks are shape selective heterogeneous catalysts that facilitate a broad range of oxygenate reactions[96], including Baeyer-Villager oxidation[97], Meerwein-Ponndorf Verley carbonyl reduction and Oppenauer oxidation of alcohols (MPVO)[98], and sugar isomerization[99]. A central question in the elucidation of elementary reaction networks in solid Lewis acids is the nature of active site heteroatom speciation. Tin heteroatoms, for example, adopt at least two distinct framework configurations: either tetra-coordinate to the framework (denoted as "closed") or tri-coordinate to the framework with an additional hydroxyl ligand (denoted as "open"). Open configurations are proposed to be the dominant active sites for glucose isomerization[100], [101] and MPVO[69], [102], [103, p. 20], while both open and closed sites catalyze aldol condensation[104]. The structure of these different Sn sites has been studied with density functional theory (DFT), as well as experimental spectroscopies such as $^{119}$Sn nuclear magnetic resonance (NMR)[105]–[107], infrared  upon adsorption of probe molecules (e.g., pyridine, deuterated acetonitrile)[69], [100], extended X-ray adsorption fine structure (EXAFS)[108], and diffuse reflectance UV-visible (DRUV)[69], [109]. DFT studies have proposed multiple structures for defect configurations of framework heteroatom sites, such as penta-coordinated Sn centers with a hydroxy ligand and protonated framework oxygen[95], [110], "open" tri-coordinate sites with a hydroxyl ligand and an adjacent framework silanol[101], [106], [111], and "defect open" sites where a proximal silicon vacancy creates a nest of silanol defects[110], [112]. In addition, the adsorption and subsequent dissociation of water at heteroatom sites to form the hydroxyl ligand and proximal silanol group has been discussed in previous

studies[113], [114]. In spite of these advances in understanding the pathways that interconvert these active site structures, the dynamics of their interconversion, and the resulting effects on observed reaction kinetics, have not been quantitatively analyzed.

To obtain fundamental, molecular-level understanding of how Sn sites interconvert under reaction conditions, ethanol dehydration is chosen as a model gas-phase probe reaction. This choice is motivated by the fact that liquid phase reactions are difficult to model accurately with DFT due to explicit solvent interactions between intermediates and transition states[115], and, DFT studies are limited in terms of the number and size of molecules that can be effectively treated in reaction networks, as the search space of relevant molecular configurations that must be analyzed increases rapidly with system complexity. Furthermore, reactive intermediate coverages are difficult to control in experiment due to the ubiquity of the solvent, and rapid deactivation in continuous liquid flow reactors[116], [117] precludes analysis of site dynamics. Ethanol dehydration therefore provides a more suitable probe of site interconversion and its effect on reaction kinetics, and it is known to proceed on Lewis acidic sites in γ-alumina[118] via both unimolecular and bimolecular pathways[119], [120] to form ethene and diethyl ether (DEE), respectively. Since reaction mechanisms on both closed and open Sn sites form DEE, computational insights are essential to understand the interconversion of active sites and its impact on the rate and selectivity of alternate dehydration pathways.

To model the ethanol dehydration reaction network, a total of 25 elementary steps and 19 reactive intermediates are first considered using DFT at the generalized gradient approximation (GGA) level. It is found that rates and reaction orders predicted from GGA-level calculations, along with entropies derived using the harmonic oscillator approximation, are insufficient to permit reliable interpretation of experimental kinetic data measured under differential conditions at which DEE is the only product formed. To enhance model fidelity, a generalized degree of rate control (DRC)[121] analysis is therefore used to identify kinetically relevant transition states and reaction intermediates, which are subjected to density functional and entropy treatments that are systematically refined. The hybrid density functional HSE06 includes a fraction of screened exact Hartree-Fock exchange[33], which improves calculated lattice constants in zeolite frameworks because it favors shorter cation-oxygen bonds[122]–[124]. More importantly, the confining pore environment introduces entropic contributions that are fundamentally distinct from similar effects on terraces of supported metal nanoparticles, because numerous anharmonic molecular

interactions make harmonic partition functions problematic for low frequency modes, resulting in errors in calculated free energies on the order of $0.1 - 0.2$ eV[125], [126]. The modes that deviate from harmonicity correspond to delocalized rotational and translational degrees of freedom and require more robust sampling of the potential energy surface (PES). The full PES can be sampled using semi-empirical force fields with Monte Carlo free-energy integrations[127], but direct use of such methods at the *ab-initio* level is limited by the speed of current computational resources. To overcome this limitation, Piccini and Sauer developed an algorithm in curvilinear normal mode coordinates to efficiently sample anharmonic features of the PES of methane adsorption in the proton form of chabazite [125]. Alternatively, Alexopoulos et al. sampled the PES of ethanol adsorption in H-MFI[128] by integrating the rotational and vibrational density of states from *ab-initio* molecular dynamics (AIMD). Both methods incorporate anharmonic corrections but are impractical to perform for an extensive reaction network. For simplicity, it may be possible, in some cases, to replace harmonic modes that have calculated frequencies below an arbitrarily chosen threshold with a higher frequency harmonic mode that approximates some aspects of rotational or translational freedom[129]. However, Jørgensen and Grönbeck have recently compared harmonic oscillator partition functions, free translational partition functions, hindered translational partition functions, and complete potential energy sampling (CPES) methods and have demonstrated that, even for CO oxidation on simple Pt(111) surfaces[130], there are non-negligible deficiencies of the harmonic oscillator approach relative to hindered translational partition function analyses and CPES sampling. The advanced partition function methods represent an improvement over simple harmonic analyses but do not explicitly include the effects of mode-mode coupling, thus motivating judicious use of CPES sampling or AIMD-related methods[131].

In this work, a tiered approach to kinetic model development is proposed, wherein partition function methods are used for the majority of the reaction intermediates, while a higher accuracy AIMD method is used for the kinetically sensitive intermediates determined by the DRC analysis. These intermediates, in turn, are identified using a generalized degree of rate control (GDRC) analysis[132]. Apparent reaction orders in water and ethanol are then determined from the fully converged model and are compared with experimental measurements to obtain a simplified rate expression derived from elementary steps. Finally, conclusions concerning the Sn site speciation that dominates reactivity are drawn.

## 3.2 Methods

All calculations are performed using self-consistent, periodic density functional theory (DFT) with the Vienna Ab-initio Simulation Package (VASP)[81]–[84], [87]. The Bayesian error estimation functional (BEEF-vdw)[31], which self-consistently includes dispersion interactions, is employed. In addition to this generalized-gradient approximation (GGA) functional, a hybrid functional, HSE06 [32], [33], using a screened columbic interaction with additional semi-empirical dispersion corrections via the Grimme approach[71], [133], is employed for selected calculations. Pseudopotentials are constructed in the projector augmented wave (PAW) framework for PBE functionals[86], [87]. The Beta unit cell is obtained from the International Zeolite Database[72]. The defect-free Beta framework is relaxed to final lattice vectors 12.66 Å, 12.66 Å, 26.54 Å. For HSE06-D3 calculations, unit cell vectors are reoptimized to 12.58 Å, 12.58 Å, 26.36 Å. The optimized cell volumes are within 1.9% and 0.2% of the IZA values for BEEF-vdW and HSE06-D3, respectively. For geometry optimizations, a plane wave cutoff of 520 eV is employed, along with a single gamma point to sample reciprocal space. Geometry convergence is performed to a force criterion of 20 meV/Å. All calculations are spin polarized. Gaussian smearing of the Fermi surface with a width of 10 meV is used due to the large band gap in the zeolite material.

Transition state geometries are obtained through the climbing-image nudged elastic band (CI-NEB) method[134], [135]. A total of 9 images are generated between initial and final states, and the Image Dependent Pair Potential pre-optimizer is employed to generate initial configurations[136]. A Lanczos diagonalization[137] scheme is used, which converges rapidly for zeolite transition states when starting from a partially converged NEB pathway. For all transition states and reaction intermediates, a partial hessian vibrational calculation of the adsorbed structure is performed. Harmonic vibrational states are used for zero-point vibrational energy corrections ($E_{ZPVE}$) and also form the basis for entropy calculations. Free energies are approximated as

$$G = E_0 + E_{ZPVE} - TS \tag{3.1}$$

where $E_0$ is the ground state potential energy obtained through DFT. Adsorption energies in the framework ($E_{ads}$) are considered relative to the doped framework and gas phase molecule

$$E_{ads} = E_{ZA} - E_Z - E_A \tag{3.2}$$

where A is the adsorbate and Z is the doped zeolite framework.

To facilitate the identification of stable adsorbate geometries, AIMD simulations at the same level of theory (BEEF-VdW) are performed. Stable configurations obtained from initial geometry

optimizations are heated to 400K and then equilibrated using a Nose-Hoover thermostat and 0.5 fs timestep. Geometries are extracted from the equilibrated simulation and then quenched to provide additional adsorbate configurations. This process is performed for selected monomolecular intermediates, including ethanol and water, as well as for some dimeric intermediates, including ethanol-ethanol dimers and ethanol-water dimers.

Rate constants for surface processes are evaluated using transition state theory, where the preexponential factor is assumed to correspond to the harmonic saddle mode. For molecular adsorption and desorption, collision theory is employed, as these processes not activated. To simulate reaction rates, a differential reactor model, similar to that developed by Gokhale et al.[138] and by Choksi and Greeley[139], is used. Numerical solution of the reactor and site balance equations is accomplished with a custom python-based solver. While the rate equations are relatively straightforward to integrate numerically, the large number of elementary steps and surface intermediates results in poor convergence of nonlinear equation solvers without the reasonable initial guesses provided by a coarse-grained differential equation solution. Thus, the scheme uses an initial transient differential equation solver to approximately locate local steady state solutions, which are then input into a nonlinear equation solver for further refinement. A rate sensitivity analysis is performed using the generalized degree of rate control[121] to identify thermodynamically and kinetically sensitive intermediates and transition states. A detailed discussion of entropy calculations, elementary steps of the reaction, the microkinetic model construction, adjustments, and error analysis can be found in the APPENDIX B.

Crystal Orbital Hamiltonian Population (COHP) analysis in semiconductors and insulators has seen success in qualitatively explaining the bonding structure of these materials by localizing a periodic wavefunction onto Gaussian orbitals. The LOBSTER[140] code, which employs COHP, is used for wavefunction localization, along with a Bader analysis[141], to determine charge transfer and Sn oxidation states.

## 3.3    Results and Discussion

### 3.3.1    T-sites in Sn-Beta

The specific distribution of Sn among crystallographically distinct tetrahedral site (T-site) locations in the Beta framework remains a topic of continued discussion[107], [108], [110], and

the local structure of Si-O bonds around each T-site may influence the energies of transition states and intermediates in the ethanol dehydration reaction network. To determine the sensitivity of adsorbate energies to Sn T-site location in Beta, the energetics of two key intermediates (water, ethanol) and one reaction step (water dissociation to form open sites) at closed sites are examined. A single Sn atom is placed in one of nine crystallographically distinct T-sites per unit cell to simulate a Si:Sn ratio of 63:1. The range in ethanol and water adsorption energies, and water dissociation energies, among these 9 T-sites is less than 0.2 eV (APPENDIX B). In a study of site stabilities in Sn-Beta, Josephson et al. report a similar narrow distribution of energies, and the wide variation of stable tin sites reported in literature are likely due to functional choice and kinetic energy cutoff, producing energy fluctuations commensurate with a multiplicity of lowest energy Sn sites[142]. For convenience, therefore, we choose the T8 site[72] for all Sn substitutions, as it has the most exothermic ethanol binding energy. However, we do not anticipate the T-siting of Sn atoms to influence the binding energies of intermediates beyond the standard error of periodic DFT calculations, which is typically around ~0.1 eV and is similar to the distribution of ethanol binding energies across all T-sites.

### 3.3.2   Site speciation

Partially hydrolyzed open sites are formed by dissociation of water or alkanols[113] on closed Sn sites, yielding a hydroxyl ligand on the Sn center (stannanol) and a corresponding silanol on a framework oxygen. Water adsorption on the closed site (W*, Figure 1) is exergonic by -0.12 eV at ethanol dehydration conditions of 404 K, and dissociation on an adjacent oxygen site proceeds with an activation free energy barrier of 0.75 eV (TS2, Figure 3.1). This adjacent oxygen site is a metastable location for the proton, which migrates to a more stable location at an oxygen *anti* to the stannanol ($W_x$*, Figure 3.1) with an HO-Sn-OH coordination angle of 160.5°, adopting a structure similar to that reported by Josephson et al.[142]. The energy difference between the *syn* and *anti* configurations is 0.12 eV. From the electron localization function and Crystal Orbital Hamiltonian Population (COHP) analysis, no significant orbital overlap exists between the framework silanol and Sn center, consistent with full cleavage of the framework Sn-O bond (APPENDIX B). A Bader charge analysis shows that the $4^+$ oxidation state of Sn is preserved in its closed and open states (APPENDIX B). Water or ethanol carriers facilitate a low barrier (0.3 eV) proton shuttling mechanism that transfers the silanol proton to the most stable *anti*

conformation, as further described in APPENDIX B. Open site energies and geometries will be referenced to this most stable conformation ($W_x$*), and thus the reaction free energy of water dissociation on open sites is 0.37 eV at 404 K.
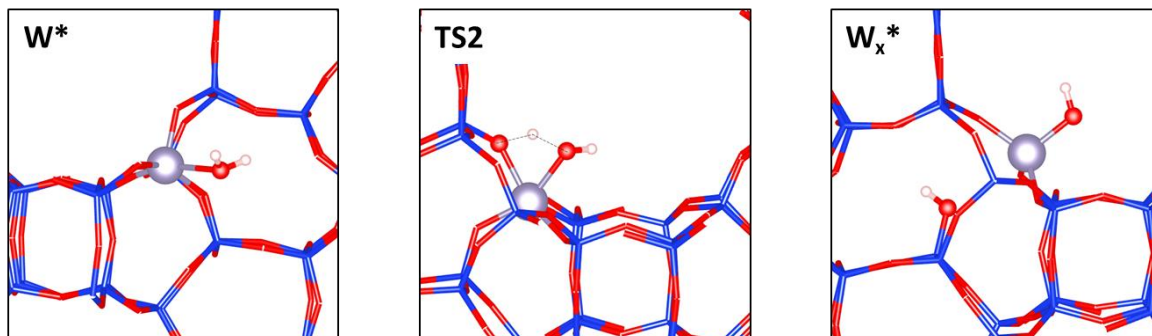


Figure 3.1 Hydroxy open site formation conformations corresponding to the lowest energy structures. W* refers to water adsorbed on the closed site, Wx* refers to the hydroxy open site where water has dissociated to form a hydroxyl ligand. TS refers to transition state, and the numbering (TS2) corresponds to the free energy diagram in Figure 3.4.

An alternative pathway for open site formation involving dissociative adsorption of ethanol is also considered based on experimental evidence by Yakimov et al. that dissociative adsorption of (secondary) alcohols is possible[143]. The free energy of ethanol adsorption (-0.31 eV) at the closed site is stronger than that of water (-0.12 eV), and results in the alkyl group facing the channel (E*, Figure 3.2). In a mechanism analogous to site opening by water, the adsorbed ethanol dissociates to form an ethoxy open site ($E_X$*, Figure 3.2). The activation free energy barrier (TS3, Figure 3.2) for ethanol dissociation (0.80 eV) is comparable to that of water dissociation (0.75 eV). A proton shuttling mechanism similar to that described above is necessary to access the most stable silanol location *anti* to the ethoxy ligand, with an EtO-Sn-OH coordination angle of 159.7° ($E_X$*, Figure 3.2). The energy difference between the syn and *anti* configurations is 0.16 eV. The reaction free energy of ethanol dissociation is 0.41 eV, endergonic relative to adsorbed ethanol. As in the case of the open site formed through water dissociation, there is no orbital overlap between the protonated framework oxygen and Sn, and Bader charge analysis on Sn indicates that the oxidation state remains 4$^+$ after opening with ethanol. For clarity, in what follows, open sites will be described according to their ligand identity as either hydroxy open sites or ethoxy open sites. We note that the formation of open sites by molecular dissociation of both water and alcohols has been

described previously[113], but the effects of reaction conditions on their speciation and relative populations during steady-state catalysis are not well understood.
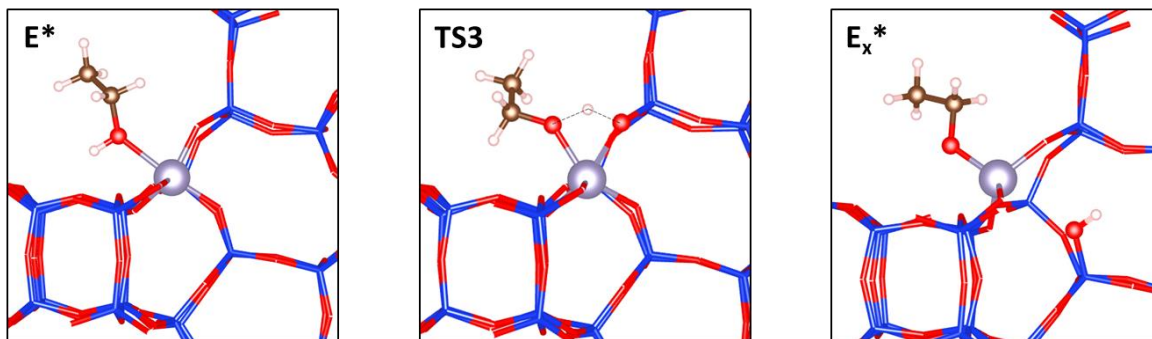


Figure 3.2 Ethoxy open site conformations corresponding to the lowest energy structures. E* refers to ethanol adsorbed on the closed site, Ex* refers to the ethoxy open site where ethanol has dissociated to form an ethoxy ligand. TS refers to transition state, and the numbering (TS3) corresponds to the free energy diagram in Figure 3.5.

### 3.3.3   DEE formation mechanisms

Direct formation of DEE involves adsorption of an ethanol dimer that subsequently undergoes bimolecular rearrangement to form DEE and water, as proposed by Christiansen et al.[144] on the Lewis acid sites of $\gamma$-Al$_2$O$_3$ surfaces. A second mechanism for bimolecular dehydration involves reaction of a dissociated ethanol and an adjacent adsorbed ethanol, as also considered by Christiansen et al.[144]. Although ethanol reaction mechanisms on $\gamma$-Al$_2$O$_3$ provide conceptual analogies for candidate mechanisms on zeolite Beta, a crucial structural difference exists between the two classes of catalysts. On the $\gamma$-Al$_2$O$_3$ surface, bimolecular ethanol dehydration requires neighboring aluminum Lewis acid sites. In contrast, tin sites in the Beta framework in the elemental composition range studied here (1–2 per unit cell) are unlikely to be paired, and although Bare et al.[108] have provided evidence for Sn site pairing in Beta frameworks, reaction barriers at paired Sn sites are higher by >0.25 eV than at isolated Sn sites (APPENDIX B). Therefore, our analysis of DEE formation will be restricted to isolated Sn sites in at the T8 position in closed, hydroxy open, and ethoxy open configurations.
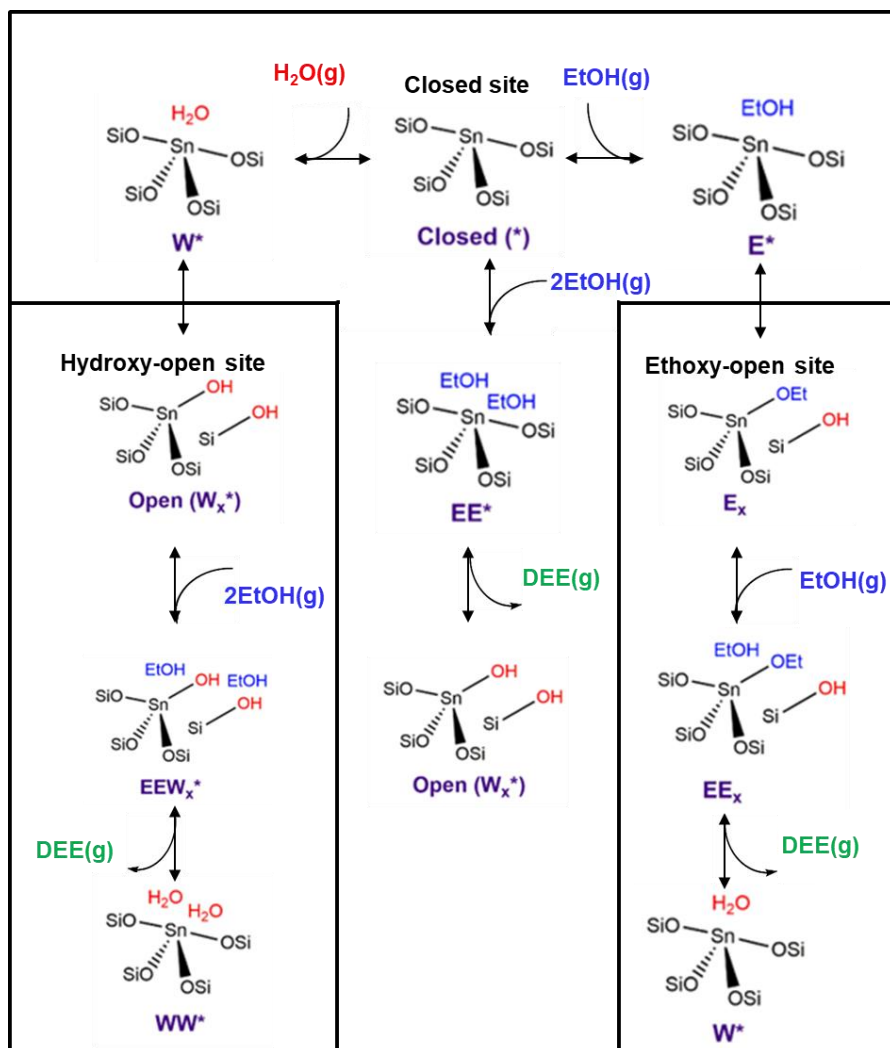
Figure 3.3 Condensed DEE reaction network, showing interconversion of closed tin sites and both hydroxy-open and ethoxy-open sites, with subsequent adsorption of ethanol and formation of DEE. Nomenclature for different Sn sites is defined in the figure. A full list of elementary steps considered is provided in APPENDIX B.

### 3.3.3.1   Closed site mediated mechanism

DEE formation on the closed site must first involve adsorption of two ethanol molecules to form an ethanol-ethanol dimer (EE*, Figure 3.4). As stated above, the adsorption free energy of the first ethanol molecule is -0.31 eV, while the differential adsorption free energy of the second ethanol is -0.16 eV. For comparison, the differential adsorption energy of a water to form an ethanol-water dimer is -0.20 eV. This second ethanol is denoted "vdW-ethanol", as its adsorption is largely dictated by van der Waals interactions through the hydroxyl group in the primary ethanol.

The interatomic distance between the protic hydrogen of the primary ethanol and the hydroxyl group oxygen of the vdW-ethanol is 1.72 Å, which, together with the magnitude of the differential binding energy, confirms that a hydrogen bond is formed (Figure 3.4).

We note that the binding energy of the second ethanol in the ethanol-ethanol dimer is referenced to that of a gas-phase ethanol molecule. However, the specific ethanol precursor that forms the dimer may originate from a weakly physisorbed state within the zeolite framework, such as that at a silanol defect. As physisorbed ethanol is in equilibrium with the gas phase, and there are no indications of internal mass transfer limitations (APPENDIX B), the barriers to intracrystallite diffusion are assumed to be low. Such barriers do not, therefore, affect the reaction kinetics, although they might be relevant for those describing alternative reactions.

At the subsequent nucleophilic substitution transition state for DEE formation (TS1, Figure 3.4), the oxygen atom of the vdW-ethanol acts as the nucleophile, attacking the alpha carbon of the primary ethanol, while its C-O bond to the leaving group (OH) is cleaved. The angle of attack between the stannanol leaving group, the ethyl electrophile, and the vdW-ethanol nucleophile is 154.6°, which deviates from the expected angle of 180° for gas phase $S_N2$ reactions that maximizes overlap of the vdW-ethanol oxygen lone pair and the C-O antibonding orbital of the primary ethanol. This deviation may be influenced by the confining pore geometry, which would strain the transition state geometry away from the most favorable angle. The distance between the stannanol group and the ethyl electrophile is 2.24 Å, while the distance from the ethyl electrophile to the nucleophilic vdW-ethanol is 2.04 Å, and the distance from the nucleophilic vdW-ethanol ethyl group to the nearest pore wall oxygen atom is 4.04 Å. The O-H bond of the nucleophilic ethanol is fully formed at the transition state and is similar in length as in the coadsorbed dimer. The protic hydrogen transfers from the vdW-ethanol to an adjacent framework oxygen to form a silanol defect.

The lowest energy final state ($DW_X^*$, Figure 3.4) is comprised of the hydroxyl open site and adsorbed DEE. The most stable adsorption configuration for DEE is on the stannanol group, with a distance of 1.76 Å between the stannanol hydrogen and the ether oxygen. The preference for adsorption at the stannanol is slight, however, as the differential binding energy of DEE adsorbed instead to the framework silanol is only 0.05 eV higher. The intrinsic activation free energy for DEE formation from a coadsorbed ethanol dimer is 1.59 eV, and the reaction free energy is endergonic by 0.38 eV.

An alternative DEE formation mechanism is an $S_Ni$-type reaction where the nucleophilic attack is constrained to be retentive, and necessitates a frontside attack[145]. This type of transition state has been observed for a set of glycosyltransferase enzymes[146] and involves a hydrogen bonding interaction between the leaving group and the nucleophile. As the classical $S_N2$ angle of attack, described above, may be restricted by the geometry of the confining pore, the frontside attack mechanism could be a plausible transition state configuration. In the $S_Ni$ mechanism, the protic hydrogen of the nucleophilic vdW-ethanol is transferred to the stannanol leaving group, directly forming an adsorbed water molecule. The distance from the methyl group of the vdW-ethanol to the nearest pore wall oxygen atom is 5.38 Å, corresponding to a more tightly bound transition state complex than for the $S_N2$ case. The intrinsic barrier for the $S_Ni$ mechanism is higher by 0.66 eV (APPENDIX B). Thus, the enthalpic penalty of straining the $S_N2$ transition state complex is less severe than that incurred by adopting the frontside nucleophilic attack angle.
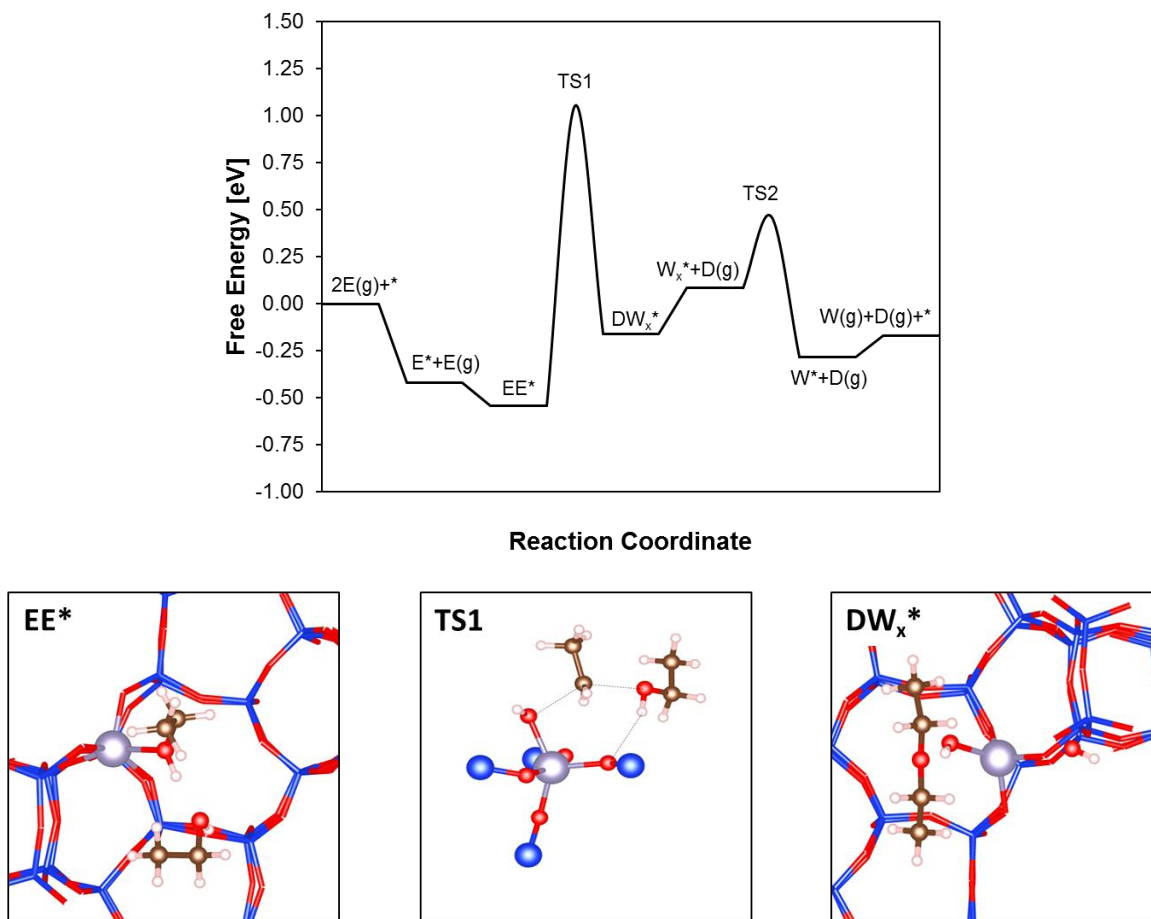
Ethoxy open site mediated mechanism Figure 3.4 Closed site reaction mechanism and selected adsorbate geometries. Free energies are evaluated at 404 K and 1 bar. For clarity, the pore wall is not shown in the TS1 diagram, and diethyl ether is referred to as D in the reaction diagrams. Nomenclature for the other reaction intermediates and Sn sites is found in Figure 3.3.

### 3.3.3.2

Beginning with an ethoxy open site formed by ethanol dissociation, other DEE formation mechanisms are possible. Adsorption of molecular ethanol on the ethoxy open site (EE$_X$*, Figure 3.5) is exergonic at -0.33 eV and is mediated by hydrogen bonding with the framework silanol. The interaction distance between the proton of the framework silanol and the hydroxyl oxygen of the adsorbed ethanol is 1.84 Å. DEE forms via nucleophilic substitution, where the ethoxy ligand behaves as the nucleophile. In a concerted step, the adsorbed ethanol is protonated by the framework silanol, forming water as a stable leaving group, while the ethyl electrophile is attacked by the nucleophilic ethoxy ligand (TS4, Figure 3.5). The bond angle between the leaving group

(water), electrophile (ethyl), and nucleophile (ethoxy) is 150.6º. The distance to the nearest oxygen atom in the opposite pore wall is greater than 5 Å, indicating minimal steric interaction based on atomic distances. The distance between the nucleophile and electrophile is 2.40 Å, while the distance from the electrophile to the water leaving group is 2.02 Å. The free energy of activation is 1.66 eV, and the reaction free energy is exergonic at -0.33 eV. The ethoxy open site is closed in the process of protonating the leaving group to form the closed Sn site and coadsorbed DEE and water. The most stable final state configuration involves adsorption of water on the Sn and a hydrogen bonding interaction between water and DEE (DW*, Figure 3.5). The interaction distance between the hydrogen from water and the etheric oxygen is 1.73 Å.

The possibility of forming a retentive $S_N$i-type transition state from the ethoxy-ethanol dimer was considered as an alternative to the backside attack $S_N2$ mechanism presented above. Here, the ethoxy ligand again behaves as the nucleophile. The nucleophilic ethoxy ligand attacks the ethanol in a concerted mechanism where the hydroxyl leaving group forms a bond to Sn, yielding a hydroxy ligand (APPENDIX B). An ethyl fragment is once again the electrophile, forming DEE and breaking the ethoxy-Sn bond. The silanol is not necessary to protonate the leaving group, therefore this mechanism behaves as a ligand transfer process in which the ethoxy ligand is replaced with a stannanol to preserve the structure of the silanol and form DEE. The free energy of activation for the ligand transfer mechanism is higher than that of the $S_N2$-type mechanism by 0.2 eV.

The $S_N2$ mechanism on the ethoxy open site is analogous to a Brønsted acid-like dehydration mechanism mediated by protonation of the ethanol. The Lewis acid-mediated mechanism differs from the Brønsted acid-mediated one, however, because the electronic structure of the nucleophile is modulated by the strength of the interaction with Sn. There is a cooperative effect of the Sn and the framework silanol in stabilizing the nucleophile and the leaving group, which lowers the activation barrier compared to a case involving direct ligand transfer in which Sn must stabilize the nucleophile and electrophile simultaneously. On an oxide surface such as γ-$Al_2O_3$, adjacent Lewis acid sites stabilize the leaving group and nucleophile separately, as described by Christiansen et al.[144]. Here, the framework silanol that is formed when Sn is opened by ethanol acts as a second site that stabilizes the leaving group, while Sn stabilizes the nucleophile.
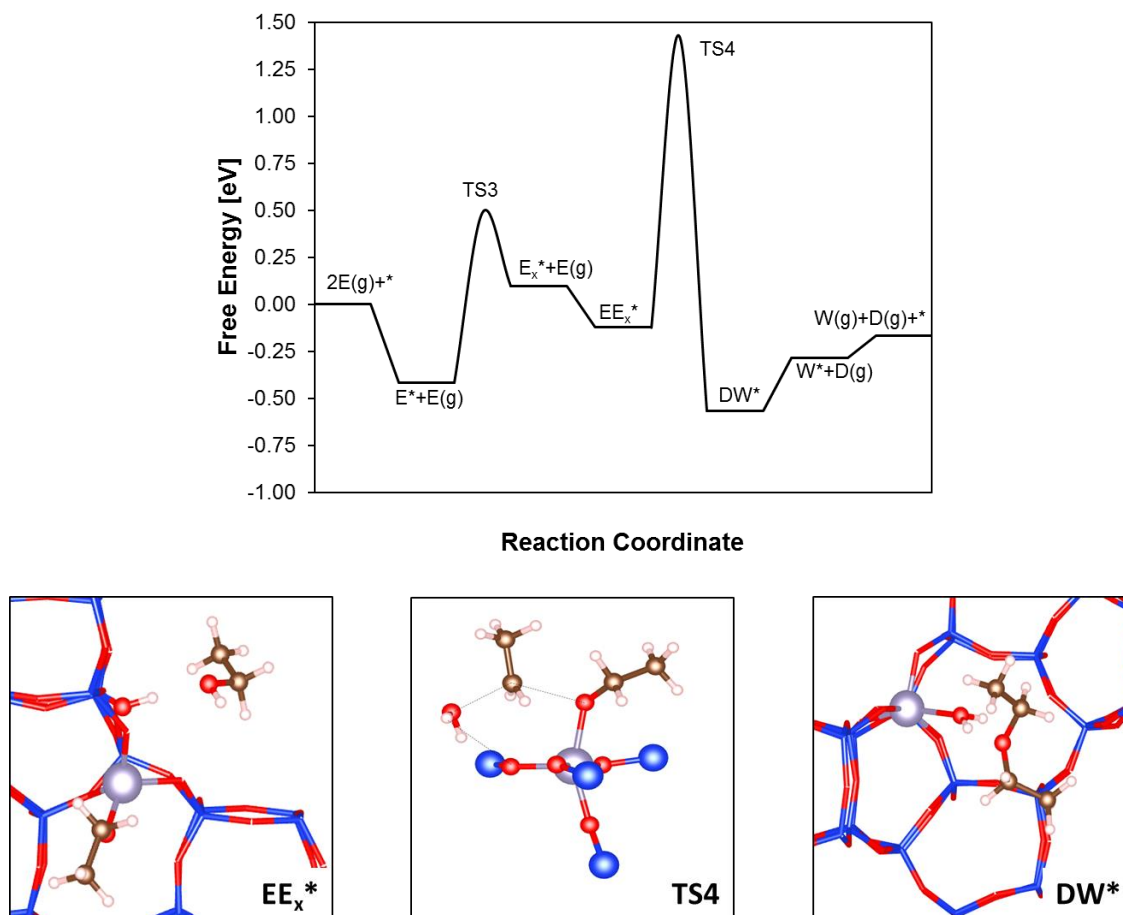
Figure 3.5. Ethoxy open site reaction mechanism and selected adsorbate geometries. Free energies are evaluated at 404 K and 1 bar. For clarity, the pore wall is truncated in the TS4 diagram, and diethyl ether is referred to as D in the reaction diagrams. Nomenclature for the other reaction intermediates and Sn sites is found in Figure 3.3.

### 3.3.3.3   Hydroxy open site mediated mechanism

The hydroxy open site can adsorb an ethanol-ethanol dimer, introducing an additional distinct mechanism for bimolecular DEE formation. Coadsorption of two ethanol molecules onto a hydroxy open site can be described by multiple adsorption geometries. One ethanol can form a hydrogen bond with the stannanol while the second forms a hydrogen bond with the framework silanol. Either of these ethanol molecules may alternatively form a hydrogen bond with the other ethanol rather than the stannanol or silanol, generating two additional possibilities. The most stable configuration is the former, with one ethanol on each OH site (EEW$_x$*, Figure 3.6). As discussed

above, the binding energy for the first ethanol that makes up the dimer is -0.07 eV, and the differential binding energy for the second ethanol is -0.24 eV.

At the transition state (TS6, Figure 3.6), the ethanol adsorbed on the framework silanol is protonated in a concerted step while the ethanol adsorbed on the stannanol acts as the nucleophile. The protic hydrogen of the nucleophilic ethanol can transfer to the stannanol, forming water and closing the active site. The attack angle is 155° and deviates from the expected 180°, suggesting that additional electrostatic interactions with the surrounding pore stabilize this alternate configuration. The distance between the water leaving group and the ethyl electrophile is 2.07 Å, and the distance from the electrophile to nucleophilic ethanol is 2.22 Å. The most stable final state involves a trimeric adsorbed complex of two water molecules and DEE (DWW*, Figure 3.6). A hydrogen bonding network is formed involving a strongly bound water molecule, a weakly coadsorbed water molecule, and the ether oxygen in DEE. The distance from the strongly bound water to the ether oxygen is 1.76 Å, and that from the strongly bound water to weakly bound water is 1.79 Å. The intrinsic activation free energy for this process is 1.67 eV with a reaction free energy of -0.30 eV. We note that this mechanism of DEE formation bears some resemblance to a mechanism proposed by Knaeble and Iglesia[147], in which a Brønsted acidic hydroxyl group on a polyoxometallate (POM) cluster protonates ethanol, while the nucleophilic ethanol transfers its proton to a different oxygen site.

Intriguingly, the tin center does not directly influence the electronic structure of the hydroxy open site pathway since protonation of the nucleophile occurs through the framework silanol. The Brønsted acidic character of this silanol has been discussed by Josephson et al[142]. The silanol, in turn, has no electronic overlap with Sn, as shown from the COHP analysis for hydroxy open sites (APPENDIX B). Hence, the Lewis acidic character of Sn appears to influence dehydration transition state energies more weakly than the deprotonation energy (DPE) of the framework silanol, as the metal atom predominantly affects the energy needed to close the open site. The DPE, in turn, is a probe-independent descriptor of the intrinsic strength of Brønsted acids that correlates with the intrinsic activation barriers of reactions mediated by ion-pair transition states[55], [148], [149]. Additionally, since there is no electronic interaction between the framework silanol and the Sn center, the DPE of framework silanols formed through site opening will likely be similar for different Lewis acidic heteroatoms.
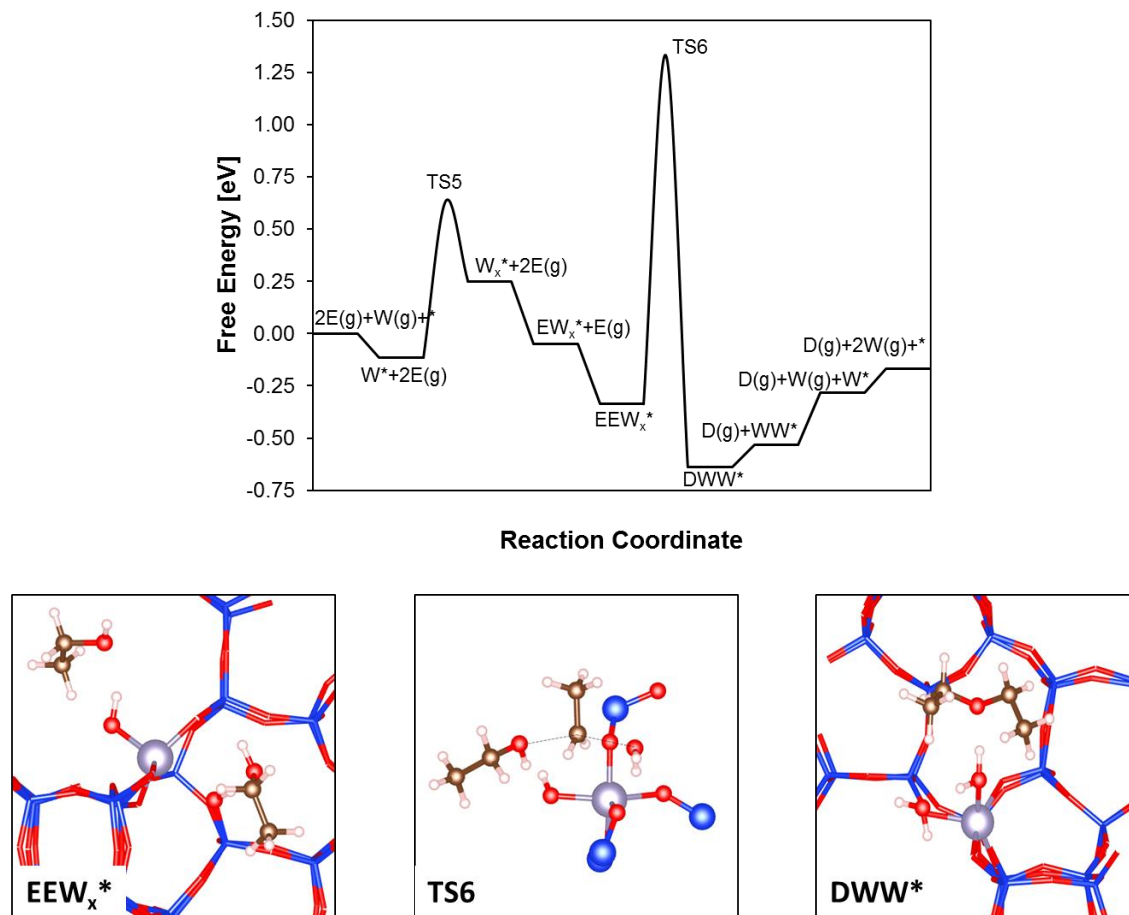
Figure 3.6 Hydroxy open site reaction mechanism and selected adsorbate geometries. Free energies are evaluated at 404 K and 1 bar. For clarity, the pore wall is truncated in the TS4 diagram, and diethyl ether is referred to as D in the reaction diagrams. Nomenclature for the other reaction intermediates and Sn sites is found in Figure 3.3.

Figure 3.7 compares the free energy profiles for the various site-specific pathways (closed, hydroxy open, ethoxy open), with all pathways placed on a common energy reference of stoichiometric reactant gases and a closed Sn site. Adsorption, desorption, and site opening elementary steps have been lumped for clarity, highlighting the distribution of intrinsic and apparent activation barriers relative to the gas phase (see also Table 3.2).
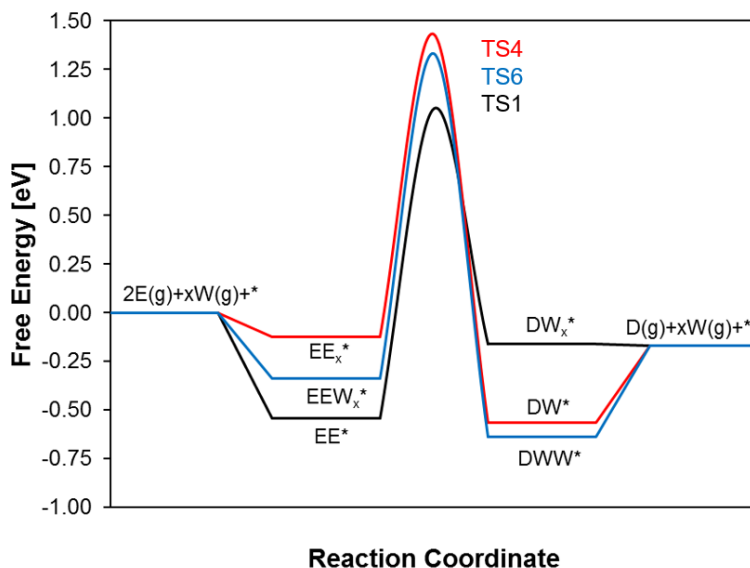
Figure 3.7 Lumped DEE formation mechanisms with different Sn site speciations. Free energies are evaluated at 404 K and 1 bar. Black – closed site, blue – hydroxy open site, red – ethoxy open site.

The apparent activation barrier relative to gas phase for the closed site mechanism is 0.28 eV lower than the barrier for the hydroxy open site mechanism, and 0.38 eV lower than that of the ethoxy open site mechanism. This result may relate to the observation that the formation of hydroxy and ethoxy open sites from closed sites is endergonic, and the free energies of ethanol-ethanol dimer species adsorbed on these sites are hence penalized relative to the ethanol-ethanol dimer adsorption on closed Sn sites. The relative stability of the closed sites may, in turn, be due to the low chemical potentials of gas phase ethanol and water and to the local structure of the beta framework. These results suggest that DEE formation will be primarily mediated by closed Sn sites, but this conclusion depends on the relative populations of the various sites during reaction conditions. These populations may, in turn, be influenced by factors that are not described by the free energy diagrams, such as the coproduction of water and associated hydroxyl open site formation. Therefore, catalytically-relevant site populations can only be quantified through the development of a detailed microkinetic model.

Table 3.1 Kinetic barriers for DEE formation on different Sn sites

| Sn site | Intrinsic barrier (eV) | Activation barrier relative to gas phase (eV) |
|---|---|---|
| Closed | 1.59 | 1.05 |
| Hydroxy open | 1.67 | 1.33 |
| Ethoxy open | 1.66 | 1.43 |

### 3.3.4 Ethene formation mechanisms

While the primary focus of this study is on ethanol dehydration at conditions where DEE is the only product formed, consideration of the monomolecular dehydration products (ethene) permits prediction of selectivity at other reaction conditions. The experimental DEE formation rate per mole of Sn at 404 K is at least two orders of magnitude greater than that of ethene (ethene was formed below the experimental detection limit). Thus, an additional test of the accuracy of a microkinetic model is to verify that DEE formation is preferred when ethene formation mechanisms are also included. Inclusion of these additional mechanisms also permits extension of the microkinetic model to higher temperatures where ethene formation may be favored.

On a Sn closed site, the formation of ethene requires $C_\alpha$-O and $C_\beta$-H scission, which may be either concerted or sequential. The concerted pathway proceeds with a lower overall barrier, as ethanol can form a 6-member ring transition state. In this transition state, an OH ligand is transferred to the Sn, while a hydrogen from the $\beta$ carbon is transferred simultaneously to a framework oxygen forming a hydroxy open site. The methyl hydrogen must be transferred to an oxygen adjacent to the stannanol, which is metastable compared to silanol formation *anti* to the hydroxy ligand. As discussed above, a proton shuttling mechanism mediated by water or ethanol allows the hydroxy open site to adopt its most favorable configuration. At the transition state, the $C_\alpha$-O bond of ethanol elongates to 2.21 Å, and the $C_\beta$-H bond elongates by 0.33 Å as the hydrogen lies equidistant between the $C_\beta$ and framework oxygen. The free energy of activation for this process is 1.96 eV with an endergonic free energy of reaction of 0.67 eV.

Ethene can also form through a bimolecular mechanism starting from ethanol adsorbed onto an ethoxy open site. The ethoxy ligand acts as a base to break the $C_\beta$-H bond by a classical

E2 mechanism. Simultaneously, the framework silanol protonates the adsorbed ethanol to form water. The $C_\alpha$-O bond of the adsorbed ethanol elongates to 2.23 Å, while the $C_\beta$-H bond increases to 1.26 Å, with a distance of 1.43 Å to the ethoxy ligand. The intrinsic activation free energy for this mechanism is 1.83 eV, with an exergonic free energy of reaction of -0.14 eV. The most favorable final state configuration is an ethanol-ethene-water trimer with ethanol bound to the Sn site at a distance of 2.27 Å. Water forms a hydrogen bond 1.80 Å away from ethanol, while ethene lies 3.46 Å from the ethanol $C_\alpha$.
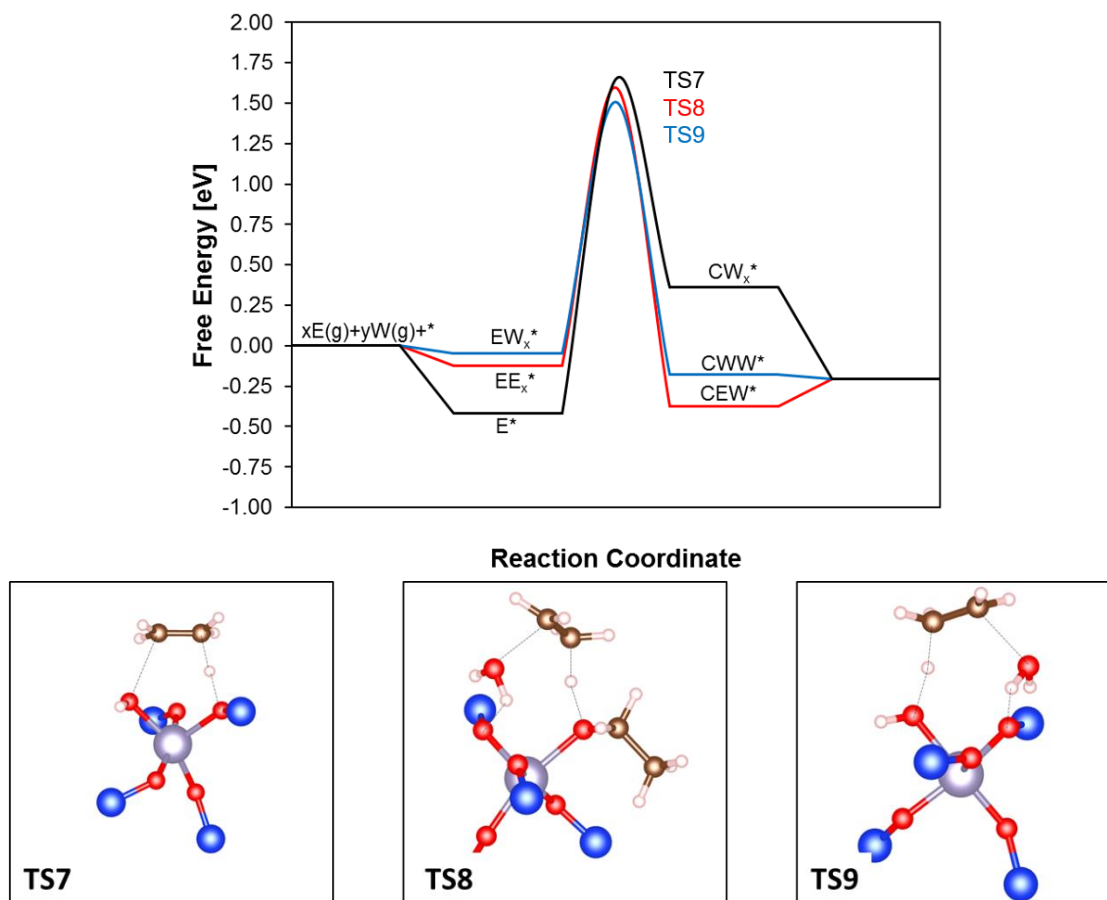


Figure 3.8 Ethene formation on closed sites (TS7), ethene formation on ethoxy open sites (TS8), and ethene formation on hydroxy open sites (TS9). The pore wall is truncated for clarity.

Ethene formation on the hydroxy open site is closely related to that on the ethoxy open site. Instead of ethoxy behaving as a base to remove the βCH, however, the stannanol acts as a base. The C-O bond elongation is 2.25 Å, differing by 0.02 Å compared to the ethoxy open site pathway. The βCH bond elongates to 1.27 Å, and the transferred hydrogen is 1.41 Å from the stannanol. The βCH distance is within 0.01 Å, and the distance to the base is within 0.03 Å of the ethoxy

open site pathway. The intrinsic activation free energy for this process is 1.51 eV, with an exergonic free energy of reaction of -0.13 eV. The lumped ethene formation free energy diagram (Figure 3.8) shows higher intrinsic activation energies than for DEE formation (Figure 3.7), suggesting selectivity toward DEE. As mentioned above, however, this conclusion is sensitive to the population of the various types of Sn sites, which will be further elucidated via microkinetic modeling.

### 3.3.5 Ethanol dehydration kinetics

Free energy diagrams of reaction pathways and transition state structural characterization are useful for defining the space of plausible catalytic elementary steps. However, direct comparison with experimental kinetic measurements, which is necessary to verify mechanistic predictions, is not possible without microkinetic modeling. An accurate microkinetic model can, in turn, provide information that may be inaccessible to experiment, such as the identities of the most abundant surface intermediates (MASI) and kinetically relevant steps, and these fundamental kinetic insights may ultimately be used to develop trend-based descriptions of how reaction conditions and heteroatom identity influence reaction rates and selectivities.

### 3.3.5.1 Microkinetic model development

To develop and optimize the microkinetic model, we introduce a self-consistent method of model calibration in which sensitive parameters are identified and subsequently treated at higher levels of theoretical accuracy[139], [150], [151], including hybrid functional calculations for potential energies and molecular dynamics simulations for entropies. To identify sensitive parameters, the generalized Degree of Rate Control (GDRC)[121] is calculated for every reactive intermediate and transition state, normalized by the total DEE formation rate. The first iteration of the microkinetic model is constructed using BEEF-vdW rate constants with harmonic oscillator-derived entropies for adsorbates and standard partition function methods for entropies of gas phase species. A more detailed discussion of the microkinetic model construction, as well as structures of all intermediates, is included in APPENDIX B.

Once rate-controlling intermediates are identified, hybrid functional calculations with HSE06 and improved entropy analyses are performed. A mode decomposition method for calculating adsorbate entropies was developed, where low frequency modes are visualized and

replaced with translational and rotational degrees of freedom, as appropriate (APPENDIX B). In the zeolite framework, free translational diffusion of adsorbates is not possible due to site isolation. Despite this, AIMD calculations of molecular adsorbates show localized translational motion around the adsorption sites, which indicates highly anharmonic potential energy wells. A 1-D square potential is used to approximate these wells, where the width of the square well is estimated from AIMD calculations. Rotational modes, both with and without hindering potentials, are treated with classical partition function methods. Finally, higher frequency modes that cannot be identified as localized translations or rotations are treated using harmonic vibrational partition functions.

Although unfeasible for every reaction intermediate, the entropies of kinetically and thermodynamically sensitive intermediates are calculated using integration of the Vibrational Density of States (VDOS) obtained from atomic trajectories[128]. Atomic trajectories are determined through AIMD with a NVT thermostat at 404 K, and a 0.5 fs timestep is used for 10 ps of equilibration followed by a 15 ps production run. The atomic velocities are then analyzed according to the method by Lin et al.[152], [153] by decomposing the VDOS into ideal gas, rotational, and vibrational degrees of freedom.

A comparison of entropy calculations at 404 K for ethanol monomers and dimers is provided in Table 3.2, including the standard quantum harmonic oscillator method, the Campbell-Sellers relationship[154], which is a semi-empirical correlation for weakly-bound surface intermediates whose entropies are dominated by two dimensional quasi-translational modes, the mode-decomposition method, and the AIMD/VDOS approach.

Table 3.2 Selected entropy comparisons for surface-bound intermediates.

| Adsorbate | Harmonic entropy[a] (J mol$^{-1}$ K$^{-1}$) | Campbell-Sellers entropy (J mol$^{-1}$ K$^{-1}$) | Mode-decomposition entropy (J mol$^{-1}$ K$^{-1}$) | AIMD entropy (J mol$^{-1}$ K$^{-1}$) |
|---|---|---|---|---|
| Ethanol (E*) | 141 | 177 | 169 | 195 |
| Water (W*) | 63 | 111 | 109 | - |
| Ethanol-ethanol (EE*) | 319 | 354[b] | 348 | 372 |
| Ethanol-water (EW*) | 205 | 288[c] | 282 | 390[d] |
| Ethoxy open (E$_x$*) | 151 | - | 182 | - |
| Hydroxy open (W$_x$*) | 59 | - | 105 | - |
| DEE-water (DW*) | 294 | - | 362 | - |

[a]Imaginary frequencies replaced with a 20 cm$^{-1}$ mode, similar to[155]
[b]Referenced to uncorrelated gas phase ethanol
[c]Referenced to uncorrelated gas phase ethanol and water
[d]Sum of ethanol and water contributions

The standard quantum harmonic oscillator underestimates entropies of adsorbed intermediates relative to the Campbell-Sellers approximation, which accounts for translational degrees of freedom. The inclusion of these translational degrees of freedom, in turn, was determined to be important, as translation was observed in AIMD simulations of adsorbed monomers and in visualization of the low frequency harmonic modes. However, the use of the Campbell-Sellers entropy for coadsorbed dimers does not account for the mutual exclusion of identical ethanol molecules, motivating the exploration of mode decomposition approaches. Based on the localized translational character observed in AIMD simulations, the explicit mode decomposition method used particle-in-a-box translation partition functions with diffusion lengths derived from short 5ps AIMD simulations. The mode-decomposed entropies are within 10 J mol$^{-1}$K$^{-1}$ of the Campbell-Sellers entropies, as adsorbates were observed to have two localized degrees of translational freedom. While the Campbell-Sellers approximation is valid for closed-shell molecular adsorbates on different Sn speciations, the entropy change of dissociation to form defect

sites involves open-shell species. To improve estimates of the ethoxy- and hydroxy-open sites, therefore, the mode decomposition method is applied with mode assignments being made based on visualization of harmonic modes. The AIMD/VDOS approach is particularly useful for ethanol monomers and dimers, as it provides a more accurate entropy treatment than the mode decomposition method by including the coupling between anharmonic rotations and vibrations, albeit at a much higher computational cost. With this approach, for example, the entropy of the ethanol-ethanol dimer is found to be 24 J mol$^{-1}$K$^{-1}$ less than the weakly interacting mode-decomposition method.

We note that both the mode decomposition and AIMD/VDOS methods are expected to perform better than the purely harmonic mode approximation, which excessively localizes the molecular adsorbates. In the case of the ethanol-water dimer, AIMD predicts a strongly bound ethanol with entropy similar to the ethanol monomer, and a weakly bound water with entropy similar to an ideal gas state. This delocalization of adsorbate water is not represented in the harmonic mode approximation, which thus greatly underestimates the entropy of the ethanol-water dimer. However, we additionally note that while the mode decomposition entropy is expected to provide a better approximation than the harmonic entropy, the AIMD method is necessary to properly predict experimentally observed kinetic behavior, as is discussed further below. Since AIMD calculations are expensive due to their duration, we suggest first using a mode decomposition method, with short-duration AIMD of a few picoseconds to observe translation lengths, and finally perform a full 15ps or longer AIMD run to obtain anharmonic entropies for the most sensitive intermediates, as determined by the DRC.

In addition to improving the entropic contributions to the free energy, the electronic structure of intermediates can be improved by hybrid DFT functionals, such as HSE06.  These constitute a natural progression toward higher computational accuracy in potential energy calculations because of the exact-exchange contributions that properly localize electron density. The excessive delocalization of electron density by typical GGA-level functionals produces systematic errors in non-conducting oxides[85], and some of this error can be corrected through use of hybrid functionals.  HSE06 does not, however, treat long range dispersion interactions, as shown in APPENDIX B, and thus a Grimme D3-type semi-empirical dispersion correction is added[71], [133]. To quantify the effects of these factors on adsorption energetics, focusing on dimeric species due to their rate-sensitivity, a hypothetical reference state is established

corresponding to two adsorbates at separate Sn sites that are non-interacting. The energy of this configuration can then be compared to the corresponding energy of a dimeric adsorbate and an empty Sn site as shown in Equation 3.3. The difference in potential energy between these two states will be referred to as the dimerization energy, which only includes the energy of reorganization of the adsorbates and additional dispersion interactions gained through dimerization.

$$2E^* \rightleftharpoons EE^* + * \tag{3.3}$$

With this metric, it is found that the ethanol-ethanol and ethanol-water dimers have lower energies when treated with BEEF-vdW as opposed to HSE06-D3 (optimized geometries of these intermediates, however, show no significant differences between BEEF-vdW and HSE06-D3). To compensate for this excess dimer stabilization in BEEF-vdW, differential binding energies are adjusted by +0.12 and +0.15 for the ethanol-ethanol dimer and water-ethanol dimer in subsequent iterations of the microkinetic model, as discussed further below. A full figure of binding energies comparing BEEF-vdW, PBE, PBE-D3, HSE06, and HSE06-D3 is available in APPENDIX B.

### 3.3.5.2   Microkinetic model refinement and mechanistic analysis

The generalized degree of rate control for intermediates and transition states based on mode decomposition entropies and BEEF-VdW energies implies that the reaction rate is sensitive to adsorption energies of ethanol monomers, ethanol-water dimers, and ethanol-ethanol dimers, which have the largest GDRC values of $-1.66 \times 10^{-2}$, $-1.14 \times 10^{-5}$, $-9.83 \times 10^{-1}$. These energies then become the focus for two additional tiers of model accuracy, as described above.  The results of the three tiers are summarized in Figure 3.9, first using a purely quantum harmonic oscillator entropy description and BEEF-VdW energies, second using the mode decomposition method with BEEF-VdW energies, and third with AIMD entropies and HSE06-D3 corrected dimerization energies. Using a purely harmonic oscillator entropy for all adsorbed intermediates, the ethanol reaction order approaches zero at lower ethanol partial pressures than is observed experimentally, suggesting that the harmonic oscillator approach underestimates the entropy of adsorbed ethanol monomers. The ethanol reaction order of zero is likely due to a convoluted effect of differential binding energies between the ethanol monomer and dimer species as evidenced by the HSE06-D3 dimerization energies, as well as the presence of coupled anharmonic entropic modes in the dimer. Without the HSE06-D3 dimerization energy correction, ethanol orders are zero at ethanol partial pressures above approximately 5 kPa. When applying the mode decomposition (MDE)

approximation for entropies and dimerization correction, the ethanol orders remain nonzero over the entire experimental pressure range studied (0.5kPa – 35kPa ethanol).

Better agreement with the experimental orders is achieved, however, when replacing the ethanol monomer, ethanol dimer, and ethanol-water dimer entropies with the full AIMD/VDOS integrated entropies. Water reaction orders agree well with experiment at this level of treatment, and the DEE rate and selectivity are nearly quantitatively consistent with the measurements. The ethanol reaction order is higher (still sub-unity), however, than what is measured in experiment. This modest discrepancy is likely because the ethanol-ethanol dimer binds too weakly when incorporating the HSE06-D3 energies and AIMD integrated entropy. A small reduction of the binding energy (0.06 eV) is sufficient to remove this discrepancy, and this is the only fit parameter in the entire model. The model is also robust against numerical uncertainties; propagation of a 0.1 eV error centered on the calculated free energies of adsorbates and transition states had a negligible change on the generalized degree of rate control (APPENDIX B). These results highlight the usefulness of tiered treatments of microkinetic parameters using both theoretical DRC analysis and comparisons to experimental reaction orders and rates. The iterated DRC analysis captures trends and provides semiquantitative agreement with experimental orders and rates; achieving quantitative agreement with all measurable quantities requires a small residual parameter adjustment.

The site interconversion steps are found to have DRC values more than three orders of magnitude below those of the bimolecular rearrangement steps, demonstrating that site equilibration is achieved under reaction conditions. Effectively, open and closed sites readily interconvert to achieve their equilibrium distribution, which in turn depends only on the chemical potentials of ethanol and water. Significantly, this result demonstrates that the numbers of open and closed Sn sites determined *ex-situ* or after specific gaseous pre-treatment steps cannot be directly correlated with reaction rates under steady-state conditions. Additional evidence for this conclusion is provided by our kinetic measurements. Experimental turnover rates are similar when normalized by the total number of Sn sites (within a factor of ~2 at 404 K) among six samples with varying Sn contents ($2–5\times10^{-4}$ mol Sn g$^{-1}$, or Si/Sn=30–95), but normalization of rates by the number of open Sn sites quantified *ex situ* increases the scatter in turnover rate measurements among these six samples (APPENDIX B). In fact, this phenomenon can be directly simulated by seeding the reactor model with variable initial populations of open sites, similar to a catalyst

sample containing a non-equilibrated distribution of open sites under *ex-situ* conditions. Similar equilibrium coverages of open sites are obtained at steady-state in all cases.

The reactive intermediates with surface coverages identified by the generalized DRC to be rate-controlling include ethanol monomers, ethanol-ethanol dimers, ethanol-ethoxy dimers, and water-ethanol dimers. Figure 3.9 displays DEE rates and surface coverages over an ethanol pressure range of three orders of magnitude (0.1 kPa $H_2O$, 404 K). As discussed above, the optimized microkinetic treatment captures experimental trends quite well. At conditions where experimental data are available, the ethanol order is sub-unity, and the surface contains a mixture of ethanol monomer, ethanol-ethanol dimer, and ethanol-water dimer species. As the ethanol pressure increases beyond 100 kPa, the ethanol order approaches zero, and the surface becomes covered in ethanol-ethanol dimers.
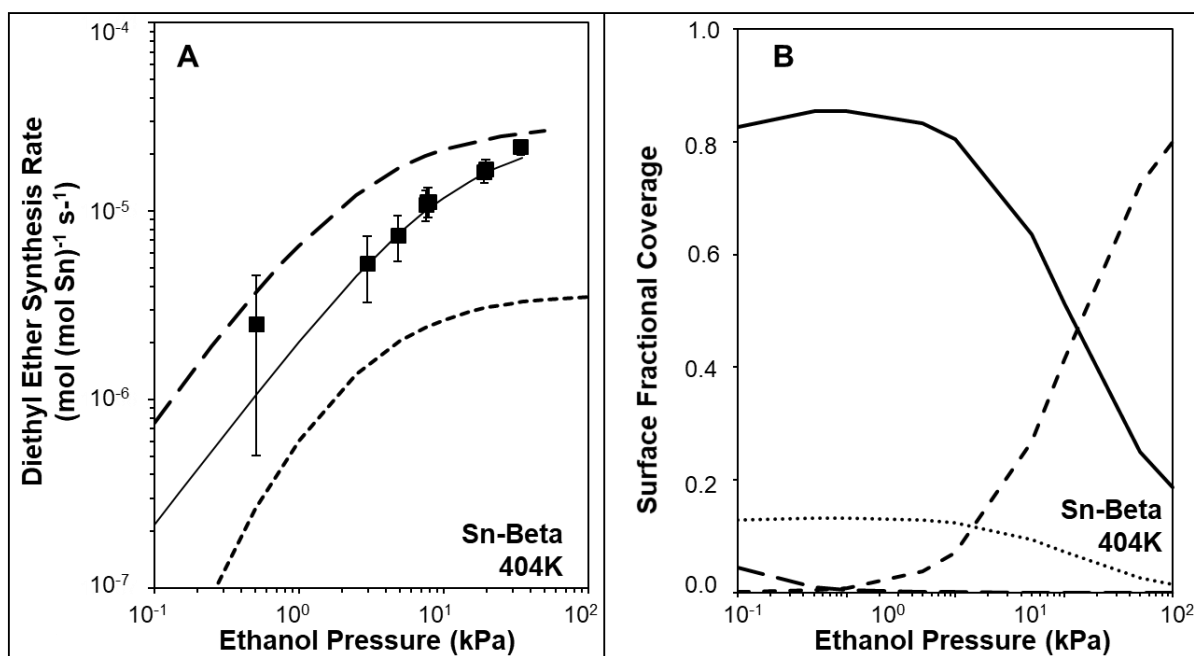


Figure 3.9 A) Ethanol reaction orders at 404 K, 0.1 kPa water partial pressure. . Rate predictions at increasing levels of theoretical treatment are provided which include purely harmonic oscillator entropies (short dashed lines), mode decomposition method using AIMD-derived diffusion distances (long dashed lines), and the full entropy treatment with anharmonic integrated entropies (solid line). B) Surface coverages at 404K and 0.1 kPa water partial pressure at the full quasi-harmonic level. Ethanol monomer E* (solid line), ethanol dimer EE* (short dashed line), empty site * (long dashed line), ethanol-water dimer EW* (dotted line).

At low ethanol partial pressures, below 1 kPa, the coverage of empty Sn sites begins to increase, which might eventually lead to an ethanol order greater than unity at ethanol partial pressures much lower than what we can access experimentally. However, as the adsorption of ethanol is highly exothermic, few vacant Sn sites are present at the relevant pressures. This fact, coupled with the presence of a non-negligible coverage of ethanol-water dimers resulting from competitive adsorption of water, leads to ethanol reaction orders less than unity (see section 3.3.5.3 for additional discussion).

Under reaction conditions, the abundance of vacant ethoxy and hydroxy open sites is predicted to be below 1%. The contribution to DEE formation from the closed site mechanism is 99% of the total DEE formation rate, with the ethoxy open site accounting for slightly less than 1% of the total rate and the hydroxy open site mechanism having a negligible contribution to the total DEE formation rate. This higher turnover rate from the closed site mechanism is due to both the negligible coverage of open sites under reaction conditions and the lower kinetic barrier, relative to the gas phase species, of the closed site mechanism (Figure 3.7). These results demonstrate that open sites contribute only marginally to ethanol dehydration turnovers on Sn-Beta.

Table 3.3 Selected generalized DRC for reactive intermediates and transition states. Level of theory includes HSE06-D3 and AIMD entropy scheme.

| Adsorbate | Generalized DRC |
|---|---|
| Ethanol (E*) | -0.55 |
| Ethanol-ethanol (EE*) | -0.37 |
| Ethanol-water (EW*) | -0.08 |
| Closed site TS (TS1) | 0.99 |

Water orders and coverages are calculated at fixed ethanol partial pressure and fixed conversion and shown in Figure 3.10. At low water partial pressures, the water order approaches zero, and at higher partial pressures, the water order approaches -1, consistent with measured reaction rates and kinetic inhibition by water. Indeed, the dominant water intermediate at high water pressure is found to be the ethanol-water dimer. This result is fully consistent with DRC

analyses that give a modest negative value for ethanol-water dimers (-0.11), indicative of an inhibitory species.
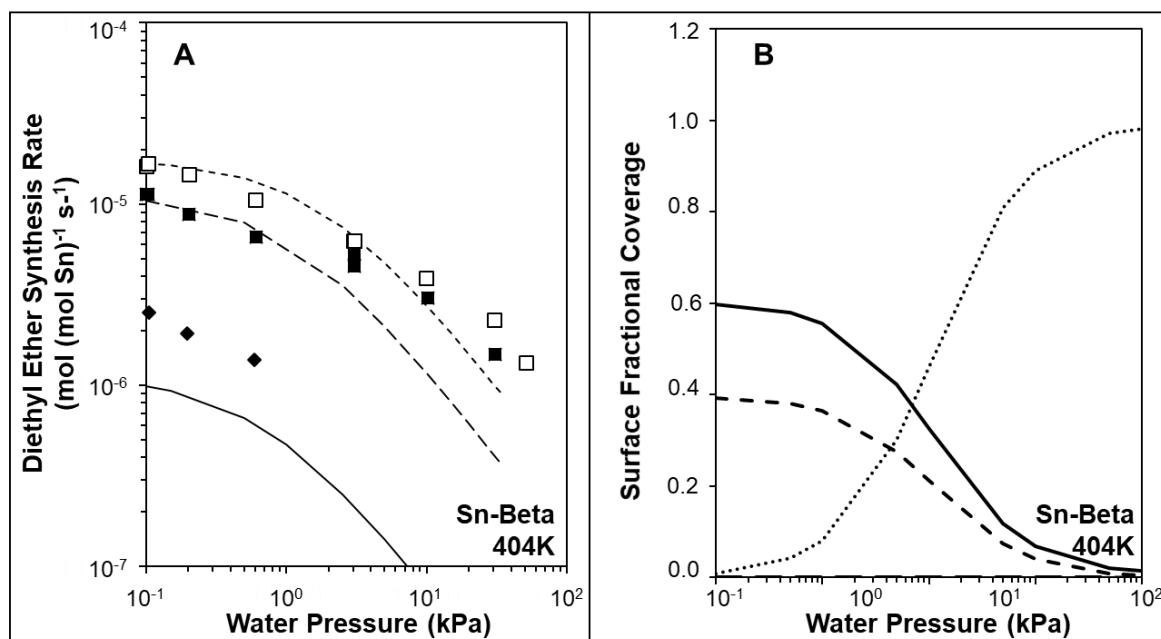


Figure 3.10 A) Water reaction orders at 404 K and 20 kPa ethanol partial pressure (short dashed line and open squares for theory and experiment), 8 kPa ethanol partial pressure (long dashed line and filled squares for theory and experiment), 0.5 kPa ethanol partial pressure (solid line and filled diamonds for theory and experiment. B) Surface coverages are at 404K and 8 kPa ethanol partial pressure. Ethanol monomer E* (solid line), ethanol dimer EE* (short dashed line), empty site * (long dashed line), ethanol-water dimer EW* (dotted line). All calculations at full integrated VDOS level.

### 3.3.5.3   Simplified mechanism and rate expression

Using the generalized degree of rate control analysis and knowledge that the kinetically relevant pathway is mediated by the closed site, a simplified rate expression for ethanol dehydration can be derived. Over the range of reaction conditions studied, the intermediates with an appreciable degree of rate control and surface coverage are ethanol monomers (E*), ethanol-ethanol dimers (EE*), and ethanol-water dimers (EW*). All adsorption and desorption steps are quasi-equilibrated, and there is site equilibration between closed and open sites regardless of ligand identity. From these observations, the mechanism can be reduced to three intermediates, three quasi-equilibrated elementary steps, and one rate determining step (Figure 3.11).

$$
\begin{array}{lll}
(1) & E(g) + * \xrightleftharpoons{K_1} E^* \\
\\
(2) & E(g) + E^* \xrightleftharpoons{K_2} EE^* \\
\\
(3) & W(g) + E^* \xrightleftharpoons{K_3} EW^* \\
\\
(4) & EE^* \xrightarrow{k_4} DEE(g) + W(g) + *
\end{array}
$$
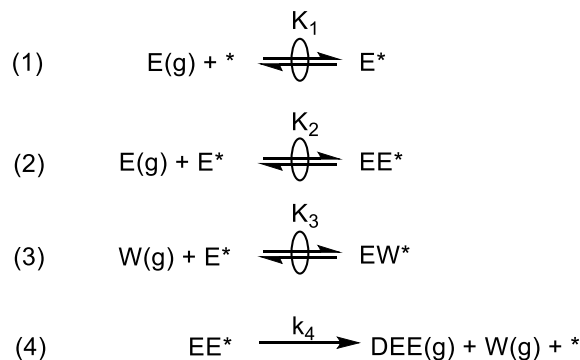
Figure 3.11 Simplified reaction mechanism derived from the generalized degree of rate control.

The mechanism in Figure 3.4 can be used to derive a rate expression of DEE formation per active site in terms of ethanol and water partial pressures, as well as rate and equilibrium constants of the elementary steps:

$$
\frac{r_{DEE}}{L} = \frac{k_4 K_1 K_2 P_E^2}{1 + K_1 P_E + K_1 K_2 P_E^2 + K_1 K_3 P_E P_W} \tag{3.4a}
$$

where $r_{DEE}$ is the rate per unit surface area, "L" denotes the total number of catalytic Sn sites, and $\theta$ denotes the fractional coverage of a given reactive intermediate. However, since the coverage of vacant sites is negligible, the unity term in the denominator can be neglected, yielding

$$
\frac{r_{DEE}}{L} = \frac{k_4 K_2 P_E}{1 + K_2 P_E + K_3 P_W} \tag{3.4b}
$$

A detailed derivation is provided in the APPENDIX B. Equation (3.4b) predicts ethanol reaction orders of between zero and unity, depending upon the relative partial pressures of ethanol and water, in agreement with our experimental results. We note, however, that equation (3.4b) will not hold in the limit of extremely low ethanol partial pressures (below what we have accessed experimentally) where the coverage of empty sites becomes relevant and where the ethanol order could approach two. In general, this simplified rate expression provides a model that can be used to extract intrinsic rate and equilibrium constants from measured kinetic data. In addition, future computational searches over zeolites with different topologies or Lewis heteroatom identities could be more rapidly performed by focusing on these key descriptors of the reacting molecules.

### 3.4 Conclusions

A mechanistic study of ethanol dehydration to diethyl ether in Sn-substituted zeolite Beta was performed using a combination of DFT calculations and experimental kinetic measurements, which were linked through microkinetic modeling. The kinetic modeling results at the level of GGA functionals and harmonic oscillator-derived entropies compare poorly with experimentally measured rates and reaction orders. Although performing hybrid functional calculations and AIMD entropies for all reactive intermediates is infeasible, a hierarchical scheme of microkinetic model development that employs higher accuracy methods for kinetically sensitive intermediates provides an efficient approach to capture the critical physicochemical features of the ethanol dehydration reaction network. Here, the generalized degree of rate control is used both as a criterion for distinguishing rate-determining pathways and as a criterion for employing higher accuracy methods. The BEEF-vdW functional, used for its self-consistent van der Waals correlation, overbinds ethanol-water (EW*) and ethanol-ethanol (EE*) dimers in comparison to HSE06-D3, perhaps due to imprecise descriptions of hydrogen bonding interactions that dominate many of the differential binding energies in this study. For kinetically sensitive intermediates, an AIMD-based integration scheme treats the long-range anharmonic framework interactions, and further improves agreement with experimentally measured orders. The model allowed for rationalization of experimentally observed reaction orders and identifies ethanol-water dimers as the dominant inhibitory surface species. Methods such as these can be broadly applied to microkinetic models requiring higher accuracy methods for a subset of intermediates.

Closed and open sites are found to interconvert in quasi-equilibrated processes under reaction conditions, and distinct mechanisms for dehydration on each site are considered. Dehydration transition states at each type of site show similar intrinsic barriers, and the dominant pathway is mediated by closed Sn sites. Indeed, under experimentally studied reaction conditions (404K, 1-35kPa ethanol, 1-35 kPa water), the relative coverages of ethoxy and hydroxy open sites were less than 1%, with the dominant surface intermediates being ethanol monomers and ethanol-ethanol dimers. Mechanisms considered on the hydroxy-open site show a concerted transition state involving both the Lewis acidic character of the tin center in addition to the weak Brønsted acidic character of the adjacent framework silanol, via a transition state geometry reminiscent of that in ethanol dehydration previously studied on Brønsted solid acids.

The dynamic conversion of tin sites of different coordination under reaction conditions introduces additional possibilities for influencing the reactivity of Lewis acid zeolite catalysts. Depending on the applied chemical potential of water or other alkanols, the equilibrium distribution of sites under reaction conditions can be controlled. This opens an avenue to influence selectivity by preferentially enhancing rates of specific pathways that may be catalyzed on different heteroatom coordinations. These findings show how the relative stability of different active site structures under reaction conditions must be understood to gain a mechanistic understanding of reactions catalyzed by Lewis acid zeolites and to provide additional strategies for tuning the catalytic properties of these materials.

# 4. DISTINCT CATALYTIC REACTIVITY OF SN SUBSTITUTED IN FRAMEWORK LOCATIONS AND AT DEFECT GRAIN BOUNDARIES IN SN ZEOLITES

## 4.1 Introduction

In CHAPTER 3 a microkinetic model of ethanol dehydration in Sn-Beta was developed which described the interconversion of Sn sites between closed and hydrolyzed open. This chapter will summarize the salient features of Bates et al.[156] with respect to the computational models developed that contribute to the conclusion that defect-open Sn sites, which are structurally distinct from hydrolyzed-open Sn sites do not catalyze ethanol dehydration. Heterogeneous distributions of Lewis acid sites have been characterized by deuterated acetonitrile stretches as either 2316 cm$^{-1}$ (Sn$_{2316}$) or 2308 cm$^{-1}$ (Sn$_{2308}$) which have been correlated to catalytic rates such as Sn$_{2316}$ for glucose isomerization[100] and other sites with aldol condensation. The precise structure of these two sites is not understood. The formation of hydrolyzed Sn sites as shown in CHAPTER 1 and CHAPTER 2 are energonic relative to the adsorption water molecules, and their coverage under reaction conditions is significantly lower than that of closed Sn sites. The presence of measured 2316 cm$^{-1}$ peaks may indicate a Sn site that cannot reversibly close; however, previous models in the literature propose defect open sites as being formed by Si vacancies proximal to the Sn site which form silanol nests that cannot be hydrated and closed, resulting in a permanent stannanol ligand[69], [107]. Why vacancies would form in proximity to Sn sites is also not understood.

In this work *in-situ* pyridine titrations were used to quantify the densities of active sites, which find a subset of most reactive Sn sites in Beta. Through experimental techniques Sn$_{2316}$ sites are shown to correlated with stacking faults in Beta due to an intergrowth of two distinct polymorphs. A computational model was constructed which included defect-open sites at stacking faults based on a 2×2×1 Beta supercell in order to compare their ethanol dehydration reactivity with that of closed sites,[157] and show that the apparent activation free energy for bimolecular

ethanol dehydration (referenced to the ethanol monomer) is 65–74 kJ mol$^{-1}$ higher at stacking fault-defect open sites than at closed sites, because the former are unable to interconvert between open and closed configurations, thus requiring the reaction mechanism to proceed through higher energy transition states. The experimental and theoretical evidence provided indicate that the dominant active sites for ethanol dehydration are not the defect-open Sn sites (Sn$_{2316}$), in contrast to glucose isomerization, and instead comprise 17–26% of the closed sites (Sn$_{2308}$) as indicated by in situ pyridine titration of a diverse range of Sn-zeolites.

## 4.2    Methodology

Periodic, self-consistent density functional theory (DFT) calculations with the Vienna Ab-initio Simulation Package (VASP)[158]–[160] was employed for all electronic structure calculations at stacking fault defect-open Sn sites. The computational parameters were chosen to be consistent with our previous work on ethanol dehydration in Sn-Beta to allow for comparisons among calculations at both closed and hydrolyzed-open Sn sites in Beta ("framework sites"), and stacking fault sites. For all calculations, the Bayesian error estimation functional (BEEF-vdw)[161] was used with projector augmented wave (PAW) pseudopotentials[162], [163] along with a plane wave cutoff of 520 eV. All calculations were performed spin-polarized.

The stacking fault model is depicted in Figure 4.1a,b. The model was constructed based on TEM images of stacking fault defects in Beta zeolites.[164] A 1-D periodic cell was built by first tiling polymorph A and polymorph B bridged by three "bea" composite building units (CBUs). Individual mor, bea, and mtw CBUs were then individually manipulated to form a natural tiling and link the two polymorphs at the double-pore region. The resulting structure consisted of 422 oxygen atoms and 202 silicon atoms. Domains of  polymorph A or B in Beta crystals typically continue for multiple nanometers between stacking faults,[164], [165] so the model was terminated following a single A and B repetition and capped with hydrogen atoms, to maintain a similar strain on the structure as if it were repeated. Along the plane parallel to the double pore, periodicity was maintained as an infinite stacking of A and B polymorphs. This direction of periodicity provides well-needed structural rigidity to the model and allows calculation of van der Waals energies of guest molecules in the double-pore region that include interactions along the length of the pore. This structure was then relaxed to a force criterion of 30 meV Å$^{-1}$. The sizeable memory requirements demanded by this model in VASP 5.3.5 necessitate careful selection of an appropriate

number of computer nodes and band parallelization for the researcher's specific hardware. Initial geometric relaxations were performed without spin polarization, and spin polarization was included in a subsequent relaxation.

Nudged elastic band (NEB) calculations were performed in the stacking fault model with the climbing image method (CI-NEB).[166], [167] CI-NEB calculations were converged to a force criterion of 75 meV $\text{Å}^{-1}$, which is higher than previously used by us for framework sites in Beta.[157] This force criterion is needed because of the large unit cell size, and poor convergence of the CI-NEB algorithm for systems with multiple low-frequency modes.[157], [168] The Lanczos diagonalization method, which is typically successful for refining transition states to force convergence criteria of 30 meV $\text{Å}^{-1}$, , is computationally demanding, and slow to converge for a system of this size. Despite the less stringent force criteria employed for stacking fault sites compared to the traditional framework models for Beta, transition state energies can still be compared between the models due to the otherwise identical calculation parameters. The faulted intergrowth of the A and B polymorphs in the double pore leads to seven distinct tetrahedral locations with the configuration $(HO)\text{-}Si\text{-}(OSi\equiv)_3$, and no Si-OH groups are sufficiently proximal to allow condensation. Sn substitutions were considered at all seven locations to yield defect-open sites with the configuration $(HO)\text{-}Sn\text{-}(OSi\equiv)_3$. $C_2H_5OH$ binding energies at all seven defect-open sites were within 0.20 eV, suggesting that they are chemically similar. The *ab initio* molecular dynamics (AIMD) adsorption configuration sampling methods used previously[157] were inaccessible due to the model sizing, requiring manual selection of adsorbate configurations. Free energy calculations in the stacking fault model required unique assumptions because of the large unit cell. Zero-point energy corrections were assumed to be equivalent to those calculated previously for analogous adsorbates at standard framework Sn sites (hydrolyzed-open or ethoxy-open)[157] because of their similar adsorbate structures and active site ligands. In addition, vibrational and rotational entropies of each adsorbate were considered equivalent to those at standard framework Sn sites. The translational entropy of adsorbates in stacking fault sites was calculated by replacing the low-frequency translational modes with localized free particle diffusion constants by adjusting the accessible diffusion length. Without AIMD trajectories to calculate the accessible diffusion length,[157] the lengths were adjusted to account for the ~2× larger accessible pore volume surrounding stacking fault sites. Edge lengths for ethanol monomer species were increased from 3 Å to 6 Å, corresponding to a 10 J $\text{mol}^{-1}$ $\text{K}^{-1}$ increase in entropy. An entropy

increase of 23 J mol$^{-1}$ K$^{-1}$ for ethanol-ethanol dimers corresponded to changing the accessible diffusion length from 5 Å to 10 Å. Ethoxy intermediates had similar entropies at both defect-open sites and framework sites because the degrees of freedom as a ligand on the Sn site are assumed to be approximately similar for both types of sites

## 4.3    Results and discussion

### 4.3.1    Grain boundary site computational model

A computational model of Sn substituted at a stacking fault grain boundary was constructed by following the tiling pattern developed by Wright et al.[164] (Figure 4.1), where one layer of polymorph A and one of polymorph B meet and form a double-pore structure with seven T-atoms within the pores terminated by hydroxyl groups. It is periodic in one dimension along the axial direction of the defective pore (Figure 4.1b) to provide structural rigidity. Sn was substituted at one of the locations in the lower part of the defective pore (Figure 4.1a, gray atom), leading to a (OH)Sn(OSi≡)$_3$ structure with a stannanol group and no nearby Si-OH that can form a closed site by condensation with the stannanol, which can be described as defect-open.[169] This model differs from previously used defect-open models because they were created by removing a Si T-atom from the otherwise intact crystal structure of polymorph A, resulting in a hydroxyl nest including 3 Si-OH groups and the stannanol.[169], [170] Sn at the chosen defect-open location in
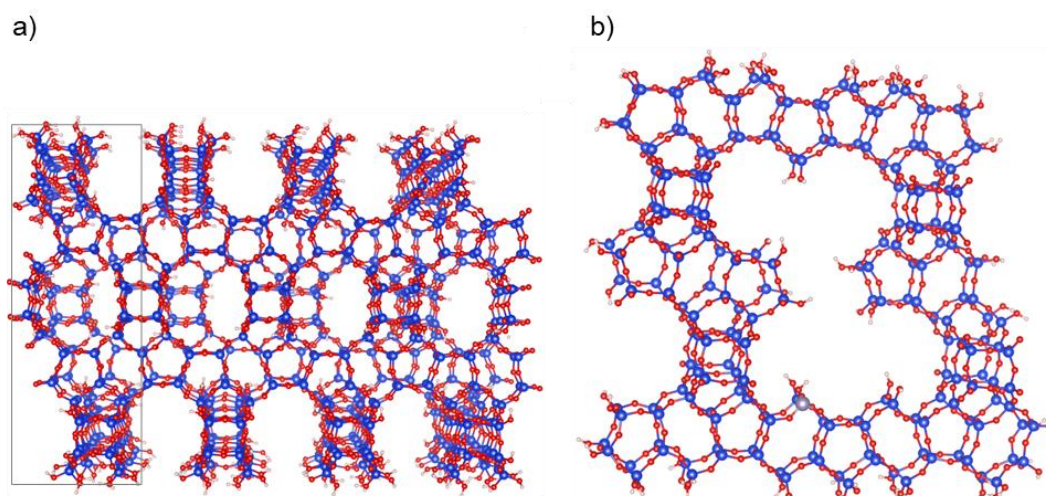


Figure 4.1 (a) View of the stacking fault defect model developed in this work, with Sn substitution in the defect-open configuration, and (b) view rotated 90° to show periodicity in one direction, with the unit cell enclosed in the gray box. Blue = Si, Red = O, Gray = Sn, White = H.

the stacking fault is representative of any site in the defective pore that prevents forming closed sites, as evidenced by the similar calculated ethanol binding energies among the seven different defect-open locations (APPENDIX C) The model therefore captures the distinct structural features of Lewis acid sites located within defective regions at stacking faults in Beta zeolites and permits comparing their reactivity with traditional models of Lewis acid sites within Sn-Beta, as we discuss below.

### 4.3.2   Free energy diagram of ethanol dehydration at grain boundary sites

The Gibbs free energies of adsorbed intermediates and transition states involved in concerted and sequential bimolecular ethanol dehydration pathways were calculated at the stacking fault defect-open site and compared with previously calculated free energies for the concerted dehydration mechanism at closed sites, which is the sole kinetically-relevant pathway (degree of rate control = 0.99), as determined by microkinetic modeling that included sequential pathways and interconversion between hydrolyzed-open and closed sites.[157] These pathways are compared on a free energy diagram in Figure 4.2, with the gas-phase species that are involved at each reaction coordinate position listed above the plot. We note that the computational complexity of the model prevents vibrational frequency calculations; thus, zero-point energies (ZPEs) were considered equivalent to the same reactive intermediate at framework sites calculated previously,[157] and ZPE changes for transition states were assumed equal to their initial state. These ZPE approximations can introduce errors on the order of 10 kJ mol$^{-1}$ in apparent free energy barriers.

The pink pathway corresponds to the concerted mechanism at closed sites (denoted *) calculated previously,[157] where diethyl ether forms via an $S_N2$-like transition state (TS1, Figure4.2b) from a co-adsorbed ethanol-ethanol dimer intermediate (EE*) with an apparent activation free energy of 125 kJ mol$^{-1}$ (referenced to E* + E(g), because this gives first-order kinetics consistent with experimental measurements). It is worth noting here that the $S_N2$ transition state is stabilized by forming a hydrolyzed-open site (W$_x$*), with its stannanol acting as the leaving group, and one framework O atom acting as a Brønsted base[171] to accept the alcohol proton from the nucleophilic ethanol and to begin to form a proximal silanol. This site can then complete the catalytic cycle by kinetically-irrelevant product desorption and site-closing steps, where the stannanol and proximal silanol recombine to form surface-bound water. In contrast, defect-open
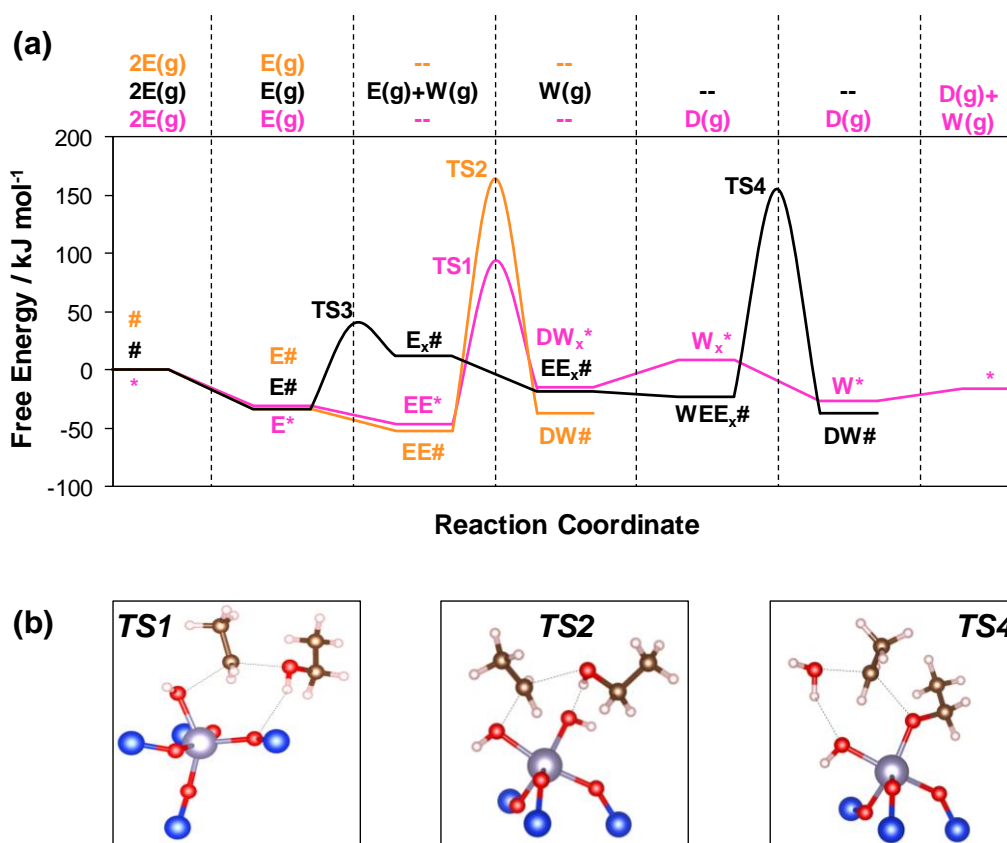
Figure 4.2 (a) Gibbs free energies of adsorbed intermediates and transition states calculated by DFT, referenced to two gas-phase ethanol molecules, for bimolecular ethanol dehydration at closed framework Sn sites (*) via a concerted pathway (pink, calculated from CHAPTER 3), and at stacking fault defect-open sites (#) via a concerted pathway (orange) or a sequential pathway (black). Product desorption steps are omitted from the stacking fault defect-open pathways for clarity. The gas-phase species at each position along the reaction coordinate are included above the plot area. (b) Transition state geometries for bimolecular dehydration at the closed site (TS1), and the stacking fault defect-open sites via the concerted pathway (TS2) and the sequential pathway (TS4). Intermediate geometries are provided in Figure S57.

sites do not have these interconversion pathways available to them because of geometric constraints and so must traverse distinct mechanistic pathways. If defect-open sites are the predominant sites (A) for ethanol dehydration, the activation free energies at these sites, properly referenced to adsorbed intermediates that give first-order kinetic behavior, should be lower than this value of 125 kJ mol$^{-1}$. A concerted mechanism was calculated on the stacking fault defect-open site (denoted #) and corresponds to the orange pathway in Figure 4.2. Gas-phase ethanol adsorbs at the Sn center to form the ethanol monomer intermediate (E#) with an adsorption free energy of -35 kJ mol$^{-1}$. The similarity of this adsorption free energy to that calculated at closed sites (-31 kJ

mol$^{-1}$)[157] reflects compensations among entropies, van der Waals energies, and electronic contributions to adsorption that are distinct at the stacking fault defect-open site (APPENDIX C). In particular, while the entropy of ethanol adsorbed at the stacking fault defect-open site is at least 10 J mol$^{-1}$ K$^{-1}$ greater than at closed Sn sites, the van der Waals dispersion energy as calculated using the method by Grimme[172] is weaker by 9 kJ mol$^{-1}$. A second gas-phase ethanol molecule adsorbs in an octahedral configuration to the Sn to form the ethanol-ethanol dimer intermediate (EE#) with a differential adsorption free energy of -19 kJ mol$^{-1}$ and a differential adsorption enthalpy within 5 kJ mol$^{-1}$ of that at the closed site. This similarity reflects compensation between the weaker van der Waals dispersion energy and a stronger adsorption energy at the stacking fault defect-open site. An octahedral configuration was not stabilized at closed Sn sites, which preferred a hydrogen-bonded ethanol-ethanol dimer structure that minimized geometric distortion in the framework and increased the degree of favorable interactions with the confining pore.

Despite a stannanol group bound to Sn, the transition state (TS2, Figure 4.2b) differs from that previously reported on hydrolyzed-open sites[157] because defect-open sites lack a Brønsted acidic proximal silanol. At the hydrolyzed-open site, the proximal silanol donates its proton to the hydroxyl group of the ethanol being attacked, forming water as a leaving group and simultaneously closing the site by re-forming the Sn-O bond, while the stannanol group accepts a proton from the nucleophilic ethanol to form adsorbed H$_2$O at the newly-closed site (APPENDIX C). In TS2, the stannanol serves the same function to deprotonate the nucleophilic ethanol and form water, but the leaving group instead is the hydroxyl group of the second ethanol molecule, which transfers to the Sn atom to re-form the stannanol group at the defect-open site. The hydroxyl leaving group of TS2 is less stable than a H$_2$O molecule, leading to an intrinsic activation free energy of 218 kJ mol$^{-1}$, or an apparent activation free energy of 199 kJ mol$^{-1}$, when referenced to gas-phase ethanol and the ethanol monomer. This apparent activation free energy is 74 kJ mol$^{-1}$ higher than that calculated at the closed site (125 kJ mol$^{-1}$), and so this pathway cannot account for the reactivity of the predominant active sites on Sn-Beta. The apparent enthalpic and entropic contributions to the high apparent activation free energy are 157 kJ mol$^{-1}$ and -103 J mol$^{-1}$ K$^{-1}$, respectively, indicating the lower reactivity is a consequence of the enthalpy at the transition state, because the $\Delta S^{\ddagger}_{app}$ value of -103 J mol$^{-1}$ K$^{-1}$ is similar to -116 J mol$^{-1}$ K$^{-1}$ at the closed site. The higher transition state enthalpy is likely related to the less-stable hydroxyl leaving group. With the conclusion that

concerted mechanisms are unfavorable at defect-open sites, we explored ethoxide-mediated sequential pathways to broaden the space of potential mechanisms.

The sequential pathway at the stacking fault defect-open site (black line Figure 4.2) begins like the concerted pathway, with adsorption of gas-phase ethanol to form an ethanol monomer, E#. The ethanol monomer then eliminates $H_2O$ to form an ethoxy group at the site ($E_x$#) and gas-phase water, with a reaction free energy of 46 kJ mol$^{-1}$, and an intrinsic activation free energy of 74 kJ mol$^{-1}$ (APPENDIX C). A second gas-phase ethanol molecule adsorbs at the Sn center to form an ethoxy-ethanol complex ($EE_x$#), with a differential adsorption free energy of -30 kJ mol$^{-1}$. The ethoxy-ethanol complex may rearrange to form diethyl ether, but this transition state (APPENDIX C) is highly geometrically-constrained because the proton of the nucleophilic ethanol molecule must transfer to the O atom of the ethoxy it is attacking to regenerate the stannanol group of the defect-open site, leading to a high intrinsic activation free energy of 231 kJ mol$^{-1}$. Instead, a gas-phase water molecule (perhaps desorbed during the ethoxy formation step) adsorbs to form a water-ethanol-ethoxy complex (APPENDIX C), with a differential adsorption free energy of -5 kJ mol$^{-1}$. This water molecule lowers the intrinsic activation free energy to 179 kJ mol$^{-1}$ by donating a proton to the hydroxyl leaving group of the adsorbed ethanol to form a stable $H_2O$ leaving group, and simultaneously regenerating the defect-open site stannanol group (TS4, Figure 4.2b). The reduction of activation barriers by $H_2O$-mediated proton transfer pathways has been noted before in theoretical studies of glucose isomerization catalysis.[173] Different MARI species along the water-assisted sequential pathway may give first-order kinetics (E#, $E_x$#), but the reaction free energy to form $E_x$# is similar to that for forming $E_x$* at framework sites (within 6 kJ mol$^{-1}$), where previous microkinetic modeling predicted the coverage of $E_x$* was <1%. Thus, E# is a more plausible MARI species, leading to an apparent activation free energy at defect-open sites of 190 kJ mol$^{-1}$. While this apparent activation free energy for the sequential pathway may be competitive with that of the concerted pathway at the defect-open sites (199 kJ mol$^{-1}$), it is higher than that of the concerted pathway at closed sites (125 kJ mol$^{-1}$). Thus, our calculations indicate that defect-open sites are not the predominant sites for ethanol dehydration.

### 4.3.3 Role of grain boundary sites in ethanol dehydration kinetics

The insights provided by these calculations were used next to re-assess the identities of sites A and B that were titrated by pyridine *in situ* during ethanol dehydration catalysis. Assuming

$Sn_{2316}$ sites are defect-open sites, and because the calculated apparent activation free energy barriers for ethanol dehydration at these sites are at least ~50 kJ mol$^{-1}$ higher than those measured at either A sites or B sites, then both A and B sites are a subset of $Sn_{2308}$ sites that correspond to framework Sn sites. DFT-calculated apparent activation free energies (404 K, relative to the ethanol monomer) at closed sites consistent with those measured on A sites are also consistent with their identity as closed framework Sn sites ($Sn_{2308}$). The density of A+B sites quantified at $t_1$ (after initial deactivation transients) is in reasonable agreement with parity for $Sn_{2308}$ sites, consistent with this assessment. This supports the conclusion that the predominant sites (A) correspond to 17–26% of $Sn_{2308}$ sites, with B sites accounting for the remaining $Sn_{2308}$ sites, and that these sites differ in their reactivity predominantly by their entropies of activation. The generality of this correlation to different Sn-zeolite samples (Sn-MFI-F-129, Sn-Ge-BEC-F) that lack distinct $Sn_{2316}$ sites, and its insensitivity to increased $H_2O$ pressures (0.1–1 kPa $H_2O$), indicates that this subset of $Sn_{2308}$ sites is structurally distinct from the remaining $Sn_{2308}$ sites, but that $CD_3CN$ IR is not sensitive to this difference.

Although currently available spectroscopic probes cannot distinguish between A sites and B sites, the ethanol dehydration kinetic probes that distinguish them are sensitive to free energies of ethanol dehydration transition states that involve simultaneous Sn site-opening, a salient feature of the DFT-calculated pathways that results in stabilization of transition states at framework closed sites over those at stacking fault defect-open sites. As a result, more-reactive and less-reactive framework Sn sites may be sensitive to the energetics associated with closed-to-open site interconversion during the reaction coordinate, which we speculate may reflect heterogeneities in local structure caused by crystallographically-unique framework T-site locations; such phenomena may be amenable to further detailed examination by DFT calculations that are beyond the scope of the current study. The stacking fault defect-open site model used here provides evidence that such sites do not contribute to measured ethanol dehydration reactivity, and we anticipate it will be useful to accurately model reaction coordinates that do occur at them such as glucose isomerization, which would benefit from the larger void space and nearby hydroxyl groups in the surrounding environment. The defect-open site possesses Si-OH groups that would stabilize hydride shift transition states similar to pathways calculated on hydrolyzed-open sites[173], [174] because their Si-OH groups lie within distances sufficiently proximal (Sn-H(O-Si) distance of 4.6 Å compared with 3.5 Å at the hydrolyzed-open site, APPENDIX C) to donate hydrogen bonds to

glucose or co-adsorbed $H_2O$ molecules at transition states. Their double-pore structure may also enable facile diffusion of glucose and fructose molecules, as suggested as an explanation for the lower reactivity of Sn-MFI zeolites.[173] The structural diversity of zeolite frameworks that host Sn sites in both framework and defect-open configurations confers reactivity for a broad range of oxygenated molecules.[175]–[178]

## 4.4 Conclusions

A structural model of stacking fault defect-open sites was developed and enabled assessing their ethanol dehydration reactivity to determine whether they are the predominant sites (A) titrated by pyridine *in situ*. DFT-calculated apparent free energies of activation (404 K, diethyl ether formation transition state relative to the adsorbed ethanol monomer and gas-phase ethanol) for concerted and sequential pathways at stacking fault defect-open sites were higher than at closed Sn sites[157] by 65–74 kJ mol$^{-1}$, indicating these sites do not contribute to ethanol dehydration reactivity at 404 K. Calculated transition state structures at stacking fault defect-open sites are less stable enthalpically because of their constrained geometries and less stable leaving groups, in contrast to transition states at closed sites that adopt less-constrained geometries and stabilize leaving groups by site-opening at the transition state. The predominant sites for bimolecular ethanol dehydration quantified by *in situ* pyridine titrations are therefore consistent with 17–26% of $Sn_{2308}$ sites quantified by $CD_3CN$, rather than the defect-open sites that give rise to a $CD_3CN$ IR peak at 2316 cm$^{-1}$. This fraction of framework Lewis acid sites is similar in Sn-Beta-F and Sn-Beta-OH materials with a wide range of Sn contents (0.9–5×10$^{-4}$ mol Sn g$^{-1}$) and synthetic provenance (-F, hydrothermal; -OH, post-synthetic), and additionally in Sn-MFI-F and Sn-Ge-BEC-F materials.

We have identified the structural features that lead to distinct Sn site configurations in Beta zeolites, and reasons for their different reactivity. Defect-open sites ($Sn_{2316}$) are distinguished by their inability to form closed configurations and preserve nearby Si-OH groups, the former feature causing their negligible bimolecular ethanol dehydration reactivity, and the latter resulting in their predominance for glucose-fructose isomerization. Framework Sn sites ($Sn_{2308}$), on the other hand, are distinguished by their ability to interconvert between closed and hydrolyzed-open configurations during catalysis, a critical feature that facilitates bimolecular ethanol dehydration. The different site requirements of these two probe reactions at Sn Lewis acid sites in Beta zeolites,

and the structural diversity of their frameworks that allows them to host different Sn site configurations that catalyze both types of reactions, can rationalize the broad application of Sn-Beta for diverse chemical conversions of oxygenated molecules.[175]–[178] This structural diversity in active site coordination afforded by the intergrowth of Beta polymorphs, which contain frequent occurrences of defect grain boundaries at stacking faults that pronounce defect-open site configurations, may also have catalytic consequences for Brønsted acid-catalyzed reactions in H-Al-Beta zeolites, which are applied in a variety of hydrocarbon transformations.[179]–[182] The approach taken here to reach these conclusions requires synthetic, spectroscopic, and theoretical techniques working in concert, all of which are undergirded and driven by the guiding principles of the turnover rate[183] and its accurate quantification with the aid of chemical titrants under reaction conditions.[184]

# 5. SYNTHESIS OF BUTADIENE BY LEWIS ACID FUNCTIONALIZED BETA

## 5.1 Introduction

Microporous solid acids, such as zeolites, with metal heteroatoms incorporated into tetrahedral framework sites catalyze a variety of oxygenate chemistries such as glucose isomerization[185], Baeyer-Villiger oxidation of ketone[186], aldol cross-condensations[187] among others. In particular zeolite Beta has been identified for its stability in liquid water[188]. Incorporated metal heteroatoms, such as Sn, Ti, Hf, Zr, and other $4^+$ or $5^+$ metals behave as Lewis acids. Platform chemicals, such as 1,3-butadiene were traditionally produced from naptha steam cracking; however, the transition to shale and unconventional petroleum resources introduces a shortage of olefins[9], [10]. The synthesis of olefins like butadiene from renewable feedstocks, such as ethanol provides an alternative technology to future fine chemical production[20]. Early conversion of ethanol to butadiene, studied by Ipatiev and later Quattlebaum, Toussaint, and Dunn examined how alumina catalyzed butadiene through a proposed aldol condensation of acetaldehyde forming crotonaldehyde[189]. Recently, zeolite catalysts containing Lewis acid metal atoms have been proposed to catalyze the synthesis of butadiene from ethanol, when a co-catalyst to dehydrogenate ethanol to acetaldehyde is present[190]–[193]. These studies have used Zr and Ta containing zeolite Beta; yet, there has not been a fundamental study to examine the role of framework structure on the kinetics of butadiene synthesis.

Butadiene synthesis on Ta and Zr-Beta is proposed to occur through a sequential Guerbet coupling reaction, in which ethanol is first oxidized to acetaldehyde, where aldol condensation forms an aldehyde. This aldehyde is then hydrogenated and dehydrogenated to form butadiene[190], [191]. A similar mechanism has been proposed in the synthesis of butanols from ethanol on the hydroxyapatite structure[194], where crotonaldehyde formed in the aldol condensation undergoes MPV reduction with ethanol to form butanols. Other alkaline zeolites with cation exchanged lithium and potassium sites have also been studied for ethanol coupling to form butanols[195]. For Ta and Zr-Beta, the active structure and kinetics for each elementary reaction to form butadiene from mixtures of ethanol and acetaldehyde has not been considered from first principles. Here, we construct a microkinetic model for butadiene synthesis in Zr-Beta which

allows for determination of reaction kinetics at differential conditions and determination of the concentrations of surface intermediates at reaction conditions.

For incorporated $4^+$ heteroatoms in zeolites, metals have been proposed to exhibit at least two speciations, one tetrahedrally coordinated to the zeolite framework with four Si-O bonds (a closed site), or another where one bond is replaced with a hydroxyl ligand that results in three Si-O bonds and hydroxyl ligand (an open site)[196]. The structure of open sites in Beta has been discussed as being formed through dissociative adsorption of water[112], [113], [197], nearby silicon vacancies that form proximal silanol nests to metal sites[107], and recently formed by stacking faults caused by the intergrowth of the 2 enantiomeric polymorphs of Beta[156]. Both closed and open speciations of Sn sites have been studied for ethanol dehydration[198] and fructose etherification[199] where the basic framework oxygen atoms participate in the formation of transition states.

The interplay of open and closed sites has been discussed for elementary reactions in the synthesis of butadiene, where the structure of active metal heteroatoms controls the structure and energetics of transition states. The formation of acid-base pairs at Lewis acid sites in Beta has been implicated as necessary to perform the aldol condensation reactions for Hf, Sn, and Zr metals, where the framework oxygen atom behaves as a base and abstracts a proton from the carbonyl group to stabilize an enolate.[187] Others have proposed an alternative mechanism where direct coupling of acetaldehyde can occur in Zr-Beta without formation of an enolate at defect open sites[200]. Crotonaldehyde formed from the aldol condensation step can then be hydrogenated, which is proposed to occur through the MPV reduction of crotonaldehyde with ethanol to form butanol. For Ti, Sn, Zr, and Hf-Betas, alkoxide groups are formed at hydrolyzed metal centers which undergo an intermolecular hydride shift to the carbonyl[103]. The framework oxygen of the hydrolyze open site can they perform the second hydrogenation forming the product alcohol. Alkoxides of ethanol have been shown to form readily at Lewis acid sites in Beta[113], [198]. The dehydration of alcohols has been studied for unimolecular and bimolecular pathways with ethanol in Sn-Beta[198]; however the mechanism by which crotyl alcohol undergoes dehydration at Lewis acid sites in Beta has not been considered. Unselective pathways in addition to those discussed are also plausible, for example dehydration of ethanol. The coupling of higher carbon number products has also been reported; however, the confining pore environment of Beta provides practical limits to the accessible volume to form products.

This work provides the first comprehensive microkinetic model of butadiene synthesis in Zr-Beta from a mixture of ethanol and acetaldehyde. This model includes the possibility of closed and open Zr sites participating in the reaction network, both hydrolyzed open and defect open at stacking fault sites. The primary unselective pathways, dehydrations to form ethylene and diethyl ether are also considered. A tiered microkinetic modeling approach is used to traverse the reaction network, where Campbell's degree of rate control is used to determine kinetically relevant transition states and reactive intermediates, which can be iteratively improved with successively more accurate entropy approximations. Ab-initio molecular dynamics (AIMD) is performed on these kinetically relevant intermediates to more accurately predict rate and equilibrium constants used in the microkinetic model. We find the stability of the enolate in aldol condensation to be rate limiting at differential conversion, where Zr active sites are covered in a diverse collection of ethanol and acetaldehyde dimeric species. Hydrolyzed open sites are determined to be necessary for the aldol condensation and MPV reduction reactions, and the basic lattice oxygen of closed Zr sites is necessary to dehydrate crotyl alcohol to 1,3-butadiene. Defect open sites are not active for crotyl alcohol dehydration and have higher potential energy barriers for aldol condensation than hydrolyzed open sites referenced to the same surface intermediate. The stability of hydrolyzed open sites, and consequently enolates and hydrolyzed ethanol is found to control the kinetics of butadiene synthesis, which is related to the ability of the zeolite framework to stabilize the resulting restructured metal center. From this, we have a criterion (stability of hydrolyzed sites) in choosing other zeolite frameworks with the goal of improved butadiene synthesis rate and selectivity.

## 5.2 Methods

### 5.2.1 Density functional theory methods

All density functional theory (DFT) simulations were performed using the Vienna Ab-initio Simulation Package (VASP) [81]–[84], [87], with similar parameters as we have used of previous reports in Sn-Beta[156], [198]. The Bayesian error estimation functional (BEEF-vdW) was employed with includes self-consistent dispersion interactions. The projector augmented wave (PAW) pseudopotentials were included. Beta unit cells obtained from IZA were relaxed before substituting Sn heteroatoms to simulate the strain exerted by a low heteroatom density. Optimized lattice constants included optimized cell volumes within 1.9% of the IZA values. Defected Sn-

Beta lattices formed through stacking faults were constructed as we have previously reported[156], where our structure file is available for download. This model was made by tiling individual Beta structural building units (sbus) to reproduce a fault where the A and B Beta polymorphs would meet in a representative crystal. All calculations were performed spin polarized in order to treat transition states where bond formation and bond breakage can change electronic orbitals. The plane wave cutoff was fixed to 520 eV for all calculations and Gaussian smearing of the Fermi surface was performed.

Transition states were obtained using the climbing-image nudged elastic band (CI-NEB) method[134], [135]. The image Dependent Pair Potential pre-optimizer was used to help generate initial reaction coordinates where rotation prevents direct interpolation of images[136]. The Lanczos diagonalization method[137] was used once a partially converged NEB was obtained which shows a clear transition state. Vibrational frequency calculations using the partial Hessian approach for adsorbates was used to correct for zero-point vibrational energy. For all calculation the zeolite framework was fixed in their equilibrium lattice positions. We have previously shown for Sn-Beta that even at near bulk liquid loadings the gamma point framework vibrational frequencies did not shift significantly (CHAPTER 7).

To help identify the lowest energy configurations for adsorbates, short duration *ab-initio* molecular dynamic (AIMD) simulations (order of 1-2ps) were performed in the NVT ensemble at 500K, which were then quenched to their ground state. This method has been reported previously as a useful technique to identify adsorbate configurations in microporous materials where the relatively flat potential energy surface is difficult to span exhaustively through chemical intuition.

### 5.2.2   Calculation of rate constants and free energy

While potential energies are directly evaluated through VASP, an accurate determination of entropy for free energies and from them, rate constants. Many reports in the literature, which include our own contributions, have described how the harmonic oscillator approximation to entropy is insufficient to estimate the entropy of adsorbates in microporous environments. This has been described as related to the flat potential energy surfaces which correspond to partial diffusion and rotation degrees of freedom which are not well reproduced in the harmonic oscillator limit. Methods to explicitly model the energy surface beyond the harmonic oscillator approach often involve higher order techniques such as AIMD or other methods of potential energy sampling

(PES). These higher order methods are unfeasible for every reactive intermediate, especially as reaction networks become more expansive as the field naturally evolves. To address the complexity of managing appropriate entropy estimation schemes for reaction networks, we employ the Campbell Generalized Degree of Rate Control (GDRC)[132] as a criterion for identifying reactive intermediates and transition states which are rate sensitive, and which are quasi-equilibrated. This technique has been used previously to study metal/support bifunctional effects for water gas shift, and for ethanol dehydration in Sn-Beta. This tiered approach is designed to use the highest-level methods for intermediates and transition states which change coverages and turnover rates. The reaction network is modeled where low-frequency harmonic modes are inspected and decomposed into their associated rotational and translational degrees of freedom, both free and hindered. Transition state entropies (entropies of activation) are also decomposed by their low frequency modes, neglecting the fundamental mode of the reaction coordinate.

This initial model can be fed into the microkinetic modeling framework to evaluate the GDRC of all intermediates and elementary steps, and these intermediates can then be approximated at higher levels of computation, either higher order functionals such as meta-gga or hybrid functionals, as well as the more demanding AIMD or potential energy sampling to improve entropy calculations. Specific to this work, we use a similar method to refine the entropy of adsorbates. To evaluate translational degrees of freedom, the principle root-mean-square fluctuations from the center of mass obtained from AIMD was used as described previously[128]. Rate constants for all processes were calculated using transition theory, where the pre-exponential factors included the entropy of activation for the elementary step. Adsorption and desorption rate constants were calculated form collision theory, used previously in microkinetic modeling[35], with a sticking coefficient of 1.

### 5.2.3 Microkinetic modeling of reaction rate constants

From the derived rate constants of elementary steps, a CSTR reactor model was used, which would be equivalent to a flow reactor operating under differential conditions. The CSTR equation is numerically convenient, as it allows for integration to steady state rates at a fixed residence time. Thus, initial concentrations of gas phase reactants could be fed and diluted, while the residence time could be modulated to ensure differential conversion of products. We have used the same code published previously to build the reactor equations using SymPy (symbolic python),

allowing for the automatic generation of mass balances from plain text and VASP input files. A linear solver was further used due to the slow conversion of some elementary steps from the reactor model, which used the steady state rates as initial conditions to further refine forward and reverse reaction rates. All rates are reported as initial turnover numbers ($s^{-1}$), normalized per catalyst active site (incorporated Sn atoms). Product conversions are maintained below 1% to better represent differential experimental kinetics.

The generalized degree of rate control was calculated using the same microkinetic modeling package previously discussed. This package can individually modify each rate and equilibrium constant to evaluate the degree of rate control with the same reactor equations. Reaction orders were evaluated similarly using implemented parallelization of the microkinetic package. Correlated two point errors of binding energies were evaluated in the same package.

## 5.3    Results and discussion

### 5.3.1    Atomistic models of Zr-Beta

A single Zr atom per unit cell was replaced with Si at the T8 site of Beta, based on previous reports made on Sn-Beta. Adsorption of dissociated intermediates have been shown to be linearly related among the same T atom[113], and dissociation of oxygen molecules was not found to vary significantly among the T-sites of Beta. The T8 site also sits at an intersection in the Beta framework, where all nearest neighbor framework oxygen atoms exposed to the 12-member ring channel structure. This T8 was hypothesized to be especially accessible to larger reactive intermediates due to the presence of an intersecting space and would provide a representative example of any Tsite in the Beta framework. As has been reported previously,[113], [197]–[199] we will consider how oxygenate molecules can adsorb and dissociate forming so-called "hydrolyzed-open" sites. As shown in CHAPTER 2 and CHAPTER 3, water (W) and ethanol (E) can form hydroxy-open ($W_x$) and ethoxy-open ($E_x$) sites similar to Sn-Beta[198], and various $4^+$ metals in the CHA framework including Zr[113].

Hydrolyzed open sites are not the only possible type of open site configuration, as defects formed through Beta crystallization can produce stacking faults where enantiomerically distinct polymorphs intergrow[201]. While these "defect open" sites are not the active site for ethanol dehydration in Sn-Beta[156], we have considered their role in butadiene synthesis. Hydroxyl

ligands do not have to be formed through dissociative adsorption like hydrolyzed open sites and are present at defect open sites by their undercoordinated Si-O bonds at the stacking fault. The model we have reported previously, has been reduced in size to permit calculation of larger and more complex intermediates, due to its exceptionally large size (~4 Beta unit cells). The binding energy of key intermediates was not found to differ significantly from this reduced stacking fault model as compared to the full stacking fault model we have previously reported (APPENDIX D).

### 5.3.2 Mechanisms for butadiene formation

A schematic of the proposed generalized mechanism for butadiene synthesis shown in Figure 5.1, which includes sequential aldol condensation to form crotonaldehyde, MPV reduction of crotonaldehyde to crotyl alcohol with ethanol as a hydrogen donor, and dehydration of crotyl alcohol to form 1,3-butadiene. On Zr-Beta, the possibility of speciated open and closed sites introduces additional complexity into which determination of active site ensembles is complicated. The presence of water in product formation as well the feed from upstream processing can form inhibitory water dimer and trimer intermediates, as well as shuttle hydrogen and reduce strain on transition states. Ethanol can proceed through unimolecular and bimolecular dehydration mechanisms to form ethylene and diethyl ether (DEE) as we have reported in Sn-Beta. Defect open configurations of Lewis acid heteroatoms, formed at grain boundaries, represent another unique subset of potential active site. Larger ($C_4+$) products can also be formed through higher aldol condensation reactions. The formation of all such intermediates were considered; however, it is always possible additional pathways may occur which we have not included. As will be shown, the predominant surface coverages at differential conditions are of ethanol and acetaldehyde containing intermediates, and at differential conditions the formation of higher products is unlikely by virtue of the low product yields considered. When relevant, alternate mechanism which have been considered will be outlined alongside the lowest free energy paths.
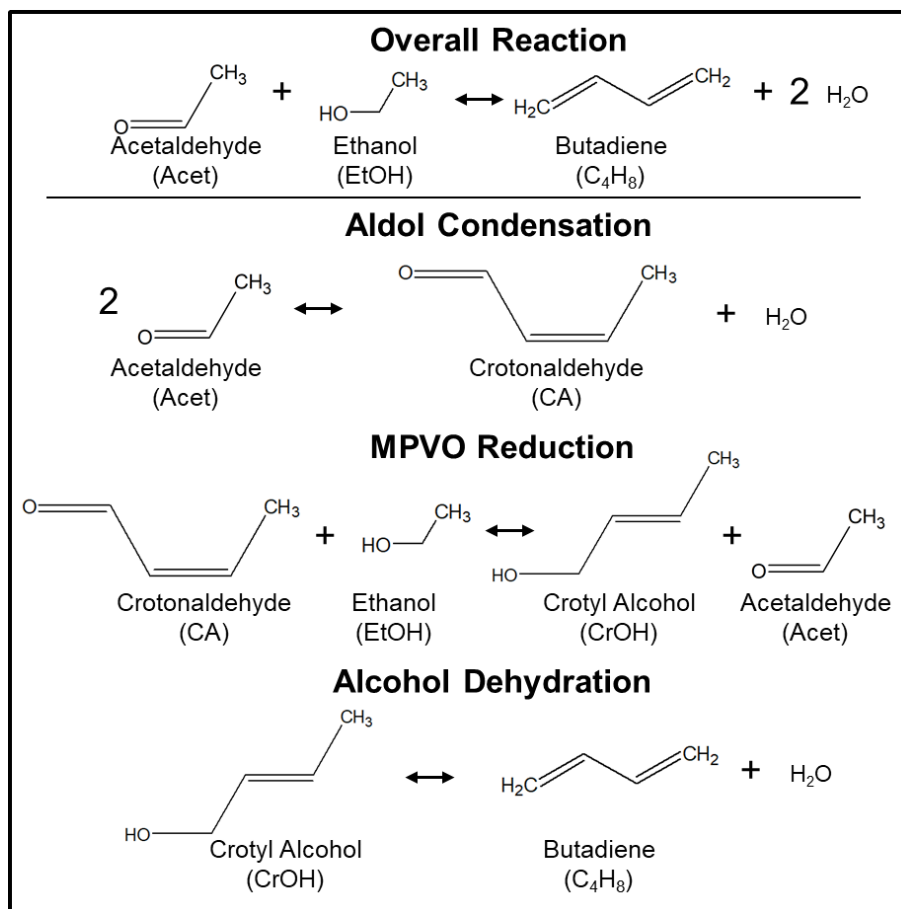
Figure 5.1 Schematic of Butadiene synthesis from the aldol condensation, MPVO reduction, and alcohol dehydration elementary reactions.

### 5.3.3 Aldol condensation in Zr-Beta

Many mechanisms for aldol condensation in zeolites have been previously reported in the literature, which differ in how the initial C-C coupling is performed, which then requires dehydration of the hydroxy-aldehyde to form the desired unsaturated aldehyde. For this reaction we seek to specifically couple acetaldehyde to form 3-hydroxybutanal which will dehydrate to form crotonaldehyde. The classical mechanism for aldol condensation on oxides involves formation of an enolate which can then then attack the electron-poor alpha carbon on a second acetaldehyde, where in conjunction with a hydrogen shift, produces 3-hydoxybutanal. Previous reports in Lewis acid Beta have shown computationally that the direct formation of an enol is unfavorable for open sites in Zr-Beta[200]. We have also found that formation of the enol form of acetaldehyde is unfavorable, and Figure 5.2 shows a stepwise mechanism in which a hydroxy open

site can ligand exchange its hydroxy group with an enolate where charge balance on the zeolite framework is maintained through the weakly Bronsted acidic proton imparted by the dissociative adsorption of water. The free energy barrier, referenced to an acetaldehyde covered surface at 500K, which will be shown later through microkinetic modeling is the most abundant surface intermediate at these conditions, is 1.25 eV (TS2). This is lower than alternative mechanisms involving direct C-C coupling by protonation from the weakly Bronsted acidic framework proton, and enolate formation on closed Zr sites. One alternate mechanism with a competitive free energy barrier referenced to the MASI is shown in TS1a in which an enolate is formed by assistance of a coadsorbed water molecule to a nearby framework oxygen atom. This differs from TS2, in which the site is first opened with water to the closest (*syn-*) oxygen, followed by water assisted transfer to the most stable (*anti-*) oxygen, where the hydroxyl ligand is exchanged by donation of the B-CH to form water and an enolate. In TS1a the B-CH is transferred to a water molecule, and then a *syn* oxygen is protonated. This mechanism, while possessing a higher barrier of 1.45 eV at the T8 site, is worth mentioning as interesting for T sites where the *anti* oxygen configuration is energetically unfavorable, due to occlusion of the oxygen by 4 and 5 member ring structural building units which prevent access of water or other hydrogen shuttling molecules to form hydrolyzed open sites with an *anti* configuration. The enolate formation mechanisms provided here differ from those discussed previously, as the flexibility of the zeolite framework in hydrolyzing sites with barriers comparable to those of other elementary steps was not considered. While these hydrolyzed sites are less stable than adsorbed water, they are formed as reactive intermediates which can stabilize enolate formation.

After formation of an enolate, an additional acetaldehyde molecule can adsorb exergonically to form an acetaldehyde-enolate pair ($AEn_x$*), with direct coordination of acetaldehyde to the metal center. The enolate can now attack the coadsorbed acetaldehyde, at the electron-deficient alpha carbon, shown in TS3 with a free energy of activation relative to an
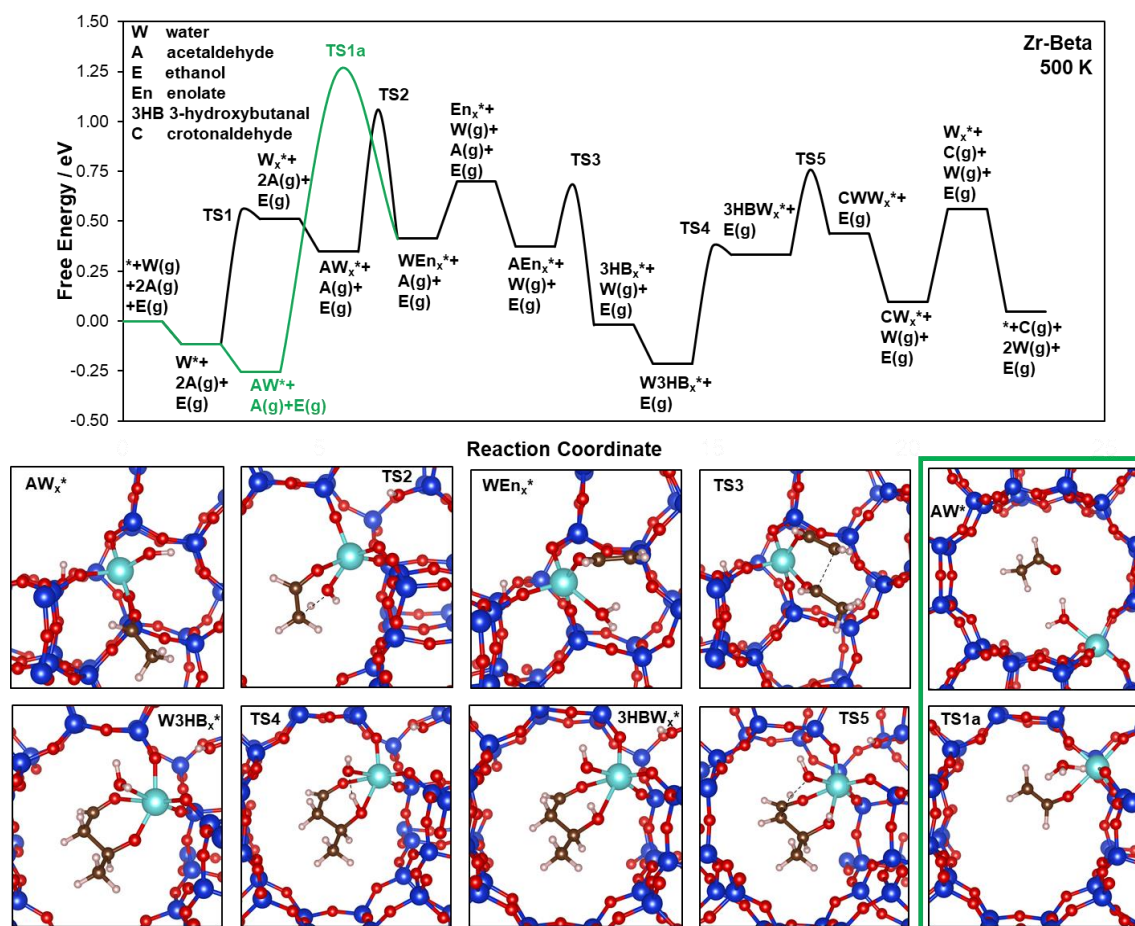
Figure 5.2 Free energy diagram for aldol condensation. Select transition states are reactive intermediates are provided in the subfigures below.

acetaldehyde covered surface of 0.87 eV, significantly lower than that of enolate formation. This would be in line with classical chemical intuition that once a reactive enolate is formed, the coupling with an aldol is facile. The product state is the corresponding alkoxide ($3HB_x$), with a favorable reaction free energy. The 3-hydroxybutanal alkoxide shown in Figure 5.2 binds in a bidentate configuration through is hydroxy and aldehyde groups. This can be ligand exchanged with adsorbed water (TS4) with a reaction free energy barrier of 0.56 eV to form 3-hydroxybutanal and a hydrolyzed open site ($3HBW_x$) This intermediate adsorbs in a similar bidentate configuration as the alkoxide hydroxybutanal, through its hydroxyl and carbonyl groups. As shown in the subpanels of Figure 5.2, there is ample space in the Beta 12-member ring pore to accommodate 3-hydroxybutanal. The formation of such acetaldols has been reported for the same reaction in Ta-Beta[190].

The dehydration mechanism to form crotonaldehyde from an acetaldol has not been discussed in Lewis acid zeolites, and report the barrier to be 0.95 eV formed by transfer of the beta C-H to the hydroxyl ligand of the hydrolyzed open site, forming water. This then results in a barrierless scission of the 3-C-OH bond to release crotonaldehyde, a water formed from the acetaldol, and a hydrolyzed open site formed from the acetaldol hydroxyl group. Both conformers of crotonaldehyde have been considered for elementary steps to ensure, when feasible, the more stable conformer is formed. Dehydration may also occur through an intramolecular dehydration, in which the beta C-H can shift to the hydroxyl group to release water and crotonaldehyde without requiring a hydrolyzed open site, but the prohibitively high barrier of this process makes it unlikely that closed Zr sites can dehydrate the acetaldol (APPENDIX D). Another possible mechanism is to use the acetaldol to hydrolyze the closed Zr site, and in the process release crotonaldehyde. The barrier for this process is also prohibitively high (APPENDIX D). Like the enolate step, formation of hydrolyzed open sites greatly reduces the activation barrier for acetaldol dehydration. The product complex can then desorb to produce water and crotonaldehyde, and the hydrolyzed open site can close with water assistance to recover a closed Zr-Beta site. The overall stoichiometry of the elementary reaction is preserved in which two acetaldehydes form crotonaldehyde and water with a catalytic water molecule involved in the site speciation.

### 5.3.4 MPV reduction of crotonaldehyde to crotyl alcohol

Crotonaldehyde formed from aldol condensation of acetaldehyde is hydrogenated to form crotyl alcohol. Without molecular hydrogen, a hydrogen donor is required, in which case ethanol has been used in Lewis acid zeolites[190], [191], [193] as well as hydroxyapatite[194] to form crotyl alcohol through MPVO reduction. The mechanism for MPVO reduction is like that proposed by Luo et al[103] in which a partially hydrolyzed metal site dissociates an alcohol and assists the intermolecular hydride shift, in which the resulting ketone desorbs, and reassociation of an alcohol through a framework proton forming the product alcohol and a closed metal site.
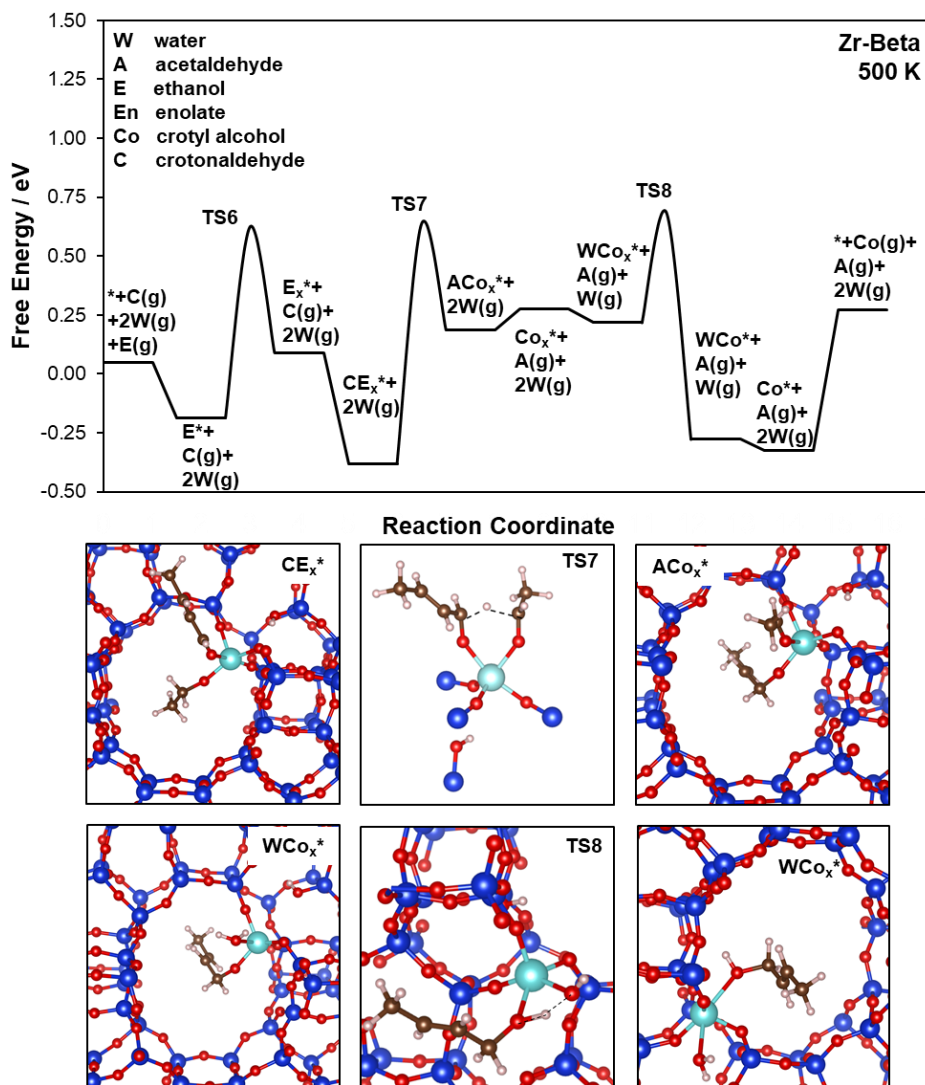
Figure 5.3 Free energy diagram for MPVO reduction of crotonaldehyde. Select transition states are reactive intermediates are provided in the subfigures below.

Ethanol can adsorb exergonically to a Zr-Beta site, where in can dissociate to form an ethoxy open site ($E_x$*) which has been proposed previously to be involved in ethanol dehydration[198]. An ethoxy open site can be also formed through ligand exchange of a hydroxy open site. Crotonaldehyde adsorbs exergonically to the ethoxy open site, with a free energy of adsorption of -0.47 eV. The crotonaldehyde-ethoxy complex ($CE_x$*) is show in Figure 5.3, there the ethoxy and crotonaldehyde can fit when allowed to occupy intersecting pores. The MPVO reduction transition state includes the intermolecular hydride shift with Zr adopting a near-octahedral configuration. Figure 5.3, TS7 has the surrounding zeolite framework cut away to

highlight the hydride shift structure, with the relative position of the framework silanol. The free energy of activation for the MPVO reduction step is 0.82 eV. The final state is a coadsorbed acetaldehyde and crotyl alkoxide with an endergonic reaction energy. Acetaldehyde can then desorb, and crotyl alcohol can be formed through re-association with the framework proton through water as a hydrogen shuttle. The free energy barrier of alcohol reassociation is 0.87 eV, 0.05 eV different from the hydride shift step. The product crotyl alcohol adsorbs strongly to Zr with a free energy of adsorption of -0.33 eV. Crotyl alcohol can now desorb or further dehydrate to form the desired product, 1,3-butadiene.

### 5.3.5  Crotyl alcohol dehydration

Crotyl alcohol must dehydrate from a hydrogen on the terminal carbon, which produces the unsaturated diene. This dehydration is complicated by the double bond in crotyl alcohol which restricts the alcohol from adopting a conformation where direct intramolecular dehydration is possible. The isolated Zr sites in Beta present to obvious avenue to a dual site dehydration where tandem sites could dehydrate crotyl alcohol. Bronsted acid sites such as H-Beta with incorporated aluminum sites may readily dehydrate crotyl alcohol. With assistance of a water molecule, which would be ubiquitous under reaction conditions, Zr-Beta sites can dehydrate crotyl alcohol to 1,3-butadiene.

Crotyl alcohol formed from MPVO reduction, can form a coadsorbed complex with water, which as shown in Figure 5.4 WCo* adopts an octahedral configuration with crotyl alcohol required to span along the length of the pore. Dehydration occurs through a mechanism analogous to that we have proposed previously in Sn-Beta for bimolecular ethanol dehydration, which involves hydrogen transfer to a *syn* oxygen and scission of the alpha C-O bond. Forming a hydrolyzed site. As shown in Figure 5.4 TS9, the transition state complex allows for protonation from the terminal carbon to the catalytic water shuttle, onto the framework oxygen. Simultaneously, the alpha C-H bond breaks, releasing *trans* 1,3-butadiene. The free energy barrier relative to an acetaldehyde MASI is 1.30 eV (compare with the barrier for enolate formation, referenced to the same surface of 1.25 eV). The product state includes water hydrogen bonded to the framework proton of the hydrolyzed open site, with butadiene weakly physisorbed within the pore. To complete a catalytic cycle, water can butadiene can desorb, and the hydroxyl open site can re-
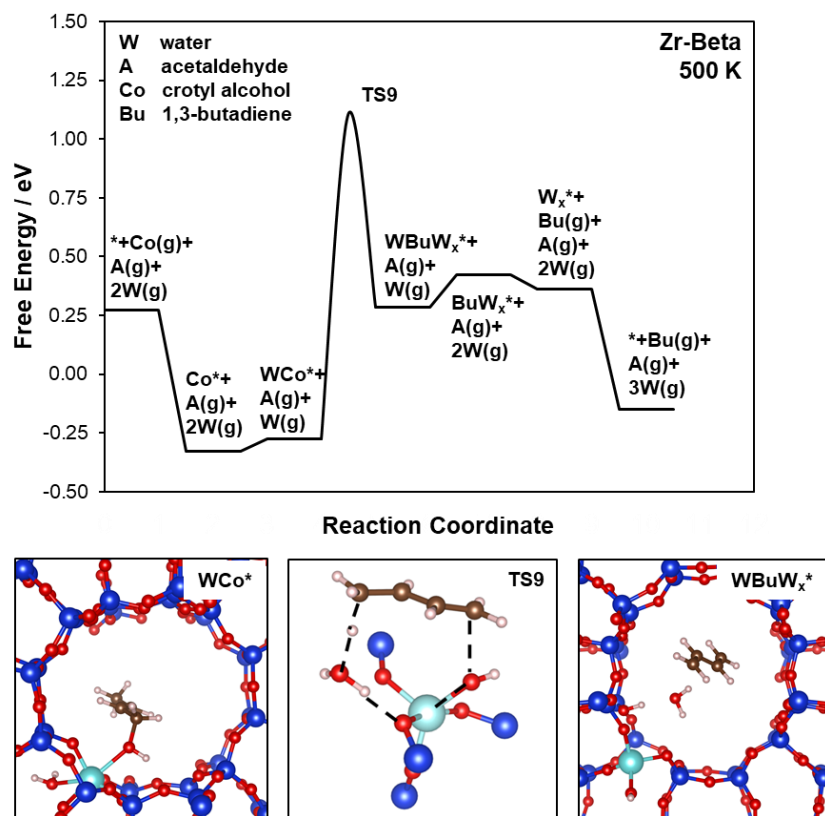
Figure 5.4 Free energy diagram for dehydration of crotyl alcohol. Select transition states are reactive intermediates are provided in the subfigures below.

associate forming water which can desorb producing an overall reaction stoichiometry of crotyl alcohol forming *trans* 1,3-butadiene and water and recovering the closed Zr site. An alternative mechanism can be considered, analogous to the H-Beta case, in which the framework silanol of a hydrolyzed open site can protonate the hydroxyl group of crotyl alcohol and the terminal C-H can be accepted by the Zr-OH ligand forming water and closing the site. This mechanism has a higher intrinsic barrier than dehydration on a closed site with water assistance (APPENDIX D) This is similar to our findings in Sn-Beta for bimolecular ethanol dehydration[198], where the weakly basic framework oxygen can accept a proton which is more favorable than dehydration on a hydrolyzed site, despite the enthalpic gain of site closure.

### 5.3.6 Ethanol dehydration side reactions

As ethanol is required for the MPVO reduction of crotonaldehyde, and ethanol will likely be present from an upstream dehydrogenation process to produce acetaldehyde (such as a copper

or silver catalyst) it is likely that the bimolecular dehydration of ethanol to form diethyl ether (DEE) is an important unselective pathway to consider. The strongly exergonic adsorption of ethanol observed on Sn-Beta makes it likely that under reaction conditions, both acetaldehyde and ethanol compete for active sites.

Ethanol dimers may go through a bimolecular dehydration pathway to produce DEE. The most favorable mechanism on closed Zr sites, analogous to that considered on Sn-Beta[198]. An ethanol dimer can initiate an $S_N2$ nucleophilic attack leaving behind a hydroxyl ligand on the Zr, with transfer of a proton to a nearby *syn* oxygen forming DEE and a hydroxyl open site. This hydroxyl open site can then close and desorb water completing a catalytic cycle. Ethanol dimers adsorb exergonically with an adsorption free energy of -0.30 e. The reaction free energy barrier for the $S_N2$ mechanism has a reaction free energy barrier refenced to an ethanol covered surface of 1.8 eV, which is higher than the enolate formation step and MPV reduction. Although this would at first glance indicate that DEE formation is less favorable, the ratio of aldol condensation and bimolecular dehydration rates depends on the coverages of surface intermediates at reaction conditions, where the exergonic binding energy of ethanol dimers may compete with acetaldehyde adsorption resulting in an ethanol covered surface. Microkinetic modeling will be used to address the coverages of reactive intermediates, which accounts for the relative concentrations of surface-bound intermediates.

### 5.3.7   Butadiene synthesis at Beta stacking faults

All mechanisms considered thus far are at internal tetrahedrally coordinated Zr atoms incorporated into Beta T sites. Due to the existence of two chiral structural polymorphs in Beta, their intergrowth can cause stacking faults which prevent the formation of fully framework-incorporated T sites[201]. Lewis acid heteroatoms incorporated into these stacking fault sites are undercoordinated and have hydroxyl terminations which cannot associate with a framework silanol to close, as is the case of hydrolyzed open sites[156]. Defect open sites were not found to be the active site for ethanol dehydration in Sn-Beta, as the framework oxygens could not accept a hydrogen without breaking an additional framework oxygen bond forming a double hydroxyl coordinated Zr. As such, defect open sites were not considered form crotyl alcohol dehydration, as there would be nothing to accept the terminal C-H. Furthermore, the size of crotonaldehyde does not permit direct dehydrogenation at the Zr center by itself. The MPVO reduction requires

two hydrogenations of crotonaldehyde, and the absence of a framework silanol to rehydrate the crotyl alkoxide would require additional ligand exchanges to release crotyl alcohol, since dehydration to butadiene cannot occur at grain boundary sites. Furthermore, from microkinetic modeling, MPVO reduction is not rate determining to form butadiene, and so MPVO at grain boundary sites will not be considered in this work.
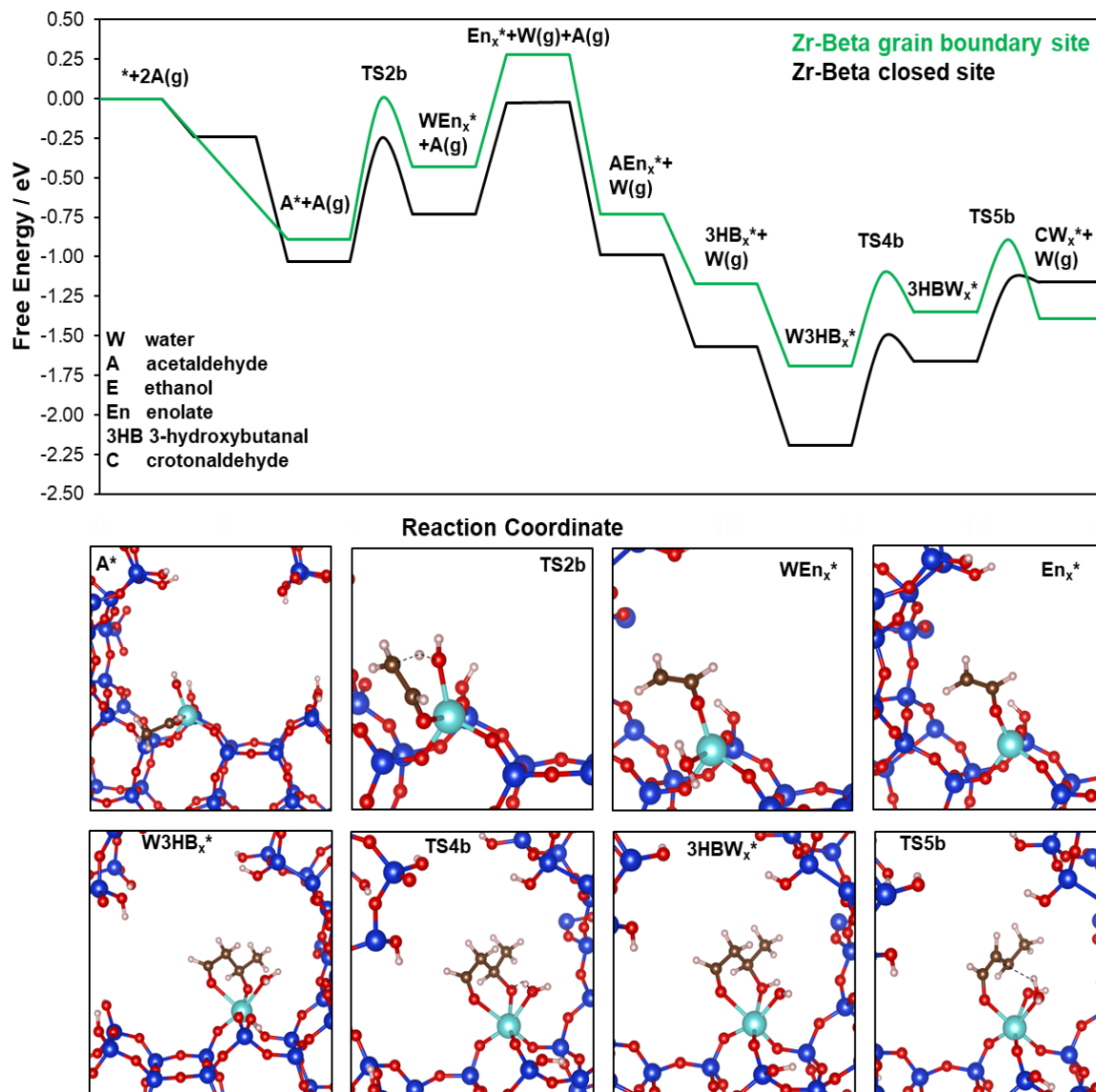


Figure 5.5 Potential energy diagram for aldol condensation at internal closed Beta Zr sites, and defect open Zr sites formed through grain boundary growth.

Aldol condensation at grain boundary sites is plausible, as direct interaction with the framework proton is not necessary to produce crotonaldehyde. Figure 5.5 compares aldol

condensation at hydrolyzed open Zr sites and defect open Zr sites at grain boundaries. Presented here is a potential energy analysis at these two sites, as consideration of entropy changes for the large number of complex intermediates is difficult due to the size of the grain boundary model. Acetaldehyde can first adsorb to the Zr center, and undergo the same ligand exchange, transferring a beta C-H to the hydroxyl ligand, forming an enolate and three framework Zr-O bonds (TS2b). The intrinsic barrier to form an enolate relative to an acetaldehyde covered surface at a defect open site is 1.17 eV as compared to an internal beta site which is 1.01 eV. These potential energy barriers are quite close; however, it is likely that entropy would further distinguish them, as the transition state entropy for both transition states is likely similar, as both include similarly chemisorbed ligands. The entropy of the initial states, which would be an acetaldehyde covered surface, would be different at the two sites, as the defected double pore volume could increase the number of microstates available to an adsorbed acetaldehyde, resulting in a larger entropy than an internal non-defect Zr site. Therefore the $\Delta\Delta S^{/}$ of internal versus grain boundary sites would be negative, indicating the difference between the defect open site free energy barrier and internal free energy barrier is larger than predicted from the potential energy diagram.

The defected double pore structure reduces the number of van der Waals contacts made between adsorbates and reactive intermediates, which is more strongly felt by small adsorbates, such as acetaldehyde. This, in part, is one factor leading to the overall weaker adsorption of smaller reactive intermediates at defect open sites. The geometry of the defect open site, where Zr is in a different configuration than internal Zr, could also contribute to the difference in transition state energies, as the Zr orbitals overlap differently due to bond lengths and angles to the surrounding framework oxygen atoms. The difference in acetaldol formation (TS4, TS4b) is more favorable for the defect open site, with intrinsic barriers of 0.68 eV and 0.59 eV, respectively. The barrier for acetaldol dehydration via ligand exchange (TS5, TS5b) is similar for both sites, 0.51 eV and 0.46 eV, respectively. Due to the greater stability of the enolate on internal Zr sites, we will consider internal sites in the microkinetic models; however, we cannot rule out completely that defect open sites at grain boundaries may contribute to the observed aldol condensation rate.

### 5.3.8 Butadiene synthesis kinetics

The mechanistic pathways presented previously were used to construct a microkinetic model for butadiene synthesis which includes the unselective pathways to form DEE. Additional

adsorption/desorption steps including dimers of ethanol, acetaldehyde, water, and crotonaldehyde were added based on previous experience modeling ethanol dehydration where at high partial pressures of ethanol or water, dimeric species became most abundant. A full list of elementary steps considered is provided in APPENDIX D.

A range of ethanol and acetaldehyde partial pressures were scanned, with a constant background feed of 5 kPa water. The reactor pressure was fixed at 1bar, with an inert gas stream. The reactor residence time and number of Zr active sites was set to ensure a conversion <1% of ethanol and acetaldehyde. The overall rate is defined as the net butadiene desorption rate. Figure 5.6 shows the butadiene desorption rate as related to partial pressures of ethanol and acetaldehyde in the feed. Initial rates are low ($10^{-7}$-$10^{-9}$ $s^{-1}$) which reflects the sequential nature of the catalytic cycle, in which desorption of crotonaldehyde and crotyl alcohol are likely. To better quantify the observed rate dependence on reactant mixtures, the surface coverages and reaction orders with respect to acetaldehyde are presented at two representative conditions, one within the high rate region (5.5 kPa EtOH) and one within a lower rate region with a higher ethanol partial pressure (23.4 kPa EtOH). At the lower ethanol pressure (Figure 5.6b) Zr active sites are dominated by a limited number of intermediates. At all conditions, the concentration of empty Zr sites is low (<1%) reflecting the exergonic adsorption energies of acetaldehyde and ethanol. At acetaldehyde lean conditions, <5 kPa acetaldehyde, the surface is dominated by ethanol and ethanol-ethanol dimers, and as the acetaldehyde partial pressure increases to acetaldehyde rich conditions, the coverages of ethanol and ethanol-ethanol dimers begins to decrease. Acetaldehyde -acetaldehyde dimers do not exhibit hydrogen bonding, and while their coverage is non-negligible, even at high pressures of acetaldehyde their coverage is lower that acetaldehyde monomers. Acetaldehyde can form dimers with water, which has a coverage on the order of 10-20%.

The order plot in Figure 5.6d at 5.5 kPa EtOH, has a positive, sub-unity order (~0.88) with respect to acetaldehyde, where ethanol coverages are high, and the adsorption of acetaldehyde to form crotonaldehyde is rate limiting. Rates react a maximum where the surface has a near-stoichiometric coverage of ethanol and acetaldehyde. Due to the difference in acetaldehyde and
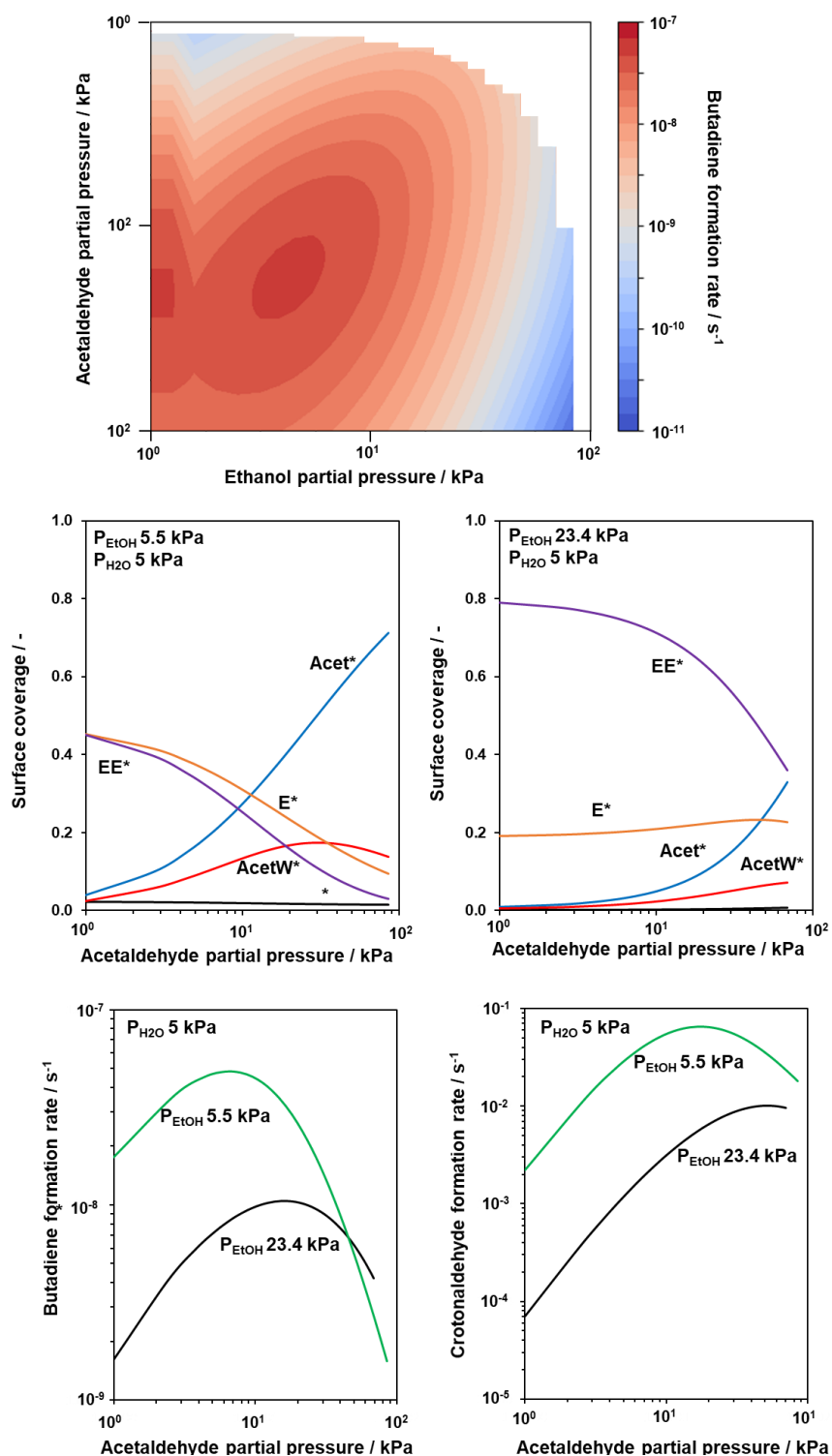
Figure 5.6 Kinetics of the butadiene synthesis reaction. (a) net butadiene desorption rate at 1 bar fixed total pressure. (b) surface coverages at $P_{EtOH}$ 5.5 kPa and (c) surface coverages at $P_{EtOH}$ of 23.4 kPa.(d) net butadiene formation rate. (d) net crotonaldehyde formation rate.

ethanol adsorption constants, the conditions at which a near-stoichiometric surface coverage is achieved is skewed relative to the incoming feed conditions. The predicted feed ratio where acetaldehyde and ethanol monomers are equal coverage is 2:1 acetaldehyde and ethanol. This is expected from the ratio of equilibrium constants for adsorption of ethanol and acetaldehyde (73.84 and 152.78, respectively) as defined from their free energy of adsorption, which reflect the ratio of expected coverages. This same ratio is reflected at the higher ethanol pressure (Figure 5.6c) where at acetaldehyde lean conditions the coverage of ethanol-ethanol dimers is dominant on the surface, due to the hydrogen bonding interaction that favors dimer formation. A similar sub-unity order (~0.74) is observed for butadiene formation at acetaldehyde lean conditions. At acetaldehyde rich conditions and low (5.5 kPa) ethanol pressures, the acetaldehyde order approaches -2, reflecting inhibition. At high (23.4 kPa) ethanol pressures, the acetaldehyde order is -1, indicating a mechanistic difference in the inhibition process.

Initial rates for aldol condensation, measured as the crotonaldehyde desorption rate, are 3-5 orders of magnitude higher than butadiene synthesis rates, far above ethanol dehydration rates, which are 3-6 orders of magnitude lower than aldol condensation. Reaction orders in acetaldehyde lean conditions are greater than unity, 1.6 for 5.5 kPa ethanol and 1.75 for 23.4 kPa ethanol, reflecting the requirement of two acetaldehyde molecules to couple to form crotonaldehyde, which is sub second order due to the higher coverages of ethanol monomers and dimers. At acetaldehyde rich conditions, acetaldehyde orders become negative, which for 5.5 kPa ethanol has a -1.37 order.

A degree of rate control analysis allows a more careful examination of what elementary steps are rate determining, which in conjunction with a thermodynamic degree of rate control shows also what reactive intermediates are rate determining. A fixed ethanol partial pressure of 3.16 kPa was chosen, with three acetaldehyde partial pressures were chosen in different kinetic regimes, acetaldehyde lean (1.78 kPa acetaldehyde), near-stoichiometric surface composition (5.62 kPa acetaldehyde) and acetaldehyde rich (56.23 kPa acetaldehyde). DRCs were calculated for each elementary step and summarized in Table 4.1. A constant 5 kPa background of water was included for each condition. At all conditions, the rate determining step with the highest degree of rate control is crotyl alcohol dehydration to form butadiene. This is hardly surprising as the low concentration of crotyl alcohol in the sequential mechanism, as well as high free energy activation barrier contribute to the observed high degree of rate control. Following this, is the coadsorption step to for an acetaldehyde-enolate complex to then couple and form 3-hydroxyl butanal. The

instability of the enolate site contributes to the low concentration of enolates at steady state conditions. The DRC for this step decreases as partial pressure of acetaldehyde increases. Enolate complexation with water has a non-negligible degree of rate control which becomes more rate limiting as the partial pressure of acetaldehyde increases, indicating the low stability of enolate sites at the surface. The coadsorption of ethoxy open sites and crotonoaldehyde are rate limiting at all acetaldehyde partial pressures, due again to the low population of ethoxy open sites at steady state, which is necessary for the MPVO reduction step to occur.

Table 5.1 Degree of rate control for butadiene synthesis

|  | 1.78 kPa A(g) | 5.62 kPa A(g) | 56.2 kPa A(g) |
|---|---|---|---|
| $WCo^*<->WBuW_x^*$ (TS9) | 0.96 | 0.96 | 0.96 |
| $En_x^*+A(g)<-> En_xA^*$ | 0.51 | 0.48 | 0.31 |
| $En_x^*+W(g)<->WEn_x^*$ | 0.32 | 0.43 | 0.63 |
| $E_x^*+C(g)<->CE_x^*$ | 0.27 | 0.28 | 0.20 |
| $AW_x^*<->WEn_{x^*}$ (TS2) | 0.06 | 0.12 | 0.20 |
| $WCo_x^*<->WCo^*$ (TS8) | 0.04 | 0.05 | 0.13 |
| $CE_x^*<->ACo_x^*$ (TS7) | 0.03 | 0.02 | 0.01 |

The actual enolate formation step (TS2) has a low degree of rate control (0.06 at 1.78 kPa A(g)) reflecting that it is the stabilization of the enolate which is rate limiting, and not the elementary step for it to form from a hydrolyzed site. The intermolecular hydride shift and hydration of the crotoxide formed from the intermolecular hydride shift have nearly negligible degrees of rate control, indicating that the MPV step is not rate limiting at these conditions, but rather the stability of the ethoxy open site. We can also consider the kinetic relevance of individual reactive intermediates (Table 4.2), where the only intermediates with thermodynamic degrees of rate control greater than 1% are enolates, ethoxy open sites, and crotyl open sites.

Table 5.2 Thermodynamic degree of rate control for butadiene synthesis

|  | 1.78 kPa A(g) | 5.62 kPa A(g) | 56.2 kPa A(g) |
|---|---|---|---|
| $En_x^*$ | 0.60 | 0.72 | 0.87 |
| $E_x^*$ | 0.43 | 0.51 | 0.47 |
| $Co_x^*$ | 0.05 | 0.02 | 0.05 |

The kinetically relevant intermediates are again inferred to be the hydrolyzed active structures, with the enolate possessing the highest thermodynamic degree of rate control. As acetaldehyde partial pressure increases, the kinetic importance of enolate stability becomes more important, as reflected by its low coverage at reaction conditions. Ethoxy open sites have a similar thermodynamic rate control at all conditions studied, which is insensitive to the acetaldehyde gas pressure. Crotyl open sites have a thermodynamic degree of rate control of less that 10%. Therefore, both DRC and TDRC implicate that the stability of hydrolyzed sites, whether they are enolates, ethoxy open sites, or crotyl open sites control the kinetics of butadiene synthesis, in addition to the final dehydration of crotyl alcohol to butadiene. Thus, it is advantageous to think of strategies to stabilize hydrolyzed sites, either by metal heteroatom identity or by local framework structure to find zeolites where the shape of Si-O bonds are conducive to stabilize hydrolyzed configurations.

## 5.4 Conclusions

A fundamental mechanistic study of butadiene synthesis from a mixture of ethanol and acetaldehyde was performed using density functional theory to aide in identifying what material properties of microporous materials can promote faster kinetics and higher selectivity to chemical products. It was shown that Lewis acid sites in Zr-Beta catalyze the elementary reactions to synthesize butadiene, including aldol condensation, MPV reduction, and dehydration. Zr-Beta is a poor ethanol dehydration catalyst, suppressing the rate of bimolecular dehydration. Hydrolyzed open sites can form enolates with apparent activation barriers lower than bimolecular dehydration through a hydride shift mechanism to the hydroxyl ligand, forming an enolate open site and water. This enolate is less stable than adsorbed acetaldehyde but can readily react with a second acetaldehyde forming the alkoxide of 3-hydroxybutanal. Dehydration of the alkoxide proceeds with a lower apparent activation barrier than enolate formation, releasing crotonaldehyde, water,

and a hydrolyzed open site. MPV reduction of crotonaldehyde to crotyl alcohol is catalyzed by Zr sites hydrolyzed open by ethanol forming ethoxy open sites. The MPV reduction apparent activation barrier is lower than enolate formation, producing crotyl alcohol. Crotyl alcohol dehydration can occur at Lewis acid sites where a framework oxygen atom can accept a terminal hydrogen from crotyl alcohol to form butadiene, water, and a hydrolyzed open site.

The rate determining step for butadiene synthesis is the enolate formation in aldol condensation, where the ability of the zeolite framework and metal heteroatom to stabilize the enolate controls the rate of butadiene formation. Despite crotonaldehyde and crotyl alcohol adsorbing exergonically to Zr sites, selectivity to butadiene at differential conversion is low, not due to slow kinetics of the elementary reactions, but due to the sequential process to form butadiene. At high conversion, where the concentrations crotonaldehyde and crotyl alcohol are high, the rate of MPV reduction and dehydration is similar to that of aldol condensation. This indicates the role of the microporous environment in promoting longer intracrystalline residence times to convert reactants into longer timescale models. In the limit where sequential reaction along the crystallite is important, a non-Langmuirian process must be used to understand kinetics at high conversion. At low conversion, microkinetic provides insight into the fundamental kinetic processes of each elementary reaction. Open sites, with their Brønsted acid framework protons and hydroxyl ligands, are necessary for dehydration, as well as the elementary reactions of butadiene synthesis. While the equilibrium coverage of hydrolyzed sites under reaction conditions are low, they can activate gas molecules to catalyze subsequent catalytic steps, such as enolate formation or MPV reduction. The flexibility of the silica matrix that forms the zeolite allows gas molecules to functionalize active sites in microporous materials. As the formation of open sites deforms the zeolite framework, it is possible that the local silica structure around the heteroatom active site plays a role in transition states that involve hydrolyzed sites, as the local silica structure controls the distortion of heteroatom tetrahedra and determine the relative stability of hydrolyzed intermediates. Stabilization of these sites by choice of zeolite framework would reduce the barrier for enolate formation, as well as reduce the enthalpic penalty to form an ethoxy site for MPV reduction, reducing the barrier of reaction relative to desorption of crotonaldehyde.

# 6. LOCAL STRAIN EFFECTS IN LEWIS ACID FUNCTIONALIZED ZEOLITES

## 6.1 Introduction

The structural diversity of zeolites is well-known, with a multitude of pore and channel geometries that influence the size separation of the materials, as well as catalysis that occurs in their pores through stabilization of transition states and reactive intermediates. Throughout this dissertation we have considered silica-based zeolites which have individual Si atoms replaced by $4^+$ metals that introduce Lewis acidity to the framework to catalyze chemical reactions. To form the porous structure of the zeolite framework, as opposed to bulk amorphous silicas, individual silica rings must combine such that repeating pores are formed, which are metastable relative to bulk amorphous silica. The set of silica rings that comprise a zeolite are referred to either secondary building units (SBUs) or composite building units (CBUs) which form a discrete number of silica structures that comprise the zeolite structure[202], [203].These building units can then be tiled together such that all tiles are interior of a generalized polyhedron[204].

Each of these building units are comprised of silica, yet the local structure of each silicon atom is by necessity deformed to accommodate the diverse space of structures. This is possible due to the flexibility of $SiO_2$ rings, which is reflected in the heterogeneity found in silica surfaces where both the silica units and number of hydroxyl groups formed can vary dramatically. Fundamental studies of surface structure are complicated by the conditions of synthesis and characterization. Early surface science experiments in ultra-high vacuum (UHV) were able to determine oxygen-terminated surfaces, although these reflect the difficulty in individually characterizing different surface structures[205], [206]. Theoretical studies have identified key structural motifs for the structure and reactivity of silica surfaces; yet, the issue of heterogeneity in surface terminations remains[207], [208]. Recent work with reactive potential models have been used to simulate realistic heterogenous silica surfaces identifying ensembles of silica structures[209]. Zeolites are unique in that the diversity of silica structures in the building units is a discrete and countable number of structures specific to that framework.

Zeolite catalysts containing protons can have acid sites characterized by their deprotonation energy (DPE), a probe-independent descriptor for the acid strength of a material by virtue of its independence to the surrounding environment by size, and are thus an intrinsic measure of acid

strength[210], [211]. DPEs were correlated with methanol dehydration rates for various solid acids[148], but calculated DPEs in zeolites are insensitive to the framework structure or proton location within a diverse set of zeolite structures[212]. This further indicates that for Brønsted solid acids, it is the shape and size of voids, and not the differences in their acid strength that controls the stability of intermediates and transition states. It is less clear; however, what role the framework has when reconstruction, for example by site hydrolysis shown to be necessary for ethanol dehydration in Sn-Beta[156], [198] and aldol condensation in Zr-Beta (CHAPTER 5) distorts fundamental building units which have framework-dependent shape. An analogy can be made back to silica surfaces, where Coperet and coworkers have shown that grafted single Cr[213] and Co[214] atoms on well-designed silica surfaces have specific chemical reactivity dependent on the local structure of heteroatoms in the silica matrix. Sweitzer et al. have also shown how strained 3-membered siloxane rings supporting single Zn sites behave as Lewis acids[215]. Here the local structure around Lewis acids introduced by the flexibility of silica is necessary to understand the catalysis of sites in these materials. For site hydrolysis, when reconstruction with the zeolite framework occurs, that acid site location may influence catalysis for specific structural motifs brought about by fundamental building unit shape.

## 6.2    Methods

The *ab-initio* techniques used in CHAPTER 5 of this thesis were identical to those used here. The specific codes used to automate calculating hydrolyzed sites are described in 6.3.1, these techniques were crucial for screening a large design space of framework-heteroatom pairs. Methods to deconvolute the effect of van der Walls energy (vdW) from the confining wall to calculate an intrinsic stability independent of the pore wall is considered in 6.3.2. Two methods for explaining the differences in hydrolyzed site stability for intrinsic binding energies of the same heteroatom type are presented in 6.3.3 and 6.3.4 which are the root-mean-squared deviation (RMSD) from an ideal tetrahedron, as well as the local Euler-Lagrangian strain to deform an ideal tetrahendron into the hydrolyzed site. These methods provide fundamental insight into how Lewis acid sites in zeolites can restructure, which we have shown to be important for both ethanol dehydration in CHAPTER 3 and CHAPTER 4 as well as for aldol condensation and MPV in CHAPTER 5.

## 6.3    Results and discussion

### 6.3.1    Automation of hydrolyzed site calculations

An algorithm to automate the screening of hydrolyzed open sites is provided here which draws heavily from the neighborlist methods from the Atomic Simulation Environment (ASE)[216]. The code uses the .cif files from the International Zeolite Association database (IZA)[72] which are annotated with the crystallographically distinct T atom locations. First a framework structure such as AEL is obtained from the IZA database. Lattice constants must first be relaxed to their equilibrium positions based on the choice of functional and cutoff energies to be used in all adsorption calculations. A ligand identity to be placed on the heteroatom must be provided as a .xyz file, in its alkoxy form ($CH_3CH_2O$ for an ethoxy open site). The heteroatom identity must then be chosen (In theory any element can be used, however the charge will only balance in the case of a $4^+$ heteroatom). For each distinct T site, a subdirectory is made which includes the heteroatom substituted at the given T site. For zeolites with unit cells less than 10 Å, the unit cell is repeated to make a supercell that is at least 10 Å on each side to prevent adsorbate-adsorbate interactions in small unit cells. The unit cell is then translated to place the heteroatom defect in the center of the unit cell, to ease visualization and figure-making.

Once a heteroatom is placed in a given T site, the ASE neighborlist algorithm is used to find the atomic indices of the four oxygen atoms bound to the heteroatom. The heteroatom and surrounding oxygen atoms define a distorted tetrahedron. Four analytic planes are calculated based on the adjacent oxygen locations, which define the faces of the distorted tetrahedron. The faces are labeled S0-S3, the 4 sides where ligands or adsorbates can be introduced. From previous studies in Sn-Beta, adsorption only occurred at faces of the tetrahedron, and bonding was never observed at the tetrahedral edges. This is also based on studies of literature reports in similar materials. The ligand structure can then be stitched onto a tetrahedral face through oxygen. This is accomplished by adding a ghost atom to the ligand that defines the anchor of the binding site (in the case of an alkoxide, the ghost atom would be place *ortho* to the O-R group. Once the ligand has been placed, the ligand is rotated around the M-O-R bond and the van der Waals energy is calculated according to the method of Grimme[71], [133]. The van der Waals energy is not variational, and thus cannot be used to minimize forces, however static DFTD3 calculations can be performed as the ligand is rotated. Local minima in the van der Waals energy are then chosen as candidate structure to perform full GGA-level DFT calculations. Thus, the van der Waals energy is used as a pre-

optimizer to identify initial configurations that maximize favorable contacts with the surrounding pore. To compensate charge on the zeolite framework, the oxygen that does not form the plane defining adsorption has a hydrogen atom capped. This ensures oxygen atoms are placed in *anti*-configurations which we have found to be the most stable hydrolyzed open site structure.[113], [198] In addition, if ligand atoms collide with the framework atoms, those configurations can be removed, to prevent ligands from getting stuck inside of small rings which are inaccessible by molecular diffusion. In summary the directory structure will have the following appearance O-R/FRM/Tx/Sy/Cz where O-R is the type of ligand chosen, FRM is the chosen zeolite framework, Tx is a T-site in the framework, Sy is a tetrahedral side of the T site, and Cz is a configuration of a side of a t site in a framework of a give ligand identity. For methoxy open sites in Beta, we would expect (1 ligand) * (1 framework) * (9 Tsites) * (4 sides) * (4 configurations) = 144 calculations. The number of configurations taken from each side can be chosen (more configurations may provide a better chance of capturing unusual confirmations, although the code already chooses the most stable configurations first. The number of sides relevant for adsorption may be less than 4, depending on the sbu structure, which is determined by counting collisions with the surrounding framework. Tristan Maxson, an undergraduate intern in the Greeley group, provided python code pieces which were invaluable to constructing the full algorithm

For frameworks that have non-uniform pores (for example MOR which has pores and side-pockets) it is useful in some cases to be able to sort between T sites accessing each pore structure. In some cases, the same T site may have tetrahedral faces that access different pores. The code then takes the volumes of framework atoms and determines the minimum distance between the ligand oxygen and the nearest framework atom. This is accomplished by defining a M-O vector, and collisions with the pore along a cone defined by the M-O vector are searched. Collisions with the surrounding pore are considered using a cone around the M-O vector as many planes of tetrahedral sides are not parallel to the surrounding pore, resulting in an overestimation of the minimum ligand-pore distance. Of course, if the raw minimum pore distance is calculated, it would result in the closest Si or O atoms, which is independent of the pore size, thus the cone constraint ensures that only Si and O atoms on the opposite side of the pore are considered. A post-processing code was also developed which takes converged sets of calculations and refines down the most stable configuration for a given T site (or given tetrahedral face if desired). Binding energies can be determined using a library of empty zeolite calculations performed at each T site, and a suitable

gas phase reference energy. This automation is not restricted just to hydrolyzed sites but can be used for closed-shell adsorption by removing the charge balancing tag and providing a .XYZ file of the desired closed shell molecule. As an example, to determine the range of ethanol binding energies and then ethanol dissociation energies in Beta across all T sites, an ethanol .XYZ file and ethoxy .XYZ file can be provided, which would then generate a set of ~144 * 2 calculations, where the only inputs are the .cif from IZA, and the .XYZ files. When combined with a library of zeolite total energies and the total energy of gas phase ethanol, a map of all energies in the Beta framework for ethanol adsorption and dissociation can be built.

The code is only capable of performing rigid rotations of the adsorbate or ligand, which has restricted the use of this code to smaller adsorbates and ligands, with a carbon number of less than 4. Large adsorbates could have internal rotations that can allow them to fit favorably in the zeolite pores, which cannot be sampled using the present implementation. A naïve solution would be to provide .XYZ files of multiple adsorbate conformations which can be searched. An automated structure library could be coupled to this which determined all possible rotations of a given molecule; however, these solutions would be poorly scaling. Ideally, it would be nice to develop a simplified classical potential which could do a pre-optimization that was variational, subject to a frozen zeolite framework. Perhaps even a few picoseconds of classical MD could provide an even better range of candidate structures which would have the same scaling for all sizes of adsorbates.

### 6.3.2   Van der Waals energy partitions

To probe what role the local structure of Lewis acid T sites has in stabilizing adsorbates or hydrolyzed sites, it is necessary to remove the non-local confinement interactions. Performing simulations using a GGA functional that neglects vdW interactions (such as PBE for example) will predict adsorbate structures which do not account for the favorability of orienting such that vdW energies are maximized, or perhaps more generally the compensation of vdW energy and enthalpic de-stabilization at the binding site due to re-orientation. Therefore, it is more amenable to perform DFT structure relaxations using a functional the includes vdW energies (in this case BEEF-vdW) and then using the converged structure file, calculate the vdW energies directly. The adsorption energy can be corrected by subtracting the vdW energy of the adsorbate in the pore, thus recovering

the electrostatic and orbital energy contributions to the adsorption energy, but in an adsorption configuration which is more realistic to experiment by including the maximization of vdW energy.

Through integration with post-processing codes used in Lewis acid adsorption and dissociation, vdW partitions can be performed by reading the structure file output (for VASP a CONTCAR) and using the ASE atoms and neighborlist functions, calculate the D3 dispersion energy of the total system, and divide the system into the framework atoms and adsorbate molecules to calculate the D3 energy of adsorption at the optimized structure in the zeolite. This energy is then subtracted from the total adsorption energy, to recover a binding energy only including the electrostatic and orbital energies. Figure 6.1 shows the correlation in methanol and ethanol dissociative adsorption energies in 12 MR channels for all T sites. Colors correspond to incorporated heteroatoms and shapes correspond to framework type. Adsorption of alkoxides in linearly related across a range of T site environments in Beta and MOR indicating the spread in binding energies of T sites with the same as well as different metal heteroatom identities. Methanol dissociative adsorption energies (referenced to a bare zeolite and gas phase methanol molecule) are shown in Figure 6.1 for Ge, Hf, Sn, Pb, Ti, and Zr heteroatoms in the AEL, AHT, BEA, CHA, FER, MEL, MOR, and VFI frameworks for each structurally distinct T-atom location among all tetrahedral faces. Only the most stable adsorption configuration for this data set includes nearly
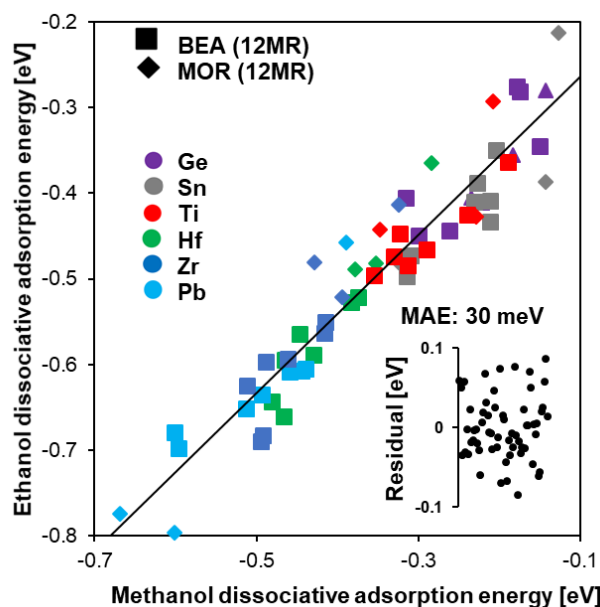


Figure 6.1 Scaling relationship between methanol and ethanol dissociative adsorption energies in similarly sized BEA and MOR 12 member rings across different T atoms and heteroatom identities. The slope is nearly 1 with a mean absolute error of 30 meV.

3000 individual calculations for hydrolyzed methoxy sites. The T site index refers to the T site ordering of sites in the IZA database, so the first datapoint of a given framework is the T1 site in that framework. Figure 6.2a is the total methoxy dissociative adsorption energy. The total range in in energies is nearly 1 eV across all frameworks and heteroatoms and the range of energies within the same heteroatom across all frameworks and T sites is greater than 0.4 eV for all heteroatoms (0.44 eV Ge, 0.62 eV Hf, 0.49 eV Pb, 0.44 eV Sn, 0.63 eV Ti, 0.62 eV Zr). These differences are convoluted with the change in pore size and shape, which affects the vdW energies across each data series. Figure 6.2b compares only the vdW energies, are more exothermic for smaller pore zeolites (AEL, AHT, MOR side pockets) than larger pore zeolites (BEA, MEL, VFI). Methoxy groups in CHA have similar vdW energies as BEA, which is due to the chambers in CHA having a similar volume as BEA intersections, despite CHA only having 8 MR windows for access. EMT shows a range in vdW energies as T sites in EMT be accessible to either the 12 MR pore or a smaller side pocket. As expected, vdW energies do not differ significantly across different heteroatoms at the same T location.

Removing the non-local vdW effects in Figure 6.2c reveal a heterogeneity in hydrolyzed methoxy dissociation energies that have similar ranges of at least 0.40 eV for the same heteroatom identity in diverse frameworks. The total range in methoxy dissociative binding energies is 0.82 eV for all types of heteroatoms in all frameworks considered. For the synthesis of butadiene from acetaldehyde and ethanol, I have shown how the reactive intermediates with the largest degree of thermodynamic rate control are enolates and ethoxy open sites, which catalyze aldol condensation and MPV reduction. In ethanol dehydration in Sn-Beta, I have also shown how transition states involve the transfer of hydrogen to a framework oxygen acting as a Brønsted base forming a hydrolyzed open site product state. If heterogeneities are observed in the stability of hydrolyzed states which are independent of the confining environment, the rules by which T sites that stabilize such sites is necessary to define new design rules for catalysis with Lewis acids. Upon inspecting the hydrolyzed sites in diverse frameworks, it was observed that final state geometries differed depending on heteroatom identity and zeolite framework, with energies that reflected each site's ability to reconstruct and adopt an energetically favorable configuration. It was hypothesized that the difference in stability was due to the local structure of the distorted Polyhedra that formed the zeolite T site, and that this structure would influence the stability of hydrolyzed sites.
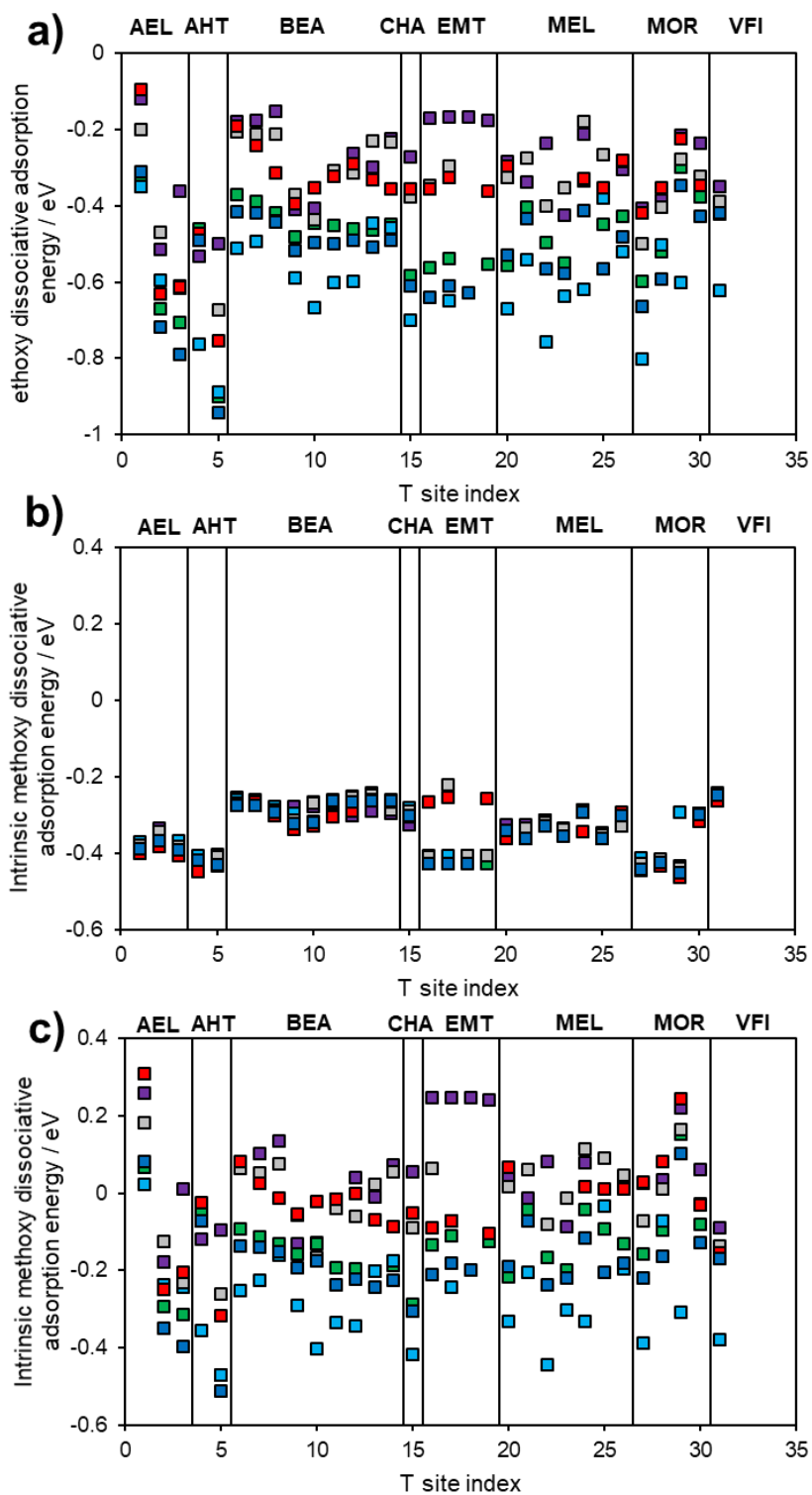
Figure 6.2 (a) ethoxy dissociative adsorption energy among a range of zeolite frameworks, for t sites ordered by their site index. Colors are the same as for figure 6.1. Purple (Ge), grey (Sn), red (Ti), green (Hf), blue (Zr), light blue (Pb).

### 6.3.3 Tetrahedral distortion

Metrics for determining the distortion of polyhedra include quadratic elongations which relates deviations in bond lengths and bond angles[217], [218]. T sites are distorted from ideal tetrahedrons due to the silica rings comprising structural building units (sbu) which must curve to form cylindrical pores or chambers. Using the atoms and neighborlist functions in ASE, a set of structural descriptors could be tested against the dataset of hydrolyzed open sites to relate the stability of hydrolyzed sites among different frameworks independent of the vdW stabilization.

A general python platform for testing distortion descriptors in zeolites was written, which takes an optimized structure file as input, and calculate a given descriptor based on a perfect reference tetrahedron. The orientation of a T-site distorted tetrahedron is arbitrary, and thus the reference tetrahedron must be rotated and translated to minimize the root-mean-square (RMS) deviation in the reference tetrahedron and T-site tetrahedron. This was accomplished with the Kabsch algorithm[219] using quaternion rotations[220] and implemented in python by Kromann at  Universitat Basel[221]. In practice, a silica tetrahedron is generated with 109.5° bond angles and 1.60 Å bond lengths. The Kabsch algorithm then translates and rotates the perfect tetrahedron and distorted T site tetrahedron such that the RMS deviation between the two structures in minimized. Kromann's algorithm is the extended to use a reverse transformation to put the distorted T site into the same configuration as in the VASP output file, and the reference tetrahedron is subjected to the same backwards tetrahedron. This results in two tetrahedra centered at the metal heteroatom, one of which has perfect tetrahedron bond lengths and angles overlaid on the distorted VASP output tetrahedron spanned by the metal heteroatom and adjacent oxygen atoms. Using this mapping, the RMS deviation from a perfect tetrahedron can be calculated using the mean absolute vector minimum between each oxygen atom in the perfect and distorted tetrahedrons.

If the tetrahedron forming the T site is distorted, the degree of distortion quantified by the RMSD deviation which includes bond length and bond angle deviations was hypothesized to correlated with intrinsic methoxy dissociative adsorption energies. Figure 6.3a shows that the RMSD deviations of T sites are not able to predict the changes in dissociative adsorption, and rather the largest contribution to the RMSD is the size difference of each substituted heteroatom. Figure 6.3b shows how the difference in ionic radii of the incorporated heteroatoms correlates with the RMSD deviation in predicted adsorption energies. This effect of changing heteroatom size an

important fundamental property; however, by normalizing the RMSD to a characteristic $MO_2$ bond (such as
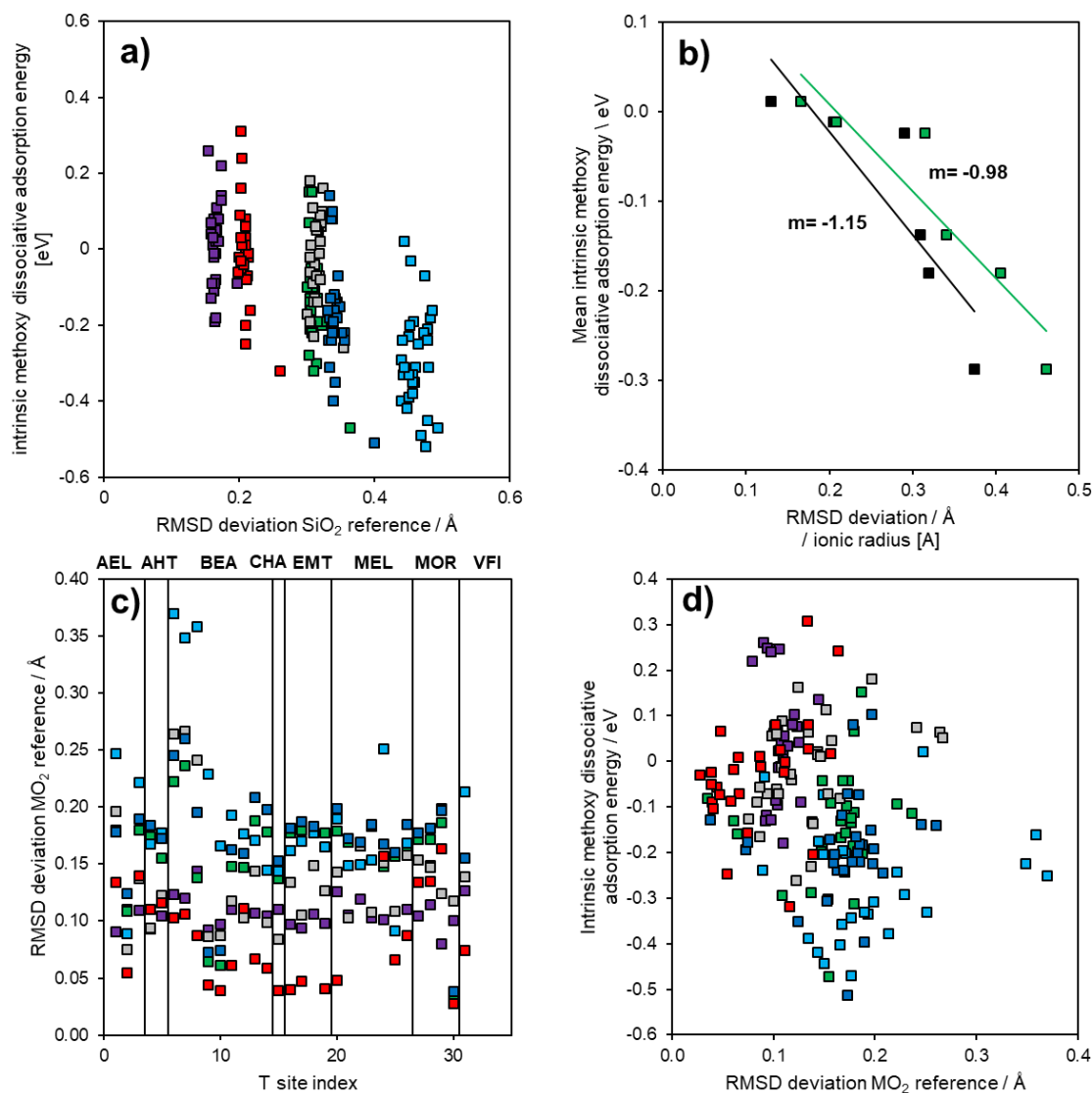


Figure 6.3 (a) Intrinsic methoxy dissociative adsorption for the range of frameworks (AEL, AHT, BEA, CHA, EMT, MEL, MOR, VFI) considered previously. Colors correspond to color scheme in Figure 6.2. (b) Mean intrinsic methoxy dissociative adsorption energy averaged across the lowest energy configurations for each framework and t site versus the average RMSD deviation (black) and heteroatom ionic radius (green). (c) RMSD deviations for all framework-tsite-heteroatom combinations with the $MO_2$ reference state which removes differences based on ionic radii. (d) Intrinsic methoxy dissociative adsorption energies related to their RMSD deviations referenced to $MO_2$. Coloring is consistent to Figure 6.2.

$SnO_2$, $TiO_2$) the second order perturbations intrinsic to each T sites would be amplified, as the deformation due to ionic radii is constant across the same heteroatom. It was considered that the deviations in the final state structure, when the metal includes the methoxy ligand would be a better descriptor for adsorption. The methoxy open site reconstructs to form a tetrahedral structure, which could be imagined as the T site having to reconstruct upon accepting the methoxy ligand to minimize the tetrahedral distortion on the heteroatom. Thus, RMSDs were calculated from the hydrolyzed open site where the three remaining framework oxygens and oxygen belonging to the ligand were compared to characteristic $MO_2$ ideal tetrahedrons. Figure 6.3c includes a comparison of final-state RMSD deviations referenced to $MO_2$ bond lengths. RMSD deviations are now similar across the range of heteroatoms, and qualitatively appears similar to the data-shape of Figure 6.2c. Pb has a large range in RMSD deviation, such as the datapoints for BEA T1-T3 sites which have RMSD deviations distributed around 0.35 Å, Some hydrolyzed sites in Pb and Sn zeolites could adopt a square-planar configuration that was not observed for the Ti, Hf, and Zr heteroatoms. Attempts to correlate the RMSD deviations of product states with the intrinsic methoxy dissociative adsorption energies are poor, as Figure 6.3d does not have any apparent correlation for each heteroatom. Despite hydrolyzed sites adopting a nearly tetrahedral configuration, the overall deviations are not able to capture the differences in binding energy across different zeolites even with the same incorporated heteroatoms. To obtain more fundamental insight into how differences in hydrolyzed site structures could be related to their formation energies, descriptors based on atomic strain were attempted.

### 6.3.4   Atomic strain measures

The RMS deviation measures described in the previous section are a total deviation measure; yet they do not capture the same detail as a strain tensor which would allow projection of vectors corresponding to the deviatoric and volumetric strains that more precisely correlate with the dissociative adsorption of hydrolyzed sites. The atomic strain tensor was calculated by the method described by Mott et al.[222] and Gullett at.[223] in which a strain tensor could be derived from the deformation gradient. In short, the local deformation of the hydrolyzed site was calculated by considering the relative positions of the metal atom and surrounding oxygen atoms with the ideal $MO_2$ tetrahedron. The Lagrangian-Green strain tensor can then be determined from the deformation gradient, $\mathbf{F}$, by the following expression

$$E = \frac{1}{2}(\boldsymbol{F}^T\boldsymbol{F} - \boldsymbol{I}) \tag{6.1}$$

As described by Gullet et al. where $\boldsymbol{I}$ is the identity matrix. The Lagrangian-Green strain tensor was chosen due to its use for elastic systems, in which a strained system can be compared to an un-deformed configuration.[223] In this way, the comparison to the hydrolyzed zeolite system is to quantify the strain caused by the inability of a hydrolyzed T site to adopt an ideal tetrahedral geometry which is assumed to be a pseudo-elastic process caused by the structure of O-Si bonds around the hydrolyzed site. Stain tensors were calculated as part of the hydrolyzed screening code allowing the calculation of vdW energies, RMSD deviations, and strain tensors automatically using an organized and intuitive workflow on the computing cluster. The principal moments of strain were determined through eigenvalue routines in Scipy, as well as coordinate-invariant metrics such as the strain determinant and trace of principal moment. Deconvolution of the volumetric and deviotoric strains was also performed, in addition to the octahedral stains including octahedral shear strain and normal strains to the octahedral planes.

To test the atomic strain descriptors, a smaller subset of framework-heteroatom pairs was chosen including AEL, BEA, CHA, EMT, FER, and VFI, and water hydrolysis energies were calculated to reduce the complexity of the system. To increase the magnitude of deviations from tetrahedron, instead of considering the most stable *anti* configurations of hydrolyzed sites, the metastable *syn* configurations were considered. The *syn* configurations are important for transition states, such as enolate formation in aldol condensation, or for bimolecular ethanol dehydration, as directly adopting the *anti* configurations is often sterically forbidden, except for large transition states. It was proposed that any water or alkoxide species could transfer a framework proton in the *syn* configuration to the *anti* configuration via a proton shuttling mechanism. Therefore, both the stability of *syn* and *anti* configurations from the local structure of T sites is important.

Correlations of intrinsic water dissociative binding energies with the largest principal moment of strain are shown in Figure 6.4 for each heteroatom and frameworks described above. For the group 4 elements including Ti, Hf, Zr mean absolute errors are less than 0.07 eV with no outliers. Principal moments of strain are large due to the *syn* conformations of hydrolyzed sites.
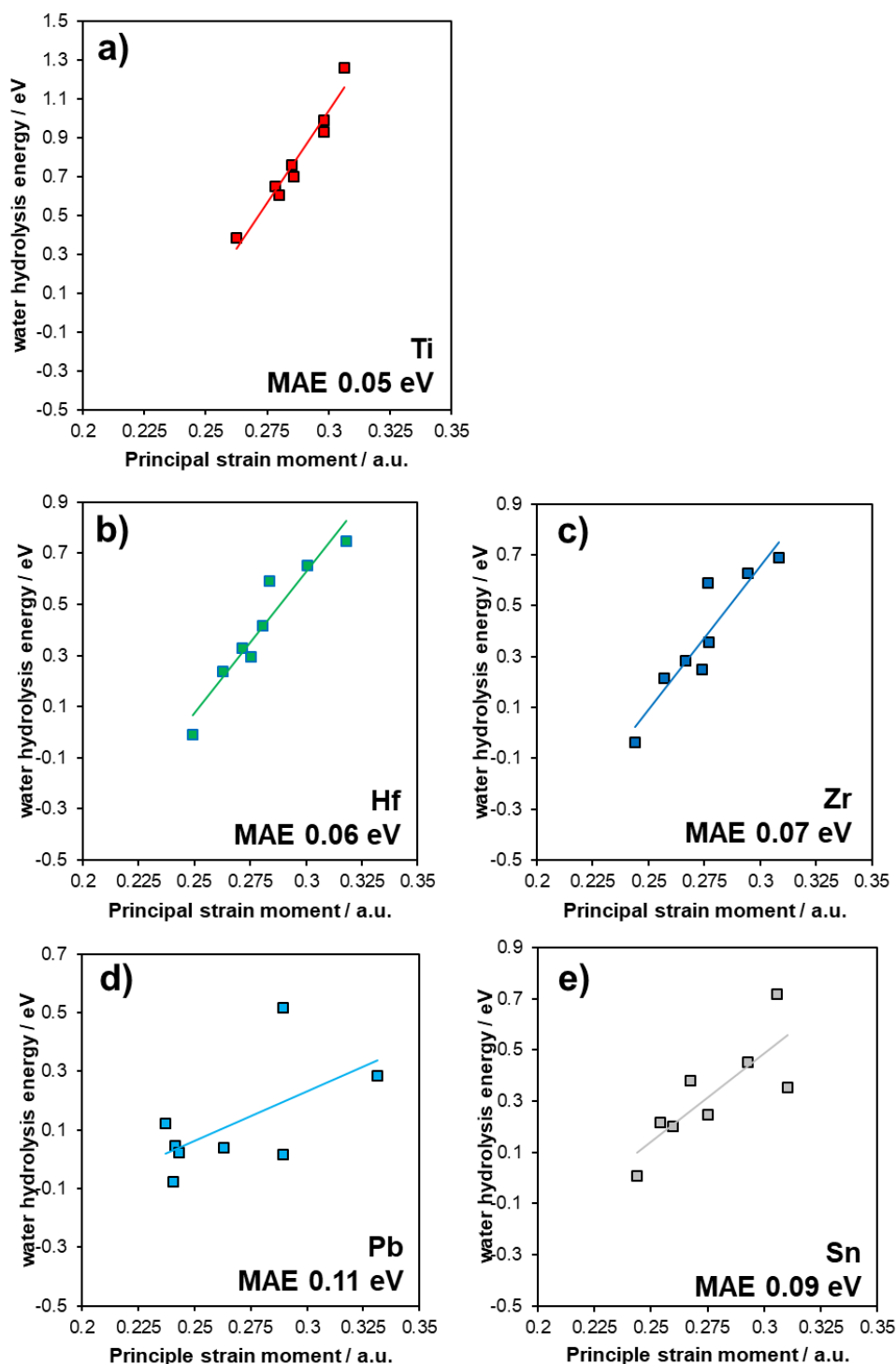
Figure 6.4 (a) Water hydrolysis for Ti-containing zeolites plotted against the largest principal moment of strain. (b) Water hydrolysis for Hf-containing zeolites plotted against the largest principal moment of strain. (c) Water hydrolysis in Zr-containing zeolites plotted against the largest principal moment of strain. (d) Water hydrolysis in Pb-containing zeolites plotted against the largest principal moment of strain. (e) Water hydrolysis in Sn-containing zeolites plotted against the largest principal moment of strain.

For the group 14 elements including, including Sn and Pb which are larger, outliers corresponding to the square-planar configurations observed for these elements. These data indicate that that as the largest principal strain moment increases, the hydrolyzed site is less stable relative to the gas phase. Since strain tensors are referenced to an ideal tetrahedron, as the elastic strain increases, and the hydrolyzed sites deviate more from an ideal tetrahedron, the dissociative adsorption energy increases. Thus, the ability of a given T site to restructure to form a tetrahedron with the incorporated ligand determines the stability of that ligand addition. Projection along the largest principal moment of strain shows that deviations in the direction of the ligand group are large, yet strain tensor determinants are nearly zero, indicating that the tetrahedral volumes are nearly like that of the ideal tetrahedrons, and the largest contribution to the strain is a deviatoric strain originating from the ligand group. At T sites in zeolite frameworks, the precise orientation of oxygen atoms controls to what degree that site can restructure upon dissociation. The closer a given T site can restructure to a tetrahedron, the most stable that hydrolyzed site will be in the framework. This then, defines a lowest possible dissociative adsorption energy, when restructuring is nearly tetrahedral. Additional calculations are required for other frameworks, as well as idealized reference structures to determine if the strain relationship is linear, and what stress these correspond to. A complete relationship is lacking; however, these data indicate some relationship
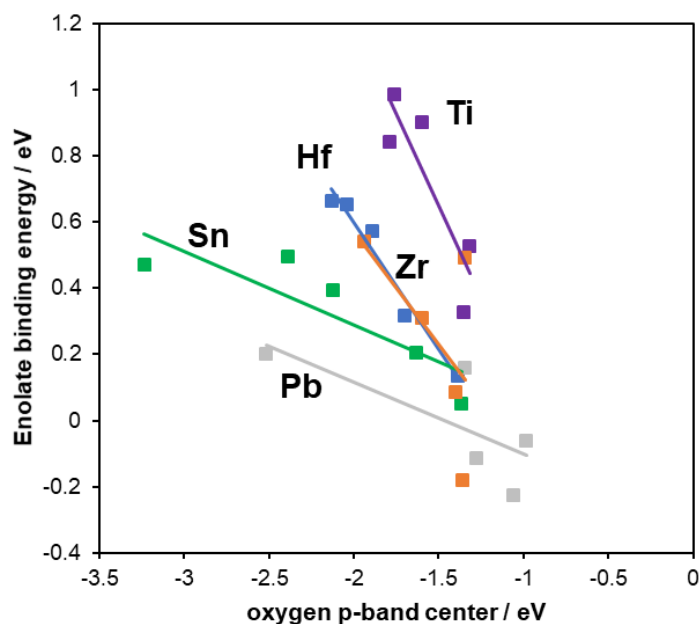


Figure 6.5 Correlations between enolate binding energy and p band centers of the framework oxygen accepting a hydrogen at the transition state.

between reconstruction along the direction of the ligand and stabilization of this final state. An electronic manifestation of how this reconstruction can affect transition states can be seen by observing how the p-band centers of oxygen atoms bound to a metal heteroatom shift in different frameworks due to their local structure. Here the binding energies of enolates, which have the largest thermodynamic degree of rate control, are compared to the p-band centers of the framework oxygen atom, behaving as a Bronsted base, at the transition state for enolate formation by the direct mechanism on closed metal sites at arbitrarily sampled T sites in the AEL, BEA, CHA, EMT, and MOR frameworks. Electronic structure calculations are difficult in zeolites due to the large unit cell size, yet the correlation provided in Figure 6.5 shows how binding energies of enolates become more stable as the oxygen $p$ band center at the transition state shifts upward. This provides a possible connection with experiment, as the acid/base properties of oxygen atoms in different frameworks could be a probe of the differences in stability of hydrolyzed sites.

### 6.3.5   A descriptor-based approach toward designing butadiene synthesis catalysts

With enolate stability identified as intermediate with the largest thermodynamic degree of rate control it is necessary to provide intuition about the types of zeolite frameworks that could improve the rates of butadiene synthesis through stabilization of reactive intermediates. The choice of framework will be made based on three independent variables, the metal heteroatom incorporated into the framework, which is governed by the linear scaling relationships developed previously[113], the magnitude of vdW energies exerted by the surrounding zeolite framework, and the strain exerted by the local structural building units of the zeolite framework which control the reconstruction of these hydrolyzed sites. This will be accomplished in the following stages. First, the stability of enolates will be related to the activation barrier for enolate formation based on a Bronsted-Evans-Polanyi (BEP) relationship to show that both the enolate stability referenced to the gas phase is related to the transition state energy, as well as for the adsorbed MARI state. This ensures that changes in the transition state affect reaction barriers measured experimentally, and therefore are consequential to the kinetics of butadiene synthesis. Then, the scaling relationship between enolates and hydrolyzed water open sites shows how the strain descriptors described previously for water can be extended into enolates, which are chemically like hydrolyzed water open sites. Finally, the relationship between strain and vdW energies is used to predict
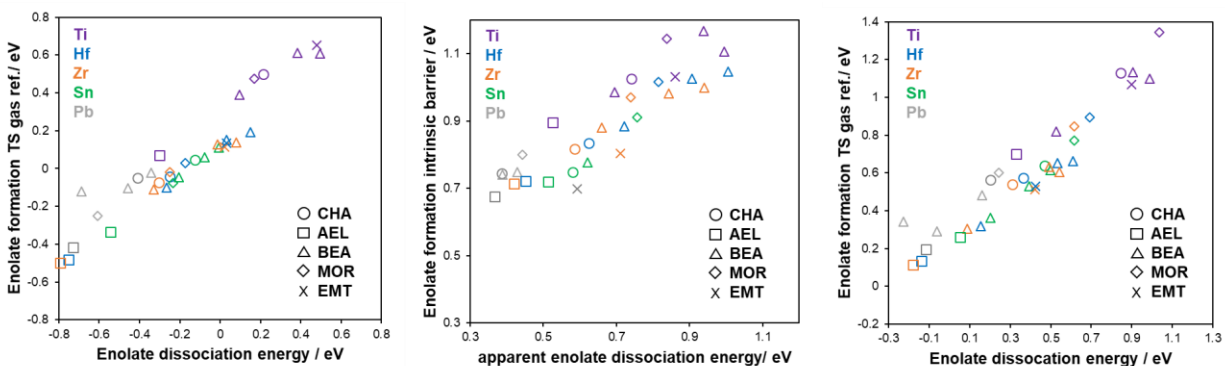
Figure 6.6 BEP relationships for enolate formation via the direct route $(A+W)^* \leftrightarrow (W+En_x)^*$. (a) BEP constructed with gas phase references for both the enolate formation energy and transition state energy. (b) BEP referenced to the MARI species from CHAPTER 5 (acetaldehyde) for both the enolate stability and transition state energy. (c) "intrinsic" BEP referenced to the gas phase but with vdW energies removed from the enolate formation and transition state energies.

enolate dissociative adsorption energies, which are related through the BEP, to correlate the activation barriers for enolate formation across different zeolite topologies based on their tetrahedral strain (related to the local structure) and vdW energy (related to the surrounding pore environment).

From the set of frameworks considered previously (AEL, BEA, CHA, EMT, MOR) the activation barriers of enolate formations were calculated using the NEB method. Transition state structures were calculated manually, using multiple initial configurations to ensure that the lowest energy transition state was identified. Figure 6.6a shows the BEP for enolate dissociation energy referenced to the gas phase, where coloring corresponds to heteroatom identity, and shape corresponds to framework time. The BEP holds across both zeolites and metals, indicating the transition state for enolate formation and the enolate are similar. The slope is nearly 1, which is expected for the late transition state associated with a proton transfer mechanism. The gas phase BEP is influenced by the vdW energy of adsorption, and so Figure 6.6c shows the gas phase BEP with the vdW energy of the enolate dissociation energy and transition states removed. The correlation is more striking, with a range of transition state energies of over 1 eV across the range of heteroatoms and frameworks. As shown in CHAPTER 5, the strong binding energy of acetaldehyde makes it likely that the surface coverage is high. Figure 6.6b shows the same BEP referenced to the acetaldehyde binding energy, representing the apparent activation energy, more relevant under reaction conditions. The range in apparent barriers is on the order of 0.5 eV,
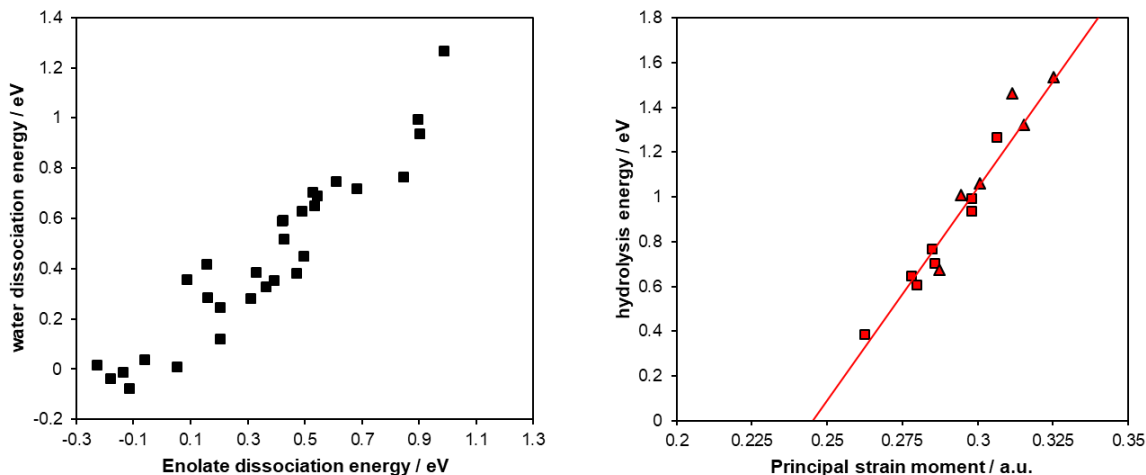
Figure 6.7 (a) scaling relationship between water dissociative adsorption energy and enolate dissociative adsorption energy. (b) strain-hydrolysis correlation for both enolate dissociative adsorption (triangles) and water dissociative adsorption (squares).

indicating the activation barriers for aldol condensation can be changed even when the coverages of acetaldehyde are high. This indicates the T site structure influences the transition states differently than the initial state. This is unsurprising as the transition state involves the reconstruction of the T site and the framework oxygen accepting a hydrogen to open the site. The dissociation energy of water can be linearly related to enolate dissociation energy by figure 6.7, which would indicate how the structure of hydrolyzed sites formed by water and acetaldehyde are similar and differ only in the ligand identity. The stability of enolate sites can be related to the principal strain, which is plotted along with the hydrolyzed open sites, shown in Figure 6.7a, for Ti heteroatoms. The strain-energy expression can be combined with the vdW energy of a given T sites to predict the total energy of the enolate sites, expressed in the following equation:

$$E_{En*} = E_{En*}^{vdw} + E_{En*}^{strain} \tag{6.2}$$

Where for a given heteroatom the total dissociative adsorption energy can be expressed as a sum of the strain and vdW energies. Transition state energies can be predicted through application of the BEP relation, allowing for a way to predict transition state energies from the enolate strain and vdW energies. It is also possible, as evidenced by the scaling relationship connecting hydrolyzed open sites and enolates, that the dissociative adsorption energy of all similar alkoxides can be correlated to the dissociative adsorption energy of hydrolyzed water sites. To illustrate how these descriptors can be used to predict binding energies, Figure 6.8 shows a heat map for enolate
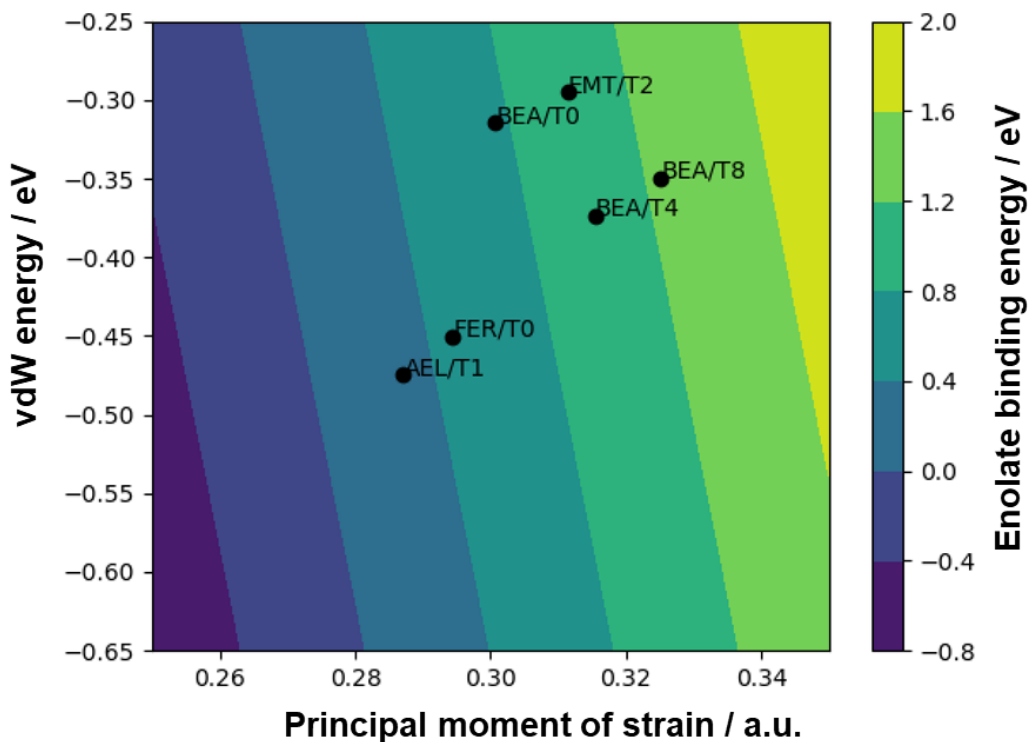
Figure 6.8 energy map of enolate formation energy referenced to the gas phase based on vdW energy and largest principal moment of strain for Ti-containing zeolites. Correlation for the frameworks provided has a MAE of 0.08 eV.

dissociative adsorption energy expressed in terms of the vdW and strain energies for Ti-containing zeolites. The MAE of the predicted energies is 0.08 eV for the limited dataset shown. Additional work is being done currently to expand the range of frameworks, as well as include the BEP relationships, and reference transition states to the acetaldehyde binding energy to predict apparent activation energies. Despite these limitations, the AEL framework has larger vdW energies and lower principal strain the any of the BEA T sites considered, and the enolate binding energies are more stable. Based on the BEP relation, this would correspond to a decrease in the gas phase activation barrier by nearly 1 eV. There must be limits to the range of strain and vdW energy, which would represent the limit where the pores are so narrow that diffusion limitations become dominant.

## 6.4 Conclusions

Here the importance of local strain on stabilizing hydrolyzed sites is presented based on the calculation of water, methanol, ethanol, and acetaldehyde dissociative adsorption to produce sites relevant to the ethanol dehydration and butadiene synthesis. It was found that the energies of hydrolyzed sites can be decomposed into local (strain) and nonlocal (vdW contacts) contributions to the total energy which reflect both properties of the zeolite framework, where strained building units form pores that stabilize the adsorption of intermediates as well as affect the coordinating environment to Lewis acids to modulate HOMO energies of the framework oxygens. These framework oxygens were shown to have different p-band centers for the same metal heteroatom which different only in their local structure. These were shown to control the energies of transition states for the direct enolate formation mechanism. Framework sites were shown to affect the enolate formation barriers even when referenced to the MARI species of chemisorbed acetaldehyde, as due to the protonation transition state structure, the framework oxygen interacts with the transition state differently than the initially chemisorbed state, reflecting a change in the apparent barriers.

This decomposition can be used to screen the stability of hydrolyzed sites (shown to have the highest thermodynamic degree of rate control for butadiene synthesis) which has been demonstrated here, albeit in a limited case. The choice of principal strain moment appears to correlate best for the group 4 metals (Ti, Zr, Hf) where hydrolyzed sites can be well-approximated as an elastic deformation from an idealized tetrahedron. For the group 14 metals (Sn, Pb) the correlation is worse, and square planar structures can be stabilized at some t sites, which are not seen for the group 4 metals. This would break the elastic deformation argument, which may underlie a more fundamental strain relationship agnostic to the choice of reference structure. Subject to this caveat, the results provided here are a way to use Sabatier-type volcano plots to correlate the kinetics of Lewis-acid catalyzed reactions allowing for the screening of unusual and poorly understood zeolite frameworks that may be good butadiene catalysts. These paradigms are necessary to help span the materials space for microporous materials, which as of now are still mostly unexplored for catalysis.

# 7. CONDENSATION OF LOCAL WATER STRUCTURES IN LEWIS ACID ZEOLITES

Author Contribution: Jason Bates conducted the experimental IR spectroscopy shown in Figure 7.4.

## 7.1    Introduction

Microporous environments are known to mediate solvent contact with internal catalytic active sites through functionalized defects but understanding the molecular-level structure of solvents in such environments remains in its infancy.  Experimentally, the structure of water around Brønsted acid sites in zeolites[224], [225] has received interest in the catalysis field for biomass conversions. The development of transferrable first principles models of local solvent structures, in turn, would permit development of a molecular understanding of well-defined point defects and their influence on the local structuring of solvents, as well as their participation in stabilizing reactive intermediates and transition states to provide intuition for the rational design of materials with tunable solvent interactions. Such tunability would be of specific interest to metal organic frameworks (MOFs)[226], carbon polymorphs[227]–[229], and zeolites[99]   where the permittivity of solvent into confined voids is directly related to the relative strengths of hydrophobic and hydrophilic interactions between solvent molecules and the substrate[230]. Among these materials, the hydrothermal stability, high crystallinity, isolated acid sites, and synthetic control of point defects[79], [80], [102], [103], [231] in zeolites make them a particularly attractive materials class for elucidation of the relationship between defect structure, local solvent properties, and the consequent impact on catalytic activity.

In Lewis acid functionalized zeolites, defects that may influence solvent interactions can be broadly classified as either heteroatom substitutions to form Lewis acid sites (such as $Sn^{4+}$ or $Ti^{4+}$) or silanol moieties formed through post-synthetic treatment. The Beta zeolite framework[72], with intersecting 12 member silica pores (Figure 7.1a-c) catalyzes oxygenate chemistries when substituted with Sn (Sn-Beta) in the presence of a polar solvent[69], [232] and is the primary focus of the present study. Sn sites interconvert between a tetravalent framework coordination (Sn, Figure 7.1d) and a trivalent framework coordination with a hydroxy ligand (SnOH, Figure

7.1e)[197], [198], introducing additional polar functionality to Sn sites which then comprise the active site for glucose isomerization[233]. In addition, silanol nests may be formed in Sn-Beta via post-synthetic grafting[234] ((OH)$_4$, Figure 7.1f), and the hydrophobicity of the framework may be tuned by introducing either low ("Si-Beta-F") or high ("Si-Beta-OH") concentrations of silanol defects. However, while some consideration has been given to condensation of water in defected zeolites, such as Silicalite-1[235], the impact of the rich space of local defects in Lewis acid-functionalized zeolites on solvent structure and associated catalytic properties is not well understood.

Herein, we present a detailed computational and experimental comparison of the structural and thermodynamic properties of local water phases surrounding point defects and catalytic active sites in Sn-Beta, and we benchmark these results against the properties of defect-free hydrophobic Beta. *Ab-initio* molecular dynamics (AIMD) is performed to probe the transient structure of water under standard conditions (300 K, 1 Bar) in contact with single periodic Beta unit cells with different defects presents. The use of AIMD, in turn, provides an unambiguous and consistent treatment of interactions between defect moieties which mediate dissimilar solvent interactions. The results show the formation of tightly nucleated water clusters between 4 and 6 water molecules chemisorbed at tetrahedrally coordinated Sn sites that do not significantly perturb water structuring, as compared to the purely siliceous materials, and which persist even at higher water densities. In comparison, (OH)$_4$ silanol nests are shown to nucleate hydrogen bonding networks that exhibit local phase behavior distinct from weakly bound water molecules which form extended chains[236]–[238], but these local networks become disrupted at the high water densities found at much higher aqueous chemical potentials. Indeed, water in the highly defected materials show perturbed OH stretching peaks, indicating stronger hydrogen bonding interactions between solvent molecules as compared to low defect Si-Beta-F materials.

## 7.2   Methods

Periodic self-consistent density functional theory (DFT) was performed using the Vienna Ab-initio Simulation Package (VASP). The computational parameters used here are consistent with our previous work in zeolite Beta[198], [239], and are described in detail below. The Bayesian error estimation functional (BEEF-vdW)[31] was chosen based on the inclusion of van der Waals interactions as well as its predictions of bulk lattice constants for Beta (reported to be within

3% [198] of that provided by the International Zeolite Association[1] database where the structural file was obtained). We note the similarities between adsorption energies of oxygenate species to Lewis acid sites incorporated in zeolites between PBE-D3 and BEEF-vdW[113], and as will be shown further, bulk liquid entropies calculated with BEEF-vdW were reasonable. Parameterized force field models of water (such as TIP4P-Ew[240] and SPC/E[241]) have found tremendous success in accurately predicting water-water interactions and hydrogen bonding; however, a DFT approach was chosen to capture the range of interactions with Sn in different ligand environments. This fundamentally reduces the accuracy in treating water-water interactions, as BEEF-vdW was not developed to treat such delicate interactions. Thus, we must be conservative in conclusions gleaned from this analysis, especially in determination of absolute entropies, due both to the functional choice and model size constrained by AIMD. We will thus restrict ourselves to discuss relative changes in water structuring and entropy, which will be indicative of general properties of water as they restructure in different confining environments.

All calculations, including AIMD, are performed at the same level of rigor as used previously to study catalysis in zeolite Beta. Spin-polarization is used with a cutoff energy of 520 eV. Forces were evaluated to a energetic cutoff of 0.1 meV, and ground state calculations were converged to a force cutoff of 30 meV / A. Gaussian smearing was employed, and a single Gamma K-point was included due to the large unit cell structure and lack of non-covalent interactions. The Projector Augmented Wave (PAW) pseudopotentials were used.
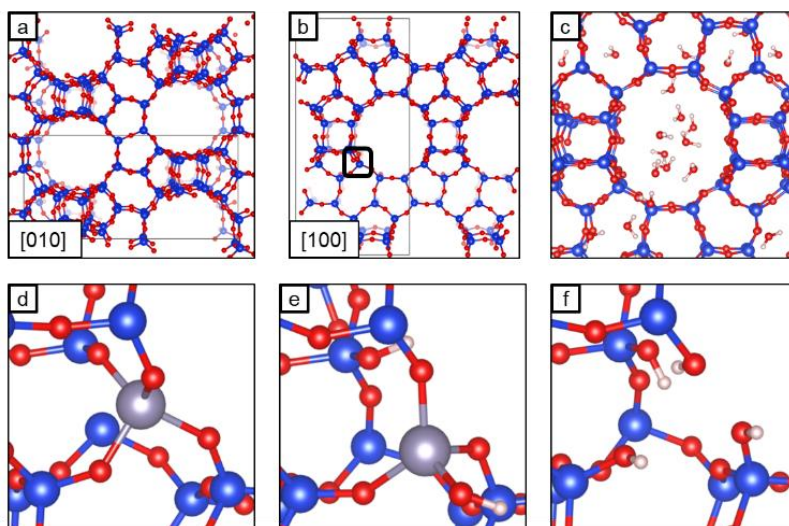


Figure 7.1 Zeolite Beta with intersecting pore structure (a,b). Water physisorbed in siliceous Beta exploring parallel and perpendicular pore structures (c). Closed Sn (d), hydrolyzed open Sn (SnOH) (e), and silanol nest (OH4) (f) at the T8 site.

### 7.2.1 Ab-initio molecular dynamics simulations

All AIMD simulations were performed in VASP. A Nosé-Hoover thermostat[242] was used to sample a NVT ensemble with a temperature of 350 K. All hydrogen atoms were deuterated, and the timestep was 1 fs. Calculations were equilibrated for 5 ps before beginning production runs. All production runs had a minimum duration of 20 ps, subject to a criterion that fluctuations in the calculated water entropies (discussed below) are lower than 3 J mol$^{-1}$ K$^{-1}$ as compared at 19 ps and 20 ps (APPENDIX F). Simulations exhibiting large fluctuations would infer non-equilibrium, requiring additional simulation time to more accurately sample configurations at equilibrium. For simulations in which large entropy fluctuations were observed, multiple initial water configurations were considered, and the simulation with the lowest Helmholtz free energy was reported. Initial water configurations could be selected either as fully randomized structures or developed from addition or subtraction of water from converged structures. Initially, low density structures were fully randomized, but as intuition was developed about stable water configurations, differential changes in previous structures became preferred. To prevent biasing structures which may be metastable at the previous water density, velocities were randomized and a full 5 ps equilibration was performed to reach equilibrium with the constraint that entropy fluctuations reduce below 3 J mol$^{-1}$ K$^{-1}$. The estimated total time sampled across 4 defects, 10 water densities plus a bare framework, and 25 ps equilibration and production, exceeds 1 ns.

To calculate the potential energy of water in each zeolite, the ensemble averaged energy of bare framework was subtracted from the zeolite including adsorbed water, which could then be normalized to an intensive property by dividing by the number of water molecules. This is referenced to an intensive energy of bulk water calculated at 350 K and 1 bar (eq 1).

$$\widehat{E_w} = \frac{\langle E_{W+Z} \rangle - \langle E_Z \rangle}{N} - \widehat{E_{bulk}} \tag{7.1}$$

Where $\langle E_{W+Z} \rangle$ denotes the potential energy of the zeolite with adsorbed water averaged through the duration of the simulation, $\langle E_Z \rangle$ denotes the potential energy of the bare zeolite averaged over the duration of the simulation. N is the number of water molecules, and $\widehat{E_{bulk}}$ is the intensive potential energy of bulk water at 350 K and 1 bar. The resulting property has units of eV (water molecule)$^{-1}$. The above relation is only reasonable in the limit where the vibrational states of the zeolite framework are uncoupled from the dynamics of water molecules. The vibrational spectrum of the zeolite framework was calculated at varying water densities, and as shown in APPENDIX

F no peaks shift even in the presence of 45 water molecules per unit cell, indicating the energetic terms are approximately separable as described above.

To simulate bulk water, 54 deuterated water molecules were confined in an 18.8024 Å by 9.3150 Å by 9.3150 Å cubic cell, to report a density of 0.9972 g cm$^{-3}$ to close agreement with the reported density of water at 298 K[243]. A simulation temperature of 350 K was chosen based on previous reports of PBE structuring of water at 298 K. A similar 5 ps equilibration and 20 ps of production runs were performed. A snapshot of bulk water supercell is shown in APPENDIX F.

### 7.2.2  Entropy calculations

The calculation of water entropies was accomplished using a in-house build of the quasi-harmonic 2-phase theory (2PT) algorithm developed by Lin, Blanco, Pascal, Maiti, and Goddard[153], [244], [245]. We have previously applied this method to estimate differences in the entropy of adsorption for reactive intermediates for ethanol dehydration[198] and acetonitrile[239] in zeolite Beta. Our implementation is described below. Periodic trajectory files from VASP are converted into the .XYZ file format using the Atomic Simulation Environment (ASE)[216] with the zeolite framework atoms removed. The trajectories are unwrapped across periodic boundary conditions and sorted by water molecule to infer molecular identity using the molecular dynamics toolbox TRAVIS[246]. From there, an in-house implementation of the 2PT theory is performed which includes decomposition of the molecular degrees of freedom into center of mass translation, rotation, and vibration. These are then individually passed through a Fourier transform filter and smoothed using a Savitzky-Golay filter producing Velocity Density of State (VDOS) functions for the translational, vibrational, and rotational modes.

The gas-like contributions to translational and rotational modes are approximated as a set of hard spheres. Thus, a VDOS for the gas-like diffusion, gas-like rotation, solid-like diffusion, gas-like diffusion, and vibrations can be individually integrated to obtain entropies according to the general relation in equation 2.

$$S = k\left[\int_0^\infty dv S^s\left(W_S^s(v)\right)W_S^s(v) + \int_0^\infty dv S^g(v)W_S^g(v)\right] \tag{7.2}$$

Where S is the entropy of a given type of motion comprised of a solid-like VDOS $S^s(v)$ and quantum harmonic weight function $W_S^s(v)$ integrated over the range of frequencies $v$, and corresponding VDOS for the gas-like component $S^g(v)$ with weight function $W_S^g(v)$ derived

from the Carnahan-Starling equation of state for hard sphere gases, as discussed by Lin et al[153], [244], [245].

Entropies calculated from this method could be compared across a range of densities and compared to the entropy of the bulk water reservoir. While the method by Lin et al. has shown success in calculating absolute entropies, our small number of guest water molecules and use of the BEEF-vdW functional makes us more conservative in comparing relative entropies across the composition space.

### 7.2.3   Hydrogen bonding network theory

The weighted clustering coefficients are calculated with the method by Barrat et al.[247] however the development of the water network connectivity diagrams  requires additional discussion. The time-averaged hydrogen bonds at each water density were calculated by the method of Durrant et al.[248] where both the distance between hydrogen bond donors and acceptors and the angle formed between hydrogen bond donors and accepts are used as criteria to determine the existence of a hydrogen bond. A maximum noncovalent distance of O-H bond distance of 3.5 A, and maximum O-H-O bond angle of 30° were used for cutoffs. Existence of hydrogen bonds between pairs of water molecules is summed for the duration of the calculation and normalized by the duration of the simulation. Thus, while each water molecule is free to donate and accept multiple hydrogen bonds at a given time, the individual hydrogen bond between a pair of water is expressed as a fraction representing the time-averaged duration of the hydrogen bond. For example, a pair of waters perpetually hydrogen bound to each other would have a connectivity of 1. A pair of waters hydrogen bound to each other for half the duration of the simulation would have a connectivity of 0.5. Thus, an adjacency matrix $a_{ij}$ can be written where if a hydrogen exists at any timestep between water molecules $i$ and $j$, $a_{ij} = 1$ and equal to zero if no hydrogen bonds are formed. A matrix of edge weights can also be constructed, $w_{ij}$ which is equal to the time averaged hydrogen bond connectivity between water molecules $i$ and $j$, which is bounded between 0 and 1. Heat maps of connectivity matrices are included in APPENDIX F. which directly visualizes the correlations between water pairs.

From the adjacency and edge weight matrices the weighted clustering coefficient as derived by Barrat et al. can be implemented, with the following equation:

$$c_i^w = \frac{1}{s_i(k_i-1)} \sum_{j,h} \frac{(w_{i,j}+w_{i,h})}{2} a_{ij} a_{ih} a_{jh} \tag{7.3}$$

Here, $k_i$ is the number of edges (hydrogen bonds) at a given vertex (water molecule), and $s_i$ is the sum over all weights at a given edge. The weights of each pair of edges are express as $w_{i,j} + w_{i,h}$, with thee product of edges between vertices *i, j, h* being nonzero if a triangle can connect all three vertices. Thus, the weighted clustering coefficient of a given vertex *i,* is calculated as the sum of all triply connected vertices weighted by their hydrogen-bonding connectivity and normalized by the maximum connectivity of hydrogen bonds at a given water density.

From the weighted clustering coefficient for each vertex, the overall clustering coefficient as averaged over the network is also given by Barrat et al.[247]

$$C^w = N^{-1} \sum_i c_i^w \tag{7.4}$$

Which is the arithmetic mean of clustering coefficients at each vertex normalized by the number of vertices, *N*. higher order moments about the distribution of clustering coefficients at a given water density can also be considered.

### 7.2.4   AIMD OD stretching peak center identification

To identify OD stretching peaks in the AIMD simulations, VDOS (described above) which include the spectrum of all water vibrational states, could be directly fitted. The advantage of using the VDOS, as opposed to a 0 K vibrational state calculation is that the perturbations in OD stretches averaged over all water molecules and sampled for the full duration, as well as approximately including temperature effects on vibrational frequencies. Peak positions were determined by performing a Gaussian fitting of the VDOS and reporting mean positions after using a Hanning filter to remove high frequency modes post-FFT. Plots of the vibrational spectra are included in APPENDIX F.

### 7.3   Results and discussion

The defect-free siliceous Beta material provides an initial baseline for understanding the dynamic structure of water in Beta frameworks. As the water density per unit cell is increased from the lowest density possible using a single unit cell (1 water per cell) to the predicted density of a bulk liquid in the accessible pore volume (23 water per unit cell, Figure 7.1f), water is observed to undergo phase transitions that are not observed in unconfined bulk water. At low water densities,

within a range of 1-3 water molecules per unit cell, molecules exhibit gas-like diffusion. As the number of molecules is increased up through approximately 5-12 waters per unit cell, uniformly dispersed chains along a pore channel are formed (7.2a), where little exploration into the perpendicular pore systems is observed. Finally, at the highest water densities, above 12 waters per unit cell, chains begin to crosslink across intersections and fill the pore channel (7.2b)[249], [250]. We note that the presence of perpendicular pores in the [100] direction are observed in the lower left and upper right corners of the high density plots and do not correspond to localized clustering. Additional images are provided in APPENDIX F.

To quantitatively explore the organization of water between the regions where water chains are observed and the upper limit close to bulk liquid density, a dynamic clustering algorithm is employed based on network connectivity theory. While methods based on Voronoi tessellations[251] are ubiquitous in classical molecular dynamics studies to determine nonlocal solvent structures[252], the limited systems sizes associated with first principles methods precludes the use of such methods or grand canonical simulations which permit longer timescales. In contrast, the connectivity method directly evaluates the correlation between hydrogen bonds, allowing a discussion of clustering[247] which does not depend on the spatial positions of water molecules. Mean clustering coefficients reflect the degree to which water molecules are localized in networks of hydrogen bonds, with a coefficient of unity implying rigid hydrogen bonding interactions, as in a solid, where each water molecule is the center of an infinitely dispersed cluster. The mean clustering coefficients for Si-Beta (Figure 7.3a, in blue), for example, show an average coefficient close to unity at a density of eight water molecules per unit cell. Note that this does not indicate that water molecules are immobile. Rather, they diffuse while maintaining a correlated network within the pore shown in Figure 7.2a. The other limit of clustering coefficients, zero, describes a perfect gas, where no hydrogen bonding events occur. Intermediate values correspond to bond networks that are transiently formed and broken, as is the case for bulk liquid water with a mean clustering coefficient of 0.74, denoted by the dashed line in figure 7.3a. Indeed, as the total water density increases, mean clustering coefficients in Si-Beta rapidly approach the bulk water limit, demonstrating that dynamic hydrogen bond restructuring is occurring, which in turn leads to enhanced crosslinking of water between pore structures (Figure 7.2b). An increase in the mean clustering coefficient at a density of 15 waters per unit cell coincides with the beginning of crosslinked networks, which delocalize at increasing density.
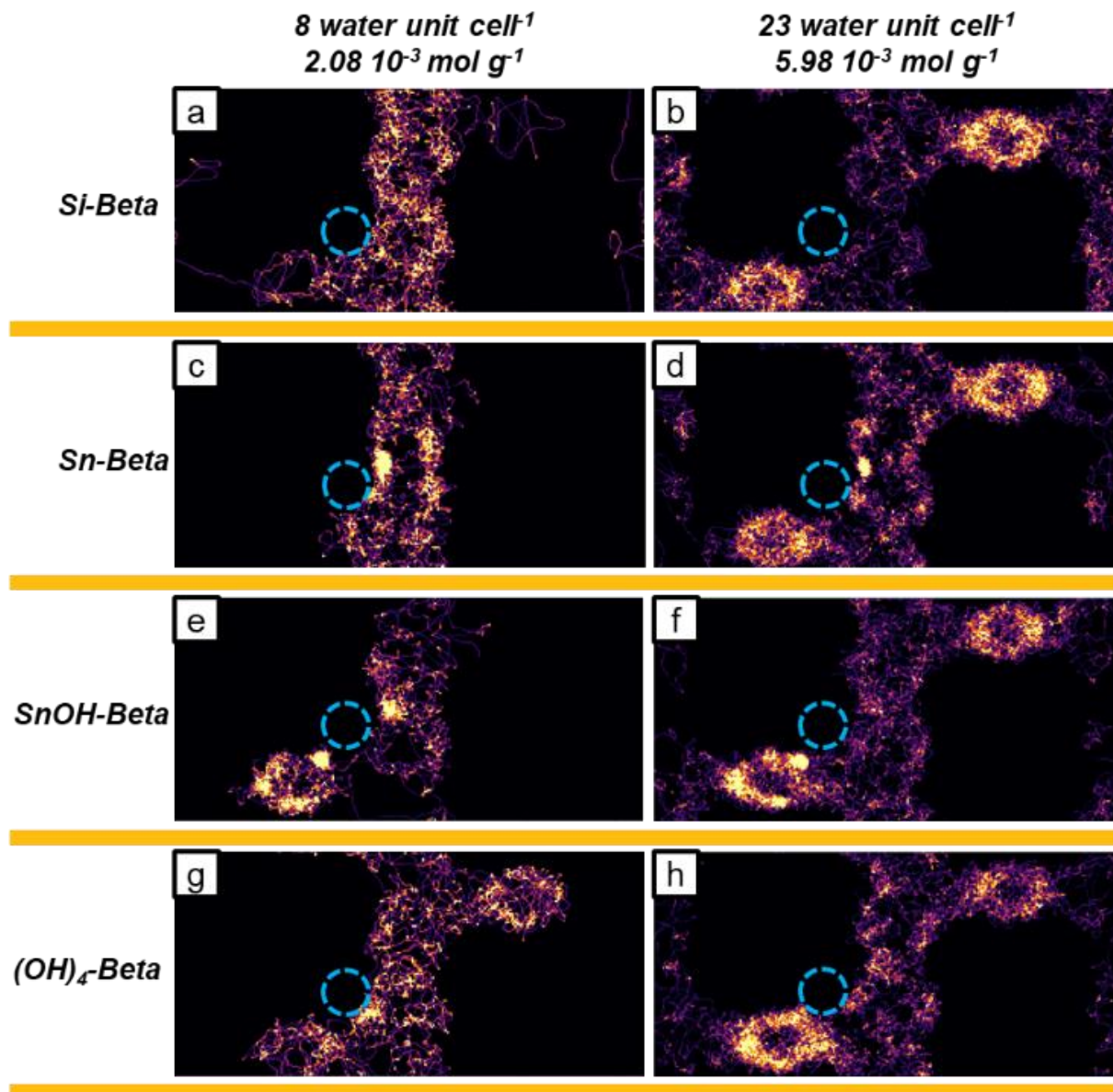
Figure 7.2 Time averaged water densities at lower (8) and higher (23) densities in waters per unit cell for each Beta material along the [010] crystal plane. Approximate location of the substituted defect indicated by light blue box. Views along the [100] plane are provided in APPENDIX F.

Qualitative differences in water trajectories as observed during simulations provide the first indication of unique water structures, which are included as characteristic snapshots and time averaged trajectory heat maps along two lattice vectors (APPENDIXD F). These depict the formation of water chains, hyper-conjugated clusters, and cross-linked networks which emerge among the defect types. It is important to keep in mind that the fixed unit cell size prevents size

extensivity of low-density water structures which may agglomerate into water dimers, trimers, and multi-mers at lower densities, especially in Si-Beta where no nucleating defects exist. As a result, detailed characterization of the gas-phase low density limit (1-3 water molecules per unit cells) is difficult as at a density of 1 water per unit cell, it is impossible to form water dimers without considering multiple unit cells. Thus, for Si-Beta at densities of 1-3 water molecules per unit cell, diffusing monomers, dimers, and trimers of water are observed. Beginning as low as 4 waters per unit cell, water molecules begin to disperse along the [100] pore direction. This is most apparent at a density of 8 waters per unit cell, where the heat density map from APPENDIX F. shows the predominant density of water in a single [100] pore with some diffusion of individual gas-phase water molecules in the surrounding space. This well-defined chain has been reported in previous classical MD literature on siliceous zeolites[236], [237]. Despite appearing to uniformly fill the pore along [010], water molecules prefer configurations closer to the pore walls, with a noticeable decrease in density in the pore center, due to favorable van der Waals interactions.  As water densities increase, filling of the perpendicular pore structure begins, while the [010] water chain persists. This crosslinking behavior has also been previously reported. Even at a density of 23 waters per unit cell, close to the expected bulk density of liquid water, non-uniform filling of pore space is still observed, where denser packing of water molecules as described by Siepman[249] must result. While these results for Si-Beta are not in themselves new, they provide confidence in the use of BEEF-vdW to qualitatively capture the physical properties of confined water and demark a comparison with the more exotic defects.

The Sn-beta defect material provides are marked contrast to Si-Beta, where low water densities are characterized by hyperconjugation of water molecules on the Lewis acidic Sn. It has been widely reported that adsorption of more than one water molecule per Sn site is common in gas phase catalysis, however the degree of conjugation under a range of solvent conditions has not been examined.  Even up to a density of 5 waters per unit cell, there is no indication of chain formation as observed in Si-Beta, and even at 8 waters per unit cell there is separation of water clusters between periodic boundary conditions as evidenced by the snapshots. Density plots show nearly complete localization to the [010] pore with regions of high density at the image center, directly interacting with the Sn atom, indicating inviscid water molecules hyper-conjugated to the Sn center. As water density increases and the filling of perpendicular pores and crosslinking

through intersections begins to occur, the higher density regions of localized water is still apparent at 23 waters per unit cell.

Hydrolysis of the Sn cation to form SnOH is accompanied with a framework silanol[113], [197]–[199], which introduce both Lewis acid and weak Bronsted acid character at the same site. A hydroxyl ligand extends into the [100] pore, with framework silanol nestled in the [010] pore, with the metal cation accessible to both pores. Consequently, all three sites (hydroxyl ligand, exposed Sn cation, and framework silanol) adsorb water. Similar to Sn-Beta, formation of water chains is not observed until higher densities near 15 waters per unit cell, as hyperconjugation of water around the three binding sites is observed, again further evidenced by time-averaged plots which demonstrate higher density regions around the Sn. Two high density spots are seen, which correspond to the clustering of water around the hydroxyl ligand and framework silanol, which are in opposite pore environments, with additional interaction directly with the Sn cation. These high-density regions persist at a density of 23 waters per unit cell where hyperconjugation of water around the intersection spanned by the three binding sites is observed.

Removal of the Sn site and terminating the four oxygens produces a silanol nest defect, which provides the most contrast to Sn-Beta and SnOH-Beta. Densities below 5 waters per unit cell, there is strong interaction with each silanol nest, which results in a high degree of localization in water structuring. Beyond saturation of the nest, a transition into chainlike water structures, like Si-Beta, with exploration of the [100] pores observed to a visibly greater degree than for Si-Beta. This greater degree of expansion may be due to silanols providing additional flexibility to the water network at this density and allowing for fewer water molecules to form the [010] chain, effectively providing additional water molecules to the network. There is no visible clustering observed for the silanol nests, indicating that the silanol groups mediate transient hydrogen bonds that do not significantly localize water. It is noted, that uniform filling of the [100] pore is observed at a density of 8 waters per unit cell, which could indicate a higher density of water throughout the diameter of the pore, possible due to a larger hydrogen bond network which compensates the weaker van der Waals interactions with the pore walls. This is; however, not observed at the highest density of 23 waters per unit cell, where the centers of the [010] and [100] pores are not uniformly filled, and no clustering is observed. In fact, the time averaged density plots of Si-Beta and (OH)4-Beta look nearly identical at a density of 23 waters per unit cell, indicating the strong

interactions with silanol nests have been attenuated, and the water network has adopted a more transient dynamic structure.

While not rigorous in their own respect, a careful analysis of the physical trajectory data can provide insights and generate hypotheses which can be further tested through more quantitative characterization methods such as the thermodynamic, network approach, and connection to experiment through OH stretching peaks. The four Beta materials behave radically differently, with Si-Beta observing no formal clustering except the formation of transient dimers and trimers, Sn-Beta forming hyperconjugated water structures which persist at all water densities, SnOH-Beta which also forms persistent water structures at all adsorption sites, and finally $(OH)_4$-Beta where initial strong interactions with silanol nests at low density is attenuated and begins to behave similarly to the transient nature of Si-Beta.

The intensive Helmholtz free energy of water in Beta described relative to the chemical potential of water vapor at 300K and $P/P^0$ of 0.05. The Helmholtz free energy of the reference state is:

$$a_{ref}\left(300K, 0.05\frac{P}{P^0}\right) = E_{DFT} + TS_{I.G.} - kTln\left(\frac{P}{P^0}\right) \tag{7.5}$$

Where $E_{DFT}$ is the total energy of a gas phase water molecule, $S_{I.G.}$ is the ideal gas entropy obtained from partition functions (estimated to be 188 J mol$^{-1}$ K$^{-1}$). The Helmholtz free energy of water in Beta is then described with the following expression

$$A_w\left(300\ K, 0.05\frac{P}{P^0}\right) = (<E_{ZW}> - <E_Z>) - TS_{ZW} - a_{ref}N \tag{7.6}$$

Where $<E_{ZW}>$ is the averaged total energy from AIMD of water and the zeolite, and $<E_Z>$ is the averaged total energy from AIMD of the empty zeolite framework. $S_{ZW}$ is the entropy of water and the zeolite, but the entropy of the zeolite upon loading with water is identical to the empty zeolite as evidenced by APPENDIX F. Therefor $S_{ZW} = S_W$ which is the entropy of water in the framework calculated from the vibrational density of states. This is then referenced to the bulk chemical potential expressed as the pure-component Helmholtz free energy of water vapor.

The Grand potential of water can be expressed as $\Omega_W = A_W - \mu_W N$. If water in the zeolite is in equilibrium with its bulk reference state, $\mu_W = \mu_{ref}$ and changes in the bulk chemical potential reflect changes in the grand potential. Thus, our choice of referencing the Helmholtz free energy to the bulk pure component free energy also reflects the grand potential which in Figure 7.3d shows stable water clusters in defected Beta. As the chemical potential is varied, as shown in

APPENDIX F. as relative chemical potentials decrease corresponding to lower pressures of pressures of the reference state, only water densities lower than 1 water per unit cell are stable for both Si-Beta and the defected Betas. As the relative chemical potentials increase, the higher density water clusters become stable, and extended water structures in the defected Betas are observed.
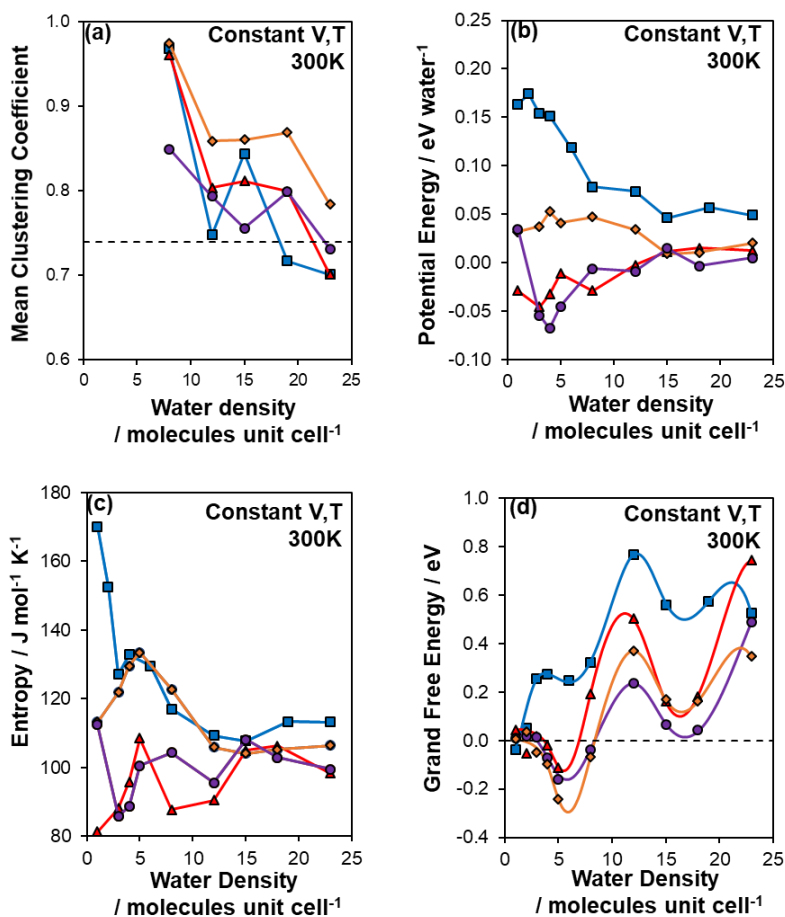


Figure 7.3 Clustering coefficients (a) and thermodynamic functions (potential energy, b; entropy, c; Grand free eneregy, d) as a function of water density for each defect: blue squares Si-Beta, red triangles Sn-Beta, purple circles SnOH-Beta, orange diamonds (OH)4-Beta.

The observed transition from isolated water chains into fully crosslinked water networks with bulk liquid-like mean clustering coefficient can be further characterized by a thermodynamic phase diagram to identify stable aqueous phases within the Si-Beta pores. The extensive Grand free energy Figure 7.3d is determined from potential energies of vapor phase water Figure 7.3b and entropy Figure 7.3c. We note that, although the resolution of the sampling statistics and associated density fluctuations obtained from such AIMD-based approaches is clearly limited by

accessible simulation time and limited unit cell sizes, the results are consistent with trends seen in classical simulations of water in carbon nanotubes[229], and other zeolite simulations[235]–[237], as well as our own experimental results (described below), and the trends are expected to be reliable. The chemical potential of water, in turn, can be directly determined from the extensive Helmholtz free energy (Figure 7.3d). In Si-Beta, two critical points corresponding to the equilibrium of chemical potentials between water in the zeolite and an external bulk reservoir is observed near 7 waters per unit cell, where individual water chains are observed, and 1 water per unit cell, a region where gas-like diffusion was observed. Additionally, a higher density equilibrium between 17 and 18 waters per unit cell, corresponding to a liquid-like phase is also observed. We remind the reader that the volume and temperature are fixed in these simulations, and the change in water density can be imagined as a change in the partial pressure of water in the reservoir, where a liquid-like condensed phase of water in Si-Beta may only be stable at pressures far greater than 1 bar, and at conditions where rupture of the zeolite framework is likely.

The combination of thermodynamic phase analysis, temporal heat maps, clustering coefficients, and physical inspection of trajectory data, as described above, provides powerful molecular-level insights into the behavior of water in defect-free Si-Beta material. In what follows, we extend these complimentary methods to explore the phase behavior of water in the presence of defects.

The addition of Sn, SnOH, and $(OH)_4$ defects is found to nucleate water clusters in pores containing the defects; however, the behavior of water at a range of densities both contrasts dramatically with Si-Beta, as well as between different defect identities. For all materials, a higher density stable phase of 16-18 water molecules was observed which corresponds to a liquid-like limit, in coexistence with the localized clusters specific to the defect identity.

Chemisorbed water and dense hydrogen-bound water, comprising a proposed cluster, are shown in Figure 7.2c for Sn-beta at low water densities (eight molecules per unit cell, which correspond to chain-like structures for defect-free Si-Beta). The entropy of water in Sn-Beta at this density is 20 J $mol^{-1}$ $K^{-1}$ lower than water in Si beta (Figure 7.3b) as water molecules are localized, which is also observed along the [100] plane provided in APPENDIX F. The localization of water is preserved at higher densities up to 23 waters per unit cell, where the defect-containing Sn beta pore retains a cluster of hyper-conjugated water near the Sn site (Figure 7.2d), with water of reduced density filling the surrounding pores. At this condition, the entropy is like that of Si-Beta.

Mean clustering coefficients in Sn-Beta are consistent across a range from 8 to 18 water molecules where they the approach the same bulk limit as Si-Beta. Critical points in the Helmholtz free energy for Sn-Beta show the existence of a stable phase of between 5-6 water molecules, consistent with the localized hyper-conjugated water structure observed.
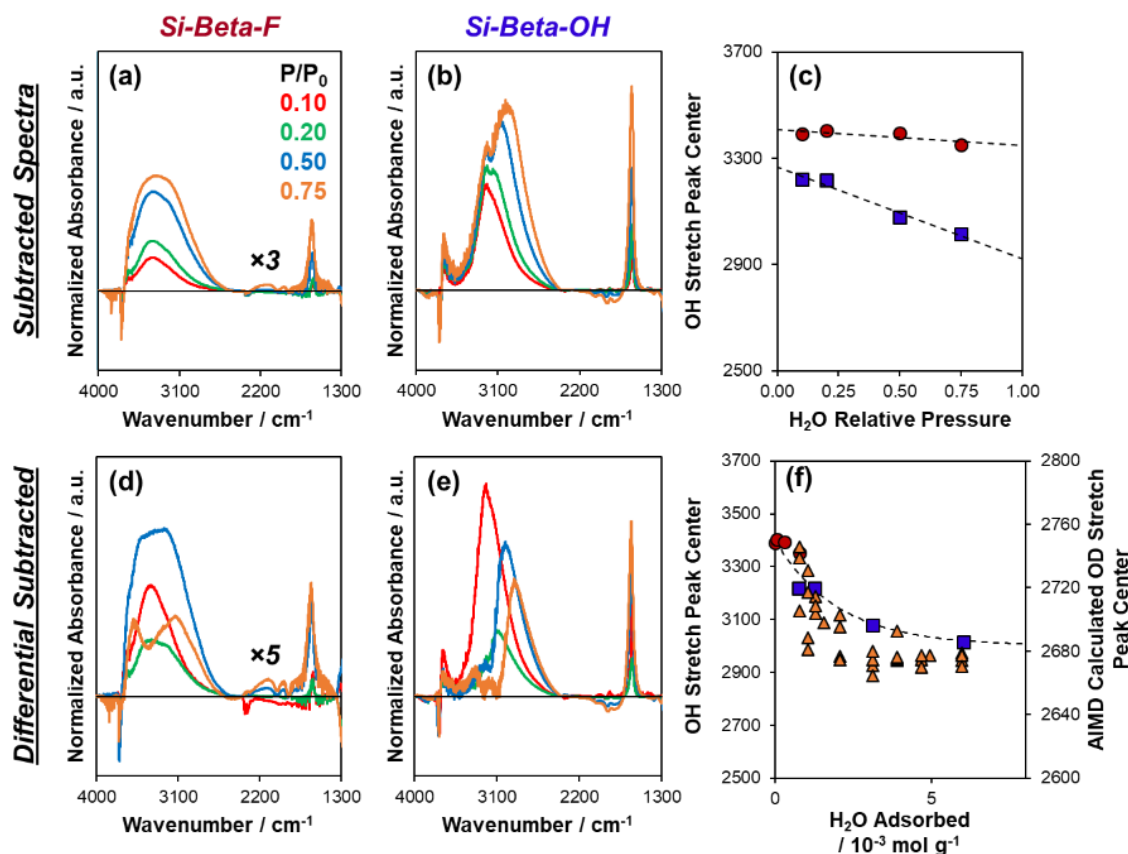


Figure 7.4 Subtracted and differential FTIR spectra for low defect (Si-Beta-F) and high defect (Si-Beta-OH) materials. Measured OH stretching peak centers versus H2O adsorption including AIMD predicted OD peak shifts (f).

SnOH-Beta at low water densities (8 waters per unit cell, Figure 7.2e) shows chemisorption and denser localized water both within the main (parallel) pore and a perpendicular pore due to interaction with the framework SnOH group as well as the adjacent SiOH group (additional structural data are provided in APPENDIX F). The entropy of water in SnOH-beta is like that of Sn-Beta, where chemisorption and dense hydrogen bonding reduce the totally entropy as compared to Si-Beta. The mean clustering coefficient of SnOH-Beta at 8 waters per unit cell is lower than even Si-Beta at the same conditions, which is due to the three adsorption sites (Sn heteroatom, framework silanol, and hydroxyl ligand) having similar adsorption energies as evidenced by the

trajectory data which show water molecules rapidly breaking and reforming hydrogen bonds between the different sites. As water density increases, chemisorption of water molecules to the SnOH group in a perpendicular pore is retained, where water molecules interact with the Sn center and hydroxyl ligand, and clustering at the framework silanol is not observed. This is more apparent when looking at the [100] plane in APPENDIX F The interactions between the framework silanol and water network are attenuated at higher densities, and localized clusters remain where the Sn heteroatom and hydroxyl ligand are exposed. The mean clustering coefficient of SnOH-Beta approaches a similar liquid-like limit, as Si-Beta and Sn-Beta. Critical points in the Helmholtz free energy enumerate stable phases very close to those in Sn-Beta, at low density 5-6 waters where localized clusters are observed.

In contrast to the two Sn defects, $(OH)_4$-Beta at low density (Figure 7.2g) has no strongly chemisorbed water molecules visually apparent.  This is despite a greater range of molecular diffusion than in Si-Beta, with exploration of the perpendicular pores as in SnOH-Beta and evidenced by an entropy nearly identical to that of water in Si-Beta after initial saturation of the silanol nest at densities below 5 waters per unit cell. Mean clustering coefficients across the full range of densities are greater than Si-Beta or the Sn defects, indicated greater correlation in hydrogen bonding between water molecules. These stronger hydrogen bond networks are mobile, and further indicate favorable water-zeolite interactions which contribute to the hydrophilicity of Beta zeolites synthesized with a high density of silanol defects.

To better understand the effect of silanol nest defects in forming more strongly correlated hydrogen bond networks, FTIR experiments were performed to characterize water correlation through perturbation of the OH stretching peak. Both high and low defect Si-Beta materials were synthesized, and the subtracted spectra were compared across a range of water partial pressures (Figure 7.4). For high defect materials, OH stretching peaks show higher stretching frequencies which indicate stronger hydrogen bonding interactions[253]. The peak shift magnitude increases with the amount of water adsorbed. The corresponding OD stretching peak shifts were calculated from AIMD, with peaks in APPENDIX F. which show a similar shift at higher water densities, as water uptake increases, indicating that the peak shifts correlate with the more strongly correlated hydrogen bonding network nucleated by silanol defects with favorable water-zeolite interactions.

## 7.4    Conclusions

The phase splitting observed for defected materials outlines the role of a local solvent structure within pores containing catalytic Lewis acid sites. The effect of water on the energetics of reactive intermediates and transition states in microporous materials can be envisioned to be largely local to the active site. This locally stable structure can be used to construct model solvent environments for future computational studies, based on stable phases of water. Instead of modeling a full pore-filling density of water, only the local solvent structure needs to be modeled explicitly, reducing the computational complexity of studying catalytic reactions in liquid phase. A more general scheme can be envisioned for other catalytically interesting materials with isolated active sites, where a local stability analysis with a limited numbers of water molecules can be performed to find the stable phase of clustered water. This local phase can then be used to model water interactions with reactive intermediates and transition states which would be consistent across a larger range of water densities.

# 8. COOPERATIVE EFFECTS BETWEEN HYDROPHILIC PORES AND SOLVENTS: CATALYTIC CONSEQUENCES OF HYDROGEN BONDING ON ALKENE EPOXIDATION IN ZEOLITES

## 8.1 Introduction

This chapter draws on techniques from CHAPTER 7 and CHAPTER 3 to estimate the entropy of adsorption using AIMD to treat anharmonic modes present when adsorbing in microporous environments. A suite of Ti-Beta catalysts were synthesized with a varying concentration of silanol nests $(SiOH)_4$ to study 1-octene epoxidation and $H_2O_2$ decomposition in the liquid phase, where turnover rates are 100-fold larger than those in defect-free Ti-Beta with the greatest densities of $(SiOH)4$ groups. IR spectra of $CD_3CN$ adsorbed onto Ti-Beta were used to distinguish adsorption onto Ti atoms, $(SiOH)_4$ groups, and siliceous pore walls. AIMD studies of $CD_3CN$ adsorption was necessary to determine reasonable values for the entropy of adsorption to each of the adsorption sites in Beta. These entropy of adsorption of CD3CN to Ti sites agrees closely with experiment (-85 versus -83 to -99 J mol$^{-1}$ K$^{-1}$, but enthalpies estimated from AIMD are lower (-20 versus -32 KJ mol$^{-1}$) measured experimentally. These CD3CN adsorption studies further validate the importance of incorporating anharmonic interactions when studying the gaseous adsorption of molecules to catalytic active sites in Lewis acid zeolites.

## 8.2 Methodology

Periodic, self-consistent density functional theory (DFT) using the Vienna Ab-initio Simulation Package (VASP) was used to model the enthalpy and entropy of adsorption in zeolite BEA.[82]–[84] The computational details and unit cell specifications were similar to those used previously to model ethanol dehydration in Sn-BEA. In short, the Bayesian error estimation

functional (BEEF-vdW) was used with projector augmented wave (PAW) pseudopotentials.[31], [86], [87] A plane wave cutoff of 520 eV was used with a single gamma point and spin polarization. A force criterion of 20 meV/Å was used for geometric convergence. Optimized BEA unit cell lattice constants were within 1.9% of that reported by the international zeolite database (IZA).[72]

Ab-initio molecular dynamics (AIMD) simulations were performed with VASP at 350 K in an NVT ensemble using a Nosé-Hoover thermostat and a timestep of 1 fs. $CD_3CN$ was modelled within these AIMD simulations. Each MD simulation was equilibrated for at least 5 ps, followed by a 25 ps production run. Enthalpy changes ($\Delta H_{CD_3CN,x}$) were defined as an ensemble average of the AIMD energies (E) for gas-phase $CD_3CN$ ($E_{CD_3CN(g)}$), the empty adsorption site ($E_x$), and $CD_3CN$ interacting with adsorption site $x$ ($E_{CD_3CN,x}$; e.g., Ti atoms)

$$\Delta H_{CD_3CN,x} = \langle E_{CD_3CN,x} \rangle - E_{CD_3CN(g)} - \langle E_x \rangle \tag{8.1}$$

where brackets denote an arithmetic averaging of accessible energies from the ensemble sampled by the thermostat.

The entropy of adsorbates was calculated using a two-phase thermodynamic model, which decomposes molecular trajectories into their translational, rotational, and vibrational degrees of freedom, expressed as the vibrational density of states (VDOS). Each VDOS was decomposed into their gaseous and solid components according to the original algorithm[153], [244], [245] and integrated to obtain entropies accounting for plasticity of the BEA framework, as previously applied in the BEA framework for ethanol dehydration. The TRAVIS molecular trajectory code was used to analyze the calculated trajectories[246]. Estimates of the entropy loss upon physisorption involved calculating the principal root-mean-square fluctuations of $CD_3CN$ from the AIMD trajectories[128]. Thus, the entropy loss from physisorption is primarily due to the reduction in translational degrees of freedom. As the adsorption enthalpies for CD3CN on Ti and $(SiOH)_4$ defects relative to physisorption are weak, the entropies of adsorption of $CD_3CN$ on Ti and $(SiOH)_4$ were calculated as the differential change in translational, rotational, and vibrational degrees of freedom relative to those calculated for the physisorbed state. This approach was necessary due to the difficulty in a direct AIMD method that describes absolute adsorption onto these sites from the gas phase. Thus, on Ti and $(SiOH)4$ defects, the entropy reduction is modified by the non-rigid modes calculated by AIMD as compared to the non-rigid modes for physisorption, including the root-mean-square fluctuations.

The T8 crystallographic T-site of BEA was used to represent substitutional doping by Ti and (SiOH)$_4$. The T8 site was chosen based upon previous reports of adsorbate stability at this site[198]. The Si atom occupying the T8 site was removed, and either the resulting vacancy was replaced with a Ti atom, or the four framework oxygen atoms were bound by hydrogen atoms to simulate a (SiOH)$_4$ site. Isolated SiOH defects were not considered computationally, as their formation at crystal grain boundaries and meso-scale defects precludes such sites from being constructed within a periodic unit cell. The simulated Si:Ti ratio within these calculations was 63:1, which corresponds to one Ti atom per unit cell.

## 8.3    Results and Discussion

Molecules of CD$_3$CN physisorb to Si-O-Si pore walls more weakly than to Ti atoms ( $\Delta H_{CD_3CN,Si-O-Si}$= -12 kJ mol$^{-1}$; versus $\Delta H_{CD_3CN,Ti}$ = -32 kJ mol$^{-1}$), as shown in Table 8.1, which is unsurprising as the adsorption of CD$_3$CN to Ti atoms involves specific Lewis acid-base interactions. As a result, entropy losses upon binding to siloxane regions are also smaller than those for Ti atoms ($\Delta S_{CD_3CN,Si-O-Si}$= -75; $\Delta S_{CD_3CN,Ti}$ = -83 to -99 J mol$^{-1}$ K$^{-1}$). The measured entropy lost upon adsorption to Si-O-Si is similar to estimates from AIMD simulations (-75 versus -67 J mol$^{-1}$ K$^{-1}$). Yet, calculated values of $\Delta H_{CD_3CN,Si-O-Si}$ are significantly larger than those measured (-22 versus -12 kJ mol$^{-1}$) and are identical to calculated values of $\Delta H_{CD_3CN,Ti}$. These systematic discrepancies between measured and calculated adsorption enthalpies likely reflect errors in the functional used to assess weak Lewis acid-base interactions. Notably, however, these calculations do seem to describe accurately the entropy for adsorption of CD$_3$CN to Si-O-Si and Ti sites.

Table 8.1 Adsorption Enthalpies and Entropies for CD3CN bound to Lewis acidic Ti atoms; SiOH Moieties, and to Si-O-Si on Ti-BEA-12.5 and Ti-BEA-F

| Sample | $\Delta H_{CD_3CN,Ti}$ (kJ mol$^{-1}$) | $\Delta H_{CD_3CN,SiOH}$ (kJ mol$^{-1}$) | $\Delta H_{CD_3CN,Si}$ (kJ mol$^{-1}$) | $\Delta S_{CD_3CN,Ti}$ (J mol$^{-1}$ K$^{-1}$) | $\Delta S_{CD_3CN,SiOH}$ (J mol$^{-1}$ K$^{-1}$) | $\Delta S_{CD_3CN,Si}$ (J mol$^{-1}$ K$^{-1}$) |
|---|---|---|---|---|---|---|
| Ti-BEA-12.5 | $-32 \pm 1$ | $-55 \pm 4$ | --[a] | $-83 \pm 5$ | $-150 \pm 10$ | --[a] |
| Ti-BEA-F | $-32 \pm 1$ | $-19 \pm 1$ | $-12 \pm 1$ | $-99 \pm 10$ | $-87 \pm 6$ | $-75 \pm 8$ |
| DFT Model[b] | $-20$ | $-41^c / -33^d$ | $-22$ | $-85$ | $-117^c / -134^d$ | $-67$ |

[a]CD$_3$CN physisorbed to Ti-BEA-12.5 was not spectroscopically observable at the pressure (0.46 kPa) and temperatures (373 – 423 K) used for van't Hoff analysis. [b]Estimated by ab-initio molecular dynamics at 350 K with one Ti or (SiOH)$_4$ per unit cell. [c]Corresponds to the adsorption of CD$_3$CN onto (SiOH)$_4$. [d]Corresponds to adsorption of three CD$_3$CN per (SiOH)$_4$ nest.

Ti-BEA-F contains primarily isolated SiOH that form through stochastic processes which introduce crystallographic defects during hydrothermal synthesis. Molecules of CD$_3$CN adsorb more weakly onto SiOH within Ti-BEA-F than (SiOH)$_4$ within Ti-BEA-12.5 ($\Delta H_{CD_3CN,SiOH}$ = -19 kJ mol$^{-1}$; $\Delta H_{CD_3CN,(SiOH)_4}$ = -31 kJ mol$^{-1}$). Moreover, CD$_3$CN bound to (SiOH)$_4$ within Ti-BEA-12.5 possess lower entropies than CD$_3$CN adsorbed to SiOH within Ti-BEA-F ($\Delta S_{CD_3CN,(SiOH)_4}$ = = -150 J mol$^{-1}$ K$^{-1}$; $\Delta S_{CD_3CN,SiOH}$ = -87 J mol$^{-1}$ K$^{-1}$). Notably, values of $\Delta S_{CD_3CN,SiOH}$ are similar to $\Delta S_{CD_3CN,Ti}$ because CD$_3$CN, when bound to isolated SiOH, are oriented into the pore of *BEA and likely possess similar vibrational entropic modes (e.g., frustrated translation, hindered rotation). AS mentioned above, we did not investigate AIMD simulations for the interaction of CD$_3$CN with isolated SiOH, because exact structure of these isolated defects within *BEA are not known.

AIMD simulations for a single CD$_3$CN adsorbed to (SiOH)$_4$ show similar enthalpic stabilities to those measured ($\Delta H_{CD_3CN,(SiOH)_4}$ = -41 versus -55 kJ mol$^{-1}$), yet underestimate the entropy lost upon adsorption ($\Delta S_{CD_3CN,(SiOH)_4}$ = -117 versus -150 J mol$^{-1}$ K$^{1-}$). It is possible, however, that silanol nests may stabilize the adsorption of multiple adsorbates, as the adsorption geometries of molecules onto (SiOH)$_4$ have not previously been elucidated. Indeed, the adsorption of three CD$_3$CN to (SiOH)$_4$ results in AIMD-derived $\Delta H_{CD_3CN,(SiOH)_4}$ values that are similar to those predicted for a single CD$_3$CN molecule, suggesting that there is minimal enthalpic change (per molecule) for the adsorption of one or multiple CD$_3$CN to (SiOH)$_4$. Further, the adsorption of
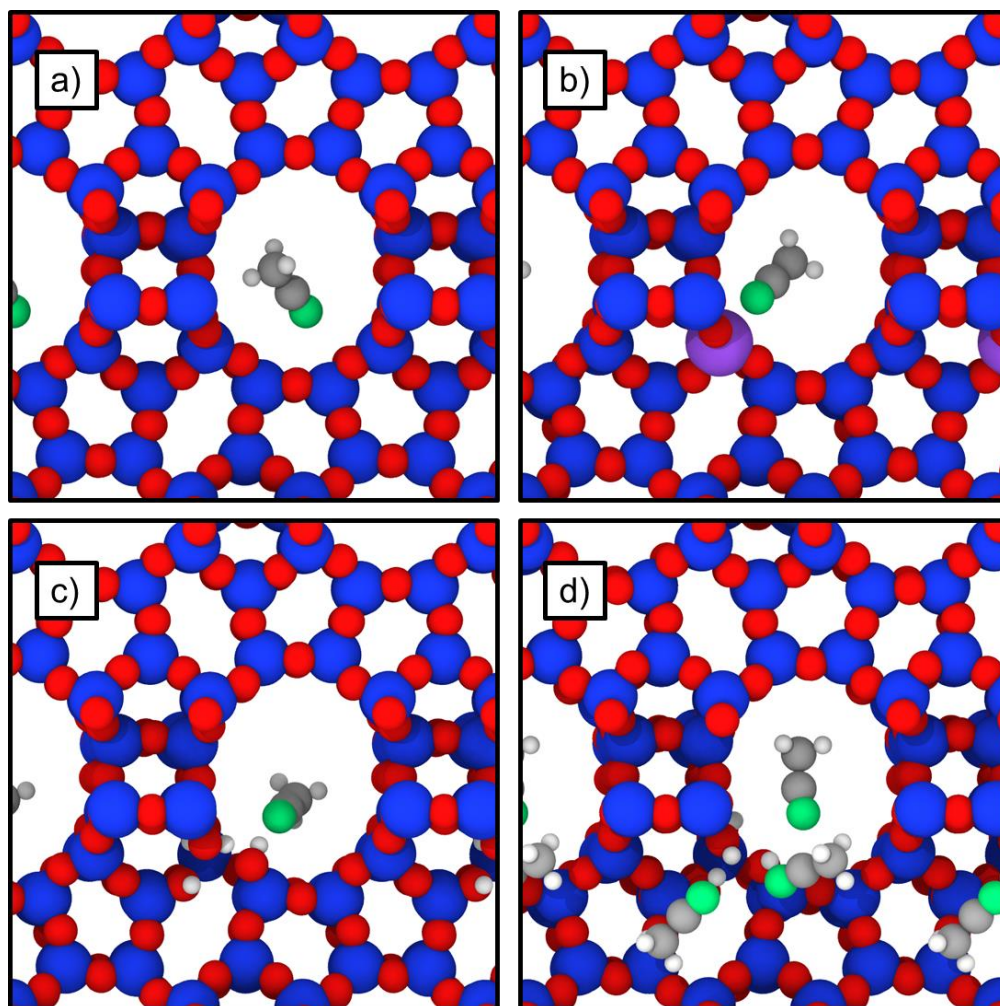
Figure 8.1 Representative geometries from AIMD of interactions between a single $CD_3CN$ adsorbed onto (a) Si-O-Si, (b) Ti, and (c) $(SiOH)_4$. Figure S12d represents the adsorption of three $CD_3CN$ onto $(SiOH)_4$, where the $CD_3CN$ on the bottom-left corner of the figure is interacting with the small side channel resulting from the vacancy within $(SiOH)_4$. Color scheme for atoms: hydrogen (white), carbon (gray), nitrogen (green), oxygen (red), silicon (blue), titanium (purple).

three $CD_3CN$ molecules onto $(SiOH)_4$ does, in fact, show average entropies lost upon adsorption that are like those measured (-134 versus 150 J mol$^{-1}$ K$^{-1}$).

The representative geometries for $CD_3CN$ bound to $(SiOH)_4$ (Figure 8.1d) shows that a molecule of $CD_3CN$ is projected perpendicularly to the 12-membered pore of *BEA in a vacancy produced from $(SiOH)_4$. The peak position of $\nu_s(-CD_3)$ is blue shifted with increasing $\theta_{CD_3CN,(SiOH)_4}$, which reflects the interaction between the $-CD_3$ moiety and an electron-rich moiety (e.g., the -OH in $(SiOH)_4$).[67] This shift in $\nu_s(-CD_3)$ supports the results from AIMD, which suggest that $CD_3CN$ may adsorb into $(SiOH)_4$ perpendicular to the main pore of *BEA in the space

afforded from $(SiOH)_4$. The adsorption of $CD_3CN$ perpendicular to the 12-membered ring of *BEA results primarily in a significant loss of rotational entropy. This interpretation (i.e., the loss in rotation entropy) is supported also by estimates for entropies of adsorption, calculated using the model of Campbell *et al*[68] that closely match the experimental values.

The differences in $\Delta S_{CD_3CN,(SiOH)_4}$ and $\Delta S_{CD_3CN,Ti}$ primarily reflect the differences in the frustrated translational and hindered rotational entropy of $CD_3CN$ adsorbed to $(SiOH)_4$ or Ti atoms, respectively. Decomposition of the translational and rotational contributions to the adsorbate entropy within the AIMD simulations (Table 8.2) show that the difference between $\Delta S_{CD_3CN,(SiOH)_4}$ and $\Delta S_{CD_3CN,Ti}$ is consistent with the difference in rotational entropy of $CD_3CN$ bound to Ti atoms versus $(SiOH)_4$. The entropy of $CD_3CN$ bound to Ti atoms and $(SiOH)_4$ was estimated also using the Sackur-Tetrode equation and the corresponding partition functions that describe frustrated translation and hindered rotation. Estimates for the entropy of hindered rotations of $CD_3CN$ bound to Ti provide a value of 40 J mol$^{-1}$ K, when the maximum degree of rotation is assumed to be 40 degrees. This estimate compares favorably to the measured difference in adsorption entropies determined experimentally ($65 \pm 10$ kJ mol$^{-1}$) and predicted from AIMD simulations (49 kJ mol$^{-1}$ K$^{-1}$) for $CD_3CN$ bound to $(SiOH)_4$ in comparison to Ti sites, which further suggests that the adsorption of $CD_3CN$ onto $(SiOH)_4$ results in the strong interaction of $CD_3CN$ with the side channel afforded by $(SiOH)_4$.

Table 8.2 Entropy Estimates for CD3CN bound to (SiOH)4 and Ti atoms at 360 K.

| AdsorptionSite | $S_{trans}$ (J mol$^{-1}$ K$^{-1}$) | $S_{rot}$ (J mol$^{-1}$ K$^{-1}$) | $S_{trans} + S_{rot}$ (J mol$^{-1}$ K$^{-1}$) |
|---|---|---|---|
| Ti[a] | 57 | 38 | 95 |
| (SiOH)$_4$[a] | 29 | -- | 29 |
| Si-O-Si[b] | 120 | 135 | 255 |
| Ti[b] | 123 | 123 | 246 |
| (SiOH)$_4$ (single CD$_3$CN)[b] | 112 | 96 | 208 |
| (SiOH)$_4$ (three CD$_3$CN)[b] | 116 | 27 | 143 |

[a]Calculated using the Sackur-Tetrode equation. [b]Calculated by decomposing the transitional and rotational contributions of entropy from the DFT model.

Values of $\Delta H_{CD_3CN,Ti}$ reflect the formation of a Lewis acid-base adduct and may seem small in comparison to $\Delta H_{CD_3CN,SiOH}$; however, the strength of these interactions are consistent with

measured heats of reaction for complexes of $CH_3CN$ and homogeneous Lewis acids.[254]–[256] For example, $SbCl_5$ is used for comparisons of Lewis acidity,[257] and the heat of formation of the $CH_3CN–SbCl_5$ is -59 kJ mol$^{-1}$ (in dichloroethane).[254] Moreover, $SbCl_5$ is a stronger Lewis acid than Ti alkoxides (e.g., $Ti(OiPr)_4$), which may possess electron affinities similar to framework Ti atoms in Ti-BEA. As such, the measured values of $\Delta H_{CD_3CN,Ti}$ on Ti-BEA-12.5 and Ti-BEA-F seem reasonable, and differences between these zeolitic materials lay predominantly in the density and types of SiOH or $(SiOH)_4$ sites.

In summary, the principal differences between the Ti-BEA do not reflect to differences between the electronic properties (i.e., electron affinity) of the active sites among these materials, therefore, any catalytic differences that may arise must relate to differences in the properties of the active intermediates, mechanism for epoxidation or density of $(SiOH)_4$.

## 8.4    Conclusions

Epoxidation of alkenes by $H_2O_2$ and $H_2O_2$ decomposition reactions occur at framework Ti atoms within Ti-BEA catalysts, and turnover rates for epoxidation depend strongly on the presence, density and proximity of the epoxidation transition states to $(SiOH)_4$ moieties. Turnover rates for 1-octene epoxidation increase monotonically with the density of $(SiOH)_4$ in Ti-BEA, where materials containing ~5 $(SiOH)_4$ (unit cell)$^{-1}$ possess rates that are 100-fold greater than Ti-BEA that are nearly defect free. Rates of $H_2O_2$ decomposition, however, are insensitive to $[(SiOH)_4]$ across the Ti-BEA tested here. These differences in epoxidation catalysis do not reflect variations in the electron affinity of the Ti active sites among the series of Ti-BEA, because neither measured adsorption enthalpies for $CD_3CN$ to Ti atoms nor ligand-to-metal charge transfer energies for Ti-OOH and Ti-$(\eta^2$-$O_2)$ species differ with the density of $(SiOH)_4$. Mechanistic interpretations of epoxidation rates measured as a function of reactant concentrations, in combination with *in situ* UV-vis measurements and radical-clock reactions with cis-stilbene, show that the mechanism for epoxidation and the identity and electronic properties of reactive Ti-OOH intermediates do not vary with $(SiOH)_4$ density.

# 9.  ETHANOL DEHYDRATION IN H-BETA WITH PARTIALLY CONDENSED SOLVENTS

## 9.1  Introduction

Conversions of biomass products typically include higher molecular weight reactions with significant water content,[15], [18], [258] which introduces additional complexity where the presence of water and elevated temperatures influence catalysts stability and the kinetics of chemical reactions. Dehydrations are one family of reactions of interest for deoxygenation of biomass feedstocks, including catalytic upgrading to fuels[259]. Ethanol dehydration has been studied on oxide surfaces[118], [120], [260], [261], polyoxometalate (POM) clusters[147], Lewis acid zeolites[198], and Brønsted acid zeolites[262], [263]. For propanol dehydration in H-ZSM-5, Density Functional Theory (DFT) techniques indicate acid sites protonate water molecules introducing hydronium ions in solution to catalyze unimolecular and bimolecular dehydration mechanisms.[264] While these hydronium ions catalyzed dehydration, it was shown that water inhibits dehydration rates by stabilization of reactive intermediates prior to the transition state relative to the transition state.[265] The strong adsorption of alcohols to Brønsted acid sites relative to water indicates that protonated acids will be bound to acid sites, even at aqueous conditions.[225] Experimental $^1$H-$^{29}$Si CP MAS NMR studies have also shown direct evidence that at low water loadings of one water per acid site that protons are bound to the zeolite framework, but hydronium ions are formed at higher water loadings, where hydronium ion interactions are attenuated as water clusters grow in size.[224] The clustering of water molecules at acid sites has been shown to affect the stability of reactive intermediates and transition states; however, the thermodynamic stability of water mixtures with reactive intermediates is not well understood, and the structure of transition states upon solvation is not well understood for mechanisms in which water molecules directly interact with the transition states.

The H-ZSM-5 catalyst is commonly chosen for dehydration studies; however, the large number of crystallographic T sites make it difficult to model computationally. The Beta framework with a smaller number of distinct T sites and intersecting straight pores has a smaller number of atoms per unit cell, making it a reasonable choice for combined DFT and experimental studies. Ethanol dehydration can be measured in a dry as well as nearly condensed solvent environment, where initial turnover rates can be measured. Thus, ethanol dehydration in H-Beta is an ideal probe

reaction to study how the presence of water molecules influences both reactive intermediates and transition states.

Clusters of water molecules around acid sites nucleated by a hydronium ion have been discussed as forming in H-ZSM-5, which are corroborated by DFT studies showing how increasing numbers of water molecules stabilizes the hydronium ion in the pores.[224] While these studies describe the structure of pure water in a porous environment, the structure of water cluster in the presence of reactants has not been addressed. To provide adsorption constants and free energy activation barriers in solvent, it is necessary to provide a consistent thermodynamic reference which is representative of the experimental kinetic process. From previous work on water structuring in Sn-Beta and (OH)$_4$-Beta, stable tightly nucleated water structures were found to coexist in equilibrium with an extended weakly nucleated water network referenced to a bulk water chemical potential. This local solvent structure of stable water is equilibrated with a known reference chemical potential of water, allowing for thermodynamic definitions of mixing between adsorbed reactant molecules and the local stable phase of water to be unambiguously assigned and compared to gas phase adsorption.

Here, a local stable phase of clustered water molecules around acid sites in H-Beta is defined, which includes 6 water molecules based on a local phase diagram calculated from Ab-Initio molecular dynamics (AIMD). Once this stable phase is defined, ethanol monomers and ethanol dimers corresponding to the most abundant reactive intermediates (MARIs) can be coadsorbed at water clusters, and the number of water molecules belonging to the local can be varied, in order to determine the number of water molecules belonging to a mixed cluster containing ethanol molecules at a fixed density. The adsorption energy of ethanol into the cluster can then be compared to ethanol in the gas phase. Transition states for bimolecular dehydration are calculated in the gas phase, in agreement with previous reports, which are then used to define suitable collective variables to perform a metadynamics simulation of ethanol dimers to directly evaluate the structure of ethanol dehydration transition states in the presence of a local clustered solvent. It was found that ethanol displaces water molecules in the clustered phase, where ethyl groups face outward from the cluster. The adsorption energies of ethanol monomer and ethanol dimers in H-Beta pores are lower than in the gas phase, reflecting the enthalpic penalty of removing water molecules from the clustered phase. Water molecules can participate in the dehydration transition state, and de-localized hydronium ions allow transition states to re-orient in geometries that

maximize their van der Waals contacts with the surrounding pore environment. These studies provide a rigorous thermodynamic treatment which can directly evaluate reaction energetics in the presence of protic solvents. It was found that the confining environment both provides a confining pore to stabilize reactive intermediates and transition states, but a protic solvent screens the charge effects of acid sites in the framework providing more enthalpically favorable configurations for transition states that maximize van der Waals contacts with the surrounding pore.

## 9.2    Methodology

### 9.2.1    Static DFT calculations

Static DFT calculations are performed using VASP[81], [84], [87] and are similar to those we have reported previously[198]. The BEEF-vdW functional was used along with a 520 eV cutoff energy, and a force convergence criteria of 0.02 meV $\text{Å}^{-1}$. The entropies of reactive intermediates was calculated using the Campbell-Sellers equation[154], [266], where adsorbates were treated like a 2-D gas. From AIMD simulations adsorbates in H-Beta were found to have large diffusion distances, due in part to interaction with the acidic proton. The Campbell-Sellers equation may not be rigorously accurate for all gas phase adsorbates, and additional AIMD and usage of the VDOS or decomposition of harmonic frequencies into translational and rotational partition functions would be more accurate; however, the goal of calculating gas phase energetics is to identify what types of reactive intermediates and transition states may be relevant under solvating conditions, and not to provide be absolute agreement with experimental kinetics.

### 9.2.2    Ab-initio molecular dynamics simulations

AIMD simulations were also performed with VASP, with an NVT Nose-Hoover thermostat[89], [242]. Water structures were heated, and then equilibrated at 373 K for at least 10 ps at a timestep of 1 ps. Production runs were performed for 20 ps. All hydrogen atoms were deuterated. The same settings were used upon introducing ethanol to the system. The potential energy and temperature of the systems were monitored and found to fluctuate normally around the mean temperature and energy. The entropy of solvated water molecules was more complicated than reported previously in Sn-Beta. The acidic proton could transfer among water molecules, preventing the participation of individual degrees of freedom for each water molecule. It was assumed that the proton entropy is constant, and so at each timestep the acidic proton was removed.

This was performed in a python code which detects which water molecule is a hydronium, and then removes the hydrogen with the longest O-H bond length from the simulation. At most, only one proton exists in the simulation, so each water molecule is scanned to find the hydronium ion. The water molecules could now be unambiguously partitioned, and then root-mean-squared (RMS) diffusion of each water molecule was calculated according to the technique of Alexopoulos et al.[128] where the 3-D translational entropy of water could be determined. The same technique was used to calculate the translational entropy of ethanol molecules introduced into the system.

### 9.2.3   Metadynamics

Metadynamics simulations were performed in VASP, similarly to the AIMD. The thermostat and masses were the same as the AIMD calculations. The positions and trajectories from the AIMD thermodynamic calculations were used to ensure a well-equilibrated simulation. The collective variables (CVs) were defined to be a carbon-oxygen bond distance of a carbon belonging to one ethanol and a carbon-oxygen bond distance of the same carbon and the oxygen atom of the second ethanol. Thus, at the transition state both C-O bond distances would be equivalent. Both types of C-O bonds are constrained to a maximum bond distance of 5 Å as the primary interest is to study the structure of the transition state, and not an excessively large number of reactant and product states. The constraints are relaxed enough to allow for restructuring of solvent around the C-O bonds, this provides space for additional water molecules to participate in the transition states. Thus, the choice of control variables does not bias the mechanism by which C-O bonds are broken and reformed in the simulation. Gaussian hills were added every 70 fs and had a height of 50 meV and width of 75 meV. These parameters were chosen based on test calculations in the gas phase where the approximate width and height of the barriers would ensure the Gaussians provided a slowly varying differential change in the free energy surface to ensure that an approximately canonical ensemble is preserved as the energy of the system is raised to the transition state. Convergence of the algorithm would occur when the potential energy surface is filled to become flat, which would be indicated by multiple crossings of the transition state. Analysis of the free energy surface is performed using a python code that maps each Gaussian from VASP into a matrix to be plotted. To identify the minimum energy path between basins, a modified version of Dijkstra's search algorithm was used. In short, the free energy surface is discretized into a graph data structure where points of a specified height are connected to neighboring points. By specifying

a range of start and end nodes from basins in the free energy diagram, Dijkstra's algorithm is a shortest-path tree algorithm that then finds the minimum total energy path to connect the reactant and product basin. The advantage of Dijkstra's algorithm is it can be generalized into higher-dimensional space by increasing the number of neighboring nodes.

## 9.3 Results and discussion

### 9.3.1 Acid sites in H-Beta

Among the 9 T-sites in Beta, it is proposed that deprotonation energies are independent of their position in the framework[212]; yet, the size of the ethanol molecule requires a consideration of all T-sites to determine a lowest energy reference configuration. Each T-site has four adjacent framework oxygen atoms, which can face distinct pore environments in Beta, either within channels or facing intersections. As a result of this, every T-site/oxygen pair was screened by adsorption of ethanol. The maximum deviation in binding energies for ethanol was 0.21 eV, and if we compare only the lowest energy oxygen site for each T-site, the maximum deviation in ethanol binding energy is 0.08 eV. At reaction conditions of 373K, kT is 0.03 eV, and the difference in binding energies among all acid sites is 2.7 times the thermal energy. The most stable T-site for ethanol adsorption was found to be the T9 site, but any of the T-sites could be candidates based on the narrow distribution of binding energies. A table of all energies can be found in the APPENDIX G.

### 9.3.2 Gas phase dehydration mechanisms in H-Beta

Gas phase ethanol dehydration in Beta was performed to discriminate between the alkoxide or associative mechanism[147] as well as determine what role excess water has in stabilizing the alkoxide and associative mechanisms to provide intuition to develop solvation models in partially condensed conditions, as well as provide a consistent basis for comparison upon solvation. From experimental kinetics, the most abundant surface intermediate is solvated ethanol monomers, and thus all free energies will be reported relative to ethanol monomers. The three lowest free energy
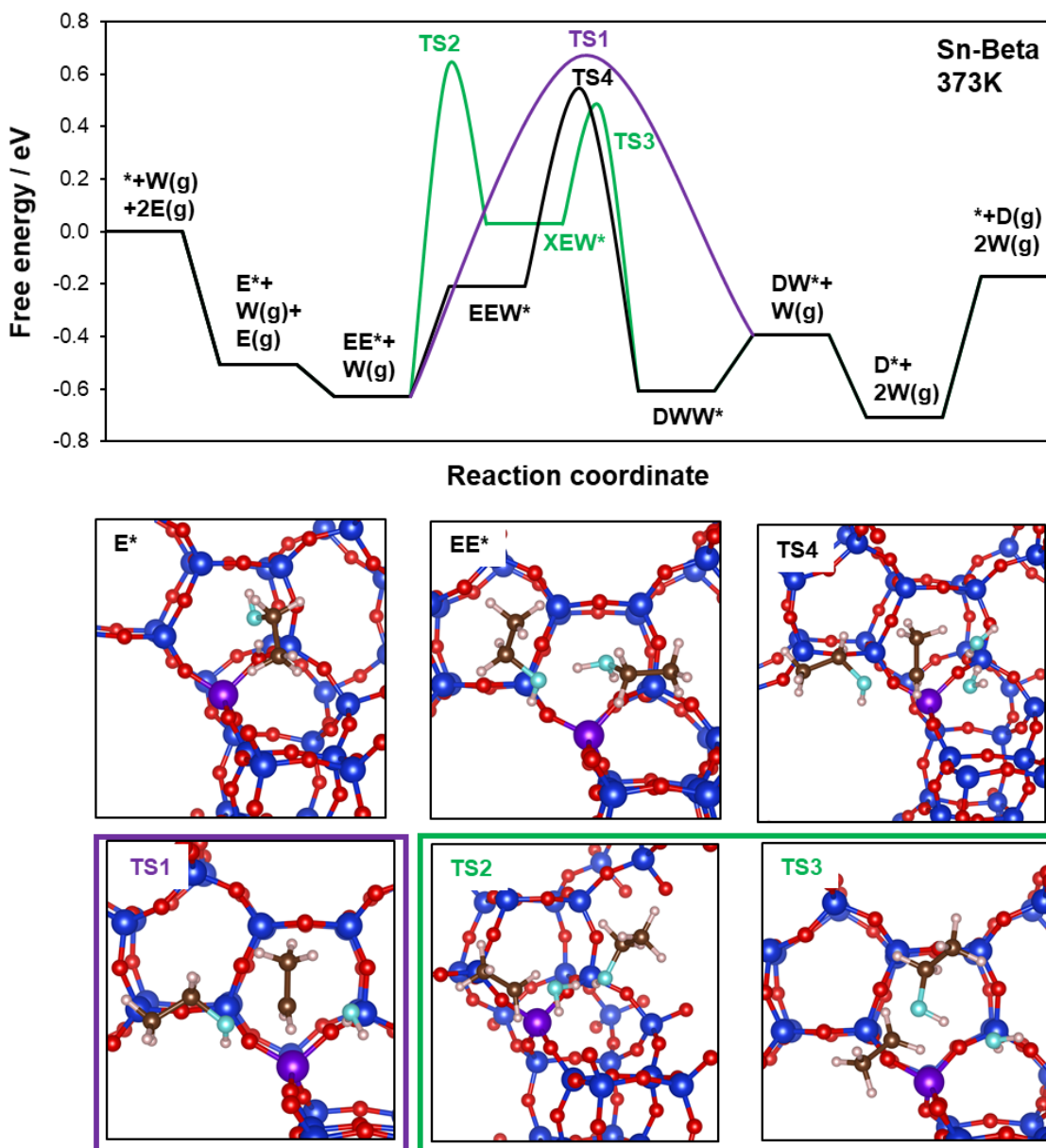
Figure 9.1 Reaction network for ethanol dehydration in H-Beta in the gas phase. Lowest energy pathway is shown in black which includes the EEW* intermediate. The direct associative pathway without water assistance is shown in purple through EE*. The ethoxide mediated pathway is shown in green, with water assisted $S_N2$ substitution for DEE formation and ethanol assisted ethoxide formation.

of activation pathways are shown in Figure 9.1, where diverging transition states are color-coded. Images of selected reactive intermediates and transition states are provided in the figure subsets.

Ethanol first adsorbs to the Bronsted proton, without protonation of the hydroxyl group. Adsorption of ethanol is exergonic, by nearly 0.5 eV at 373 K, which is expected for alcohol

adsorption onto strong protic acids. Upon coadsorption of a second ethanol molecule, the first ethanol is protonated and forms a hydrogen bond to the second ethanol molecule. This protonated dimer has been discussed previously in solid acids[147], [267], where adsorbing alcohols are protonated. The protonated dimer can undergo a conformational change to adopt an $S_N2$ transition state with a free energy barrier of 1.18 eV when referenced to the ethanol monomer MASI (TS1). A diethyl ether (DEE) molecular and water is formed, with regeneration of the Bronsted proton back to the framework. This proton, by the nature of the inversion of the SN2 transition state will be transferred to a different oxygen site than considered for ethanol adsorption. From the tetrahedral configuration of each Al site, only two oxygen atoms are accessible, where the third oxygen is accessible in the perpendicular pore. Despite the movement of protons at the transition state, the presence of protic water and ethanol molecules allows facile migration of protons to any of the four framework oxygen atoms. As we have referenced adsorption to the most stable oxygen atom, it is reasonable that any protons shuttled by reaction can be re-equilibrated to their most stable configuration rapidly. A similar argument was presented for the position of framework hydrogens at hydrolyzed open sites for Lewis acid zeolites. DEE and water readily desorb from the acid site and complete a catalytic turnover.

In the presence of water, it is hypothesized that coadsorbed water molecules at that the acid site may participate in the $S_N2$ transition state. TS1 includes a 6-member ring transition state structure spanned by the protonate dimer to the adjacent framework oxygen atoms with donate and accept protons. 6-member ring transition states generally stable; but at a high coverage condensed water it is likely that larger ring transition states could be formed. The coadsorption of a protonated ethanol dimer with an additional water molecule has an endergonic adsorption energy, as the enthalpy of adsorption is slightly positive (+0.08 eV) as compared to adsorption of water on a bare acid site (-0.65 eV) or coadsorption of water and an ethanol monomer (-0.67 eV). This change in enthalpy of adsorption reflects the stability of the protonated dimer, which is broken up by the additional water forming a protonated ethanol-ethanol-water trimer. Despite the endergonic formation of a protonated trimer, the $S_N2$ transition state to form DEE and two water molecules (TS4) has a lower apparent free energy of activation relative to an ethanol monomer MASI by 0.13 eV as compared to the protonated dimer (TS1). This indicates that water molecules coadsorbed to acid sites can lower the barrier for ethanol dehydration by reducing ring strain and proton transfer to the adjacent framework oxygen.

The alkoxide mechanism involves an SN2 substitution forms an ethoxide, which can then undergo an additional $S_N2$ substitution to form DEE and water. An alkoxide can be formed from a protonated dimer there an ethyl group is transferred to the framework producing water. The apparent free energy barrier for this elementary step (TS2) is 0.09 eV higher than the ethanol-ethanol-water trimer elementary step (TS4). The final state ethoxide-ethanol-water (XEW*) intermediate is less stable that gas phase ethanol and water by 0.03 eV. The alkoxide cannot participate in hydrogen bonding due to its alkyl group, which results in a physisorbed ethanol-water dimer which does not interact with the alkoxide. The alkoxide-ethanol-water complex can then undergo an $S_N2$ substitution reaction to form DEE and two water molecules. The apparent free energy barrier is lower than that of the alkoxide formation barrier, as once the ethanol molecule is activated, it will readily react.

### 9.3.3   Solvation of ethanol in H-Beta

To interrogate the role solvent in stabilizing the ethanol MASI and transition states, it is necessary to identify stable solvent phases with varying densities of solvated ethanol molecules. From experimental measurements, only ethanol monomers and ethanol dimers at acid sites are observed under reaction conditions, thus limiting the range of ethanol conditions to be simulated. A comprehensive phase diagram of mixing thermodynamics of water and ethanol at acid sites in Beta is beyond the scope of this work and would be better accomplished with classical potentials. From the study of water clustering in Sn-Beta, the local nucleated phase of water at aluminum acid sites could be determined as a consistent reference phase when comparing the free energies of solvating ethanol molecules from the gas phase into water clusters at acid sites. Water densities were varied from 5-8 waters per unit cell, which was chosen based on the size of local clusters in Sn-Beta and $(OH)_4$-Beta. Entropies were calculated by taking RMS deviation from each AIMD simulation[128]. A phase diagram for intensive water free energy is provided in (APPENDIX G), which identifies 6 water molecules as the local intensive free energy minimum. A larger phase diagram spanning the ranges considered in Sn-Beta and $(OH)_4$-Beta would not provide additional detail, as it would extend to the low-density gas-phase and bulk liquid limits.

Throughout each simulation, the acidic proton solvated into the water cluster, hydrogen bonding to the surrounding waters. This solvated proton has been observed by other groups studying aluminum zeolites where the presence of multiple water molecules solvates acidic

protons.[224], [268] Proton shuttling is facile, which complicates entropy calculations as each proton transfer is a collision causing the angular velocity to be discontinuous in the reference frame of individual water molecules. Therefore, the acidic mobile proton was eliminated from each simulation, and only the RMS diffusion of water molecules were included in entropy simulations. This implicitly assumes the entropy of the solvated proton is the same across water densities. This approximation is justified as the contribution of the individual proton entropy is small relative to the system entropy dominated by water diffusion. The RMS diffusions also assumes the rotational and vibrational degrees of freedom to be constant across the range of water densities. The similarity in vibrational degrees of freedom is also likely a good approximation across a narrow range of water densities, as vibrational state frequencies will shift in the gas phase and solid phase limits. As the phase diagrams provided here are across a smaller range of similarly solvated states, the vibrational degrees of freedom are similar across the range of conditions considered here. The consistency of rotational states is more contentious, as it is likely that even with small changes in density the rotational states may change more substantially. The discontinuity in rotation due to proton shuttling presents a complication in evaluating rotational degrees of freedom in the traditional AIMD methods such as the VDOS or non-rigid moments of inertia. One potential technique would be re-scaling of the moments of inertia before the collision, and translating the moment of inertia after each collision back to their initial configuration to smooth the moments of inertia and allow partition function methods for calculating rotational entropies.

Once the local stable phase of water was determined, an ethanol molecule was introduced into the system. A series of AIMD simulations were performed with a fixed number of ethanol molecules and a varying number of water molecules from 6 down to 1 per unit cell. The entropy of ethanol upon solvation was also calculated as the RMS diffusion. Adsorption of solvated ethanol was calculated according to equation 9.1

$$\Delta G_{EtOH\ ads} = G_{EtOH\ aq.} - G_{zeolite} - G_{EtOH\ gas} - N_W G_{W\ solv.} \qquad (9.1)$$

Where the free energy of adsorption of ethanol into the solvent phase is calculated as the total free energy of ethanol and water solvated in the zeolite pores relative to the free energy of the zeolite framework (which is formally equivalent to the potential energy, as the vibrational states are considered insensitive to the density of water and ethanol at this range), the free energy of gas phase ethanol, and the free energy of the number of water molecules in the clustered state. Thus, this represents a gas phase ethanol molecule adsorbing into a cluster of water at the active site. To
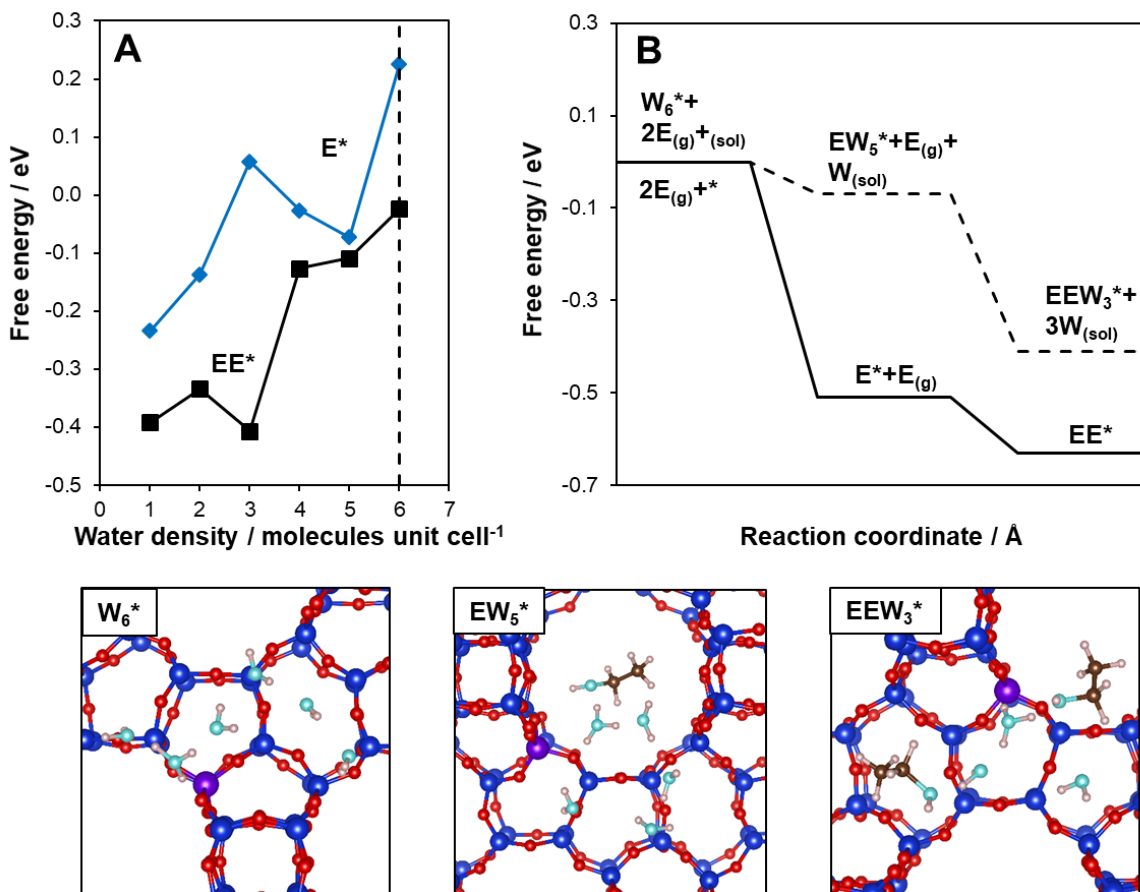
Figure 9.2 Solvated thermodynamics of ethanol monomers and ethanol dimers in H-Beta. (a) Thermodynamic phase diagram for coadsorption of water and ethanol in Beta at varying water density per unit cell based on translational entropy. (b) Free energy diagram comparing adsorption of ethanol in the gas phase and ethanol adsorbed in a solvating environment incorporating enthalpy and entropy losses due to water being expelled from the solvent phase.

maintain thermodynamic consistency, only the translational degrees of freedom for ethanol gas are considered to keep the entropy of solvated ethanol and gas phase ethanol consistent. This process could also be repeated for an ethanol dimer, shown in Figure 9.2.

The adsorption of ethanol monomers and ethanol dimers shed water molecules from the local nucleated phase an extended solvent phase away from the acid site, present in the two phase region discussed in the Sn-Beta and $(OH)_4$-Beta study. The dashed line in Figure 9.2a indicates the stable pure water local phase of 6 water molecules. Ethanol monomers adsorb exergonically as the water cluster size decreases, indicating the non-polar ethyl groups of ethanol reduce hydrogen bonding in the mixed cluster state. As ethanol adsorbs more exergonically in the gas phase than water at the acid site, as the water cluster size decreases, the mixing of ethanol and

water becomes less stable as the fraction of water in the solvent phase approaches 0. Despite this end behavior at very low water densities, a locally stable phase of a ethanol monomer and 5 water molecules ($EW_5$*) is observed in Figure 9.2a. The adsorption of solvated ethanol can be compared with gas phase adsorption, such as shown in Figure 9.2b where solid lines indicate a bare acid site which can adsorb ethanol, like that as shown in Figure 9.1. Dashed lines indicate adsorption into the solvent where the solvated active site is represented as the local pure-phase water cluster ($W_6$*), a non-local solvent phase of mobile water molecules (sol) and gas phase ethanol. The ethanol monomer adsorbed state is expressed as the locally stable $EW_5$* mixed cluster determined from Figure 9.2a, where there is one water molecule ejected from the local cluster into the de-localized mobile solvent phase $W_{(sol)}$. The mobile solvent phase is assumed to also be in equilibrium with the external bulk water chemical potential, and the addition of another water into this phase will not change the bulk chemical potential. A second ethanol molecule can then adsorb into the cluster, with a local mixed stable phase of $EEW_3$*, and the adsorbed state can be expressed as $EEW_3$* with 3 water molecules ejected into the extended mobile water phase ($3W_{(sol)}$).

Solvated ethanol monomers adsorb weakly to acid sites as opposed to gas phase ethanol (+0.58 eV), which reflects the compensating effect of disrupting hydrogen bonds in the pure water cluster upon adsorption. Although ethanol can participate in hydrogen bonding with the surrounding water molecules, the ethyl tail protrudes into the adjacent pore so that only the hydroxyl end participates in the water cluster. This is shown in the subset image in Figure 9.2, $EW_5$* shows the ethanol monomer on the periphery of the mixed cluster. Although this is a single image of the AIMD simulation, in general ethanol is not fully mixed into the center of the cluster. The ethanol dimer state when solvated adsorbs +0.22 eV more weakly than the gas phase dimer, where again the disruption of hydrogen bonding decreases the ethanol dimer binding energy relative to the gas phase. The single frame image in Figure 9.2, $EEW_3$* shows a central hydronium ion, with the two ethanol molecules on the periphery, with hydroxyl groups participating in hydrogen bonding with the central waters and hydronium.

By constructing a thermodynamic phase diagram for local water nucleation in H-Beta, the thermodynamics of ethanol adsorption in a solvating environment were identified provides a fundamental understanding of how gases in nearly condensed solvating environment interact with acid sites. These models; however, do not address the solvent structure at the transition state for ethanol dehydration. From the experimental kinetics, it is the apparent transition state energy

referenced to the ethanol monomer state which defines the turnover rate of reaction. To include the effects of solvent re-organization at the transition state, a metadynamics simulation of ethanol dehydration in the solvating environment was performed which can then describe the solvent structure environment across the full reaction mechanism.

### 9.3.4 Ethanol dehydration Metadynamics

A metadynamics calculation was performed based on a representative density of 5 waters and an ethanol dimer. The collective variables chosen were one ethanol C-O bond distance, and a C-O' bond, which is the distance between the same carbon and the oxygen belonging to the second ethanol. In the reactant state, shown in Figure 9.3a, the C-O bond distance is ~1 Å, and the C-O' bond is longer, as the two ethanols are free to diffuse around as they choose. At the transition state (region B in Figure 9.3), both the C-O and C-O' bonds are nearly equidistant for the $S_N2$ substitution. In the product state (region C in Figure 9.3), The C-O' bond is ~1 Å as the ethyl group has transferred to the other ethanol molecule. The C-O bond is longer now, as the product water
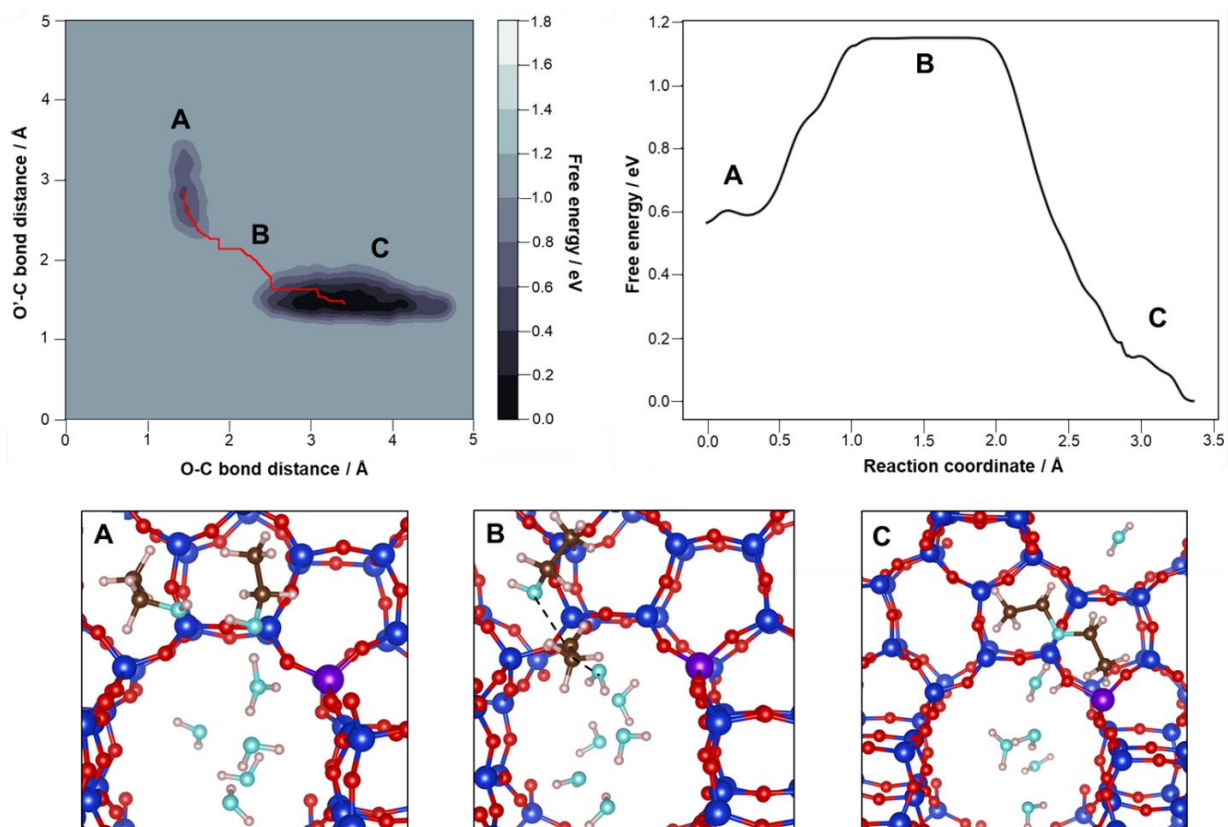


Figure 9.3 Metadynamic free energy map of ethanol dehydration in H-Beta. Upper left, minimum energy path spanning the two collective variables described in text. Upper right, free energy path in red from upper left mapped in 1-D showing the activation barrier for ethanol dehydration

and carbon in DEE can now diffuse around as they choose. As these collective variables do not specify how the $S_N2$ transition is adopted, it does not preference how many water molecules participate in the transition state. As shown for gas phase dehydration Figure 9.1 one or more water molecules can participate in the dehydration transition state to lower the reaction free energy barrier.

The metadynamics simulation is not fully converged, as the potential energy basins have not been completely sampled, and the potential energy is not flat. This is an ongoing calculation, but the preliminary results show one barrier crossing. The transition state region (B) is flat, because hills have not been added to the transition state as there has been only one crossing. Thus, the minimum energy path in the region of B should not be overinterpreted as these regions will fill and become more peaked with additional simulation time. Region A shows the ethanol dimer on the periphery of the water cluster, with the hydronium ion solvated into the water cluster. Region B shows the single transition state obtained so far. This transition state does not involve any water molecules, and shows a similar bimolecular $S_N2$ substitution as found in the gas phase, where the C-O and C-O' bond lengths are nearly equidistant, and the angle of attack is nearly 180°. The solvated transition state differs from the gas phase as the substitution no long must occur near the Al atom. In gas phase, because the acidic proton is not solvated, a proton must be transferred back to the basic oxygen in order to maintain charge on the zeolite framework. Due to the presence of solvent, the charge is effectively screened, which is reflected in the large mobility afforded to the hydronium as it can transfer through the cluster. As a result of this, the geometry of the transition state is affected and able to better form favorable van der Waals contacts with the surrounding pore, as opposed to the gas phase where the non-solvated proton restricts the geometry of the transition state.

The final state includes a DEE molecule which weakly interacts with the surrounding water cluster. DEE has two non-polar ethyl groups and cannot donate hydrogen bonds. DEE can accept a hydrogen bond from water, but in general its is less correlated to the water cluster than the ethanol dimers. As a result of this, there may be a penalty for the reverse reaction, as ethanol dimers are more stabilized by the water cluster than DEE. If DEE is not stabilized by the water clusters, there is an enthalpic penalty for DEE to incorporate into the cluster, for the reverse reaction to occur. For the reverse reaction, DEE and water must adopt a specific configuration for an ethyl group to transfer to water forming a protonated ethanol dimer. In the initial state, ethanol dimers can both

accept and donate hydrogen bonds making it more favorable for them to adopt the correct configuration to initiate the $S_N2$ substitution and form DEE. Though not fully converged, the initial metadynamics simulation already outlines key difference between dehydration in gas phase versus in the presence of condensed solvents.

## 9.4    Conclusions

Ethanol dehydration is readily catalyzed by protons in solid acids; yet the role of condensed solvents in stabilizing reactive intermediates and transition states is poorly understood. While previous literature reports have discussed the solvation of protons and experimental kinetics of other alcohol dehydrations in aqueous phase, the precise structure and function of how water and the zeolite framework interaction is shown here to be different as opposed to the gas phase. From AIMD simulations and metadynamics, in conjunction with static DFT calculations, the ability of local clustered water around acid sites to stabilize transition states can be characterized in detail. In gas phase, ethanol dimers are protonated by the zeolite framework and undergo a $S_N2$ substitution to form DEE and water. The free energy barrier of this transition state can be lowered through a catalytic water molecule reducing the ring strain induced by the requirement that a proton be returned to the acid site to balance charge. This fundamentally tethers the transition state to the pore wall where the acid site is located. The coupled mechanism, which occurs by first forming an alkoxide at the acid site and then undergoing $S_N2$ substitution is less stable that the associative mechanism initiated by 0 or 1 catalytic waters.

To study the effect of solvent on the ethanol dehydration reaction, a thermodynamic phase diagram of stable nucleated phase of water was constructed which identified clusters containing 6 water molecules to be locally stable. Ethanol molecules could then we included in the clusters, with their free energy of adsorption defined in terms of the stable pure water cluster energy and gas phase free energy of ethanol. It was found that an $EW_5^*$ mixed cluster and $EEW_3^*$ mixed cluster was locally stable for ethanol monomers and dimers, respectively. The displacement of hydrogen bonds upon adsorption of ethanol reduces the adsorption energy of ethanol relative to the gas phase, and the ethyl groups of ethanol force ethanol molecules to the periphery of the water clusters. The acidic proton is solvated and forms a hydronium ion which can transfer to adjacent water molecules.

From unconverged metadynamics, ethanol dehydration in solvent occurs unconstrained by the necessity of proton transfer to the zeolite framework, as the water cluster can screen electrostatic interactions. This imparts the solvated transition state additional flexibility in being able to maximize its van der Waals contacts with the surrounding pore environment. In the product state DEE is unable to participate in hydrogen bonding, and therefor in solvent there is an additional enthalpic penalty to bring DEE into the water cluster to initiate the reverse reaction and re-form the ethanol dimer.

Microporous materials in addition to stabilizing reactive intermediates and transition states through confinement, also influence the stability of solvents entrained within their pores. This confined solvent can in turn influence the structure and stability of the reactive intermediates and transition states differently than in the gas phase. Here we have shown how for the ethanol dehydration reaction, water has a non-innocent effect in changing the conformation of transition states and reactive intermediates, which provides addition methods for tuning the catalytic reactivity of solid acids through engineering of favorable solvent interactions in addition to confinement.

# 10. ZINC PROMOTION OF PLATINUM FOR LIGHT ALKANE DEHYDROGENATION: INSIGHTS INTO CATALYST GEOMETRIC AND ELECTRONIC STRUCTURE

## 10.1 Introduction

The recent surge in gas production from shale formations throughout the United States presents a tremendous opportunity to develop catalytic innovations that efficiently transform hydrocarbon resources (i.e., methane, ethane, propane, butanes) directly into value-added chemicals and fuels with reduced environmental impact by selectively activating paraffinic C-H bonds[1]. Although various routes to synthesize alkene and aromatic building block molecules over metal-containing catalysts by dehydrogenation[2] and cyclization[3], respectively, have been well-studied, issues regarding long-term catalyst stability, product selectivity, and turnover rates (TOR) still remain problematic[4-5]. Many of the challenges associated with developing new materials to overcome these limitations can only be addressed at the molecular level.

Noble metals, such as Pt, are well-known for exceptional performance in hydrocarbon catalysis, particularly for hydrogenation and isomerization reactions, due to their affinity for paraffinic C-H bonds[2]. While structure-insensitive reactions, such as alkene hydrogenation and alkane dehydrogenation can occur on isolated Pt sites, it has been shown that larger Pt ensembles, such as nanoparticles, catalyze structure-sensitive reactions, including cracking and hydrogenolysis[6-10]. Since the reactivity of metal nanoparticle surfaces is determined by the electronic states through the valence *d*-bands, which is a region in the partial density of states (DOS)[11-12], one way we may alter the electronic structure of these surfaces, and hence, their reactivity, is by alloying or promoting the surface with various co-adsorbed atoms or molecules that can influence the availability and energies of the valence electrons to form chemical bonds with adsorbates. For example, the addition of Zn or Sn to Pt-containing catalysts has led to

improved alkene selectivity during alkane dehydrogenation[13-15]. It has been suggested that these ad-metals modify the electronic properties of the noble metal sites by donating electron density and weakening the adsorption of $\pi$-bonded alkenes; thus, inhibiting the formation of coke precursors[15-18]. Recent experimental work by Childers et al.[19] has also shown that Zn addition to supported Pd catalysts can enhance propylene selectivity during propane dehydrogenation (PDH). The improved catalyst stability is attributed to the formation of a PdZn alloy with isolated Pd surface sites that eliminate the structure-sensitive hydrogenolysis pathway[20].

Experimentally, the electronic structure of metal nanoparticles on heterogeneous catalysts can be accessed by using $L$ edge, resonant inelastic X-ray scattering (RIXS) to monitor the occupancy of the $d$-band filled and unfilled states[21-22]. As a hard X-ray, two-photon process, RIXS permits the elucidation of electron excitations between inner-shell and valence levels within a specific element under working reaction conditions, thus making it possible to directly probe the surface chemistry at metal active sites and map the entire $d$-band spectrum to identify electronic descriptors of catalytic activity. As shown for the Pt $L_3$ edge in Figure 10.1, absorption of a photon with energy $\Omega$ promotes a 2$p$ electron to an unoccupied state in the 5$d$ valence shell and leaves behind a core hole that is subsequently refilled by an electron from filled orbitals. Filling of the core hole results in an emitted photon whose energy is dependent on the energy of the filled orbital. With a high-energy resolution spectrometer, the energy ($\omega$) of the fluorescent photon from the filled 5$d$ orbital can be determined (e.g., Pt $L\beta_5$ transition). The difference in energy between $\Omega$ and $\omega$ represents the overall energy transfer of the system ($\Delta E$).
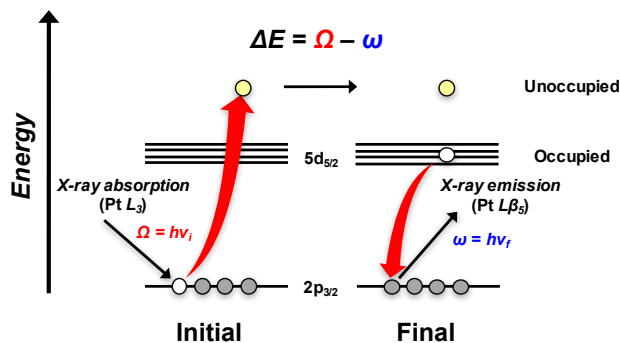


Figure 10.1 RIXS Energy Scheme for Pt 2p$\leftrightarrow$ 5d Transitions

Many of the valence-to-core X-ray emission studies to date have been focused on the $K$ edge ($s \rightarrow p$) for inorganic and bioinorganic metal complexes to examine metal-to-ligand charge transfer as

well as changes in bonding and anti-bonding states[23]. However, the *K* edge cannot access chemical information on the valence *d* electrons that are relevant for catalysis. While RIXS has successfully been applied at the *L* edge for 3*d* and 4*d* transition metal complexes to examine crystal field splitting and orbital occupancy[24-26], there are relatively few studies on 5*d* metals[22, 27-28], such as Pt, that examine the electronic structure of supported noble metal nanoparticles and explain their importance as heterogeneous catalysts.

Here, we show how the capabilities of RIXS analysis can provide a unique fingerprint for the catalytic properties of Pt/SiO$_2$ and PtZn/SiO$_2$ dehydrogenation catalysts. Using ethane dehydrogenation (EDH) as a probe reaction, we show how this spectroscopic characterization of metal nanoparticle valence electronic states and composition can be correlated with kinetic measurements of catalytic performance to describe how Zn addition to Pt/SiO$_2$ modifies the metal nanoparticle geometric and electronic surface structures to affect C$_2$H$_4$ selectivity and TOR per surface Pt atom. We further establish that DFT calculations are capable of accurately predicting the RIXS spectra for Pt and PtZn, which contain additional electronic structural information for these materials; thereby, complementing and strengthening existing *d*-band models.

## 10.2  Methodology

### 10.2.1  Static DFT calculations

All calculations were performed by using self-consistent, periodic density functional theory (DFT), as implemented within the Vienna Ab-Initio Simulation Package (VASP)[48-51]. The Perdew-Burke-Ernzerhof exchange-correlation functional was used for all calculations[52]. The projector augmented wave (PAW) core potentials developed from PBE calculations were used[53-54]. For the Pt and PtZn bulk lattice optimizations, a cutoff energy of 600 eV and a 20x20x20 Monkhorst-Pack K-point grid with Methfessel-Paxton smearing was used to accurately reduce Pulay stress. Lattice constants are converged to within a force criterion of 0.02 eV Å$^{-1}$, which resulted in lattice parameters of 3.98 Å for Pt and 2.88 Å and 3.53 Å for the *a* and *c* unit vectors, respectively, of PtZn. For DOS calculations on the Pt and PtZn bulk, a cutoff energy of 1000 eV and a 30x30x30 Monkhorst-Pack K-point grid was implemented along with tetrahedron Blöchl smearing. The projected density of state (PDOS) was lm-decomposed according to the Wigner-Seitz radius provided by the PAW potential. Close packed surfaces corresponding to the (111) for

Pt as well as the (110) and (101) surfaces for PtZn were cut from the lattice optimized bulk. Each surface was a 5 layer slab with 10 Å vacuum. Cell dimensions for the Pt surface were 5.62 Å, 5.62 Å, and 29.18 Å along the *a*, *b*, and *c* unit vectors, respectively, including vacuum. Cell dimensions for the PtZn(110) surface were 4.08 Å, 3.53 Å, and 28.16 Å along the *a*, *b*, and *c* unit vectors, respectively, including vacuum. Cell dimensions for the PtZn(101) surface were 4.58 Å, 2.88 Å, and 28.93 Å. A comparison of the predicted RIXS planes for the (110) and (101) surfaces is included in Section 4 of the Supporting Information. The bottom two layers were fully constrained and the rest of the slab was allowed to relax to a force criterion of 0.02 eV Å$^{-1}$. An energy cutoff of 400 eV, 6x6x1 Monkhorst-Pack K-point grid, and Methfessel-Paxton smearing was found to minimize Pulay stress and converge total energies. DOS calculations were performed with a 1000 eV cutoff energy, 8x8x1 Monkhorst-Pack K-point grid, and tetrahedron Blöchl smearing by using the relaxed surface geometries.

## 10.2.2 PtZn surface terminations

For the tetragonal PtZn unit cell, the (110) and (101) terminations are more closely packed than the (111) termination. The (110) and (101) terminations have different surface lattice distances, and both were considered in Figure S8. The RIXS planes were similar for both surface terminations although the high intensity peak was slightly broader for the (110) surface.

## 10.2.3 Theoretical RIXS distributions

To provide additional insight into the relationship between the *d*-band DOS and the shape of the RIXS planes, a simplified DOS model was developed. The occupied and unoccupied electronic states were approximated as rectangular distributions subject to the following constraints applied independently to the occupied and unoccupied states: (i) the DOS must be non-zero at the Fermi energy ($E_f$) to maintain metallic character of the band, (ii) the band centers of the occupied and unoccupied states of the rectangular DOS must reflect the corresponding *d*-band centers of the true DOS, and (iii) the integral of the complete rectangular and true *d*-band DOSs must be equivalent to accurately reflect the total number of electrons in the band. As each rectangle was individually fitted by this procedure, the band filling of Pt was also preserved. A schematic representation is shown in Fig. S9 for the PtZn alloy.

By varying the width of the unoccupied DOS and maintaining a constant height, the RIXS tail became more prominent, but at a constant intensity. The unoccupied DOS were decomposed further into two rectangles, where the second rectangle had a lower height. This lower height approximated a DOS distribution where the density of unoccupied states decreased at higher energies relative to $E_f$. The high intensity peak remained throughout this distribution; however, it decreased similarly to the experimental spectra at increasing energies. We note that the $d$-DOS in a DFT calculation can only be carried out to a finite number of states, and high energies are less accurate to the true band structure where additional scattering processes become more likely. Thus, the longer and higher intensity tails in the experimental spectra were likely due to a combination of higher energy $d$ states and potentially scattering across other unoccupied orbitals above the $d$ states. The structure of the high intensity peak also changed, although it appeared to be less sensitive to the continuum of unoccupied states.

To probe the influence of the width of the occupied states on simulated RIXS spectra, the width of the occupied states for the rectangular DOS developed in Fig. S10(c) was increased by manually adjusting the lower bound of the rectangle at constant height. While this adjustment changed the number of electrons in the band, it allowed for a simplified analysis which showed that the location of the energy transfer peak ($y$-axis in Fig. S10) was modulated by the occupied state energies. Decreasing the width of the rectangle shifted the energy transfer to a lower value, while increasing the width shifted the energy transfer to a higher value. Thus, the energy separation at which bond formation is favorable is modulated by the occupied states, while the tails of the distribution appear to be more strongly correlated to the density of unoccupied states (Fig. S11).

## 10.3 Results and Discussion

Energy differences between the unoccupied and occupied Pt $5d$ states for reduced Pt/SiO$_2$ and PtZn/SiO$_2$ catalysts were examined with *in situ* RIXS by monitoring the Pt X-ray absorption and emission signals in fluorescence under a flow of 3% H$_2$ and balance He (50 ml min$^{-1}$) at 100 °C. The X-ray emission intensity was measured as a function of the incident and emitted photon energies for the Pt $L_3$ XANES and $L\beta_5$ regions, respectively. Additional transitions, such as the $3d_{5/2} \rightarrow 2p_{3/2}$ ($L\alpha_1$), $3d_{3/2} \rightarrow 2p_{3/2}$ ($L\alpha_2$), and $4d_{5/2} \rightarrow 2p_{3/2}$ ($L\beta_2$) edges, can also be examined by selectively measuring these emission energies with the RIXS spectrometer. Thus, RIXS is able to

produce an *in situ* map of the full *d*-band DOS for the supported metal nanoparticles with far greater detail than is possible by using other spectroscopic techniques.

The experimentally measured RIXS spectra for Pt/SiO$_2$ and PtZn/SiO$_2$ in 3% H$_2$ at 100 °C are presented in Figure 10.2 as two-dimensional contour plots that show the energy transfer ($\Delta E$) as a function of the incident photon energy ($\Omega$). For Pt/SiO$_2$, the maximum RIXS intensity (red region) occurred at $\Omega = 11,564$ eV with an energy transfer of 4.0 eV. Addition of Zn to Pt/SiO$_2$ shifted the maximum RIXS intensity to higher energy transfer by approximately 2.0 eV at 11,566 eV ($\Delta E \sim 6$ eV), with a high intensity tail that extended along the diagonal to 11,572 eV. The higher energy transfer transitions were more intense for PtZn compared to Pt due to the larger transition probability between the occupied and unoccupied 5$d$ states in the bimetallic sample. A comparison of the main peaks along the diagonals in Figure 10.2 for Pt and PtZn with the Pt $L_3$ XANES revealed a shift in RIXS maxima that corresponded to the 0.9 eV edge energy increase upon Zn addition to Pt. This shift occurred as the result of Zn and Pt alloying within the nanoparticles and, as described further below, was directly related to the measured changes in EDH TOR for the Pt/SiO$_2$ and PtZn/SiO$_2$ catalysts.

Simulations of *in situ* RIXS spectra for Pt and PtZn were performed on Pt(111) and Pt$_1$Zn$_1$(110) surfaces and are also shown in Figure 10.2. The (111) and (110) close-packed surface orientations were chosen in order to represent the bulk nanoparticle surface structures of Pt and Pt$_1$Zn$_1$, respectively. Calculated bulk and surface *d*-DOS were averaged for Pt(111) and Pt$_1$Zn$_1$(110) in order to approximate the Pt and Pt$_1$Zn$_1$ nanoparticles, respectively. The formalism for calculating RIXS spectra from the DOS has been discussed elsewhere[22, 31-32]. RIXS intensities ($F$) were calculated from the following equation[22]:

$$F(\Omega, \omega) = \int_{\varepsilon_i}^{\varepsilon_j} d\varepsilon \, \frac{\rho_d(\varepsilon)\rho_d'(\varepsilon+\Omega-\omega)}{(\varepsilon-\omega)^2+\frac{\Gamma_n^2}{4}} \tag{10.1}$$

Here, $F$ was calculated by integrating over the DOS energies ($\varepsilon$) for the occupied valence states ($i$) and unoccupied valence states ($j$), where $\boldsymbol{\rho_d}$ and $\boldsymbol{\rho_d'}$ are the partial *d*-band DOS of Pt for the occupied and unoccupied states, respectively. The lifetime broadening of the 2$p_{3/2}$ core hole ($\boldsymbol{\Gamma_n}$) was taken as 5.41 eV[22]. This method does not account for interactions from the photoexcitation process; however, it has been shown to give accurate results when compared to experiment[22]. The calculations, which were performed by using the *d*-band DOS obtained through self-consistent DFT calculations, exhibited similar features to the experimental spectra. In particular, the
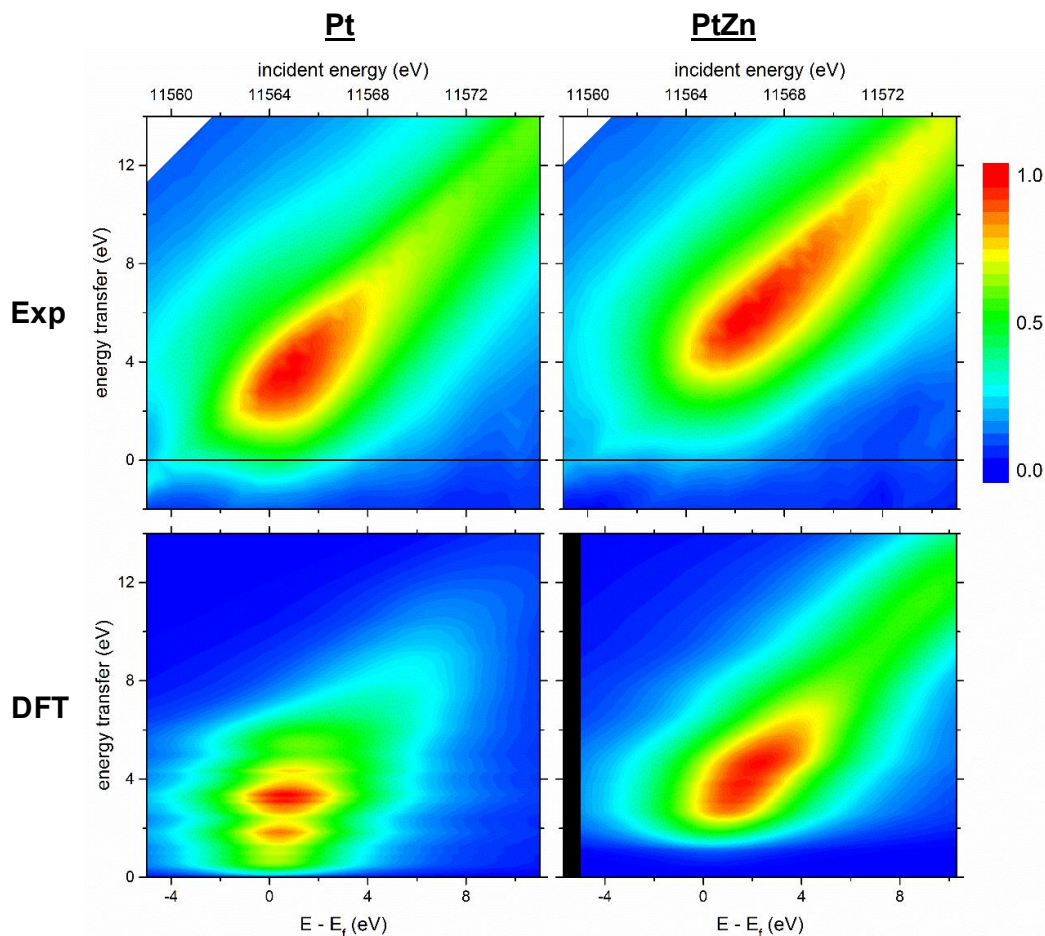
Figure 10.2 **.** RIXS planes for supported Pt and PtZn nanoparticles. Comparisons between experimentally (Exp) measured RIXS for 9.70 wt.% $Pt/SiO_2$ at 100 °C in 3% $H_2$ with calculated RIXS for Pt(111) by DFT (left column), and experimental RIXS for 9.53 wt.% Pt – 9.28 wt.% $Zn/SiO_2$ at 100 °C in 3% $H_2$ with calculated RIXS for $Pt_1Zn_1$(110) by DFT (right column).

simulations revealed a ~1.8 eV increase in the energy transfer of the RIXS maximum that occurred at ~0.9 eV higher incident energy than on Pt(111), in agreement with the measured 0.9 eV edge energy increase for $PtZn/SiO_2$ from *in situ* XAS.

Previous theoretical studies have provided strong evidence that the metal *d*-band center is a useful descriptor of catalytic activity for various transition metals and alloys[11-12, 33-36]. For the present study, the calculated Pt *d*-band center for monometallic Pt(111) was found to be -2.19 eV and was shifted upward to -2.08 eV for $Pt_1Zn_1$(110), as shown in Figure 10.3. Use of a modified electronic structure descriptor[37], which includes the *d*-DOS width, yielded modified *d*-band centers and widths of -0.64 eV and -0.61 eV for Pt and $Pt_1Zn_1$, respectively. Such small changes are within

the uncertainty of DFT calculations and do not differentiate the electronic properties in these samples. Indeed, when compared to the calculated $L\beta_5$ RIXS spectra for Pt(111) and Pt$_1$Zn$_1$(110) in Figure 10.2, it is evident that the RIXS planes, which contain information corresponding to the surface $d$-band DOS that affects catalytic activity, correctly describe trends in the PtZn vs. Pt RIXS signatures, and provide additional detail about the Pt valence electronic structure, including a more direct comparison between theoretical and experimental spectra for Pt and PtZn than does the $d$-band model alone.
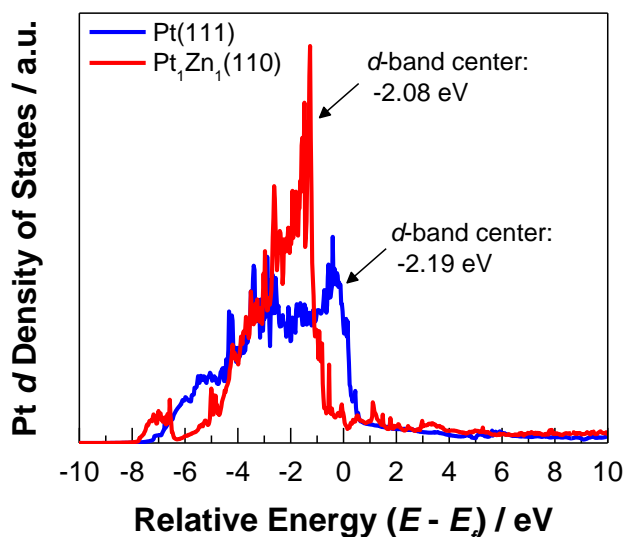


Figure 10.3 Projected density of states (DOS) for $d$ orbitals of Pt(111) and Pt$_1$Zn$_1$(110). The vertical axis represents the electron density and the horizontal axis corresponds to the energy relative to the Fermi energy ($E_f$).

The effect of Zn addition on the energy levels of both the occupied and unoccupied Pt $5d$ bands, evaluated from the energy transfer ($\Delta E$) and Pt $L_3$ edge energy obtained during *in situ* RIXS and XANES, respectively, is shown in Figure 10.4. Compared to monometallic Pt, the occupied Pt $5d$ bands in PtZn were shifted by approximately 1.1 eV further below the Fermi energy, while the unoccupied bands were shifted to higher energies by approximately 0.9 eV. As discussed in Section 4 of the Supporting Information, the lower energies of the occupied states led to an upward shift in the high intensity peak for the PtZn alloy compared to monometallic Pt, while the extended unoccupied states led to a longer tail for PtZn compared to Pt. This combination of lower energy for the filled and higher energy for the unfilled electronic states changes the relative energy between the Pt $d$ orbitals in PtZn/SiO$_2$ and the adsorbate electrons, which modifies bond formation

and increases the number of reaction turnovers per Pt site per unit time. Previous microcalorimetric and DFT studies by Dumesic and coworkers[16-18] have shown that the addition of Zn and Sn ad-metals to Pt- and Pd-containing catalysts weakens the interaction of the metal surface with $C_2H_4$ to inhibit production of coke-forming ethylidyne species. These findings align with the kinetic and structural characterization results from the present study that show suppressed coke deposition and TOR enhancement on the $Pt_1Zn_1$ nanoparticle alloys. Furthermore, DFT calculations and *in situ* RIXS measurements indicate that the mechanism of this electronic promotion of Pt by Zn for EDH is driven by changes in energy of the Pt $5d$ electrons, rather than a change in electron occupancy due to electron donation as previously suggested for $PtZn^{13, 15}$ and $PtCu^{36}$, which effectively reduces the binding energies of adsorbates and increases the TOR per surface Pt.

A major challenge in the development of catalytic materials is the ability to identify the most important properties of a solid surface which govern its chemical reactivity. The molecular level insight obtained in the present study provides a model to suggest that control of the geometric structure of the Pt active sites affects product selectivity, while control of the metal promoter affects the adsorbate binding strength and TOR. Furthermore, the direct experimental validation of DFT-predicted RIXS planes for $Pt/SiO_2$ and $PtZn/SiO_2$ enables new opportunities to investigate relationships between the energy levels of filled and unfilled valence states for various Pt-
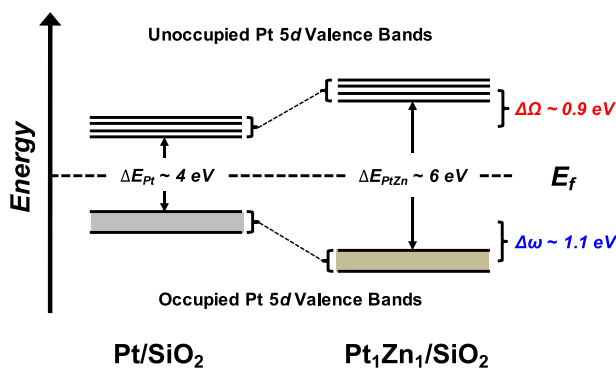


Figure 10.4 Energy Level Diagram for Pt 5d Valence Bands in Pt/SiO2 and Pt1Zn1/SiO2

containing alloys, the binding energies of adsorbates, and their effects on catalytic activity for EDH. While only monometallic Pt and the $Pt_1Zn_1$ alloy have been considered here for EDH, we envision that this approach could be applied to other nanoparticle alloys and reactions of interest.

# 11. CHANGES IN CATALYTIC AND ADSORPTIVE PROPERTIES OF 2 NM PT₃MN NANOPARTICLES BY SUBSURFACE ATOMS

## 11.1 Introduction

Supported multimetallic nanoparticles (NPs) are among the most widely used catalysts in industry and their properties are highly tunable by control of their composition and structure.[1,2] The geometric and electronic effects related to the NP surface have been well studied since the early work of Sinfelt.[3] It has been, however, very difficult to identify any subsurface effects on NPs, even while changing the subsurface metal atoms has been observed to have a large impact on single crystal model catalysts by surface science and Density Functional Theory (DFT) studies,[4-7] as well as recently in electrochemical processes.[7-9]

For supported NPs, it has been very challenging to study the effect of subsurface layers due to the difficulties in preparing and characterizing materials with the same surface structure but different subsurface phase. It was previously suggested that substituting a Pt NP core with a second noble metal improved its activity for preferential oxidation of carbon monoxide in hydrogen below 200 °C.[10,11] Nevertheless, the catalyst structure under reaction condition was not known and it was not stable at higher temperatures due to diffusion between the surface and subsurface, forming a solid solution. This type of structure has randomly disordered bimetallic surface as well as subsurface as typical for noble metal mixtures.[10,12] Further identification and investigation of the subsurface effect on supported NPs require improved methods to separately control and characterize atomically precise and high temperature stable surfaces and subsurfaces.

More stable NP core-shell structures can be achieved by intermetallic compound phases which feature precisely ordered arrays of different metals with strong hetero-atomic bonds,[13,14] resulting in reduced diffusion and minimized structural changes.[15,16] NPs with intermetallic shells

on top of a heterogeneous core have been recently shown to maintain surface ordering at high temperatures.[17] Herein, we investigate the effect of subsurface composition on supported 2 nm core-shell NPs ($Pt_3Mn$ shell on Pt core) versus full-body intermetallic NPs ($Pt_3Mn$ shell on $Pt_3Mn$ core). A $Pt_3Mn$ subsurface instead of Pt significantly improves the catalytic selectivity for C-H activation for propane dehydrogenation at 550 °C, which is correlated to a large decrease of adsorbate binding strength according to DFT calculation as well as experimental measurements. The subsurface effect offers enhanced catalytic performance and tunable adsorptive properties, demonstrating its potential in modifying NP catalysts for many reactions.

## 11.2 Methodology

All DFT calculations are performed with self-consistent, periodic, density function theory using the Vienna Ab-initio Simulation Package (VASP).[18-21] The Perdew-Burke-Ernzerhof (PBE) exchange-correlation function[22] using projector augmented wave (PAW) pseudopotentials was used.[23,24] All calculations are performed with spin polarization. For bulk lattices of Pt and $Pt_3Mn$ a cutoff energy of 600 eV was considered with a force-convergence criterion of 20 meV/Å. The Methfessel-Paxton smearing method was used with a Gamma-centered 10x10x10 K-point grid. Relaxed lattice constants for bulk Pt and $Pt_3Mn$ were found to be a=3.98 Å and a = 3.93 Å, respectively. 2x2x5 surface slabs of the (111) surface were cut for both Pt and $Pt_3Mn$ and included 10 Å of vacuum above the surface. A dipole correction was applied parallel to the plane of the slab to reduce image-image interaction errors. The bottom two layers of the slab were constrained to their bulk lattice positions while the top three layers were allowed to relax. A cutoff energy of 450 eV was used for all slab calculations with a Gamma-centered 7x7x1 K-point grid with a similar force-convergence criterion of 20 meV/ Å. High index (211) surfaces were cut from the same bulk to have 4 terrace layers and a step length of 4 Platinum atoms. A 4x4x1 Gamma-centered K-point grid was used for the high index surfaces. Adsorption of all adsorbates was considered at all symmetrically distinct (111) sites corresponding to a 0.25 ML coverage. For gas-phase adsorbate calculations, the same cutoff energy was used with Gaussian smearing of the Fermi energy in an oblong simulation box with dimensions 12x13x14 Å. For calculations with a $Pt_3Mn$ skin, a single Mn atom replaced Pt in the pure Pt(111) surface and then relaxed at the fixed pure Pt lattice constant. A similar process is used for films containing two layers of $Pt_3Mn$. For high index (211) surfaces, CO was adsorbed along the step edges. Pt d-band centers were calculated as the first

moment of the projected d-electron density of states of surface platinum atoms. The maximum allowed energy was 5 eV above the Fermi edge, consistent for all alloys. Projected density of states was calculated at the same computational parameters as reported for adsorption, with the exceptions being the use of tetrahedral smearing and a denser K-point grid of 15x15x1.

## 11.3  Results and Discussion

### 11.3.1  Olefin (C-H Activation Product) Selectivity during Propane Dehydrogenation.

We evaluated the effect of NP subsurface composition on selectivity of C-H over C-C bond activation by a model reaction propane dehydrogenation (PDH) at 550 °C for the two Pt-Mn catalysts together with the reference Pt NP catalyst.[34] The selectivity to propylene (the product of C-H activation) was compared under the same propane concentrations, but varying co-fed hydrogen concentrations. The effect of the surface composition is observed from comparison of $Pt_3Mn$-s and Pt. Fig. 3b shows that the selectivity of the Pt catalyst drops from 95% to 78% as the conversion increases in the absence of co-fed hydrogen, and further to ~ 35% as the $H_2$ to $C_3H_8$ molar ratio ($H_2/C_3H_8$) increases from 0 to 2. This is due to substantial activity for the side reaction hydrogenolysis, which breaks C-C bonds with the assistance of hydrogen, and is consistent with previous reports.[35] In contrast, for the $Pt_3Mn$-s catalyst, the C-H selectivity remains nearly constant with the PDH conversion, which is consistent with the absence of Pt phase on the core-shell NP surface. As the $H_2/C_3H_8$ increases from 0 to 2, the selectivity decreases from 95% to 82%, to a much smaller extent compared to Pt.

Comparing $Pt_3Mn$ to $Pt_3Mn$-s discloses a distinct subsurface effect that is independent from the surface structure. As shown in Fig. 3c, the selectivity of $Pt_3Mn$ remains high at 98% not only under varying conversion similar to $Pt_3Mn$-s, but also under increasing $H_2$ to $C_3H_8$ molar ratio. Increasing $H_2/C_3H_8$ from 0 to 2, which significantly lowers the selectivity of $Pt_3Mn$-s as well as Pt, has little effect on $Pt_3Mn$. The hydrogenolysis side reaction is almost completely suppressed on $Pt_3Mn$. This implies that the interaction of $Pt_3Mn$ with the reactants and intermediates is significantly altered by the subsurface composition.

The assignment of the promoted catalytic performance to different subsurface structures is strengthened by the observation that the Pt-Mn catalysts maintain their structures under reaction condition. *In situ* sXRD under propane dehydrogenation atmosphere at 550 °C and even 750 °C

recorded identical patterns including the superlattice features and peak widths compared to the reduced catalysts at room temperature and 550 °C, suggesting that the $Pt_3Mn$ surface and/or subsurface on the NPs remained ordered during high temperature reaction. Not only the $Pt_3Mn$ intermetallic catalyst, but also the core-shell NPs in the $Pt_3Mn$-s catalyst are stable during high temperature reaction due to limited solid state diffusion of Mn. After initial reduction of Mn and its subsequent diffusion into the Pt lattice, the Mn concentration near the NPs decreases, turning off further reduction by hydrogen spillover. Therefore, a structural evolution of the Pt-Mn catalysts is not observed and the NP structure is determined by the initial Mn concentration on the support surface. The stable catalyst structure in part contributes to long-term stable catalytic performance. While Pt quickly deactivates with time on-stream, both Pt-Mn catalysts do not. They show stable conversion for PDH at 550°C for at least a week with a turnover rates in the 0.1 to 1 $s^{-1}$ range as expected for Pt catalysts according to the literature.[34,36,37] STEM imaging on the spent catalysts after PDH for 1 week shows size distributions similar to those of the fresh catalysts (Fig. S9), indicating minimal particle sintering. The $Pt_3Mn$ catalyst was also evaluated for dehydrogenation of ethane, which requires higher reaction temperature. For 25 % ethane balanced in $N_2$ at 750 °C, the $Pt_3Mn$ catalyst show stable performance with > 90% selectivity at around 40 % conversion for at least 1 day, demonstrating the high temperature stability of this intermetallic phase during catalytic reaction.

## 11.3.2 Subsurface Electronic Effect on Surface Adsorption.

To better understand the observed subsurface effect on the catalytic performance, DFT calculations were undertaken on models (Figure 11.1a) representing the three catalyst structures. A $Pt_3Mn$ full-body intermetallic was considered for the $Pt_3Mn$ sample. A $Pt_3Mn$ shell on top of Pt with single or double layers of $Pt_3Mn$ was considered for $Pt_3Mn$-s. This catalyst was expected to have between one or two outer $Pt_3Mn$ layers on 2 nm core-shell NPs, since the molar percentage of the $Pt_3Mn$ intermetallic shell out of the whole NP was estimated to be between ~40-60% according to the average lattice parameter measured by $_sXRD$ and the coordination number ratio of Pt-Mn/Pt-Pt from EXAFS fits. The models were compared with monometallic Pt. The (111) facet was chosen based on its low surface free energy for both pure Pt and $Pt_3Mn$. The binding energies for hydrogen (H) and methyl group ($CH_3$, as a model chemisorbed hydrocarbon species) were calculated, since the improvement in selectivity for light alkane dehydrogenation has been

previously suggested to correlate with the altered adsorption strength of the catalyst to hydrocarbon molecules and hydrogen.[38,39] The binding energy of carbon monoxide (CO) was also calculated as well as measured experimentally. The computational results are summarized in Figure 11.1b. Compared to Pt, two layers of a $Pt_3Mn$ shell ($Pt_3Mn$-2s(111)) reduces the binding energy by 0.02 eV, 0.07 eV, and 0.09 eV for H, CO, and $CH_3$, respectively, whereas binding energies are reduced by 0.08 eV, 0.17 eV, and 0.19 eV for H, CO and $CH_3$ on the full $Pt_3Mn$ intermetallic surface. Importantly, the $Pt_3Mn$ full-body intermetallic has a weaker adsorption energy for all investigated adsorbates as compared to the $Pt_3Mn$ intermetallic shell on Pt subsurface, confirming the presence of the subsurface effect. The results are consistent with the promotion of PDH selectivity of $Pt_3Mn$ compared to $Pt_3Mn$-s, since the weaker adsorption are correlated with the preferential desorption of hydrocarbon and hydrogen species over their participation in the steps leading to C-C bond breaking.[39,40]
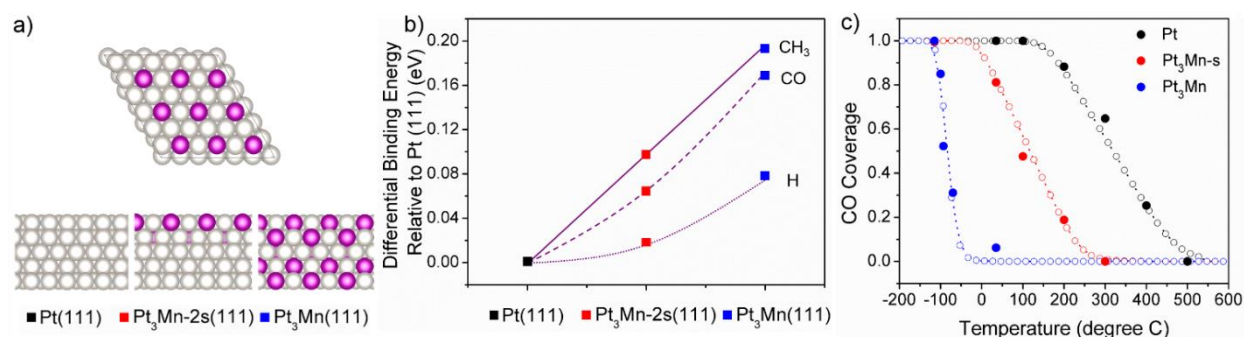


Figure 11.1 a) The structure model for a $Pt_3Mn$ (111) top surface and the side view of the models used for DFT calculation of binding energies on Pt (Pt(111)), $Pt_3Mn$-s ($Pt_3Mn$-2s(111), 2 layers of $Pt_3Mn$ on top of Pt) and $Pt_3Mn$ ($Pt_3Mn$-(111)); b) the calculated differential binding energy of H, CO and $CH_3$ on the (111) surface of Pt, $Pt_3Mn$-s, vs $Pt_3Mn$; c) CO chemisorption surface coverage vs temperature for Pt, $Pt_3Mn$-s and $Pt_3Mn$. The filled circles are experimental data, while the hollow circles and dotted lines are from the best fit to the Temkin model

The changes in catalyst adsorption capability due to subsurface effect is also evident from experimental measurements of equilibrium CO adsorption on the supported NPs, giving heats of adsorption on different catalysts. Figure 11.1c shows that all three catalysts show one-step CO desorption, including $Pt_3Mn$-s, again consistent with this catalyst having a single surface composition characteristic of core-shell structure rather than a physical mixture of Pt and $Pt_3Mn$. For Pt, CO chemisorption is saturated at room temperature.[41] In contrast, saturation uptake for $Pt_3Mn$-s is not achieved until around 0 °C whereas for $Pt_3Mn$ it is only observed below -120 °C.

Fitting the coverage-temperature data to the Temkin model (see SI),[42,43] the heats of adsorption of CO on Pt at 0 and full coverage ($\Delta H(0)$ and $\Delta H(1)$) are estimated to be $\Delta H(0) = 130$ kJ/mol and $\Delta H(1) = 70$ kJ/mol, close to literature results and giving an average heats of adsorption $\Delta H_{ave} = 100$ kJ/mol.[41] For Pt$_3$Mn-s, the best fit Temkin desorption curve results in $\Delta H(0) = 85$ kJ/mol, $\Delta H(1) = 40$ kJ/mol and $\Delta H_{ave} = 63$ kJ/mol and for Pt$_3$Mn $\Delta H(0) = 30$ kJ/mol, $\Delta H(1) = 25$ kJ/mol, $\Delta H_{ave} = 28$ kJ/mol respectively. The average heat of adsorption is lowered by 37 kJ/mol comparing Pt$_3$Mn-s to Pt. Similarly, the average heats of adsorption of Pt$_3$Mn is 35 kJ/mol lower than Pt$_3$Mn-s. These experimental results on the NP catalysts are consistent with the trends seen in the DFT calculations and correlate well with the increasing propane dehydrogenation selectivity for Pt$_3$Mn-s and Pt$_3$Mn. The changes in the reduction of heats of CO adsorption are higher than the DFT predictions,[39,40,44,45] which is likely related to adsorption on corners and edges on the NPs. We note that adsorption of CO on a model high index surface, such as the (211) step, shows the same trend between different catalyst but with a larger reduction in binding energy due to subsurface Pt$_3$Mn as compared to the (111) terrace (APPENDIX I).

Additional DFT calculations were conducted on varying model structures. Constraining the lattice constant of the Pt$_3$Mn shell to values between pure Pt$_3$Mn and Pt only changes binding energies by less than 30 meV (APPENDIX I), suggesting the absence of a major surface strain effect, which is also expected from the very similar lattice parameters between the Pt$_3$Mn and the Pt phases. In addition, a single layer Pt$_3$Mn shell on Pt does not reduce the binding energy significantly as compared to pure Pt (APPENDIX I). Therefore, Mn in the subsurface plays a key role in reducing the surface adsorption strength, most likely through bonding of subsurface atoms with the catalytic surface. This is consistent with previous DFT studies on model structures containing other elements.[6,7] According to the *d* band theory, an electronic effect leading to weaker adsorption strength is typically related with downward shifts of *d* states away from Fermi level,[46] which is indeed observed from the calculated density of states, showing a -0.05 eV shift for Pt$_3$Mn (111) compared to Pt$_3$Mn-2s(111) (APPENDIX I). This shift of the overall *d* states usually leads to lower average energy of the occupied *d* states, but is also accompanied by a small upward shift of the average energy of the unoccupied part of the 5*d* states on Pt. The latter is observed on our Pt-Mn catalysts by the Pt L$_{III}$ edge XANES. Such shifts of occupied and unoccupied *d* states were recently measured for a similar Pt$_1$Zn$_1$ intermetallic NP catalyst by *in situ* Resonant Inelastic X-ray Scattering (RIXS).[47] The shifts are similar to typical changes of the HOMO and LUMO orbitals

in a molecule upon bonding interactions and are likely results of the strong hetero-metal bonding interaction of the intermetallic compounds.[47] This study suggests that such intermetallic interaction can be manipulated by a diffusion controlled solid state transformation starting from the NP surface to the core for tuning the subsurface structure of NPs. Such controlled intermetallic formation have been demonstrated for several intermetallic compositions and are possible for many other phases, both on noble metal NP cores as well as intermetallic cores.[25-27] The resulting subsurface effect modifies the adsorptive properties of the surface sites to offer enhanced catalytic performance.

## 11.4 Conclusions

Supported NP catalysts with different subsurface composition were prepared by controlled intermetallic formation and confirmed by *in situ* characterization under reaction conditions at high temperature, allowing for evaluation of the influence of subsurface composition to the adsorptive and catalytic properties. With the same ordered NP surface, a $Pt_3Mn$ intermetallic subsurface instead of monometallic Pt significantly improved the C-H activation selectivity during propane dehydrogenation by lowering the heats of hydrocarbon and hydrogen adsorption of the surface sites. Models presented herein provide a beginning to microkinetic modeling to help in directly identifying the driving force for selectivity differences. This work highlights the distinct role of subsurface layers for altering the surface chemical and catalytic properties on NP catalysts. Such subsurface effect can be tuned via controlled synthesis of NPs with atomically precise intermetallic phases, promising a wide composition range for versatile catalyst design targeting different catalytic processes.[14]

# 12. RESONANT INELASTIC X-RAY SCATTERING MEASUREMENT AND SIMULATION TO UNDERSTAND PROMOTER EFFECTS IN PLATINUM CATALYSTS

Author Contribution: Stephen C Purdy and Jeremy Kropf conducted the experimental spectroscopy of these materials. Stephen C Purdy assisted with synthesis and characterization of the materials, as well as provided written content for spectroscopy, experimental synthesis, and data analysis in section 12.3.1. This includes Figure 12.1, Table 12.1, and part of Figure 12.4.

## 12.1  Introduction

The availability of shale gas has driven interest in new technologies to produce valuable chemical feedstocks from low molecular weight alkanes such as methane, ethane, and propane[9], [10] using catalysis. This is accompanied by the shift in refinery operations away from using naptha-based catalytic cracking, a result of changing feedstocks, to ethane cracking[269]. In ethane cracking, propylene production is decreased, which is necessary to produce propylene oxide, polypropylene, and acrylic acid, among other platform molecules. As traditional oil resources become economically disadvantageous, and shale production increases, efficient strategies for the on-purpose production of light olefins such as propylene will be required to meet the demands of downstream chemical industries with strategies such as nonoxidative dehydrogenation. Control over deactivation by reducing coking is desired; yet, a fundamental understanding of how promoter metals electronically modify nanoparticle catalysts is lacking. The connection with experimental spectroscopy, which can observe such changes, is also required to determine physically relevant descriptors of electronic promotion effects. These electronic descriptors can then be used to design new alloy catalysts for related chemistries.

Industrial dehydrogenation processes, such as the Oleflex$^{TM}$ process licensed by UOP[11] uses a platinum catalyst alloyed with tin. While this catalyst has high selectivity and stability, it deactivates in part via coke formation requiring periodic regeneration. While regeneration is relatively common in the chemical industry, as olefin production moves away from large-scale refineries and into the shale fields, catalysts that can resist deactivation and consequently require less frequent regeneration are necessary. In non-oxidative dehydrogenation, high selectivity to propylene over more deeply dehydrogenated products is required to prevent the formation of coke

precursors, which may cause deactivation by blocking active sites through unselective pathways such as C-C bond cleavage[269]. The precise mechanism of coking is not currently known, although its precise formation is thought to be dependent on reaction conditions, catalyst identity, and structure of the support[270]. To design alloy catalysts which are more resistant to coking, it is necessary to develop rational design rules to reduce the space of new materials to be tested at strenuous conditions.

The use of alloy catalysts for dehydrogenation is not a new idea, as fundamental studies by Sinfelt, Carter, and Yates showed that alloying nickel with copper breaks up ensembles of nickel, reducing the rate of hydrogenolysis without changing the rate of dehydrogenation[271], [272]. The sensitivity of heterogeneous reactions to the structure of the catalyst surface has been used to control the selectivity of dehydrogenation catalysts by preventing C-C bond cleavage events with a variety of promoter metals and structures. For Pt-Sn catalysts, the geometric effect of Sn on dehydrogenation has been the topic of much interest both experimentally[273]–[275] and with Density Functional Theory (DFT)[276], [277]. In addition to the geometric effect of alloy formation, the role of different promoters in chemically modifying the active metal is still a topic of considerable discussion in the literature.

Different alloy structures have been used to study the role of promoters in modifying the electronic structure of catalysts. The modification of platinum has been considered by subsurface transition metals[278], [279], dilute single site alloys[280], as well as polycrystalline alloys[281]; however the formation of intermetallic alloys with platinum is an attractive method for producing well-defined active sites[282]–[284] to study the promoter effect. Intermetallic alloys of platinum with various 3d metals have been reported in the literature[283], in particular $Pt_3Ti$ and $Pt_3V$[285], $Pt_3Cr$[286], $Pt_3Mn$[287], and PtZn[288], [289], among others. While many of these materials may be interesting for dehydrogenation, there is no unified chemical model to predict how modification of the electronic structure of Pt with promoter metals can help design a dehydrogenation catalyst with better coking resistance.

The most successful model to describe adsorption on catalytic surfaces is the $d$-band model developed by Hammer and Norskov[40]–[42], [290] which relates the adsorption of reactive intermediates to the density of $d$ electron states of metal catalysts. This model has been applied to understand the alloying effect of subsurface promoter metals[278] and intermetallic compounds[291, p.]. Direct measurement of $d$ band structure typically requires ultraviolet

photoemission spectroscopy[281] (UPS) or high resolution X-ray spectroscopy[292, p.] (XPS) on single crystals in ultrahigh vacuum (UHV). A new spectroscopic technique, using synchrotron resonant inelastic X-ray scattering[293]–[295] (RIXS), has been used to understand shifts in the valence level $d$ states of transition metal nanoparticles[296], [297], solvated organometallic complexes[298], and the electronic structure of Fe ions in the oxyhemoglobin protein[299]. We have previously reported on the electronic shift in valence orbitals of platinum upon alloying with Zn[289]. Computational approaches have been used to model RIXS, as we and others have reported previously[289], [296]. Using this technique, new connections to the $d$-band theory can be established by linking the spectroscopy with computation, allowing for design rules to be established with a close connection to experiment to design new materials.

In this work, we examine the relative electronic density of Pt $d$-electrons in a family of intermetallic compounds with RIXS and compare with DFT theory, using the spectroscopy as a descriptor to understand how the stability of coking precursors, such as methylidine (CH), ethylidene ($CCH_3$) and atomic carbon, which have been previously discussed in dehydrogenation studies[276], [300], to relate to spectroscopic measurements of the $d$ electronic states of platinum intermetallic nanoparticles. We find the agreement between experimentally measured RIXS spectra and computational approaches to have a mean absolute error (MAE) in predicting incident energy maxima of 0.17 eV, across a series of 7 platinum intermetallics. Similarly, the energy transfers measures deviate on average by 0.41 eV from computational models, across the same set of materials. This agreement is used to further probe the electronic characteristics of 3d transition as compared to 3d and 4d post-transition metals, as well as the adsorption of coking precursors. From insights gained by modeling the RIXS process, a new descriptor for catalyst design, the convolution integral used in modeling the RIXS, is developed which has higher accuracy in predicting carbon adsorption energies than descriptors previously reported. This connection between RIXS spectroscopic techniques and DFT provides new avenues to predict adsorption and demonstrates new ways that theory and experiment can be connected to design and screen new materials.

## 12.2  Methods

### 12.2.1  Density functional theory calculations

Density Functional Theory (DFT) calculations were performed using the Vienna Ab Initio Simulation Package (VASP) using the Projector Augmented Wave pseudopotentials. The PBE exchange and correlation functional, which has been extensively benchmarked for the treatment of metals was used for all calculations. Lattice constants for pure Pt, as well as each of the alloys were optimized using a 600 eV energy cutoff, a 10x10x10 gamma centered k point grid, and Methfessel-Paxton smearing. Lattice constants were converged to a force criterion of 20 meV / Å. All calculations are performed spin-polarized with initial magnetic moments specified to ensure the magnetic moments correspond to the lowest energy structure. Converged lattice constants for the full suite of alloys is provided in APPENDIX J.

Surface slabs were cut from each bulk according to their closest packed termination. For all $Pt_3X$ compositions a (111) surface was chosen based on the FCC structure of each bulk. PtZn has a body centered tetragonal unit cell, in which the (011) surface has the highest packing density and is chosen for modeling. All surfaces used were 2x2 surface atoms, and 5 layers with 10 Å of vacuum. The bottom 2 layers were constrained to mimic an underlying bulk, while the top 3 layers could relax to a force criterion of 20 meV / Å. The dipole parallel to the vacuum was corrected. A 7x7x1 Gamma centered k point grid was used with Methfessel-Paxton smearing.

The Density of States (DOS) for bulk and surfaces were calculated using the standard VASP projectors. For bulk, the DOS of each Pt atom was averaged along with the up and down spin channel. For surface slabs, only the topmost Pt atoms were averaged along with their up and down spin channels. For bulk, the DOS was calculated using a denser k-point grid of 15x15x15. For surfaces, 15x15x1 k point grids were used.

Moments about the *d*-band were performed by first normalizing the total density and shifting the Fermi level to 0. All moments were calculated with an upper cutoff of +5 eV above the Fermi energy, to neglect contributions from small but nonzero densities at higher energies beyond the *d*-band. To account for particle size effects, the relative number of surface and bulk metal atoms was estimated using the relation D ~ 0.9/d where D is the dispersion expressed as the ration of surface to bulk atoms, and d is the particle size in nm, was used and a weighted average of bulk and surface Pt atoms was constructed for a given particle size[301].

Adsorption of model compounds was performed at the same level of theory as DOS calculations to provide a consistent comparison between electronic structure and adsorption energy. Adsorption energies of each $CH_x$ intermediate is referenced to a stoichiometric balance of methane and molecular hydrogen according to the following relation

$$E_{ads} = (E_{CHx*} + \frac{(4-x)}{2} E_{H_2(g)}) - (E_* + E_{CH_4(g)}) \tag{12.1}$$

Where x denotes the number of hydrogens in the adsorbate molecule. Gas phase calculations were performed in a 8 Å by 9 Å by 10 Å periodic box with a cutoff energy of 450 eV, a single gamma k-point and the same force convergence criteria as used for the bulk.

## 12.2.2 RIXS modeling equations

RIXS energy planes were calculated using the $d$-projected DOS (from here denoted as pDOS). The general expression used has been used previously[289], [293], [296] and is shown in equation 12.1:

$$F(\Omega, \omega) = \int_{-\infty}^{0} d\varepsilon \frac{\rho_d(\varepsilon)\rho_d{}'(\varepsilon+\Omega-\omega)}{(\varepsilon-\omega)^2 + \frac{\Gamma_n^2}{4}} \tag{12.2}$$

Where F is the emitted intensity expressed in terms of the incident energy $\Omega$, and the emission energy $\omega$. The energy transferred is expressed as $\Delta E = \Omega - \omega$. The pDOS of the occupied (below the Fermi level) and unoccupied (above the Fermi level) are $\rho_d$ and $\rho_d{}'$. The broadening of the core hole, $\Gamma_n$ is taken to be 5.41 eV[37]. The energy of a given state is $\varepsilon$, which is used as an integration index. For each $\Omega$ and $\omega$, the range of accessible states in the second term of the numerator implicitly changes the range of the integral, while each specific emission energy $\omega$ shifts the range at which spectral broadening is apparent. Effectively, the intensity is a convolution of the occupied and unoccupied $d$-states governed by the constraints imposed by the incident and emitted energy for accessible transitions broadened by the core hole. The integral was solved on a grid ranging from -4 eV to 10 eV relative to the Fermi energy in $\Omega$, and 0 to 14 eV in $\Delta E$. This was solved using a code written in Python. High intensity peak identification was performed differently than we have reported before. Instead of reporting the point of highest intensity, a 2-D Gaussian function is fitted to the entire high intensity region to extract a mean value. This is less sensitive to sharp details in the DOS which cause non-uniform fluctuations in the broad high-intensity RIXS peak.

## 12.3  Results and discussion

### 12.3.1  Resonant Inelastic X-ray Spectroscopy Measurements

The particle size, phase composition and phase purity of $Pt_3V$, $Pt_3Mn$, $Pt_3Fe$, $Pt_3Co$, $Pt_3In$, and PtZn are described previously[287], [302], [303]. The energy transfer maximum and Pt $L_3$ edge X-ray absorption near edge structure (XANES) edge energy for PtZn is reproduced from reference[289]. The Pt-Ga catalyst was determined to be $Pt_3Ga$, with details of the characterization given in the supplemental information.
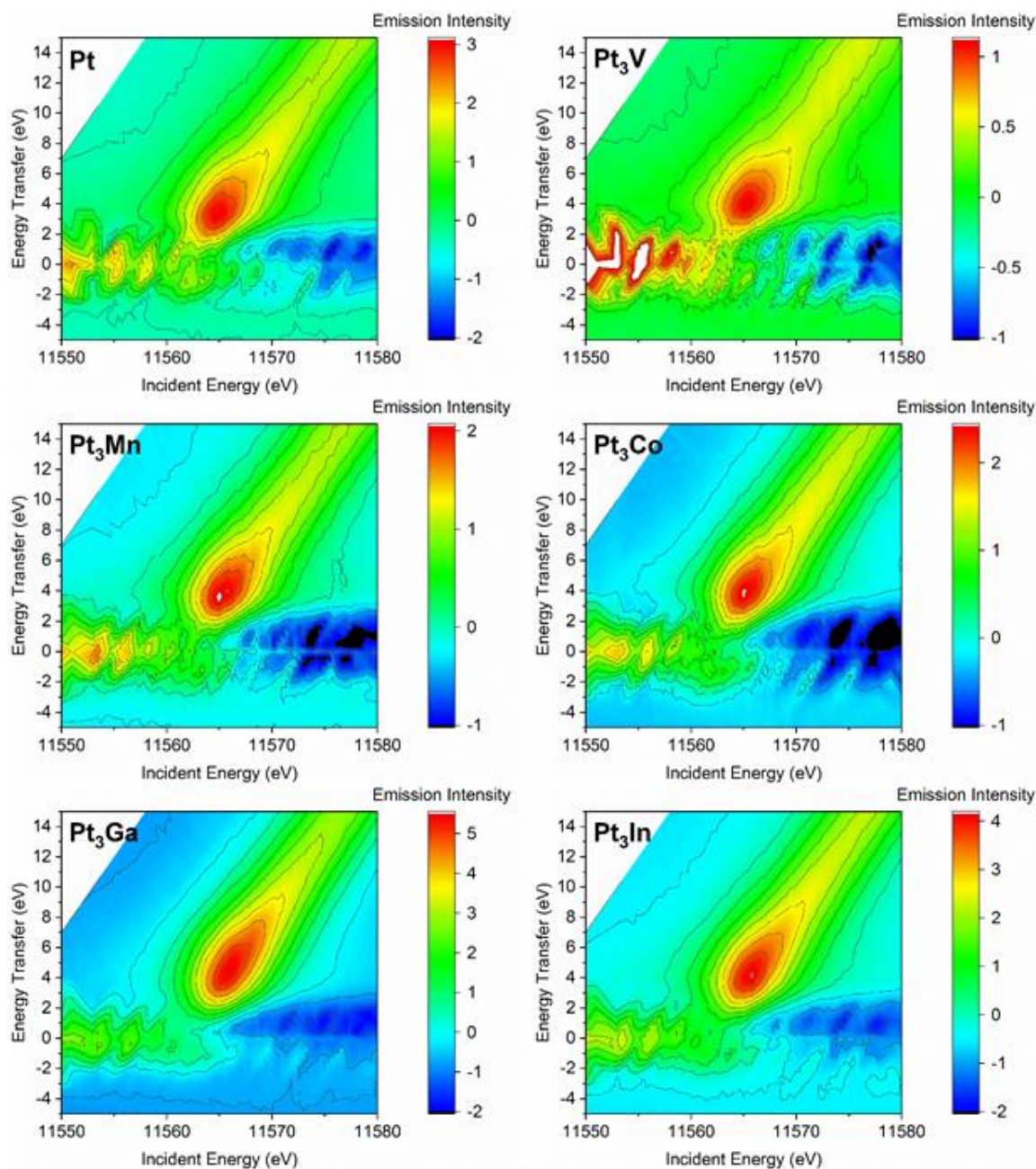
Figure 12.1 RIXS plots of Pt and Pt alloy catalysts after reduction at 550°C in 3.5% $H_2$.

RIXS plots of Pt, $Pt_3V$, $Pt_3Mn$, $Pt_3Co$, $Pt_3In$ and $Pt_3Ga$ are shown in Figure 12.1. RIXS maps are plotted as intensity maps a function of the incident photon energy on the horizontal axis, and the fluoresced photon energy relative to the elastic scattering energy, termed energy transfer, on the vertical axis. The plotted intensity is that of the fluoresced X-rays resulting from scattering. Elastic scattering occurs when the excited $2p_{3/2}$ electron decays back into its own core hole. For

clarity, the elastic scattering peak has been subtracted, and residual fluctuations at 0 energy transfer are artifacts from the subtraction. Inelastic scattering occurs when an electron other than the excited $2p_{3/2}$ electron decays back into the core hole. The bent crystal geometry of the spectrometer used in this study allows for the selective measurement of fluorescence from the $L\beta_5$ decay mode ($L_3$-$O_{4,5}$), which corresponds to a $5d_{3/2}$ or $5d_{5/2}$ electron filling the core hole. Below the absorption edge (11.5640 keV for Pt), the incident X-rays do not have enough energy to excite the $2p_{3/2}$ electron into an unfilled valence state and no fluorescence is detected. Fluorescence from the $L\beta_5$ decay mode occurs above the absorption edge and manifests in the RIXS plots as a broad maximum with an energy transfer value greater than zero. For platinum, the inelastic peak maximum occurs at an energy transfer value of 3.2 eV. Because the $L\beta_5$ probes all filled 5d states, and the $L_3$ edge probes all unfilled 5d states, the energy transfer maximum represents the energy separation between the weighted average energy of the filled 5d states and the weighted average energy of the unfilled 5d states. The broadness of the inelastic scattering peak reflects the width of the d band in platinum and platinum alloys. In the alloy samples, the energy transfer maximum is shifted to higher values (see Table 12.1), meaning the energy of both the filled and unfilled states further separate in the alloys. The shape of the inelastic scattering peak also changes, which reflects the changing distribution of states in energy in each alloy phase. As the incident photon energy increases past the $L_3$ absorption edge, the resonant enhancement of the $L\beta_5$ fluorescence mode decays and non-resonant scattering leads to a low intensity tail which increases in energy transfer with incident photon energy.

Table 12.1 : Energy transfer maximum values and Pt $L_3$ edge XANES edge energies for Pt and Pt alloy phases.

| Phase | Energy Transfer (eV) | XANES edge energy (eV) |
|-------|---------------------|------------------------|
| Pt | 3.2 | 11564.0 |
| $Pt_3V$ | 4.1 | 11564.5 |
| $Pt_3Mn$ | 3.6 | 11564.3 |
| $Pt_3Fe$ | 3.5 | 11564.2 |
| $Pt_3Co$ | 3.9 | 11564.6 |
| $Pt_3Ga$ | 4.6 | 11564.8 |
| $Pt_3In$ | 4.2 | 11564.8 |
| PtFe | 3.7 | 11564.4 |
| $PtFe_3$ | 3.8 | 11564.6 |
| PtZn | 4.5 | 11564.8 |

The energy transfer values for the platinum alloys with post transition metals (In, Ga, Zn) are larger than those alloys with 3d elements, even in $Pt_3In$ and $Pt_3Ga$ where Pt has the same number of Pt-promoter bonds as in the 3d $AuCu_3$ structures. For the Pt alloys with the 3d metals, vanadium and cobalt show the largest energy transfer values, while iron and manganese had the smallest increase in energy transfer of the alloys measured. In all cases, the energy transfer relative to platinum is larger in magnitude than the XANES edge energy relative to platinum, demonstrating that in all structures the average energy of the 5d filled states decreases in energy.

### 12.3.2  Screening of Pt d-DOS

As RIXS is a bulk-sensitive technique, to predict spectra in nanoparticle catalysts it was necessary to account for both surface and bulk metal contributions. For particles smaller than 9 nm, the fraction of surface atoms is at least 10% of the total metal content per particle, and for particles at the size scale in the present study (~1-3 nm) at least 30% of the total metal atoms are undercoordinated at the surface. Additionally, while the particle sizes for each catalyst is relatively consistent, sizes between different catalysts fluctuate, and as an approximate way to gauge the sensitivity of the spectra and electronic structure to changes in particle size, a range of dispersions were simulated from 30% – 60%  (approximately 1.5 nm – 3 nm) as well as the limiting cases of 0% and 100% dispersion (a crystalline bulk and infinite surface, respectively).

The $d$-DOS across a range of metal promoters (the full range of 12 promoters available in APPENDIX J) is shown in Figure 12.2. Platinum $d$-DOS with promoters such as Mn and Co with

half-filled $d$ bands form intermetallic alloys with Pt which have a broader range in occupied $d$ states than early transition metals such as V or late transition metals such as Cu. The half $d$-filling promoters do not significantly shift the Pt $d$-band center as compared to pure Pt (-0.07 eV and 0.07 eV for Pt in $Pt_3Mn$ and $Pt_3Co$) showing a similar electronic structure for pure Pt and Pt alloyed with a half-filled $d$-band promoter. Distinct from pure Pt, is a feature at ~2 eV above the fermi energy in $Pt_3Mn$, with relative position insensitive to particle dispersion. A similar, though smaller peak is observed for $Pt_3Co$ closer to ~2.5 eV. These higher energy unoccupied states are not unique to the half-filled $d$ promoters but observed for all alloys at varying position in intensity. In the case of Pt in $Pt_3V$, Pt in $Pt_3Ga$, and Pt in $Pt_3Sn$; The peak intensity and position changes with particle dispersion, indicating undercoordinated Pt atoms at the surface interact differently with promoter metals as in the bulk. The strongly peaked distributions of $Pt_3V$, $Pt_3Ga$, and $Pt_3Sn$ have larger $d$-band center shifts (-0.29 eV, 0.14 eV, 0.14 eV) as compared to pure Pt, reflecting the perturbation in Pt density of states by electronic interaction with promoter metals, as the geometry of each surface (except for PtZn) is similar.
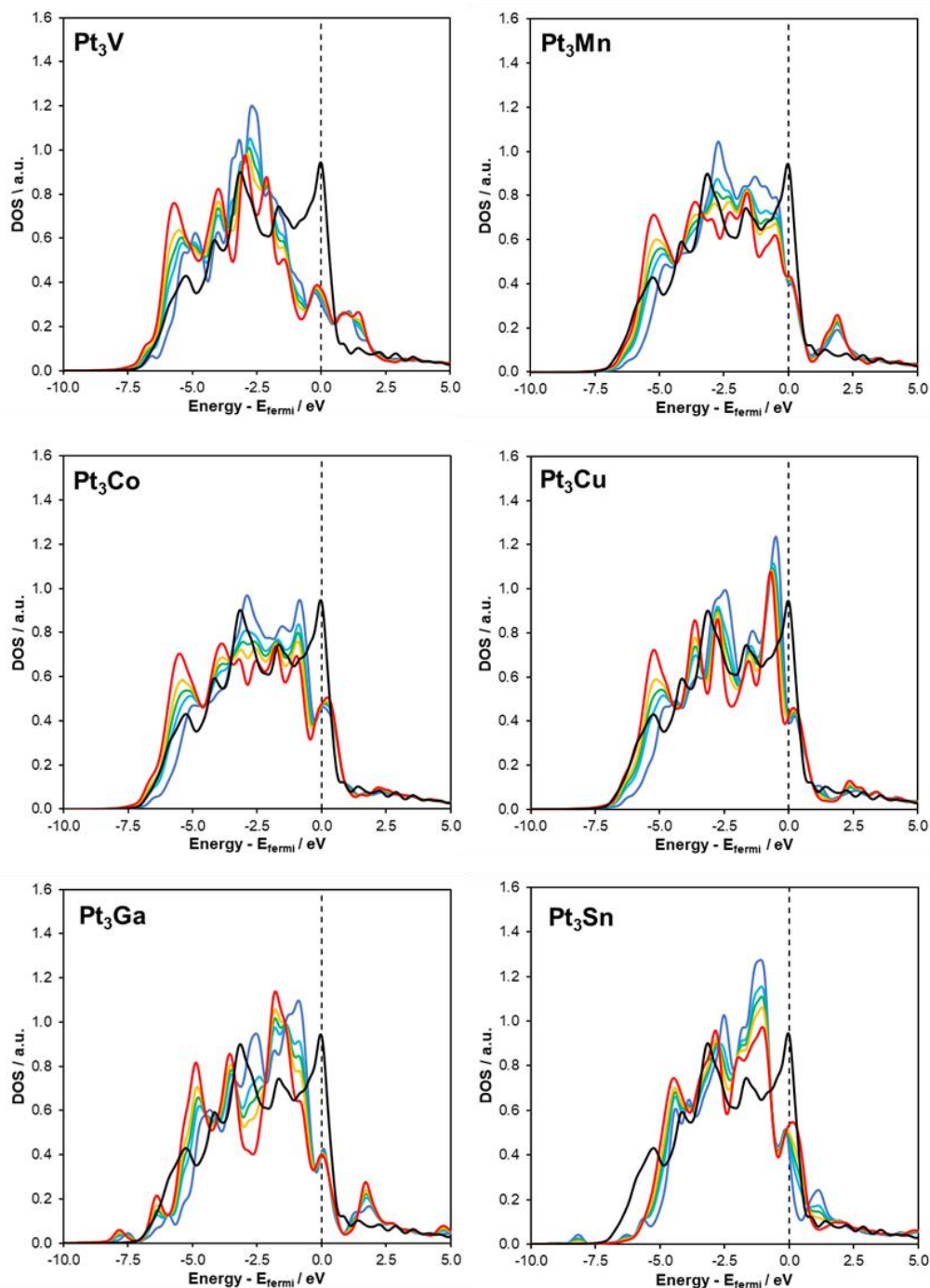
Figure 12.2 Projected density of state (DOS) of Pt bulk and surface atoms in intermetallic alloys. The DOS are plotted for increasing dispersion from 0% (red), 30% (yellow), 45% (green), 60% (cyan), and 100% (blue). Pure Pt is shown in black. The 6 other intermetallics considered can be found in APPENDIX J

As *d*-band centers shift depending on alloy identity, it is necessary to understand to what extent the fractional charge of platinum changes across the range of promoter metals. One measure

of the charge transfer associated with alloy formation is the relative filling of Pt $d$-bands in the pure metal as compared to the alloy. A shift in either the total number of $d$ electrons or relative filling of the $d$ band would indicate charge transfer between Pt and promoter atoms. The total number of electrons across all 12 promoters has a MAE of 0.01 electrons (APPENDIX J), with a maximum deviation of 0.04 electrons relative to pure Pt for PtZn, which forms a (011) closest packed surface as compared to the 111 surface for pure Pt. The relative filling of the $d$-band, expressed as the fraction of occupied Pt $d$ electron states and total Pt $d$ electron states, has a similar MAE of 0.02 electrons with a maximum deviation of 0.05 electrons (APPENDIX J). This indicates that despite the electronic interaction upon alloying observed qualitatively by the changing DOS among different promoters and shift in $d$-band center, there is no evidence of direct charge transfer between Pt atoms and the promoter metals.

The relative size of the promoters (such as 4d post-transition metals In, and Sn) introduce strain on the Pt atoms, which change the adsorption and hence electronic properties[304, p.], [305], [306]. By taking the strained lattice produced by alloying (a maximum +2.1% for Sn, and -3.1% for Fe) the changes in Pt $d$-states do not reproduce the splitting observed by alloying (APPENDIX J). Consequently, although strain has some influence the electronic properties of Pt, neither it nor charge transfer explain the observed splitting of Pt $d$-states upon alloy formation. We then are left with the conclusion that it is an interaction between Pt $d$-states and the promoter metal which maintains partial charge on each species that results in the observed splitting. While this splitting has been observed by others, in particular for Pd alloys[291], RIXS spectroscopy which probes valence states close to the Fermi energy provides additional insight into the observed $d$-DOS splitting.

### 12.3.3  Orbital shifts in RIXS

From dispersion corrected DOS plots, simulated RIXS plots were constructed to evaluate the accuracy to which shifts in the high intensity peak can be described by simulated DOS across the range of 12 promoters. To facilitate the comparison between Pt in simulated alloys as compared to simulated pure Pt, Figure 12.3 shows difference RIXS plots for the same subset of intermetallics as shown in Figure 12.3. Early transition metals such as V and Mn have a well-defined shift in intensity from approximately 0.5 eV incident energy and 0.5 eV energy transfer for Mn to nearly 1.75 eV incident energy and 4 eV energy transfer for V. This contrasts with late transition metals
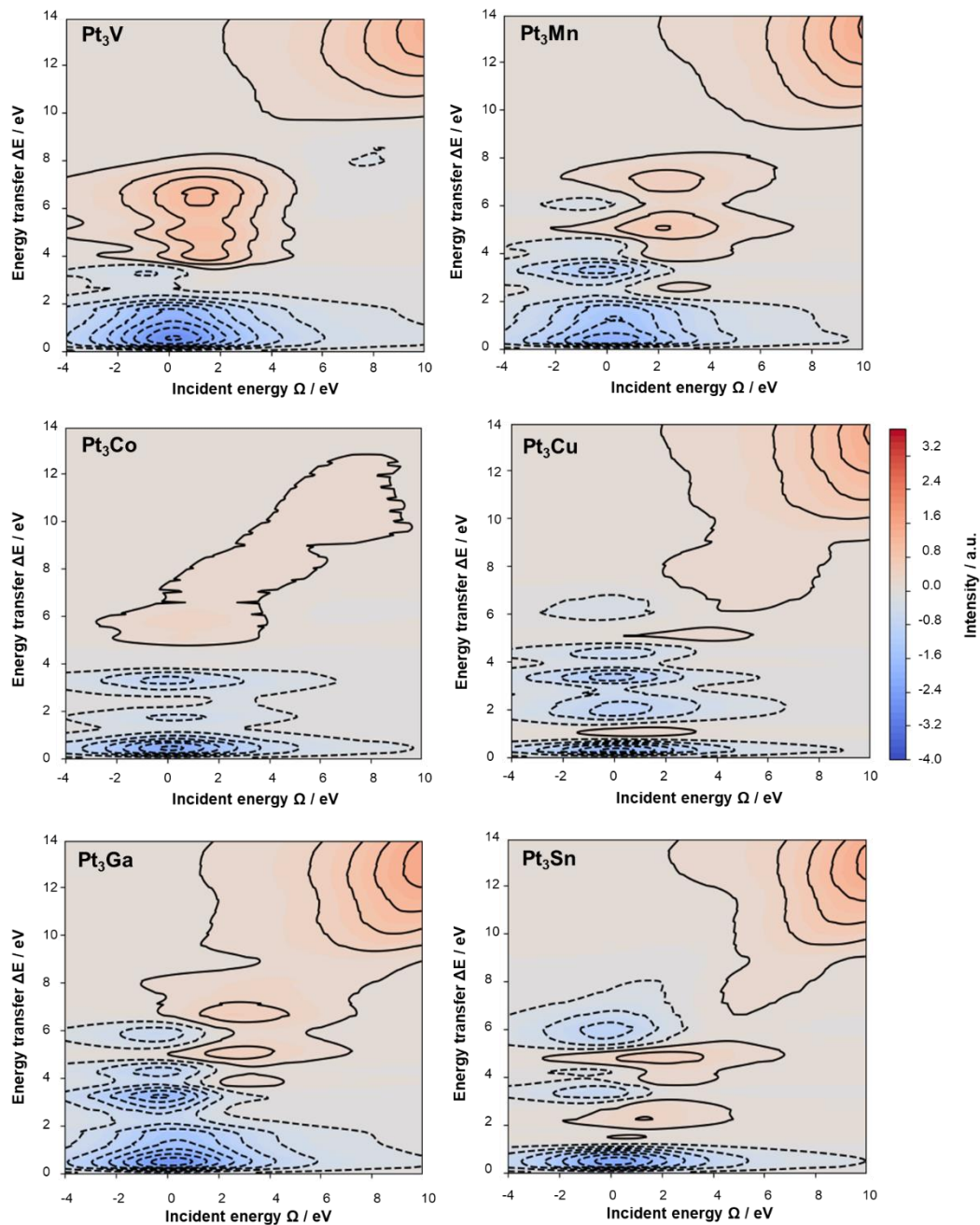
Figure 12.3 Simulated difference RIXS plots for a subset of the intermetallics. Each plot is shown at 45% dispersion, relative to a similar 45% dispersion pure Pt particle. The 6 other intermetallics considered can be found in APPENDIX J.

like Co and Cu where the shifts have lower intensity, indicating greater similarity to pure Pt. The shift to higher incident and transfer energies is also observed by late transition metals. The post-

transition metals Ga and Sn have more intense transitions than late transition metals, with a shift to higher incident and transfer energies.
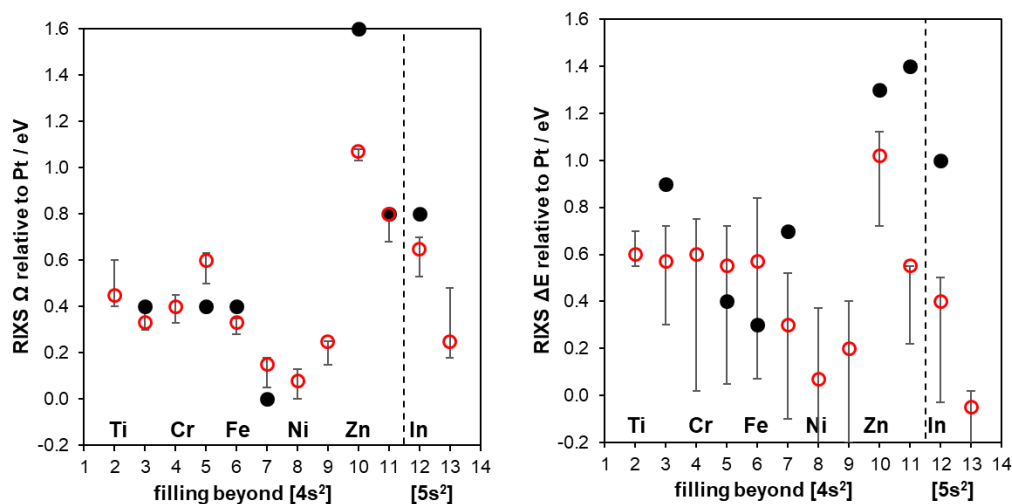


Figure 12.4 Direct comparison of simulated RIXS spectra from DFT calculated Pt d-DOS and experimental RIXS spectra. Error bars correspond to 30%-100% dispersion with 45% dispersion plotted.

As the difference RIXS plots are functions of the calculated Pt *d*-DOS, we would like to compare the experimental and simulated RIXS spectra, to consequently relate shifts in the incident energy and energy transfer to the calculated electronic structure of Pt. To extract the location of the high energy peak, which would correspond to the highest intensity of emitted X-rays, a 2-D Gaussian function is fitted to the RIXS map for each bimetallic, and then compared to pure Pt. This was calculated for each bimetallic alloy, and particle dispersion. The absolute energy of the simulated high intensity peak is likely unreliable, as all simulated spectra are reference to the Fermi energy in vacuum, as opposed to measured spectra which are referenced to the core, but also the Fermi edge. From calculations in APPENDIX J, the work function of each alloy surface is like pure Pt, reflecting a consistent difference in between each alloy and the pure Pt reference state. A complete table of simulated incident energy and energy transfer maxima is provided in APPENDIX J.

Simulated and experimental RIXS spectra for each bimetallic relative to pure Pt was compared according to the shift in high intensity peak for incident energy and energy transfer. These results are shown in Figure 12.4. The incident energy peak maximum decreases with filling of the *d*-band up until PtZn where the *d*-band fills, and the incident energy maxima are larger. PtZn

and the post-transition metal promoters Ga and In have similar incident energy maxima; yet, the incident energy maximum of Sn is lower by nearly 0.4 eV. The agreement with experiment is in general exceptional considering the convolution of occupied and unoccupied states using GGA level DFT. The MAE of predicted RIXS incident energies is 0.17 eV. Possible explanations for this agreement are that the RIXS process only includes states close to the Fermi energy, where the one electron GGA wavefunctions are still reasonable, as opposed to simulations of XAS where the inclusion of high energy states causes the electron density to fail when electrons become localized. In comparison to XPS, core-hole effects are reduced as in the RIXS process, a valence $d$-electron fills the core state, and so the RIXS final state only involves a hole in the valence states. Finally, shifts are reported relative to a reference state (pure Pt) which may fortuitously cancel some of the intrinsic DFT errors and magnify the more salient changes in the $d$-DOS. The role of changing particle size from 1.5 nm to 3 nm in the simulations has a relatively small effect (largest being Pt3Sn with a size effect of ~0.2 eV), which reflect changes in the $d$-DOS with dispersion as shown in Figure 12.2 and which not explained by changes in strain.

Energy transfer includes the relative energy change between the excitation from the core to unoccupied valence states compared to the decay from the occupied valence to the core. The energy transfer therefor relates to a relative change in the occupied and unoccupied states, as opposed to the incident energy which measures the unoccupied states. The discrepancy between simulated and experimental RIXS is much larger, which may be attributed to the sensitivity in the relative shifts between unoccupied and occupied states with particle size. This could also reflect more experimental occupied states at lower energies than those modeling with DFT. The $d$-band becomes narrower for undercoordinated surface atoms, which manifests as a pronounced particle size effect for all promoters. The particle size effect for incident energies which correlate with the unoccupied states is smaller than the energy transfer term, which indicates that the size influences the range of occupied $d$-DOS states. This can be seen in the $d$-DOS of Figure 12.2, where the change in unoccupied peak position only weakly shifts with dispersion, as opposed to the spread in occupied states. While the trend in early transition states is captured, there is a large deviation for the post-transition metals which results in a MAE of 0.41 eV. As the post-transition metals exhibit a tensile strain, it is possible that post-transition metal intermetallic nanoparticles have strain interactions which cannot be captured in a (111) slab model. This would be consistent with the particle size argument, as the incident energies are well-reproduced for the post-transition

metals which could indicate a size or strain effect which shifts the occupied states and causes the slab model to under-estimate the energy transfer.

### 12.3.4 Spectra correlations with *d* band shape

From simulated RIXS spectra using Pt *d*-DOS which correlate to experimental measures of Pt valence orbitals in nanoparticle catalysts, correlations between features in RIXS spectra and features in the Pt *d* states would strengthen the chemical intuition of using the RIXS as a predictive tool to designing alloy catalysts. The most straightforward correlation expected would be to relate a feature of the RIXS, either incident energy maxima, emission energy maxima, or energy transfer maxima, directly to the *d*-band center. While a correlation exists between the emission energy and *d*-band center (APPENDIX J), the *d*-band center is the relative position of the total band center, including occupied and unoccupied states, to the Fermi energy. This does not directly include the splitting of Pt alloy states as observed in Figure 12.2. Additional augmentations of the d-band theory, such as including the width of the band, the kurtosis of the band, or the maximum of the Hilbert transform[291], do not significantly improve correlations (APPENDIX J). We can improve these correlations by considering the spectroscopy process itself as a basis for alternative descriptors. One observation is that RIXS spectra is a convolution of the product of occupied and unoccupied states. This strict separation of states lying above and below the Fermi energy provides intuition about how a model which includes the full span of possible *d*-states, both occupied and unoccupied, such as the *d*-band center would not capture the energy transfer changes or incident energy changes which rely on the convolution of separated electronic states.

The centers of states lying above and below the Fermi level can be related to the corresponding incident energy maximum and emission energy maximum, which was calculated by the general relation $\omega = \Omega - \Delta E$. As shown in Figure 12.5a, the center of occupied *d* states underestimates the RIXS emission energies; however, the correlation between the two quantities is interesting considering RIXS emission energies include the full convolution integral and broadening function. In general, as the maximum of the emission energy maximum shifts with the occupied *d* states. A similar analysis for incident energies and the center of unoccupied *d* states is provided in Figure 12.5b with a similar average error as Figure 12.5a. The correlation is strongest for smaller shifts in unoccupied states, below 0.4 eV relative to the Fermi energy, likely due to weaker interactions with occupied states in the integrand. The correlation is worse at high energies,
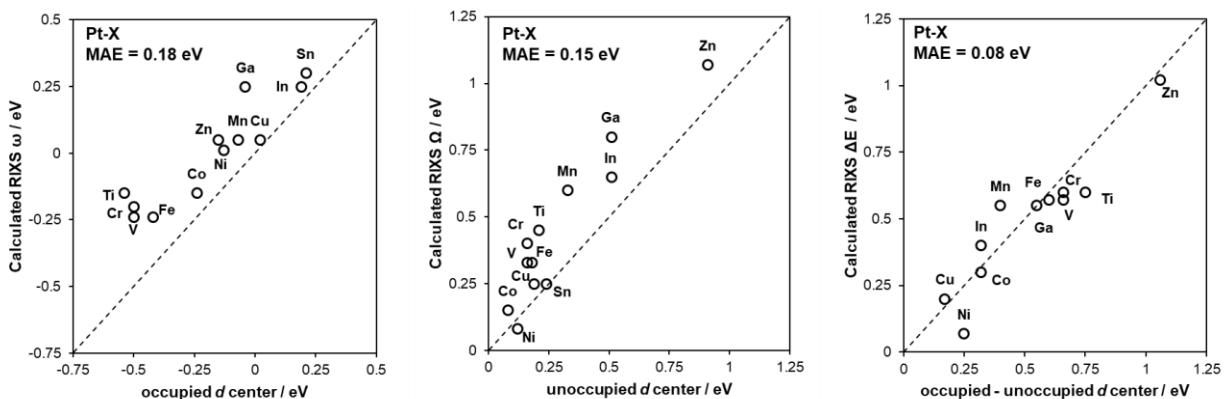
Figure 12.5 Correlations between simulated RIXS spectral features and separated *d* band descriptors across all bimetallic alloys in 2 nm particles.

where the unoccupied *d* center underestimates RIXS incident energies, which includes Zn, Ga, In. If incident energies involve favorable excitations from the core, and emission energies the favorable decay of filled Pt states to the core, it is proposed that the high intensity peak of the energy transfer would correspond to the difference between peaks in the incident and emission energy, which can be approximated by the center of unoccupied and occupied *d* states. Consequently, we propose that the RIXS energy transfer can be interpreted as proportional to the difference between the unoccupied and occupied band center. This relation is shown in Figure 12.5c, with a low MAE of 0.08 eV. There is some favorable error cancellation in the energy transfer relation, as the variance of the relative difference in unoccupied and occupied states is lower than each individual state (0.18 eV for Figure 4A, and 0.15 eV for Figure 12.5b). The range of bimetallics considered spans a range of 0 eV to 1 eV relative to pure Pt, and with a clear physical interpretation as the difference in the center of unoccupied and occupied *d* states. Discrepancies in these relationships may be due to coupling between occupied states which is implicit in the RIXS spectra and neglected in the band center analysis. The core-hole lifetime of Pt, $\Gamma$ in the RIXS equation and used as an experimental parameter contributes to changes in the high intensity peak position.

The *d* band model has found success in heterogeneous catalysis by its intuitive nature of relating the filling and shape of the metallic *d*-band to overlap and exchange with molecular adsorbates. To relate RIXS spectra, capable to probing *d* states, to the *d* band model provides additional intuition for how to best apply this technique in both the explanatory and predictive

determination of the strength of chemical bonding for reactive intermediates and transition states which can then be related to kinetics. In light alkane dehydrogenation, studies of catalyst deactivation has drawn considerable attention recently[276], [300] where the stability of atomic carbon (C), methylidine (CH), and ethylidine (CCH$_3$) has been discussed as the products of C-C bond cleavage in propane dehydrogenation that can irreversibly bond to Pt surfaces and result in coking. As current industrial processes require periodic regeneration, the stability of these coke precursors was used as a design variable to provide the link between RIXS spectroscopy and the deactivation process. This provides a natural system with which to develop RIXS correlations, although in general we note that this analysis is not inherently specific to carbon-based intermediates. To develop RIXS correlations it was necessary to determine if RIXS spectra could be related to adsorption, and whether any chemical intuition could be gained from this connection.

### 12.3.5  RIXS description of adsorption

Probe molecules relevant to deactivation; CH$_3$, CH$_2$, CH, C, and CCH$_3$ were adsorbed to the alloy slab surfaces. Larger molecules, such as other ethane or propane intermediates, were not considered as the 2x2 slab constructed for spectroscopy calculations would be too small to consider the full reaction network, and the purpose of the present study was to provide fundamental links to spectroscopy, which is more readily approached with simplified probe molecules. Despite this caveat, as expressed previously, these probe molecules have been discussed previously as precursors to other deactivation intermediates. To simplify the analysis specific the convolution of states, the core-hole broadening term of the RIXS equation was set to unity such that

$$F(\Omega, \omega) = \int_{-\infty}^{0} d\epsilon \frac{\rho_d(\varepsilon)\rho_d{'}(\varepsilon+\Omega-\omega)}{(\epsilon-\omega)^2+1} \tag{12.3}$$

Calculated energy transfer maxima using this modified expression differed on average by 0.02 eV, thus simplifying the interpretation but maintaining a similar energy maximum. Changes in the core-hole broadening term does; however, change the shape and dispersion of the simulated RIXS distribution, which would be important when fitting parameters away from the maximum value. Thus, care should be taken in ensuring a reasonable core-hole broadening term for analysis away from the high intensity peak. As adsorption is a surface process, the approximate nanoparticle models used to find correlations with experimental spectra will be replaced by RIXS spectra of the surface Pt atoms in the alloy, derived from the 100% dispersion DOS in Figure 12.2. Thus, all d bands and RIXS spectra will be of only surface Pt atoms in the slab.

The strain on Pt atoms induced by alloying or structural changes can influence the adsorption energies of intermediates. To examine whether differences in binding energies on alloys can be understood as Pt strain effects, the adsorption of carbon intermediates was considered by taking the relaxed alloy surface and replacing promoter atoms with Pt to produce a uniform Pt slab at the same strain as when alloyed. The results are summarized in Figure 12.6 where dark circles represent the adsorption energy of unsaturated carbon intermediates at the most stable adsorption configuration. For all (111) alloy surfaces CH3 was most stable at Pt top sites, CH2 was most stable on Pt-Pt bridge sites, while CH and C were most stable in 3-fold Pt-Pt-Pt hollow sites. For Pt3Ti and Pt3V, CH2, CH, and C interacted strongly with the promoter metal causing adsorption to include the promoter metal as compared to the other promoters. For the PtZn (011) surface, CH3 was most stable on Pt top sites, while CH2, CH and C were most stable of Pt-Pt bridge sites. Representative adsorbate structures are shown in the APPENDIX J. Red circles are the adsorption of the same intermediate on a pure Pt slab (both surface and all subsurface layers) at the same strain, constructed by directly replacing promoter atoms with Pt. The strain induced by the promoters had minimal effect on CH2 and CH3 adsorption, yet the binding energies of these intermediates with promoter metals change by nearly 0.7 eV for CH2 indicating the strain effect on adsorption is small at these alloy compositions and identities.

Adsorption of the more unsaturated intermediates, CH and C, show a more pronounced stain effect, where the binding energy of C on strained pure Pt varies by just over 0.4 eV across the range of promoter metals and the binding energy of CH on strained pure Pt varies by nearly 0.2 eV. Despite a stronger strain effect, the range in C binding energies is over 1.4 eV and the range in CH binding energies is over 1.6 eV. As C and CH intermediates adsorb to 3-fold hollow sites, and therefore interact with 3 surface Pt atoms, the change in Pt-Pt distance more strongly influences coordinative bonding with intermediates. A table of relevant Pt-C bond distances for different intermediates is provided in APPENDIX J. The binding energy of C and CH also do not seem to correlate with strain, indicating again that while strain effects do influence the adsorption of carbon intermediates, it does not explain neither the shape of Pt d-DOS nor trend in carbon adsorption energy. As discussed previously, the work functions of alloy surfaces and Pt surface Bader charges are nearly constant across the range of promoter metals, which cannot explain differences in adsorption between the intermediates. We therefor hypothesize that the predominant electronic effect of alloy formation is the splitting of occupied and unoccupied states observed in

the Pt d-DOS of figure 12.1, and consequently the RIXS energy transfer observed from simulations and experiment.
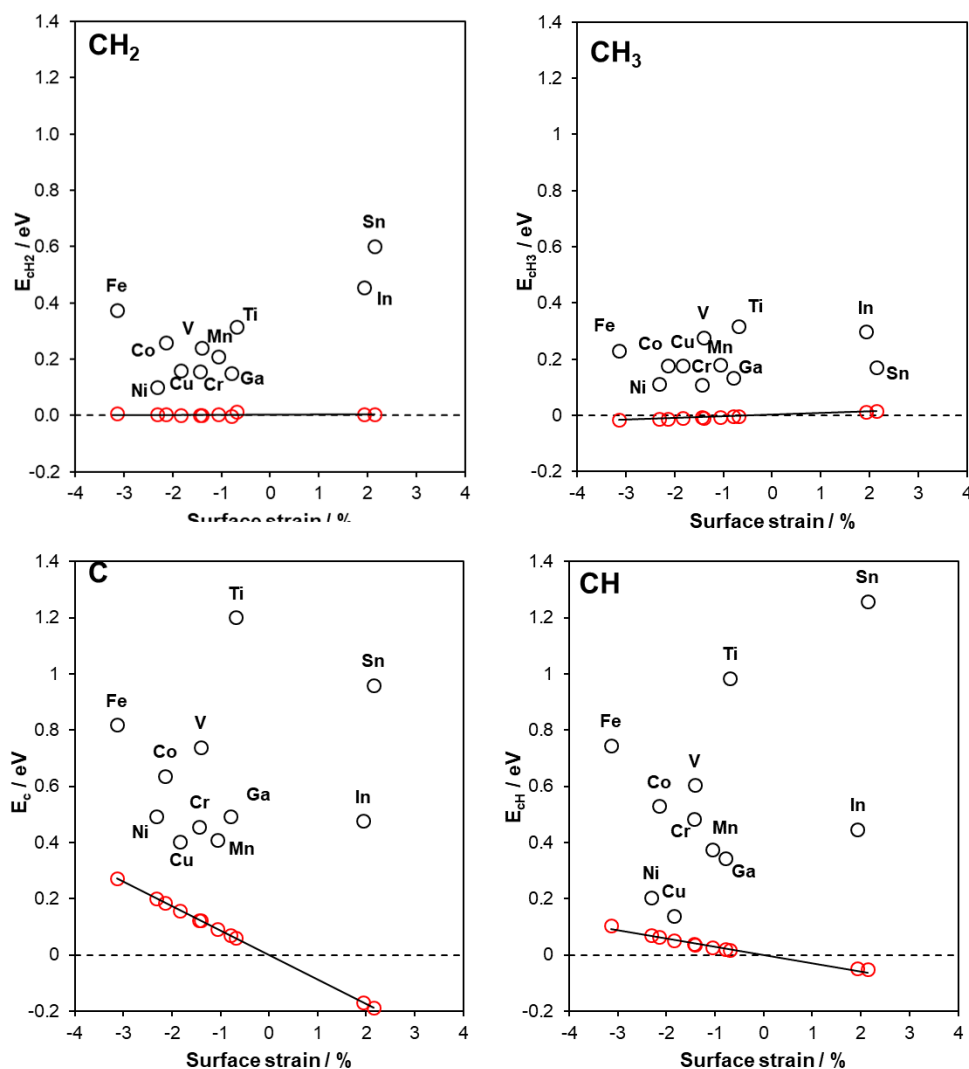


Figure 12.6 Adsorption of unsaturated methyl intermediates on alloy (black circles) and strained Pt surfaces (red circles) plotted against the surface strain. The origin corresponds to adsorption on an unstrained pure Pt surface.

The relation between the simulated RIXS energy transfer and adsorption is provided in Figure 12.7a, where strong correlation with the adsorption of carbon intermediates is observed. The 4d post-transition metal promoters are excluded from this relation, due to their exerted tensile strain; however, Ga has been included. Due to its tetragonal unit cell structure, the closest-packed surface for PtZn is (011) where adsorbates have a unique coordination number as compared to the

(111) surfaces. The energy transfer predicted for surface In and Sn promoters is negative relative to platinum, -0.07 eV and -0.22 eV, respectively. This would indicate occupied and unoccupied band centers of these promoters are in fact closer than they are for surface Pt atoms. The adsorption of C is weaker than pure Pt, 0.48 eV and 0.96 eV respectively, which cannot be explained by the theories presented here. The 4d post-transition promoters are significantly larger than the 3d post-transition metals, and the method of bonding may differ from the 3d metals. We hope this would encourage future RIXS studies for the 4d metals. For the 3d transition and Gallium; however, the correlation between calculated RIXS energy transfer and adsorption is apparent. Mean absolute errors largest for CH, 0.14 eV, while the correlation with other adsorbates are on the order of 0.06 eV. The larger errors in CH is due to the influence of oxophilic promoter metals in perturbing adsorption sites. APPENDIX J constrains the position of CH for Ti and V promoters to the same sites as the other alloys, which reduces the MAE to 0.10 eV. The adsorption of atomic carbon has been traditionally difficult to predict due to its strong multiple bonds to the metal surface, so we have benchmarked the choice of splitting in the d band against other traditional descriptors, such as the modified d band center[307], kurtosis, and skewness, as well as comparisons with the simplified occupied and unoccupied d states, as well as the Hilbert transform maximum[291], where we find the usage of the RIXS convolution has a MAE lower than any of the previous descriptors for C.

Many descriptors have difficulties in systematically treating both late-transition and early-transition metals, and much work has been focused on treatment of the late transition metals such as the Hilbert transform maximum by Xin et al[291]. The accuracy of the RIXS convolution as a descriptor for adsorption in alloys can be understood through analogies with the original Newns-Anderson models for adsorption[43], [44], where the strength of interaction is related to the coupling of metal electronic states projected onto adsorbates. Simplified d band descriptions correlate the interactions of the metal states to first order by their mean, and the relative shifts in band filling captures the relative alignment of metal and adsorbate bands to the Fermi energy. In comparing Pt atoms promoted by interaction with alloy metal atoms, the band centers are similar; however, the large degree of splitting is captured in part by the modified d-center including bandwidth byX. We can contextualize the RIXS integral as including the convolution of occupied and unoccupied d states relative to the Fermi energy, thus reminiscent of the full Newns-Anderson treatment where the distribution of occupied and unoccupied states includes higher order

perturbations in the d-band. Therefore, the RIXS integral is an extension of the d band theory which directly includes the relative distributions of the band, in the spirit of the Newns-Anderson theory.
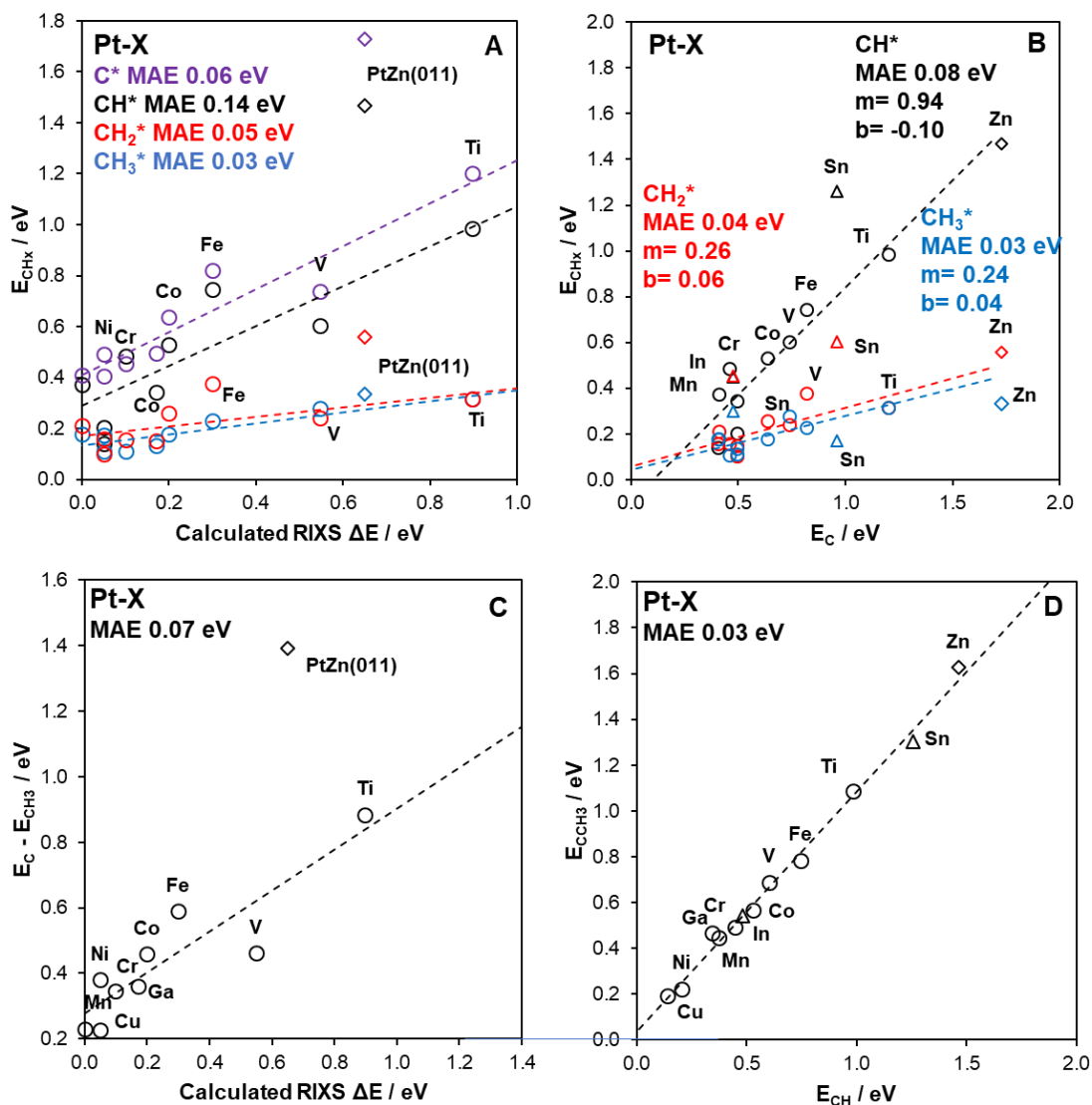


Figure 12.7 A) binding energy of carbon intermediates (C, CH, CH2, CH3) and calculated RIXS ΔE for the range of Pt-X bimetallics relative to pure Pt (Pt3X unless noted otherwise). Pure surface RIXS (100% dispersion). B) Scaling relations of CH, CH2, and CH3 against atomic carbon (C*) for the range of Pt-X bimetallics relative to pure Pt. M and b refer to the slope and intercept, respectively. C) Relative binding energy of C* and CH3* referenced to pure Pt for the range of Pt-X bimetallics. D) Scaling relationship of CH* and the chemically similar intermediate CCH3*.

The binding energy of the set of unsaturated carbon intermediates including C, CH, CH2, and CH3 are presented in Figure 12.7b, where the adsorption of each hydrogenated species is

compared to atomic C. These scaling relationships, first derived by Pedersen et al[45], have been broadly applied to a wide range of catalysts to understand the behavior of chemically similar adsorbates[76], [113], [308], [309]. From bond order conservation arguments, which define the slopes of scaling relationships, the slope of C/CH3 is expected to be 0.25, for C/CH2 is expected to be 0.50, and 0.75 for C/CH. Each relationship is regressed for the 3d metals, excluding Zn which forms a (011) surface termination. The 4d post-transition promoters, In and Sn, are excluded as they exert tensile strain as opposed to the other promoters. All three scaling relationships have MAEs less than 0.08 eV, likely due to a similar adsorbate structure. The slope of the C/CH3 relationship is 0.24, as expected for bond order conservation. This is unsurprising as for all bimetallics CH3 adsorbs to the top sites, and thus the coordination number is identical. The intercept is close to 0 eV, as all energies are referenced to pure Pt. The slope of C/CH2 is 0.26, not significantly different from C/CH3 despite a predicted slope of 0.50. This is due, in part by the interactions of CH2 intermediates with the oxophillic Ti and V promoters. APPENDIX J includes the same scaling relationships where CH2 is fixed in a configuration away from the promoter metals. In this case, the slope increases to 0.59 as both the C and CH2 adsorbates are fixed to the same site. For C/CH, the slope is greater than the predicted value of 0.75. In fact, the predicted slope is close to 1, which would only occur if the number of bonds being formed to the surface for both C and CH were the same. This is unlikely, as atomic carbon binds strongly to the surface. Similar to CH2, interactions of oxophilic promoters with the adsorbate states will shift the adsorption sites and change the location coordination for those promoters specifically. Even when constraining the position of CH and C adsorbates in APPENDIX J, the slope increases to 1.35, with a large intercept of -0.31 eV relative to platinum. The large slope and intercept indicate significantly different electronic interactions for C and CH among the different promoters which produces large deviations the predicted slopes and intercepts. Surface dipole interactions have been discussed by Choki and Majumdar as causing deviations from bond order conservation[310]. Upon alloying, atomic carbon is forced away from an fcc hollow site to the 3-fold hollow site, which breaks the typical binding configuration of carbon in fcc metals.

The existence of scaling between such carbon intermediates allows for the binding of different coke precursors in alloys to be related to each other, reducing the space of necessary calculations. In addition, it provides a consistent comparison between the sensitivity of adsorption of each intermediate to promoter identity. For example, the stability of CH3 groups do not change

significantly across the range of promoters examined. Intermediates which interact more strongly with the surface and subsurface such as C and CH, have binding energies which vary by up to nearly 1.4 eV in comparison to pure Pt. This dramatic tunability is attractive for catalysis, where in this case we seek maintain the dehydrogenation rate while preventing deactivation. We have shown that regardless of the promoter we choose, the CH3 adsorption energy, which is a proxy for the initial CH bond activation, for example in ethane or propane, which will similarly adsorb at top sites, is not perturbed. We do find, however, that the stability of coke precursors C and CH is significantly affected. We therefor seek to relate this to the relative splitting of Pt d orbitals in alloys.

Through choice of promoter metal, the degree of splitting in occupied and unoccupied orbitals can be controlled to selectively destabilize CH as compared to CH3 on Pt. This stabilization is not due to geometric differences in each Pt3X bimetallic, but rather by electronic functionalization of the Pt atom, induced by the promoter. This selective destabilization of unsaturated intermediates can be more easily seen in figure 12.7c where the differential binding energy of CH3 and C is plotted against the splitting of Pt d orbitals. PtZn does not lie on this relationship, as the adsorption site of C on PtZn is a Pt-Pt bridge as opposed to a 3-fold hollow site. The effect of changing local coordination structure has been proposed as a method for changing the underlying scaling relationship[77]. The extension to other coking precursors, like CCH3, is shown in figure 6d where the binding energy of CH is directly related to CCH3. CCH3 and CH occupy the same adsorption geometry (a 3-fold hollow site) and so their binding energies can be directly correlated and related back to the degree of splitting in occupied and unoccupied d states.

While the set of adsorbates chosen in this study is limited to single carbon atom adsorbates, we can highlight how these relationships are related to larger adsorbates with similar adsorption moieties. Figure 12.6d describes the relationship between adsorption of CH and CCH3, both relevant coking precursor molecules[300]. The relation between these species has a slope of 1, as both molecules bind through a similarly undercoordinated carbon center. All of the promoter metals, including the 4d post-transition metals Sn and In, as well as the 1:1 PtZn bimetallic fall on the same relationship, as CH and CCH3 adsorb at the same sites, producing a consistent slope. This provides the generalization of how these relationships between adsorbates and correlated to RIXS spectroscopy can be applied to other reaction chemistries of interest.

## 12.4 Conclusions

The role of promoter metal identity in alloys for heterogeneous catalysis has been a topic of fundamental importance since the early days of Sinfelt and coworkers. In this contribution, we have shown how new developments in spectroscopy (namely RIXS) have introduced new avenues for understanding how electronic functionalization of platinum can be performed by judicious choice of promoter. The specific physics of the spectroscopy, which do not include strong core-hole interactions in the final state, permit greater accessibility for GGA level DFT theory to connect with experiment, and help both validate and understand experimental data, which can then be used to predictively design new catalysts. The capability of GGA-level DFT theory to predict high intensity spectral features of RIXS is striking, although not altogether unexpected as RIXS probes the energies of electronic states close to the Fermi level. Through simulation of RIXS spectra, we have provided fundamental correlations which relate elements of the spectra obtained (incident energies, emission energies, and energy transfer) to moments of the d-band (unoccupied state centers, occupied state centers, differences between unoccupied and occupied states). These simplified d-band moments in the style of Hammer and Norskov neglect the convolution of states captured in the RIXS, yet to first order capture the fundamental chemistry of the observed shifts to provide a more intuitive understanding of the changes in Pt d-states. This connection may be especially other studies involving other alloy compositions or promoter identities.

We have also shown how the selective destabilization of unsaturated carbon intermediates can be understood as the modulation of d-state splitting by an electronic promoter effect. This splitting is experimentally accessible through RIXS spectroscopy and provides direct comparison with computational studies. We believe this method of analysis to be especially useful to study the effects of coking in light alkane dehydrogenation where the measurement of deactivation kinetics and catalyst stability are of primary interest. Beyond RIXS as a measure of adsorbate stability, we also propose that RIXS modeling can be employed as a structural diagnostic tool, where shifts in metal d-states due to changes in the general coordination number can be used as fingerprints for analyzing effect of surface coordination on electronic states. The rules which determine the correct choice of promoter metal, based on electronic effects, requires descriptors which are both accurate, but also directly accessible to experiment and theory, in order to further unify studies of catalysis such that combined approaches can be verified and expanded upon. Here we have provided a method by which properties of adsorption can be described by expanding the classical chemical

descriptors such that they are accessible to experiment and providing a rational ordering to the stability of coking intermediates.

# 13. MODELING DIFFUSION OF GOLD IN THE AU/TS-1 CATALYST

## 13.1 Introduction

Epoxidation reactions, such as the formation of propylene oxide from propylene, represent a considerable challenge for partial oxidation catalysis due to the allylic carbon in propylene which requires a soft oxidant to prevent combustion or unselective side reactions. Industrial processes to produce propylene oxide include the chlorohydrin process, which is undesirable due to the cost of using chlorine as an oxidant.[21] An alternative oxidant, hydrogen peroxide, has been discussed as a replacement to the chlorohydrin process, and has been developed by Taramasso and coworkers using a zeolitic titanium silicate (TS-1).[311] While the hydrogen peroxide process has been commercialized, there are drawbacks such as the flammability of hydrogen peroxide as well as its poor stability in liquid. Hydrogen peroxide must be produced on-site, requiring expensive separation processes.[22] It would be more efficient if hydrogen peroxide could be produced *in-situ* during epoxidation, allowing for a one step process where hydrogen and oxygen gas could be co-fed with propylene. Haruta found that nanoclusters of gold dispersed on titania could catalyze propylene epoxidation with hydrogen and oxygen, where it was thought gold formed hydrogen peroxide which would then epoxidize propylene on titania sites.[312], [313] These catalysts had low rates and poor hydrogen selectivity driving recent efforts to optimize bifunctional Au/Ti catalysts.

While small gold particles expose undercoordinated atoms which are responsible for chemical reactivity[314], the high temperatures during reaction conditions make stabilization of catalytic active sites in gold a considerable challenge. Additionally, turnover rates per catalyst mass could be improved by the isolation of titania sites using a zeolite environment, such as the TS-1 catalyst.[315]–[317]. Determination of the atomic structure of the Au/TS-1 catalyst remains necessary to obtain a fundamental understanding of how gold and titania active sites influence epoxidation catalysis, and what role the zeolite framework has in stabilizing reactants and transition states. Previous reports have proposed that nanoclusters of gold in the micropores of TS-1 catalyze epoxidation, in close proximity to framework titania sites.[318] DFT studies have also corroborated that gold trimers are stable in the TS-1 framework and catalyze direct epoxidation of propylene.[319], [320] In addition to small gold clusters synthesize by deposition, the Iglesia group

has deposited larger clusters (~1.3 nm and 2.0 nm for LTA and MFI) which are stabilized by encasement in the zeolite framework.[321] New synthesis methods developed by the Corma group have shown how small metal clusters can be stabilized in the chabazite framework, and remain stable under high pressures of hydrogen and oxygen gas.[322] These reports indicate the structure and function of metals incorporated into microporous frameworks is relevant to synthesizing stable catalysts not just for epoxidation chemistries, but other oxidation reactions which require bifunctionality.

Here a fundamental study of small gold nanoclusters in the TS-1 catalyst is presented to understand how diffusion and agglomeration of gold under reaction conditions dynamically restructures active moieties of gold atoms which form hydrogen peroxide. Ab-Initio molecular dynamics and Metadynamics were employed to determine diffusion barriers across the sinusoidal and straight channels of the TS-1 catalyst as well as intersecting chambers. The degree of electronic stabilization of titania sites in TS-1 micropores was shown to be negligible when interacting with $Au^0$ clusters, indicating no strong preference for gold nanoclusters to sites in proximity to titania. Moreover, monomers, dimers, trimers, and tetramers of gold readily diffuse through the micropores at reaction temperature, indicating the Au/TS-1 catalyst to internally sinter into TS-1 intersections. This agrees with TEM experiments showing growth of surface Au particles upon heating, caused by diffusion of internally entrained gold from the micropores to agglomerate at the TS-1 external surface, resulting in reduced epoxidation rates. The diffusion of nanoclusters is governed by the entropy loss associated with diffusion through pore channels as opposed to pore intersections, which affords reduced rotational entropy. This presents the TS-1 intersectional spaces as a natural thermodynamic sink for small gold. Therefore, it becomes important to consider how to stabilize gold clusters in the zeolite framework, either through synthetic defects or by the topology of the zeolite framework introducing physical constraints.

## 13.2  Methods

### 13.2.1  Static density functional theory methods

The Vienna An-initio Simulation Package (VASP) was used for all calculations.[82], [84], [87] A MFI zeolite framework was obtained from the IZA database[72]. Hibbitts and coworkers have shown how MFI structures obtained from the IZA database are unstable with respect to their

global minimum,[323] where ab-initio molecular dynamics can restructure the framework. While the elevated temperatures used by Hibbits were not employed in this work, the AIMD simulations of this work was able to relax structures away from the IZA predicted metastable state. The Bayesian error estimation functional (BEEF-vdW)[31] was used for all calculations with a 520 eV cutoff energy and a force convergence criteria of 20 meV/Å. These are like the parameters we have used previously in Sn-Beta and H-Beta. The lattice constants of the siliceous MFI framework were relaxed, and then a single Ti atom per unit cell was introduced at the T6 crystallographic site, based on previous computational reports[320] as well as neutron powder diffraction studies[324] which indicate the T6 site, which lies at the intersection of sinusoidal and straight channels, to be favorable for Ti incorporation. It is likely that other T sites will be populated in addition to the T6 site, as it is unlikely that Ti selectively incorporates to one site; however, the T6 is a good representative site as it faces both the sinusoidal and straight channels of MFI. A bulk gold unit cell was optimized to the same force constraints and with a 10x10x10 gamma centered k-point grid. The optimized fcc lattice constant was 4.22 Å.

### 13.2.2 Ab-initio Molecular Dynamics and Metadynamics

VASP was used to perform AIMD simulations in an NVT ensemble using a Nose-Hoover thermostat.[89] A temperature of 473 K was used which corresponds to the temperature of epoxidation kinetics, along with a timestep of 1 fs. Gold atoms were introduced into the MFI framework and inserted near the Ti center. AIMD was used to help determine locally stable gold cluster configurations, which would have been difficult to find by manually generating configurations. Ultimately, a combination of AIMD, physical intuition from the AIMD, and examination of gas phase gold cluster geometries[325] were all used to generate multiple gold cluster geometries in the channels and intersections of MFI.

Metadynamics calculations were performed in VASP for the MFI framework where the collective variables were defined to be the center of mass of the gold cluster in three dimensions. These collective variables could encode the restructuring and rotation of gold atoms as they diffuse through the framework. Metadynamics was chosen as it would provide free energy barriers for diffusion, as gold would deform from the intersections to channels. Gaussian hills were inserted every 70 fs, with a height of 50 meV and a width of 25meV. This would ensure a gradual change in the filling of the free energy surface to preserve a canonical ensemble at the epoxidation
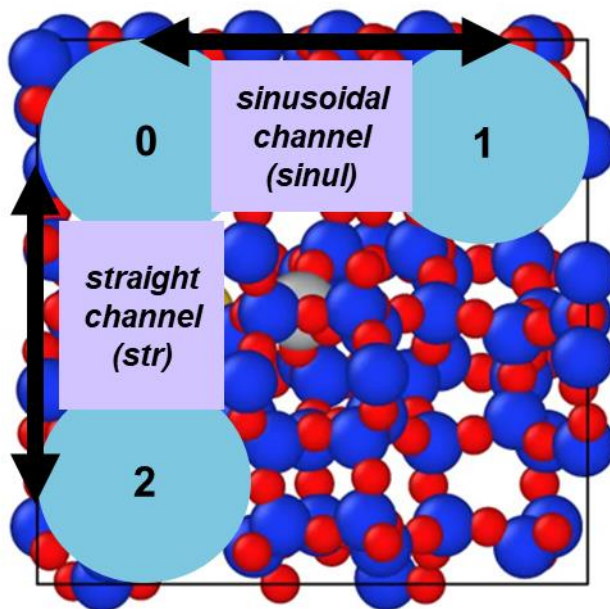
Figure 13.1 Schematic for chamber connectivity in TS-1.

temperature of 200 C. Constraints were imposed on the metadynamic simulation to restrict gold clusters to the intersection where Ti is sited, the adjacent sinusoidal pore, and the adjacent straight pore. MFI unit cells is shown in Figure 13.1 projected along the [001] direction, with three intersecting chambers highlighted (0,1,2). Chamber 0 is proximal to the titanium site, and can be connected to chamber 1 through a sinusoidal channel, or to channel 2 through a straight channel. Chambers 1 and 2 are not proximal to the titanium site. This configuration represents the minimum set of unique connected environments in MFI. Gold atoms were restricted to diffuse only within the three chambers and two channels specified, to reduce the available volumetric space. Thus, throughout this work the straight channel (defined as the path from chamber 0 to 2) and the sinusoidal channel (defined as the path from chamber 0 to 1) as the two unique diffusion pathways accessible to gold in the MFI framework.

## 13.3  Results and discussion

### 13.3.1  Gold cluster stability in TS-1

Gas phase gold clusters from gold monomers up to $Au_{13}$ were constructed with guidance from structures optimized in the literature[325] and incorporated near Ti sites in the framework. Gold reorganization energies are defined by equations 13.1 and 13.2:

$$E_{reorg,gas} = (E_{Au\ gas\ phase\ cluster} - N_{cluster}E_{bulk})N_{cluster}^{-1} \tag{13.1}$$

$$E_{reorg,zeolite} = (E_{Au\ zeolite\ cluster} - E_{zeolite} - N_{cluster}E_{bulk})N_{cluster}^{-1} \tag{13.2}$$

Where $E_{Au\ gas\ phase\ cluster}$ is the energy of gold atoms in a gas phase cluster, while $E_{Au\ gas\ phase\ cluster}$ is the energy of gold atoms confined in TS-1. All energies are referenced to the bulk gold energy $E_{bulk}$ and is formally an excess energy per gold atom. All reorganization energies are positive, as the clusters include undercoordinated gold atoms as compared to the bulk. This is used as a consistent reference state to compare the stabilization of gold in the zeolite framework as compared to the gas phase. Figure 13.2 compares gas phase reorganization energy to gold inside of TS-1 with different geometries, constrained to be a linear chain of gold atoms
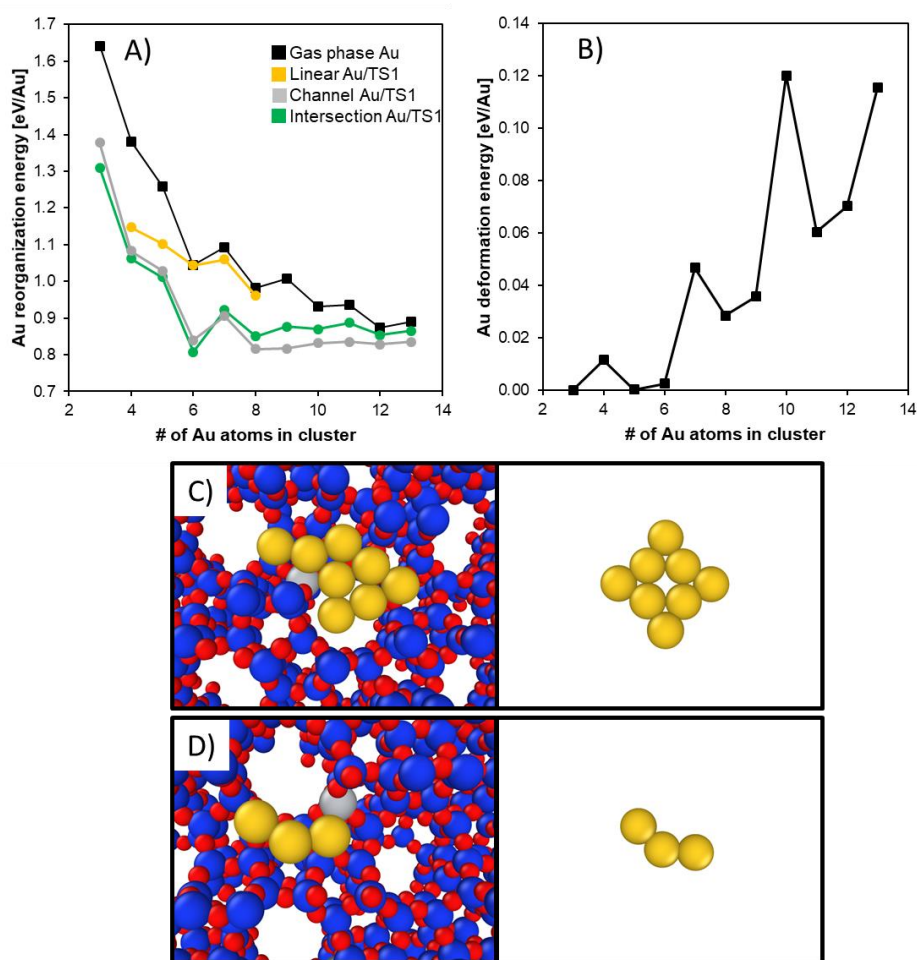


Figure 13.2 Gold cluster stability in the TS-1 framework as a function of gold size relative to gas phase gold. (a) stability of clusters defined as the reorganization energies from eqs 13.1 and 13.2. (b) relative deformation of gold clusters in the gas phase, constraining them and removing from the zeolite. (c) Au$_8$ cluster must deform to accommodate the TS-1 cluster while Au$_3$ (d) does not.

(linear), localized in the channel proximal to the Ti atom (channel), and localized in the intersection containing the Ti atom (intersection). For all atoms, linear chains were unfavored, and gold atoms adopted configurations like that predicted in the gas phase. The lowest energy Au/TS-1 structure obtained from Figure 13.2b were then constrained in all directions, and the surrounding zeolite framework was removed, to calculate the energy of the Au cluster deformed by the framework relative to the most stable gas phase cluster. These deformation energies are provided in Figure 13.2b where for small gold clusters, the deformation upon sorption into the TS-1 framework was minimal, such as the $Au_3$ cluster highlighted in figure 13.2d where no deformation is observed. For larger clusters, such as $Au_8$ highlighted in Figure 13.2c, the gold clusters deform relative to their gas phase, which requires an enthalpic penalty (Figure 13.2b). The deformation energies are relatively small relative to the van der Waals energy in the pore, and for the $Au_8$ cluster, the reorganization within TS-1 lower than for the gas phase, indicating a compensation by favorable van der Waals contacts. Due to the 10-member ring channels in TS-1, reconstructed gold forms more undercoordinated atoms than gas phase clusters reflecting that the porous zeolite framework cannot accommodate the symmetrical gas phase clusters.

### 13.3.2  Adsorption of molecular oxygen

To probe how reconstructed gold clusters in TS-1 affect the adsorption of key intermediates, molecular oxygen was first adsorbed onto each gold clusters, which is the first step in hydroperoxyl formation, where $O_2$ adsorption is followed by dissociation or activation by $H_2$. Oxygen binding energies were found to not be strongly influenced by the presence of titanium, as Figure 13.3a compares oxygen binding energies in Au/TS-1 and Au/S-1 which is the purely siliceous MFI framework. $O_2$ was found to adsorb strongly to undercoordinated gold atoms in each cluster; yet for most clusters the effect of Ti was minimal in affecting $O_2$ binding energies. For $Au_3$, $Au_{13}$, and $Au_8$ undercoordinated gold atoms were in direct proximity to the Ti atom, increasing the $O_2$ adsorption energy. When compared to the constrained gas phase clusters, $O_2$ binding energies were larger when placed in the zeolite framework due to favorable confining interactions (Figure 13.3b). Adsorption of $O_2$ at clusters deformed by TS-1 in the gas phase adsorb $O_2$ more strongly than the lowest energy gas phase gold clusters (Figure 13.3c) where clusters with an odd number of gold atoms bind much more strongly that clusters with even numbers of gold atoms. Except for $Au_{11}$, all other odd numbered clusters bind more strongly than the lowest energy gas phase cluster, where
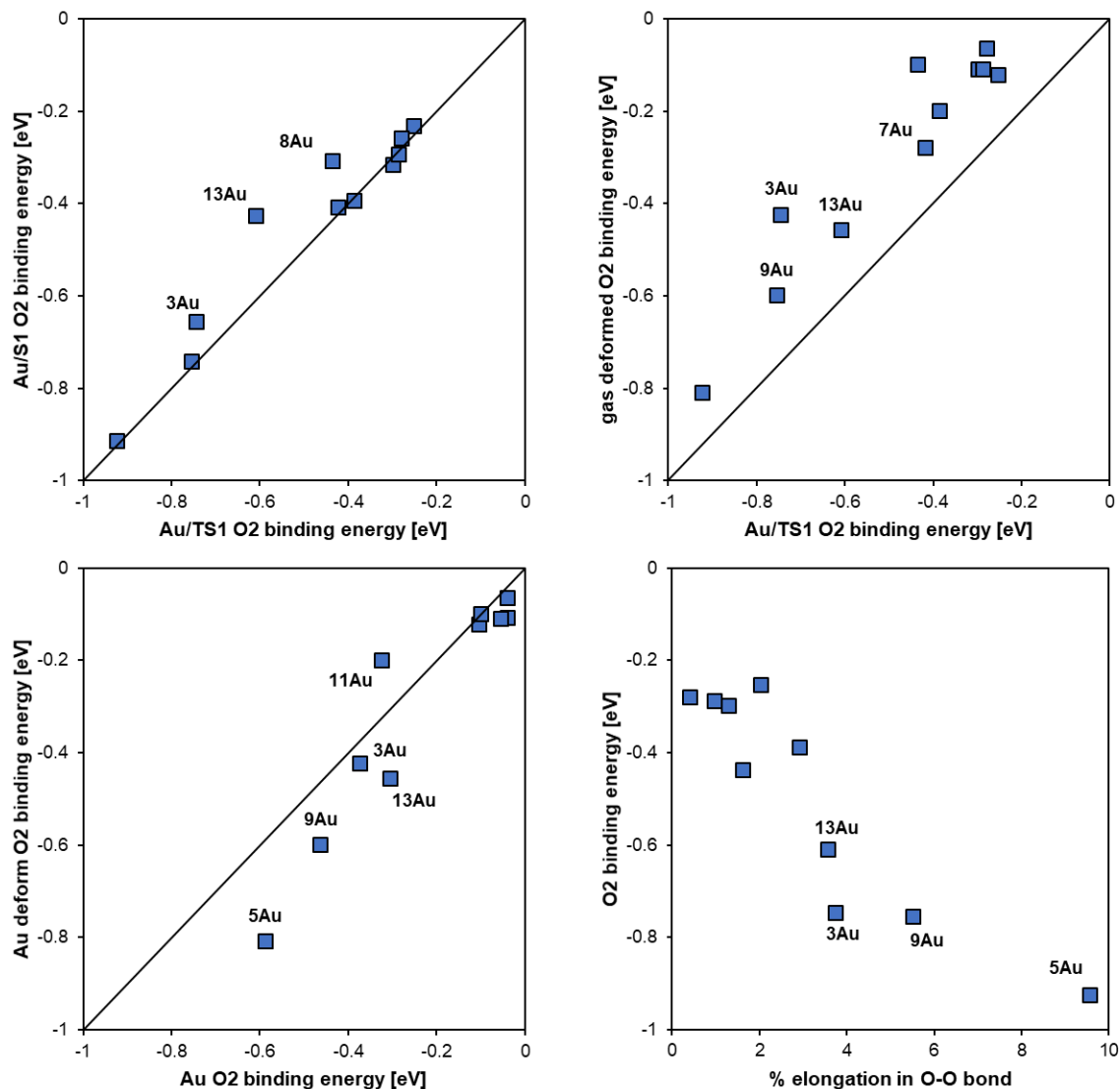
Figure 13.3 (a) binding energy of O2 in Au/TS-1 as compared to the binding energy of O2 in Au/S-1 as a function of gold cluster size. (b) binding of O2 in Au/TS-1 compared with the same Au cluster in the gas phase made by removing the zeolite framework. (c) binding energy of O2 on lowest energy gas phase clusters compared with O2 binding on deformed gas phase clusters. (d) % elongation of the O-O bond upon adsorption in Au/TS-1.

the zeolite deformation reveals additional undercoordinated gold atoms which readily adsorb $O_2$. While these cluster geometries are metastable, they are stabilized by favorable van der Waals contacts with the surrounding pore. For odd-numbered gold clusters there is an unpaired 6s electron which can interact with the triplet spin state of $O_2$, resulting in stronger adsorption. This can be seen by comparing the elongation of the O-O bond upon adsorption relative to the

adsorption energy as shown in Figure 13.4d, where the binding energy of $O_2$ increases with an increasing O-O bond distance.

While $O_2$ binding is stronger for undercoordinated gold sites in TS-1, the range in binding energies is large, indicating the thermodynamics and likely the kinetics of propylene epoxidation are strongly dependent on the size of gold clusters present in TS-1. For all gold cluster considered, the Ti site was either partially or completely occluded from access of gas molecules. Epoxidation rates are almost completely suppressed in Au/S-1 catalysts without Ti[318], indicating Ti sites are necessary for the reaction. If gold in TS-1 is preferentially stabilized at the Ti sites, it is unlikely that propylene or hydroperoxyl species could access Ti sites and react. The rules for site proximity in Au/TS-1 are there for necessary to understand the site requirements of intraporous gold for hydroperoxyl formation.

### 13.3.3 Gold monomer diffusion in TS-1

Gold at 200C was observed to freely restructure during AIMD simulations to obtain cluster geometries, where it was hypothesized that gold clusters may be mobile in the TS-1 framework under reaction conditions. Nudged elastic band (NEB) calculations were performed on gold monomers to probe the height of diffusion barriers when moving from a titanium-containing chamber (Chamber 0) and siliceous chambers (Chambers 1, 2) either by traversing the straight or sinusoidal channels (all references made from Figure 13.1). The gold monomer has no configurational entropy, so a 0K NEB calculation from one chamber to the next would capture the dominant enthalpic changes when diffusing from one chamber to the next.

Figure 13.4a shows how along the (010) crystal facet (corresponding to diffusion from Chamber 0 to 1 along the straight channel) the barrier for diffusion of a gold monomer is less that 0.1 eV across both pores. The chambers are less energetically stable due to the reduced van der Waals energy that better stabilizes monomers in the channel. Chamber 0 contains the Ti atom, and there is no energetic difference between a gold monomer siting in either chamber 0 or 2. As the energetic difference per chamber is small, and there is no diffusion barrier between chambers, gold monomers have no preference for siting near Ti atoms, and the dominant interactions with the TS-1 framework are through confinement. Gold may also diffuse perpendicular to the straight channel along the (110) crystal facet and transfer to chamber 1 along the sinusoidal channel, displayed in Figure 13.4b. The relative energetics of diffusion barriers in the (100) are not significantly different
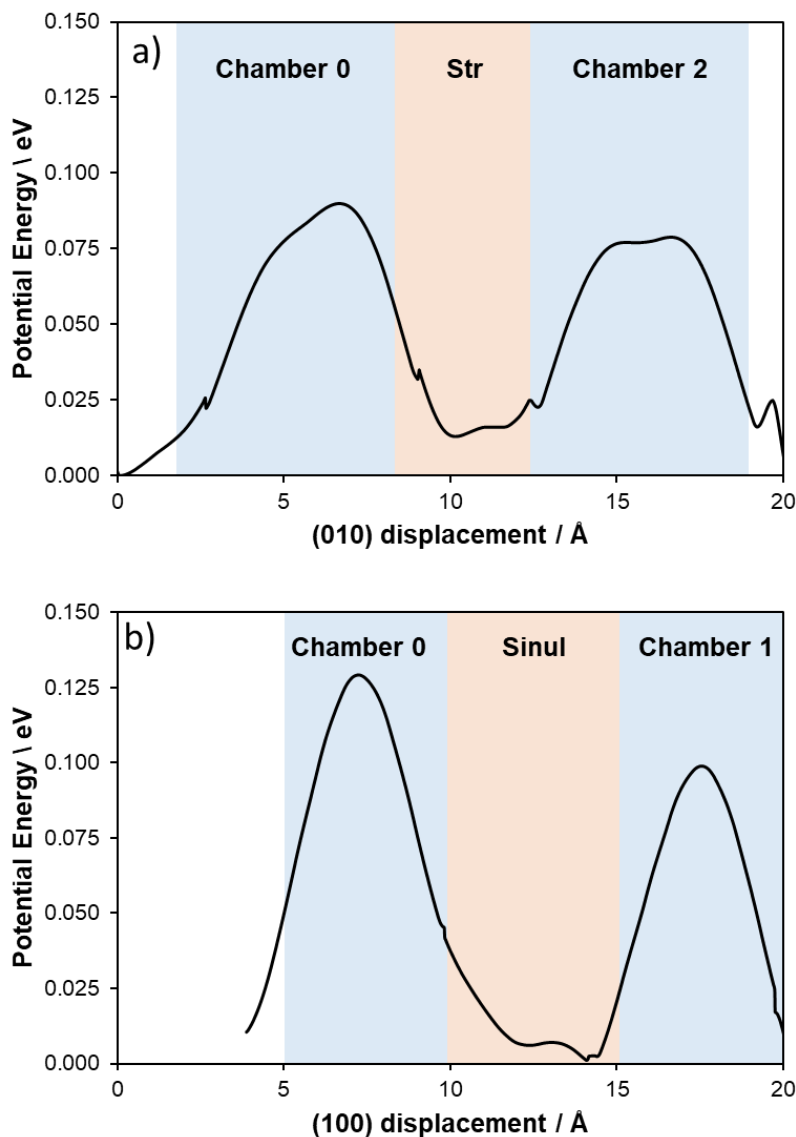
Figure 13.4 Au monomer diffusion potential energy map along the (010) straight channel (a) and the (100) sinusoidal channel (b) calculated using the NEB method

than along the (010), where the differences are on the order of 0.02 eV. There is no preference for the chamber containing Ti, indicating monomers of gold could be randomly dispersed in channels and chambers throughout TS-1.

To study diffusion of larger gold clusters, the configurational entropy of gold is important as for larger clusters the number states available for the gold cluster to re-organize is larger in the chambers than in the channels. Metadynamics simulations were performed on gold dimers, trimers, and tetramers in order to include the contributions of configurational, rotational, and vibrational

entropy of each gold cluster as it diffuses. Each cluster could explore chambers 0, 1, 2 as well as the sinusoidal and straight channels connecting them. Each Metadynamics simulation was run for at least 100 ps, with at least 1450 Gaussian hills added.

### 13.3.4 Gold dimer diffusion

The diffusion of gold dimers in both the (010) and (100) directions was performed using metadynamics with the center of mass of the cluster in each lattice direction a collective variable. Figure 13.5 shows the 3-D free energy map of gold dimers in TS-1, where brighter colors indicate lower free energy.
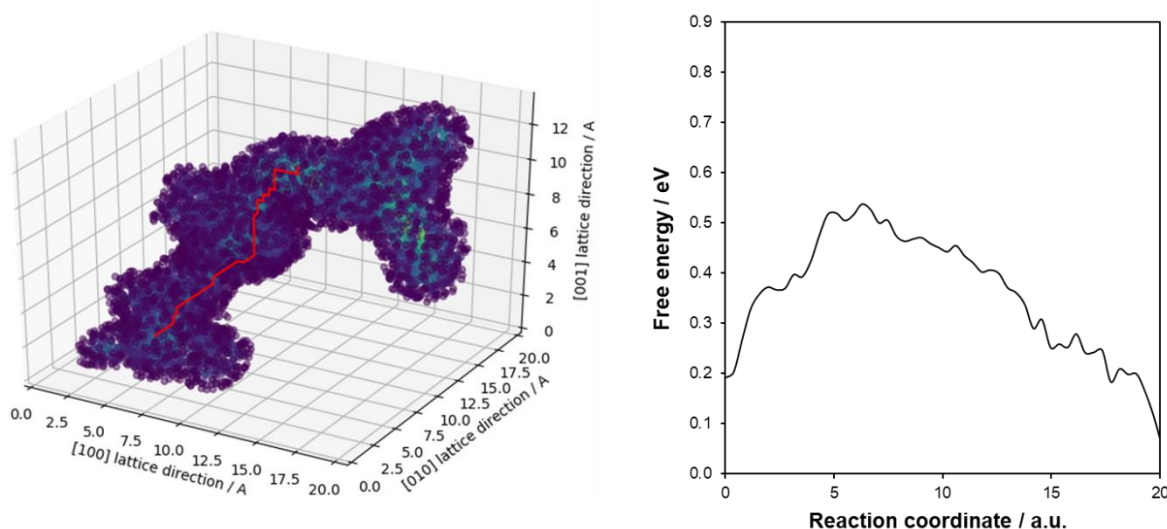


Figure 13.5 Gold dimer diffusion measured with Metadynamics. Left plot shows the free energy map along each lattice vector. The minimum energy path to travel from channel 2 to channel 0 along the straight channel is shown as a red line. The 2-D projected reaction coordinate corresponding to the minimum energy path is shown on the right, where 0 on the reaction coordinate is chamber 2 (bottom left of left figure) and 19 on the reaction coordinate is chamber 0 (back center of left figure).

Gold was observed in simulations to readily diffuse between chambers in the zeolite, and due to its size was not observed to reconstruct upon traveling through channels. Some preference for chamber 0 which includes the Ti atom was observed, as the free energy is at least 0.2 eV more stable than in chamber 0. The endpoint at reaction coordinate 20 also corresponds to the location of the Ti atom. Diffusion barriers from chamber 2 to chamber 0 are on the order of ~0.3 eV, not significantly higher than those observed for gold monomers. Multiple re-crossings of the

channel were observed during the simulation timespan, however due to the size of the collective variable space, more simulation time is still necessary.

### 13.3.5 Gold trimer diffusion

Trimer diffusion is qualitatively like that of dimers, as the linear cluster is favored, and does not have to deform to traverse the channel. The free energy map of trimer diffusion is shown in Figure 13.6, where gold diffused among the three channels considered.
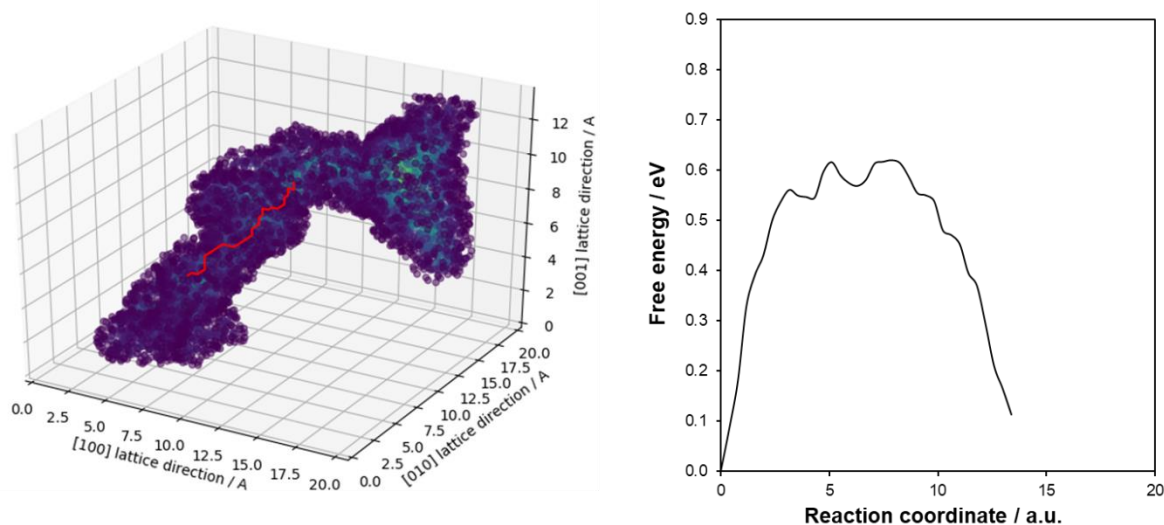
Figure 13.6 Gold trimer diffusion measured with Metadynamics. Left plot shows the free energy map along each lattice vector. The minimum energy path to travel from channel 2 to channel 0 along the straight channel is shown as a red line. The 2-D projected reaction coordinate corresponding to the minimum energy path is shown on the right, where 0 on the reaction coordinate is chamber 2 (bottom left of left figure) and 19 on the reaction coordinate is chamber 0 (back center of left figure).

The diffusion barrier for gold trimers is larger, approximately 0.6 eV with little preference for chamber 0 containing the Ti site or chamber 2 which is siliceous. Although diffusion through the channel does not involve deformation, the gold trimer is long enough that it would not have access to all its rotational degrees of freedom when diffused in the channel as opposed to chamber. This would correspond to a reduced entropy at channel sites, to manifest as an increase in the free energy barrier for diffusion. In all crossings, the gold trimer was observed to diffusion in a linear fashion without rotation. The lowest energy points for the minimum energy path also correspond to the center of chambers, not a region close to Ti like was observed for the dimers. This produces a more narrowly peaked reaction coordinate, since the free energy surface is relatively flat within

the chambers. The diffusion barrier is also flat in channels, which may be due to a uniform loss of rotational entropy across the channel structure. The pitting observed in the minimum energy path is due to unequal sampling of the chambers, despite many re-crossings being observed. This can be remedied with additional simulation time.

### 13.3.6 Gold tetramer diffusion

Tetramer diffusion is also qualitatively like the gold dimer, with key differences being a more peaked distribution and higher barrier for translation.
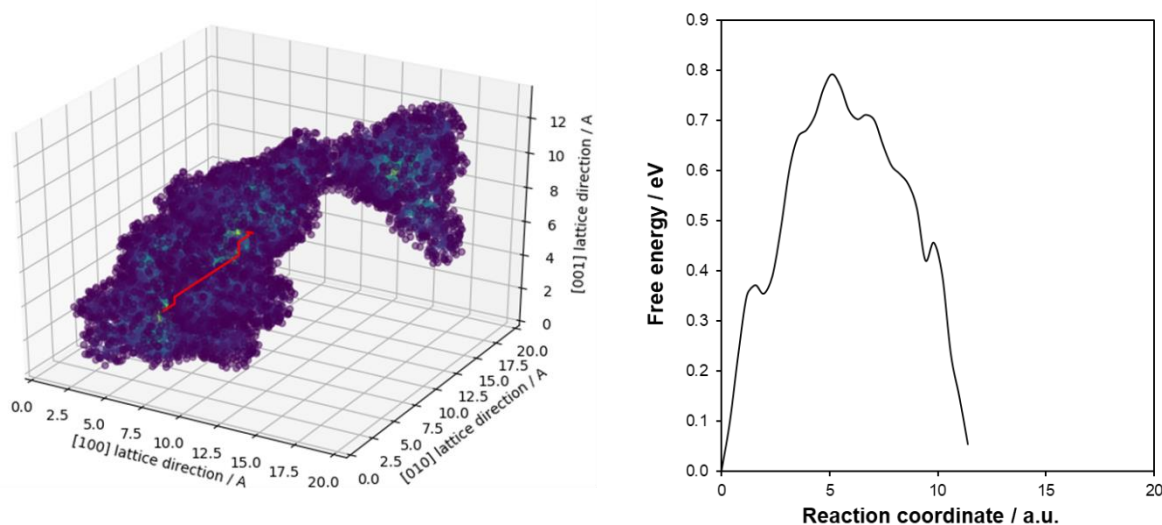


Figure 13.7 Gold tetramer diffusion measured with Metadynamics. Left plot shows the free energy map along each lattice vector. The minimum energy path to travel from channel 2 to channel 0 along the straight channel is shown as a red line. The 2-D projected reaction coordinate corresponding to the minimum energy path is shown on the right, where 0 on the reaction coordinate is chamber 2 (bottom left of left figure) and 19 on the reaction coordinate is chamber 0 (back center of left figure).

Diffusion of gold tetramers has a barrier of nearly 0.8 eV with a strongly peaked distribution that does not change between chambers 2 and 0. A purely linear structure for the gold tetramer is not most favorable, with a more packed configuration having the lowest energy. In the chambers the tetramer can adopt their coiled state freely; however, when diffusing into the channels they must uncoil, which breaks at least one Au-Au bond. Rotational degrees of freedom are reduced in the channels, like the gold trimer. In the case of gold trimers, the channel regions had a relatively flat free energy surface, due to the uniform loss of rotational entropy across the channel. Tetramers are long enough, that only when the center of mass is at the center of the

channel does it lose all rotation degrees of freedom, as when the tetramer is partially inside the channel it can still rotate gold atoms that dangle in the chambers. This is one hypothesis for the more strongly peaked barrier observed in the tetramer as opposed to the dimer and trimer.

### 13.3.7 Summary of gold diffusion

To summarize the Metadynamics results, dimers do not lose all their rotational degrees of freedom, as they are small enough to have at least hindered rotation in the chambers. Gold trimers are large enough that even hindered rotation is impossible, and they must diffuse only as a linear chain as opposed to in chambers where they can rotate. Gold tetramers are favorable to coil into a denser structure than a linear chain, but to go through the channel, it must be linear. This causes a cleavage of Au-Au bonds in addition to the loss of rotational degrees of freedom resulting in a larger free energy barrier to diffusion than the gold trimer.
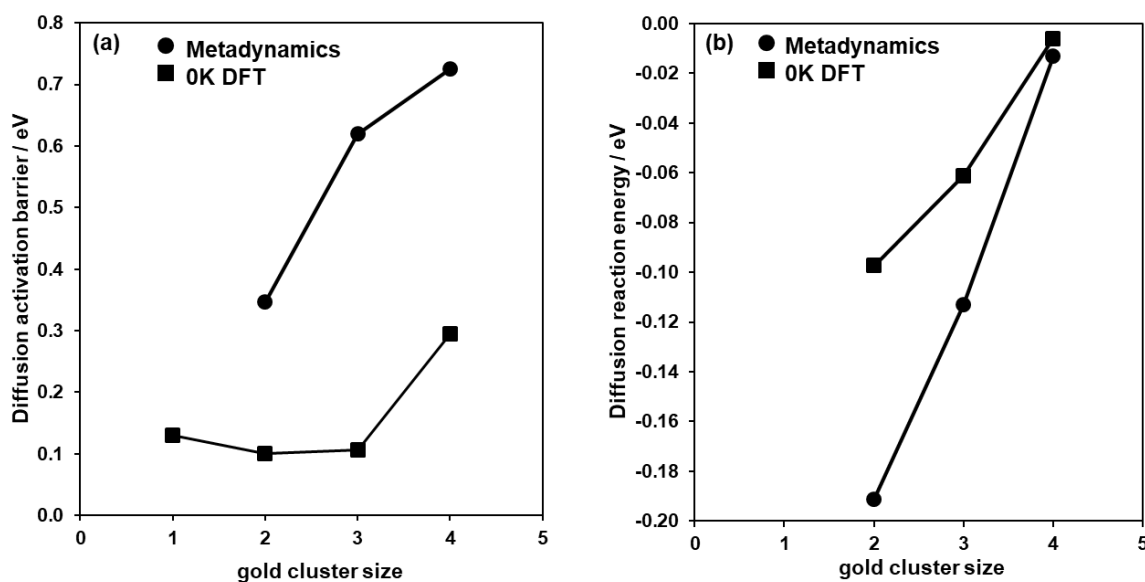


Figure 13.8 Comparisons between 0K gold diffusion calculated from quenching structures from Metadynamics. (a) The barrier for diffusion define as the difference between the highest energy in the channel relative to the lowest energy in chamber 2 (which does not contain Ti). (b) The driving force for diffusion between chambers 2 and 0. Negative values denote chamber 0 being more favorable.

Configurations of gold obtained during the Metadynamics simulation can be quenched down to 0 K to determine the purely enthalpic effects of diffusion. Figure 13.8a shows activation barriers for diffusion, for both 0 K quenched as well as metadynamic simulations. The Metadynamics

predicts an increasing barrier with cluster size, where the differential change in barrier is larger between $Au_2$ and $Au_3$ as compared to $Au_3$ and $Au_4$. The activation barriers from 0 K show a nearly negligible barrier for monomers up to trimers with the only significant difference beginning with the tetramer. This would make sense with the observation that tetramers must break Au-Au bonds in the channel, which was not observed for dimers or trimers. The trend seen in the Metadynamics could then reflect that between the dimer and trimer the dominant effect is the loss of rotational entropy, whereas between the trimer and tetramer, both have lost their rotational entropy, and the dominant effect is now the Au-Au bond cleavage observed in the 0 K barrier. Reaction energies in 13.8b show how the energetic difference between the chamber containing Ti and the siliceous chamber becomes nearly 0 for the tetramer. The smaller clusters have stronger interactions with the Ti site, which are attenuated by larger gold clusters, perhaps due to electron screening effects. Metadynamics does predict a larger interaction with Ti sites, which is still within ~0.1 eV which is being compared between two different methods, and so I will not comment on the absolute differences in reaction energy, except to point out that both the Metadynamics and 0 K simulations predict the same trend with gold cluster size.

## 13.4  Conclusions

This study marks a significant accomplishment in the scaling of theoretical methods to address differences in the TS-1 catalyst, which is difficult to model due to its complex structure and large number of atoms per unit cells. It is only with recent high-performance computers that it can be possible to perform AIMD on such a large and complex system. Despite the system, structural characteristics of gold in TS-1 were shown to be more diverse than those in the gas phase, due to the confining pore reconstructing clusters. These confined structures expose undercoordinated gold sites, which were shown to increase the binding energy of oxygen. The formation of activated atomic oxygen is hypothesized to be important to the formation of peroxide intermediates which epoxidize Ti. While small gold clusters (1-3 atoms) interact favorably with Ti sites leading to the site-proximity believed to be necessary for epoxidation, they are mobile at reaction conditions. This gold mobility was they studied to understand how the size and shape of gold determines the energetics of mobility. This was interrogated through molecular dynamics simulations which included both the enthalpic and entropic contributions to gold diffusion from between chambers and channels in TS-1. Preliminary results indicate diffusion barriers increase

with gold size, which is both due to the reduction in rotational degrees of freedom in the channels as opposed to chambers, as well as the enthalpic penalties of forming a linear chain of gold which is required to for diffusion.

These data implicate that only the smallest gold clusters (perhaps ~1-3 gold atoms) are mobile in TS-1, yet they will most likely nucleate inside chambers, where the thermodynamics do not favor proximity to Ti atoms. This would indicate two possibilities: either Ti proximity is not required, and Au and Ti can be spatially separated to some degree not currently known, or that gold clusters can transfer reactive intermediates through diffusion while bound to an intermediate. The latter is plausible, although unlikely as the size of gold capable of diffusion would be able to transfer only individual intermediates before agglomerating in large chambered clusters. It is more likely that gold and Ti need only be proximal with a neighborhood of a few unit cells. Hydrogen peroxide generated at gold sites could then diffuse to epoxidize propylene. These larger gold clusters in chambers have been shown to expose undercoordinated gold atoms which can activate $O_2$. These calculations have provided hypotheses and physical chemical understanding which can be further addressed through future collaborative studies with experimental groups to test these hypotheses.

# 14. OVERALL CONCLUSIONS AND FINAL REMARKS

"An Expert is a person who has found out by his own painful experience all the mistakes that one can make in a very narrow field."

-Niels Bohr

Many of the fundamental advances in the study of catalysis have come from understanding the concept of an "active site". The active site to those who believe in an ideal Langmuir surface would be a location on the catalyst where a chemical reaction occurs, and only by considering the "rate" at which molecules arrive and leave the "active site" can you understand the "intrinsic" catalysis. These simple concepts belie deeper complexity in a field that continues to use this paradigm to obtain a more precise picture of the active site. Efforts to define an active site have throughout history been complicated by the atomic nature of catalysis, which has rendered direct observation of mechanistic insights inaccessible except to the cleverest kinetic experiments. While such arcane techniques are just as relevant today as they have been throughout history, catalysis has been shaped by the development of new spectroscopic techniques which can be connected to kinetic experiments to provide either corroboration, or hopefully deeper fundamental knowledge. This thesis is a continued effort to strengthen the ties of quantum chemistry and physics with the study of catalytic active sites, either through kinetic experiments (such as CHAPTER 3) or through spectroscopy (such as CHAPTER 12). These connections are made in systems that *should* be the simplest possible to think of: isolated sites in zeolites, well-defined intermetallic alloys, the smallest clusters of gold; yet these systems are still poorly understood from the perspective of catalyst design. This is abundantly apparent when asked simple questions from non-experts in the field such as "what is the best zeolite to turn biomass into gasoline", or "what is the best alloy for platinum in the periodic table". Besides making the argument that these questions are overly broad, we can give the speaker the benefit of the doubt and clarify their question, "what is the zeolite that maximizes the rate of butadiene synthesis at 1 bar and 500 K given a pure feed of ethanol and acetaldehyde," but *we still cannot either intuit or obtain the information required to answer them*, at least before they lose interest in the question. These gaps represent a lack in the fundamental understanding of these "model systems" which in some small way, have been attempted. Although some of the connections and techniques such as those made in this thesis have been made before,

the work performed here goes deeper to provide new chemical and physical understanding of these systems.

It is not useful to summarize every point from this dissertation, and so those which are especially insightful will be elaborated on. With respect to Lewis acids in zeolites, the hydrolysis of alcohols proved to be a key insight into the catalysis of Lewis acid sites, one which I could not foresee upon first consideration. While open sites formed through the hydrolysis of water in zeolites had been proposed, independent work published by Dr. Tyler Josephson, who at the time was working for Professor Dionisios Vlachos at the University of Delaware, and I provided some of the first detailed DFT calculations of most stable hydrolyzed open site configurations. These structures became more important for the ethanol dehydration mechanism in Sn-Beta, where although hydrolyzed sites did not directly catalyze the reaction, the donation of hydrogen to the framework oxygen which behaves as a Lewis base stabilizes the rate-determining transition state. This finding in hindsight could have been more strongly stated the ethanol dehydration paper. This was then re-affirmed when the idea that subsets of the total Sn content in Beta could be related to Sn in stacking faults that had permanent hydroxyl ligands. These defect sites, despite possessing the same ligand identity as hydrolyzed sites, could not stabilize the same transition states as closed Sn sites because framework oxygen sites do not favorably accept another hydrogen. When considering elementary reactions for butadiene synthesis which included aldol condensation and MPV reduction, it was the ability of the framework to hydrolyze which was necessary to find transition states that had the lowest apparent free energy barriers for those reactions. Thus, while hydrolyzed sites were not the elusive "open site" discussed in literature, they could be implicated as being a key physical example of chemical reactivity for some reactions in Lewis acid zeolites.

Observations of how sites would deform upon site hydrolysis transitioned into ideas of whether the local structure of the zeolite framework, spanned by siloxane bonds to the active metal, had an influence on the stability of hydrolyzed sites and the degree of reconstruction. While these calculations will be ongoing, the strain caused by hydrolysis shows promise as a descriptor for the observed differences in hydrolyzed site stability in different materials, independent of van der Waals energy. This would make zeolites an attractive material to study the effect of strain on dopants in silica, because the active site ensembles in zeolites are known as opposed to amorphous silica. The current complexity remains direct experimental evidence, although the observed shifts in oxygen p-bands indicate a difference in how basic framework oxygens are, which calls to mind

previous discussions by Avelino Corma about conjugate basicity of Lewis acids. These findings would provide more understanding of what controls the chemistry of active sites in zeolite, which although being classical examples of a single isolated site, exhibit a wide range of chemical reactivity either through site speciation between closed and open, or the framework building units that make the active site for certain reactions.

The development of microkinetic models was a major contribution to this research, which is not typically performed in zeolites, and even more rarely for Lewis acids. To simplify the development of microkinetic models, I had worked with Tristan Maxson to make a python-based code that could directly interface with VASP and construct reaction mechanisms and tune entropy in a more intuitive way, with the expressed goal of making microkinetic models more accessible to a broader range of researchers. Specific to models in zeolites; however, is the anharmonic contributions that are present due to a locally flat potential energy surface what is crowded by a surrounding pore. While these anharmonic effects in zeolites have been extensively studied by Professor Joachim Sauer among others, ethanol dehydration showed how considerations beyond the harmonic approximation in zeolites are necessary to predict reasonable surface coverages of intermediates and connect with experimental results. This is a highly relevant case study that has broad applications to a microkinetic models in microporous materials.

To further complicate the isolated active sites in Beta zeolites, many reactions of interest, such as biomass conversions, must be performed in the presence of water, either in a nearly condensed or fully liquid phase. Solvents are yet another way to modify the active site, because of the unique interactions between solvent molecules and reactive intermediates and/or transition states. One property that makes Beta of interest for biomass conversion is its stability in water, and Professor Rajamani Gounder's group has developed many techniques for controlling the density of hydrophilic defects and active heteroatoms. From studying the structure and energetics of water around defects and heteroatoms in Beta zeolites, local clusters of water molecules were identified that formed unique hydrogen bonding networks that depended on the defect identity. By using *ab-initio* methods, a consistent basis could be used to compare all the defect identities, without having to use parameterized models. Techniques taken from broader literature, such as the local clustering analysis, were employed which provided a richer discussion of how the hydrogen bonded networks different between the type of defect or heteroatom. These local clusters are in equilibrium with more transient liquid-like hydrogen bonded networks, which allows for a decomposition into local

and non-local solvent structures that are separated by the confining zeolite environment. Although far from an original comparison, this again calls back to the similarities between zeolites and biological enzymes, where a strongly bound local solvent structure forms the active site. The importance of these local solvents in catalysis is further strengthened by the studies of H-Beta, where these solvents change the structure and stability of adsorbed intermediates in the gas phase. This local phase allows for a more detailed stability analysis to determine cluster size, even in the presence of reactive intermediates and transition states to help understand the observed changes in activity coefficients observed experimentally and connect with kinetics more closely even when solvent effects are included.

Forming meaningful connections with X-ray experimental spectroscopy is often difficult as the core-hole effects in most methods are inhospitable (though not impossible) to treat with DFT, and many methods require conditions far from those found for reactions such as ultra-high vacuum. New techniques such as RIXS are exciting both for being performed under ambient conditions, but also for their connection to theory by not involving a definite core-hole. The measurement of valence states is necessary for catalyst characterization, and this was demonstrated for intermetallic Pt alloys. Chemical intuition about how RIXS can be used to understand changes in Pt upon alloying was developed in conjunction with Argonne National Laboratory. These fundamental correlations were then directly compared with DFT, where the agreement is quantitative in comparing trends. We can extend these comparisons even farther by showing how the stability of unsaturated atomic intermediates could be related to the RIXS metrics of d-band splitting, introducing a new descriptor for understanding chemical adsorption on metal surfaces which is accessible both to theory and experiment.

Finally, the structure of active sites in the Au/TS-1 catalyst was considered through computational approaches to study the structural motifs present in different sizes of gold clusters. The interactions between Au sites and Ti sites define a unique two site environment where an experimental understanding of how these sites interact with each other is difficulted by the microporous catalyst structure. Here DFT theory is used to provide intuition into what is reasonable and unreasonable for the system, which can aid in hypothesis testing and the design of experiment. This, in my opinion, is where the theory is most powerful and directly applicable. Theory can be directly involved at every level of experiment design, which allows for continuous hypothesis testing and evaluation.

This returns to quantum chemistry in catalysis overall: it is a technique that can be continuously applied to all levels of hypothesis testing and is most powerful when used in close conjunction with experiments to test the structure of active sites and reaction mechanisms. I do not think that computation can be completely separated from experiment, as computations will always be a model system on some level, but insights from these models can both explain experiments and predict experimental results. The case of zeolites is particularly illuminating, because their internal structure makes experimental approaches impossible in specific circumstances. Here is where I think the most synergistic combination of theory and experiment can be found. The work provided in this thesis is a testament to how theory and experiment can be used to understand catalysis beyond just a metal atom in the active site. This thesis shows how the speciation of active sites, the local and nonlocal environments in active sites, the interactions of solvents with active sites, and the electronic promotion of promoter metals with active sites can be quantified with the insights gained through cooperative scientific endeavors with both computation and experiment.

## APPENDIX A: SUPPLEMENTARY INFORMATION FOR CHAPTER 1

Figure A1. Periodic CHA unit cell with Sn substitution at a T1 site.
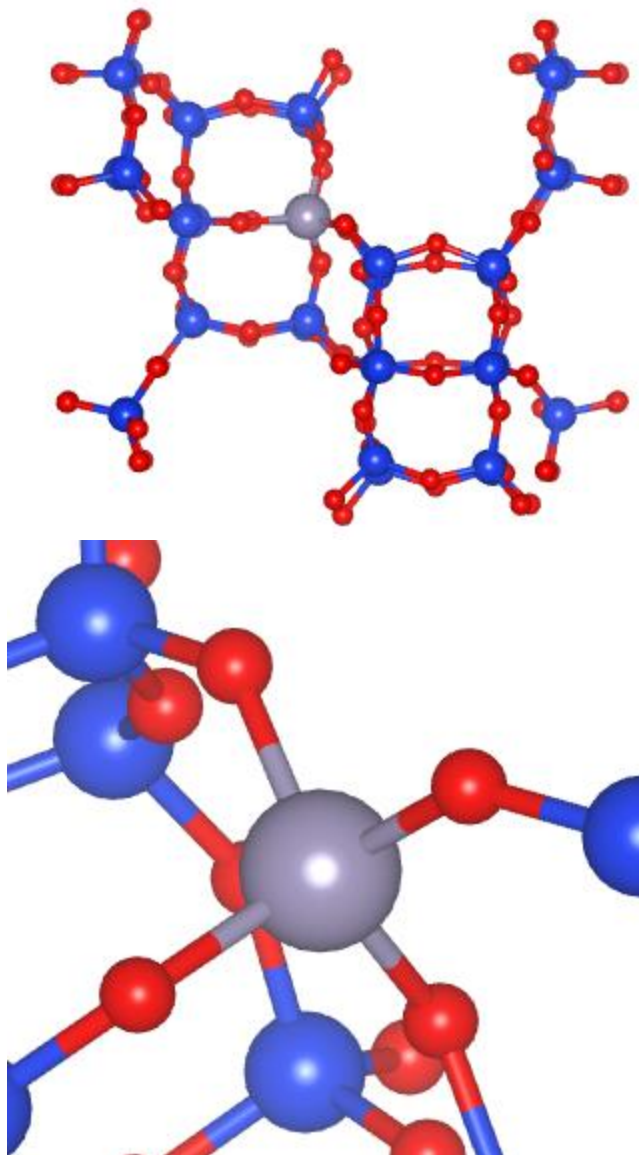


Figure A2. Possible sites for hydrogen dissociation in substituted CHA. All dissociation reactions occur at the O(4) site which is included in the 8 membered ring.

The energetics of adsorption of a single hydrogen atom at each site, relative to ½ of a gas phase H$_2$ molecule, are given in Table A1, as follows:

Table A1. Comparison of hydrogen dissociative adsorption energies for different oxygen sites.

| Oxygen site | Hydrogen dissociative adsorption energy (eV) |
|---|---|
| O(4) | 1.33 |
| O(3) | 1.36 |
| O(2) | 1.42 |
| O(1) | 1.34 |

Each oxygen site has a similar hydrogen dissociative energy, and the O(4) site is used for the calculations, as described in the body of the text.
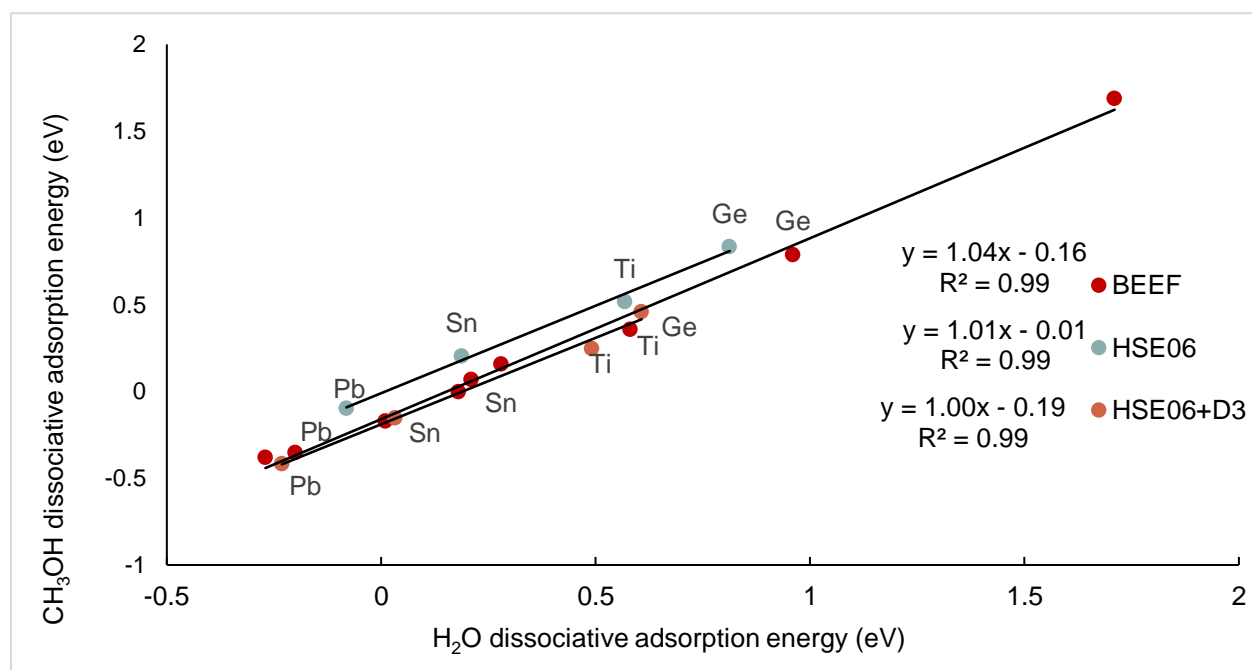
Figure A3. Comparison of the water-methanol scaling relationship with BEEF-vdW, HSE06, and HSE06-D3.

Using a scaling relationship which is established with BEEF-vdW, a smaller set of 4 heteroatoms are tested using HSE06 and HSE06-D3. For both HSE06 and HSE06-D3, the same slope as in BEEF-vdW is reproduced. The addition of the dispersion correction to HSE06 corrected the intercept to within 0.03eV of the BEEF-vdW results. Thus, in the absence of strong exchange effects, and when properly corrected for dispersion effects, the HSE06 and BEEF-vdW functionals produce the same scaling relationship for methanol/water dissociative adsorption.
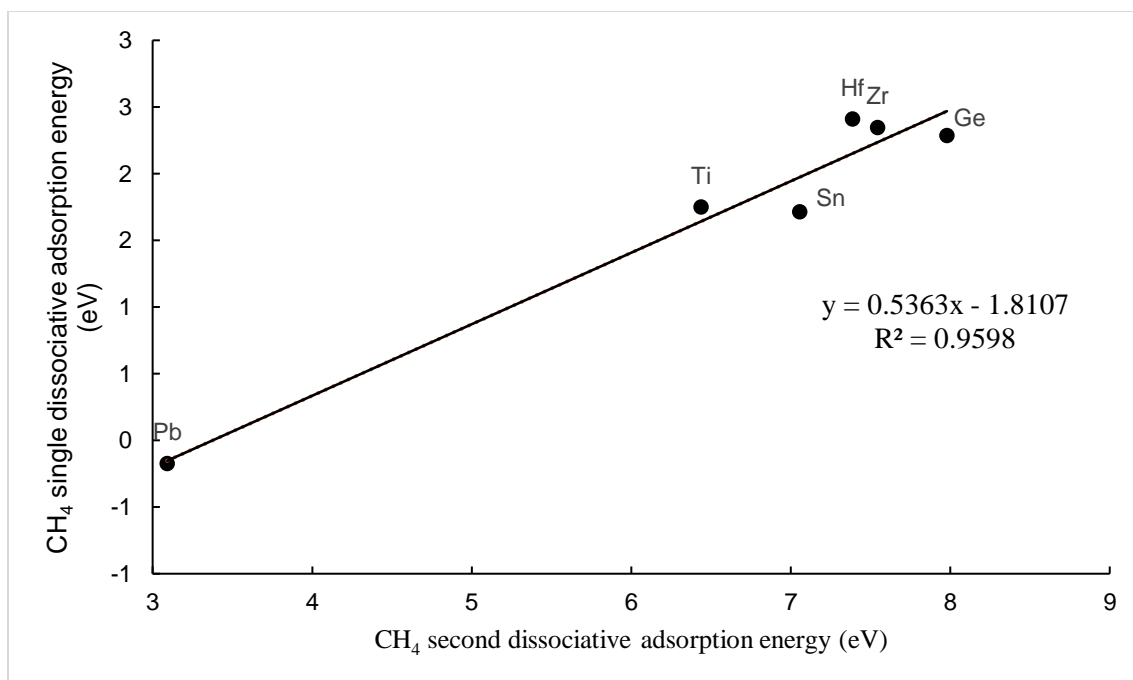
Figure A4. Scaling relationship for CH3+H vs. CH2+2H dissociative adsorption on Lewis acid chabazite zeolites. To prevent large relaxations of the zeolite cage, these dissociative adsorption calculations are performed with geometric constraints applied to the heteroatom and to the surrounding four Si atoms. See additional discussion in text.

Some scatter in Figure A4 is due to changes in oxidation state that each heteroatom undergoes after adsorption of the $CH_3+H$ and $CH_2+2H$ species.

Bader Charge analysis of heteroatom oxidation states

In order to determine the oxidation state of heteroatoms in the zeolite framework, the method of Bader charges is implemented, as also discussed in the main text. The Bader charges obtained are compared to reference bulk oxides calculated at a similar level of theory. The reference bulk oxides are chosen to be of the $MO_2$ stoichiometry to determine the Bader charge corresponding to a formal $4^+$ oxidation state, while the Bader charge corresponding to a $3^+$ oxidation state is evaluated using a bulk oxide of the $M_2O_3$ form. The Bader charges of each zeolite heteroatom are scaled and linearly interpolated based on these values to obtain a formal oxidation state.

Table A2 compares the scaled Bader charges (corresponding to formal oxidation states) of each zeolite heteroatom in the CHA framework.

Table A2. Scaled Bader charges for heteroatom substitutions in the CHA framework.

| Heteroatom substitution | Heteroatom scaled Bader charge (e-) |
|---|---|
| Ge | 3.96 |
| Hf | 4.03 |
| Pb | 4.03 |
| Re | 3.91 |
| Si | 4.00 |
| Sn | 3.99 |
| Th | 3.92 |
| Ti | 3.98 |
| Zr | 4.03 |

Table A3 shows how that the scaled Bader charge on Ti does not change significantly after adsorption of various species.

Table A3. Scaled Bader charges for adsorption on Ti-CHA

| Heteroatom scaled Bader charge (e-) | | | |
|---|---|---|---|
| $H_2O$ | $CH_3OH$ | $CH_2$ | CHOH |
| 3.95 | 3.96 | 4.02 | 4.08 |

Table A4.  Scaled Bader charges for $CH_2+2H$ and $CH_3+H$ adsorption

| | Heteroatom scaled Bader charge (e-) | |
|---|---|---|
| | $CH_2+2H$ | $CH_3+H$ |
| Sn | 3.07 | 4.21 |
| Zr | 2.92 | 3.81 |
| Ti | 3.04 | 4.02 |

# APPENDIX B SUPPLEMENTARY INFORMATION FOR CHAPTER 3

Binding energy of water and ethanol monomers at each T site in the Beta framework, in addition to water dissociation energies to form hydroxy open sites. The reference state is the corresponding gas phase species (water or ethanol) and the empty framework.

Table B1 Binding Energies of key intermediates ad different acid sites

| reference state *+X(g) | T1 | T2 | T3 | T4 | T5 | T6 | T7 | T8 | T9 | maximum deviation |
|---|---|---|---|---|---|---|---|---|---|---|
| $H_2O$ Binding Energy (eV) | -0.60 | -0.58 | -0.56 | -0.51 | -0.44 | -0.47 | -0.58 | -0.58 | -0.55 | 0.16 |
| $H_2O$ Dissociation Energy (eV) | -0.19 | -0.19 | -0.27 | -0.21 | -0.24 | -0.17 | -0.22 | -0.22 | -0.16 | 0.11 |
| EtOH Binding Energy (eV) | -0.84 | -0.81 | -0.85 | -0.71 | -0.70 | -0.72 | -0.82 | -0.88 | -0.79 | 0.18 |

Electron localization function for hydroxy open site calculated in VASP shows no overlap of electron density between the protonated framework oxygen and Sn heteroatom[326]. The remaining three framework oxygen atoms and Stannanol ligand have electronic overlap with the Sn heteroatom.
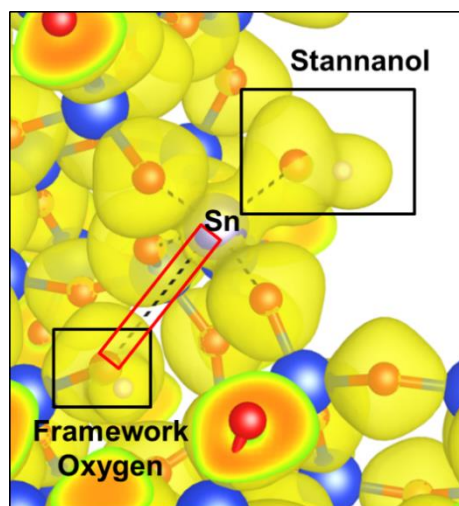


Figure B1 Electron localization function

Table B2 Oxygen bader charges

| Sn speciation | Unscaled Sn Bader charge (e⁻) |
|---|---|
| closed site (*) | 1.67 |
| hydroxy open site (Wx*) | 1.69 |
| ethoxy open site (Ex*) | 1.71 |

COHP[140], [327] bonding energies calculated from VASP wavefunctions using the Lobster code show only 4 total Sn bonds upon formation of an open site. The framework oxygen which is protonated loses its bond to Sn, while Sn forms a bond to the ligand, maintaining the $4^+$ oxidation state. Additionally, orbital energies for OEt and OH ligands are similar to those of $Sn-O_f$ bonds.

Table B3 COHP analysis of Sn sites

| Oxygen local environment[a] | | ICOHP occupation (eF) | Bond distance (A) |
|---|---|---|---|
| | $Sn-O_f$ | -5.72 | 1.937 |
| | $Sn-O_f$ | -5.72 | 1.937 |
| Closed site | $Sn-O_f$ | -5.50 | 1.950 |
| (*) | $Sn-O_f$ | -5.49 | 1.953 |
| | $Sn-O_f$ | -5.45 | 1.947 |
| | $Sn-O_f$ | -5.59 | 1.945 |
| Hydroxy open site | $Sn-O_f$ | -5.40 | 1.955 |
| (Wₓ*) | Sn-OH | -5.75 | 1.969 |
| | $Sn-O_f$ | -5.54 | 1.947 |
| | $Sn-O_f$ | -5.51 | 1.950 |
| Ethoxy open site | $Sn-O_f$ | -5.15 | 1.974 |
| (Eₓ*) | Sn-OEt | -5.80 | 1.966 |

[a] $O_f$ denotes a Sn-O bond to the framework.

Water shuttling allows for a *syn* open site with adjacent ligand and silanol to adopt a more thermodynamically stable *anti* open site. Barriers are similar for ethoxy (TS2) and hydroxy (TS4) open sites, 0.33 eV and 0.37 eV, respectively. Shown below are potential and free energy diagrams (404 K, 1 bar) for the full water-assisted opening process, as well as images of the transition state for both ethoxy and hydroxy open sites.
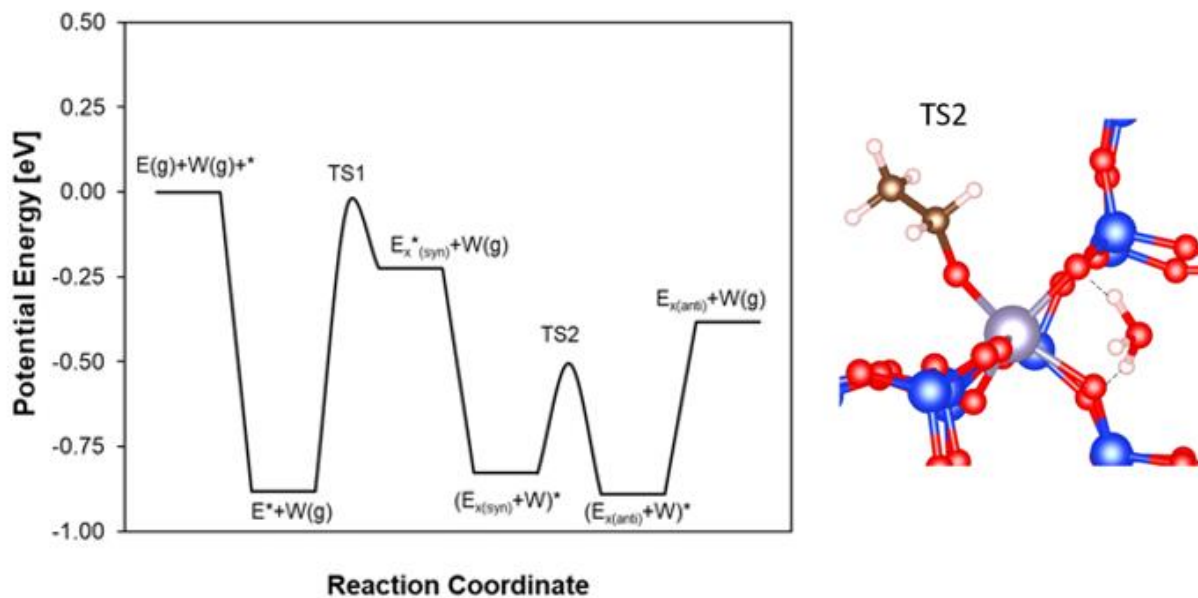
Figure B2 Water shuttling to form hydrolyzed ethoxy site
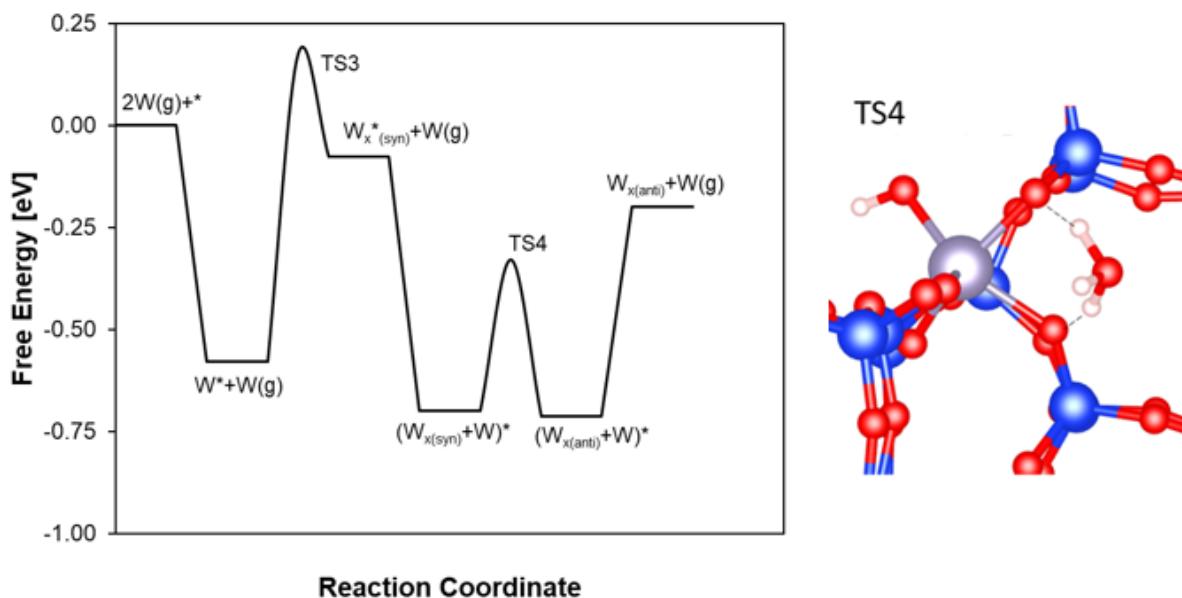


Figure B3 Water shuttling to form hydrolyzed water site

DEE formation on paired Sn sites identified by Bare et al.[108]. The 0K intrinsic potential energy barrier (referenced to $EE_x^*$, where here $E_x^*$ denotes a paired Sn site) is higher than single Sn-site Beta $SN_2$ mechanisms. The left-most Sn site adsorbs molecular ethanol while the right-most Sn site is functionalized with an ethoxy open site with framework silanol circled for clarity. This

configuration is thematically similar to the lowest barrier transition state found by Christiansen[144] for ethanol dehydration on $\gamma$-Al$_2$O$_3$.
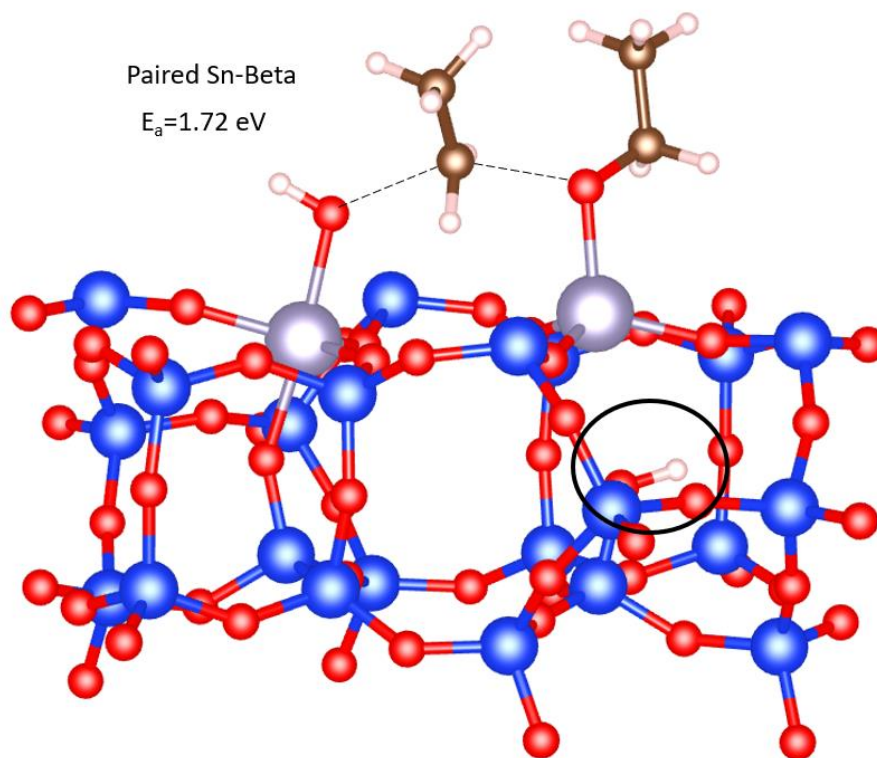


Figure B4 Paired Sn site mechanism

Complete list of elementary steps in microkinetic model of ethanol dehydration reaction network. Here "C" denotes the monomolecular dehydration product, ethene.

1. WW*↔W(g)+W*
2. DW*↔D(g)+W*
3. C2W*↔CW*+W(g)
4. E(g)+* ↔E*
5. E(g)+E*↔EE*
6. EE$_x$*↔ECW*
7. C2W*↔C(g)+WW*
8. W*↔W$_x$*
9. EE$_x$*↔DW*
10. W*↔W(g)+*
11. E(g)+EW$_x$*↔EEW$_x$*
12. E(g)+W$_x$*↔EW$_x$*
13. E*↔CW$_x$*
14. EW$_x$*↔C2W*

15. E*+W(g) ↔EW*
16. $E_x$*+E(g) ↔$EE_x$*
17. E*↔$E_x$*
18. $DW_x$*↔D(g)+$W_x$*
19. $E_x$*+W(g) ↔$WE_x$*
20. $EEW_x$*↔D2W*
21. EE*↔$DW_x$*
22. $CW_x$*↔C(g)+$W_x$*
23. ECW*↔EW*+C(g)
24. CW*↔C(g)+W*
25. D2W*↔D(g)+WW*

0K intrinsic potential energy barriers (in eV) for the $SN_2$ and $SN_i$ pathways for bimolecular dehydration of ethanol to form DEE. Images correspond to the $SN_i$ conformation ($SN_2$ provided in main text). Surrounding pore environment is truncated for clarity.

Table B4 retentive mechanism barriers

|  | $SN_2$ | $SN_i$ |
|---|---|---|
| closed (*) | 1.47 | 2.20 |
| hydroxy open ($W_x$*) | 1.32 | 2.31 |
| ethoxy open ($E_x$*) | 1.41 | 1.92 |



Closed          Ethoxy open          Hydroxy open
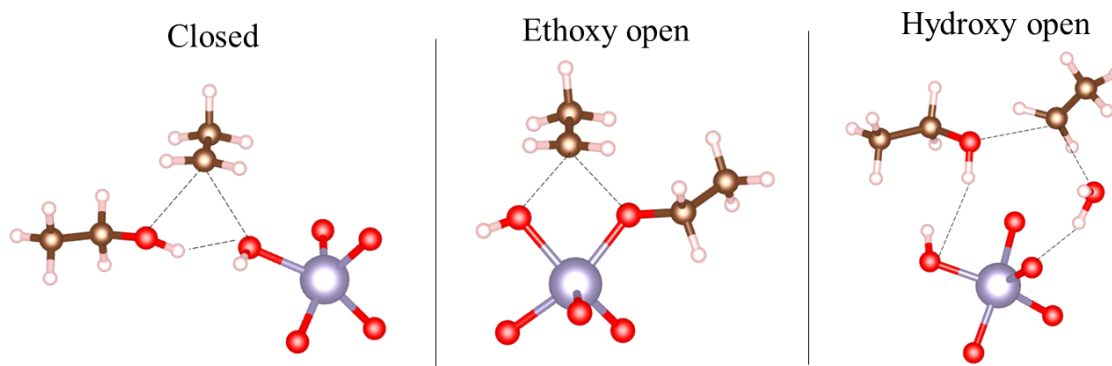
Figure B5 retentive mechanism transition states

Rate constants for gas phase adsorption are approximated using collision theory. This approximation is the most accurate for gas collisions on a flat surface. The inside pores of a zeolite are clearly not planar, but the flux of gas particles in the pore striking isolated Sn atoms is likely not significantly different. The rate constant of adsorptive processes is described by

$$k_{ads} = \frac{A_0 \Lambda}{(2\pi kT)^2}$$

where $A_0$ is the area of a surface site and $\Lambda$ is an adsorption sticking probability, which will be assumed to be one. Rate constants for surface reactions are described as

$$k = \frac{kT}{h} e^{-\frac{(G_{TS} - G)}{kT}}$$

Here, transition state theory has been applied to relate the free energy change from the transition state of an elementary step to the forward rate constant with a frequency factor approximated as the fundamental mode. Note that potential energy and entropy effects have been included in the free energy.

Equilibrium constants for each step are defined by the standard relationship

$$K_{eq} = e^{-\frac{(G_{products} - G_{reactants})}{kT}}$$

The reverse rate constants can be obtained from the forward rate and equilibrium constant with a pressure conversion term. For purely surface reactions, the reverse rate is the forward rate divided by the equilibrium constant.

Once rate and equilibrium constants for all elementary steps have been determined, a CSTR reactor model can be established for an isothermal well-mixed reactor.

Mass balance equations for each species are developed. For a gas phase species, the mass balance takes the form

$$\frac{dF}{dt} = a\big(F_0 - F - b(rate)\big)$$

where the rate term contains the rate expression involving gas phase species and F denotes the gas flowrate in molar units. The parameters a and b determine the reactor parameters, with 'a' relating to the reactor conversion and b relating to the site normalization. To compare with experimental measurements, the rates are normalized by the number of Sn sites in the same catalyst. Intrinsic rates for the reaction are very low, and reactor conversion can be constrained below 1% by consistent choice of parameter a.

For surface coverages, the rate of change is described by the expression

$$\frac{d\Theta_a}{dt} = rate$$

where the coverage of an intermediate is expressed by the sum of the rates of elementary steps. In the microkinetic code, a stoichiometric matrix is formed which can be used to identify rates of each elementary steps in an organized manner. The number of sites is constrained by the site balance, resulting in a set of differential equations numbering the total reaction species. An inert is included to maintain pressure in the reactor. Initial gas flowrates can be calculated to match experimental data, and the set of differential equations are integrated in time until steady state is achieved. At steady state, the coverages and pressures can be used to evaluate the rates of each elementary step. The total rate of product formation is defined as the total flowrate of DEE produced from desorption.

As the overall rate of an elementary step involves the subtraction of a forward and reverse rate, rounding errors can become large for steps with low overall rate. Thus, the solution from the differential equation solver is fed into a nonlinear algebraic solver to achieve better numerical accuracy. Usage of the nonlinear solver alone is difficult, however, since for a complex reaction network there may be many local roots.

Degree of rate control calculations are made by systematically varying each free energy and reevaluating the rate and equilibrium constants. A differential change is made to the free energy, and a least squares regression is made of the resultant rate constant vs. rate plot. The least squares regression is useful to determine whether the size of the differential perturbation is sufficient to maintain linearity in the numerical derivative.

From left to right
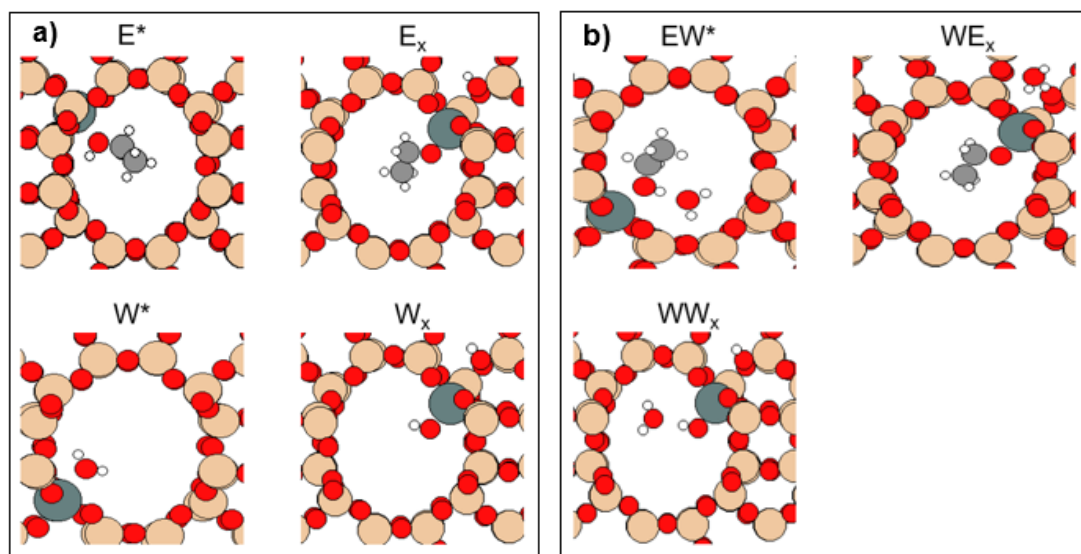


Figure B6 Set of representative adsorbate structures 1

a) ethanol monomer, ethoxy open site, water monomer, hydroxy open site

b) ethanol-water dimer, water on ethoxy open site, water on hydroxy open site
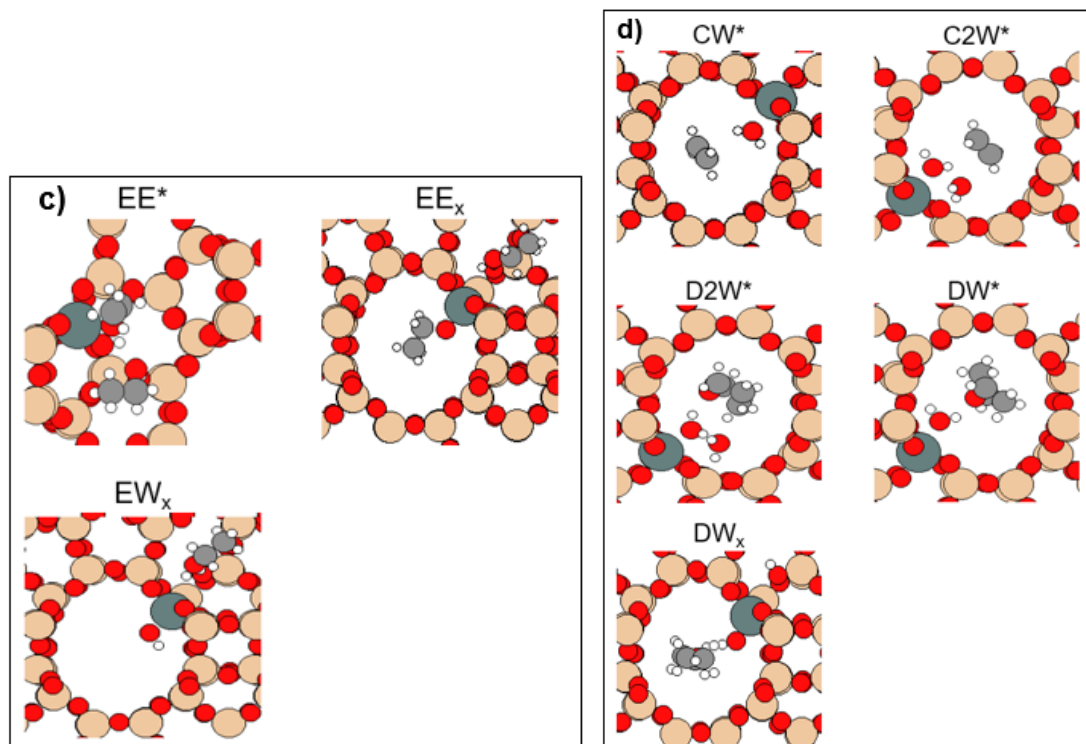


Figure B7 Set of representative adsorbate structures 2

c) ethanol-ethanol dimer, ethanol on ethoxy open site, ethanol on hydroxy open site

d) ethene-water dimer, ethene-water-water trimer, DEE-water-water-trimer, DEE-water dimer, DEE on hydroxy open site
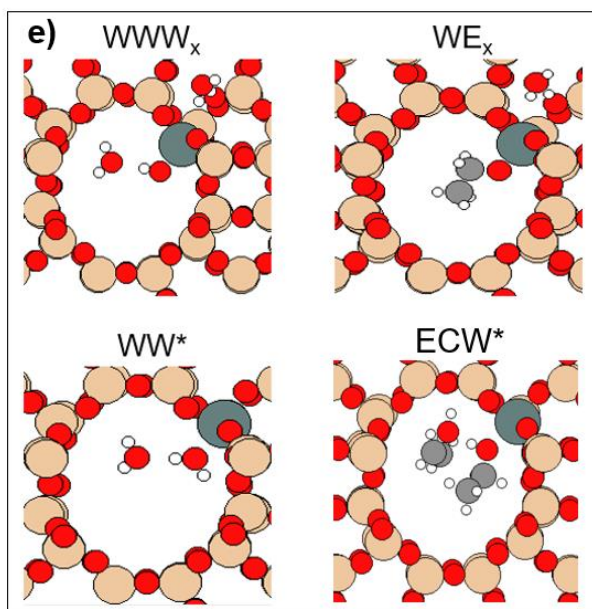


Figure B8 Set of representative adsorbate structures 3

e) water-water on hydroxy open site, water on ethoxy open site, water on hydroxy open site, ethanol-ethene-water trimer

Harmonic vibrational modes for each adsorbate and transition state was calculated, and the modes are visualized to determine contributions to different idealized partition functions for each respective mode. These partition functions are either the quantum harmonic oscillator, the free or hindered rotor, or translation in an infinite square potential. This choice of translational partition function is motivated by the particular characteristics of adsorbates in zeolites. Through inspection of the lowest frequency modes and AIMD simulations, adsorbates are found to translate around the Sn atom, but they cannot diffuse to a nearby site due to isolation of the T site. Thus, instead of using a full free translational partition function or a hindered translator, an infinite potential well is approximated around the Sn atom.

Entropies determined from the respective partition functions, as used in the microkinetic code, are provided below for each such partition function:

1) Harmonic oscillator: 
$$S_{vib} = \frac{\frac{E}{kT}}{e^{\frac{E}{kT}}-1} - \ln\left(1 - e^{-\frac{E}{kT}}\right)$$
   where E denotes the energy of the vibrational mode

2) Hindered rotators: hindered rotational modes are dependent on the free rotor partition function and the magnitude of the rotational barrier. The entropy is expressed for each rotational degree of freedom. The corresponding free rotor partition functions are
$$Q_{rot} = \frac{\sqrt{\pi}}{\sigma}\left(\frac{8\pi^2 I_{ii}kT}{h^2}\right)^{0.5}$$
   which require knowledge of the symmetry factor and principle moments of inertia. The hindering potential is expressed by
$$E_{hind} = \frac{E}{2kT}$$
   and the hindered rotational partition function is expressed as
$$Q_{hind} = Q_{rot}e^{-E_{hind}}J_0(iE_{hind})$$
   where $J_0$ is the zeroth order Bessel function. The entropy corresponding to each degree of freedom is then evaluated as
$$S_{rot} = k\left(\ln(Q_{hind}) + \frac{1}{2}\right)$$
   If the hindering potential is 0, the entropy corresponds to a free rotor about the specified principle moment of inertia. Any hindering potential reduces the entropy of the mode.

3) Translation in infinite square potential wells:

For localized translational modes, the characteristic translational length, L, is used to establish an infinite square potential. The translational partition function per degree of freedom is expressed as

$$Q_{trans} = \left(\frac{2\pi mkTL^2}{h^2}\right)^{\frac{1}{2}}$$

The entropy is then expressed as

$$S_{trans} = k\left(\ln(Q_{trans}) + \frac{1}{2}\right)$$

To obtain accuracy beyond that of mode-decomposed partition functions, entropies and free energies for adsorbed species are estimated from the two-phase thermodynamic method developed by Lin, Blanco, and Goddard[152], [153]. The crux of this method is usage of molecular trajectories from AIMD to calculate the vibrational density of states (VDOS). This calculation is performed using a python code which directly generates the VDOS from the molecular velocities. This is the same method recommended by Lin et al. and involves projecting ideal gas translational, rotational, and vibrational contributions from the VDOS. The degrees of freedom corresponding to the zeolite framework are projected out. The TRAVIS code[246], [328] is used for its ability to sort and organize molecular trajectories.

Lattice constants for the framework were individually relaxed for each functional, and a full geometry relaxation to a force constant of 20 meV/Å was performed for each functional considered. Free energies are calculated at 404 K and 1 bar.
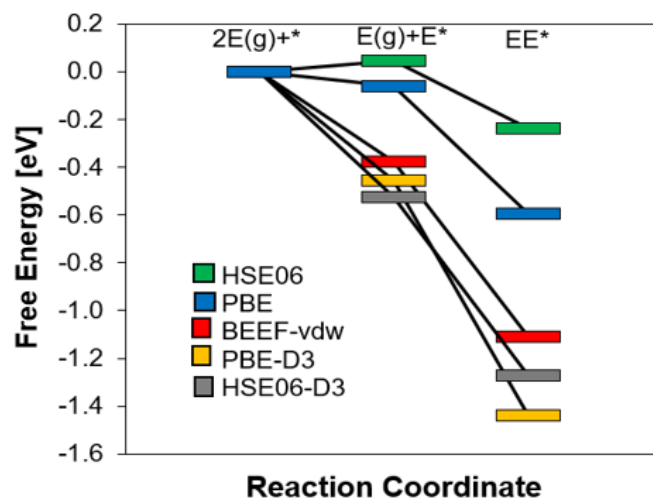


Figure B9 functional comparison of ethanol dimerization
energies

A centered 0.1 eV (+/- 0.05 eV maximum deviation) error was propogated through the optimized microkinetic model, which includes first and second order correlations in each reactive intermediate and transition state, as described in the text. The table below reports the generalized degree of rate control for the unchanged model, the change in DRC at the maximum DEE formation rate allowed by the error bounds, and the change in DRC at the minimum DEE formation rate. These changes did not introduce any additional rate-sensitive intermediates or alter the rate determining step determined from the model.

Table B5 GDRC analysis or individual error

| GDRC | unchanged | maximum DEE formation rate | minimum DEE formation rate |
|---|---|---|---|
| Closed site TS | 0.99 | 0.98 | 0.98 |
| E* | -0.55 | -0.24 | -0.83 |
| EE* | -0.37 | -0.62 | -0.14 |
| EW* | -0.08 | -0.15 | -0.03 |

$$\text{(1)} \qquad \text{E(g) + *} \quad \underset{}{\overset{K_1}{\rightleftharpoons}} \quad \text{E*}$$

$$\text{(2)} \qquad \text{E(g) + E*} \quad \underset{}{\overset{K_2}{\rightleftharpoons}} \quad \text{EE*}$$

$$\text{(3)} \qquad \text{W(g) + E*} \quad \underset{}{\overset{K_3}{\rightleftharpoons}} \quad \text{EW*}$$

$$\text{(4)} \qquad \text{EE*} \quad \overset{k_4}{\longrightarrow} \quad \text{DEE(g) + W(g) + *}$$
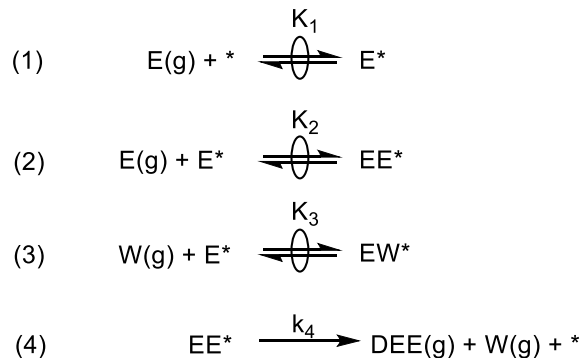
Assumptions based on microkinetic modeling results:

1) Steps 1, 2, and 3 are quasi-equilibrated

2) Step 4 is irreversible and rate-determining

3) The relevant surface intermediates at the conditions studied are ethanol monomers, ethanol-ethanol dimers, and ethanol-water dimers. The coverage of empty sites is negligible.

The overall reaction rate per Sn site is therefore:

$$\frac{r_{DEE}}{L} = k_4 \theta_{EE}$$

where $r_{DEE}$ is the rate per unit surface area, "L" denotes the total number of catalytic Sn sites, and $\theta$ denotes the fractional coverage of a given reactive intermediate. Applying the quasi-equilibrium hypothesis on steps 1,2, and 3 yields:

$$\theta_E = K_1 P_E \theta_*$$
$$\theta_{EE} = K_1 K_2 P_E{}^2 \theta_*$$
$$\theta_{EW} = K_1 K_3 P_E P_W \theta_*$$

where P is a gas-phase partial pressure, and * is the coverage of empty sites. We can write the total balance of sites L as:

$$1 = \theta_E + \theta_{EE} + \theta_{EW}$$
$$1 = (1 + K_2 P_E + K_3 P_W) K_1 P_E \theta_*$$

as the coverage of empty sites under the conditions studied is negligible. Therefore:

$$\frac{r_{DEE}}{L} = \frac{k_4 K_1 K_2 P_E{}^2}{(1 + K_2 P_E + K_3 P_W) K_1 P_E}$$

$$\frac{r_{DEE}}{L} = \frac{k_4 K_2 P_E}{(1 + K_2 P_E + K_3 P_W)}$$

Which is as presented in equation 4b of the main text.

# APPENDIX C SUPPLEMENTAR INFORMATION FOR CHAPTER 4
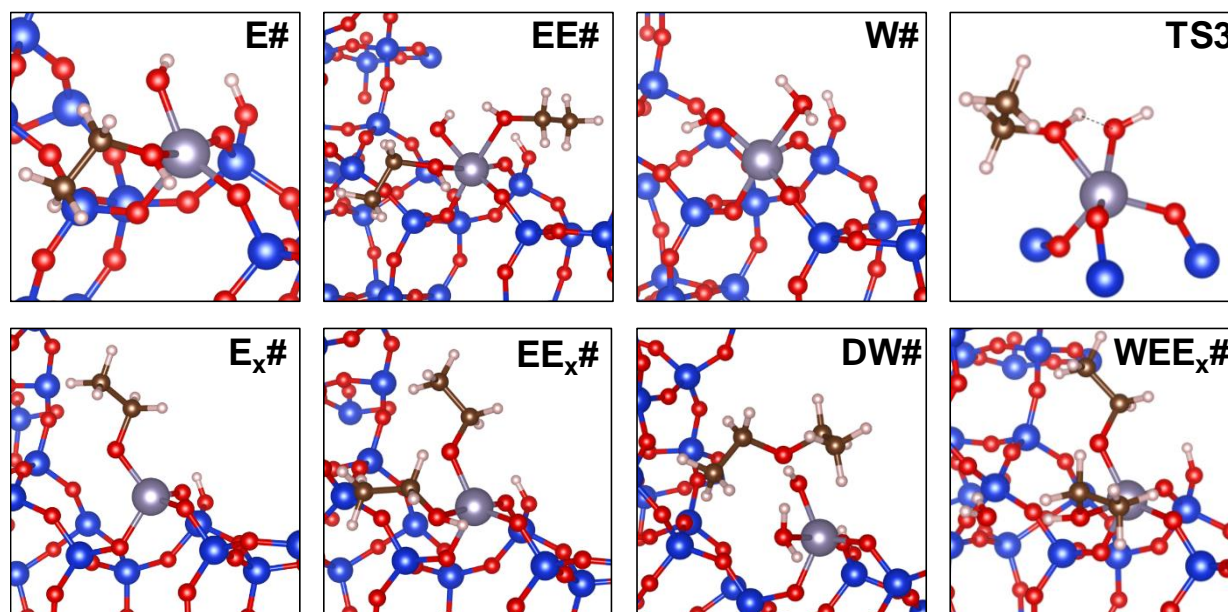


Figure C1. Geometries of adsorbed intermediates (and TS3 to form $E_x$# from E#) for the concerted pathway and sequential pathways at the stacking fault defect-open site. .XYZ files for each adsorbate are available online.
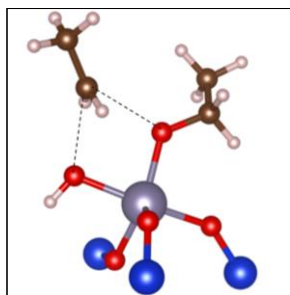


Figure C2. Transition state (TS5) for DEE formation by the sequential pathway at the stacking fault defect-open site, starting from $EE_x$# without $H_2O$ assistance, as discussed in the main text.
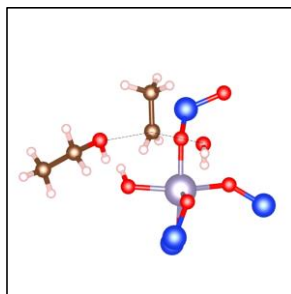
Figure C3. Transition state for DEE formation previously calculated[157] at the hydrolyzed-open site in Sn-Beta (T8).

Table C1. Apparent activation enthalpies, entropies, and Gibbs free energies (404 K) for bimolecular ethanol dehydration at stacking fault defect-open Sn sites in Beta zeolites covered by different MARI species.

| Pathway: | Concerted | | Sequential ($H_2O$-assisted) | | |
|---|---|---|---|---|---|
| MARI Species: | E#[a] | #[b] | $E_x$#[c] | $EE_x$#[d] | E#[e] |
| Expected Ethanol Order | 1 | 2 | 1 | 0 | 1 |
| $\Delta H_{app}^{\ddagger}$ / kJ mol$^{-1}$ | 157 | 78 | 19 | 90 | 145 |
| $\Delta S_{app}^{\ddagger}$ / J mol$^{-1}$ K$^{-1}$ | -103 | -214 | -310 | -209 | -110 |
| $\Delta G_{app}^{\ddagger}$ (404 K) / kJ mol$^{-1}$ | 199 | 164 | 144 | 174 | 190 |

[a]$C_2H_5OH(g)$ + E# $\rightleftharpoons$ TS2

[b]$2C_2H_5OH(g)$ + # $\rightleftharpoons$ TS2

[c]$C_2H_5OH(g)$ + $H_2O(g)$ + $E_x$# $\rightleftharpoons$ TS4

[d]$H_2O(g)$ + $EE_x$# $\rightleftharpoons$ TS4

[e]$C_2H_5OH(g)$ + E# $\rightleftharpoons$ TS4
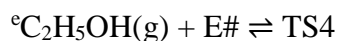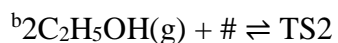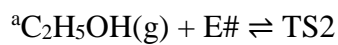
Table C2. Ethanol adsorption energies at arbitrarily numbered t-site locations in stacking fault Beta. The T4 location denotes the Sn location used in the provided structural model. The total range in binding energy across all sites is 0.22 eV

| Stacking fault T-location | $\Delta E_{ads}$ Ethanol / eV |
|:---:|:---:|
| T1 | -0.70 |
| T2 | -0.63 |
| T3 | -0.79 |
| T4 | -0.85 |
| T5 | -0.76 |
| T6 | -0.76 |
| T7 | -0.68 |

Table S.1. Differential dispersion energies calculated by the method of Grimme using the optimized geometries of E# at the stacking fault site and E* at the closed site.

| Species | $\Delta E_{vdW}$ / J mol$^{-1}$ |
|:---:|:---:|
| E* | -40 |
| E# | -31 |

# APPENDIX D SUPPLEMENTARY INFORMATION FOR CHAPTER 5

MYCROSOLVE list of butadiene reaction

CA_Ex*<->Acet_COx*
CA_H2OOP*<->CrotonOP*+W(g)
AcetOP*<->EnW*
Acet(g)+op*<->AcetOP*
E(g)+*<->E*
COH*<->COH(g)+*
CA2W*<->CA*+W(g)+W(g)
EE*<->DEEOP*
Acet(g)+*<->Acet*
COx*+W(g)<->COx_H2O*
CA(g)+*<->CA*
En*+W(g)<->EnW*
E*<->Ex*
COx_H2O*<->COH_H2O*
AcetW*<->EnW*
op*<->W*
Acet*+Acet(g)<->AcetAcet*
WAO*<->AOOP*
BuE_op*<->BuE(g)+op*
E*+E(g)<->EE*
Ex*+CA(g)<->CA_Ex*
CrotonOP*<->CA(g)+op*
EnA*<->AO*
AO*+W(g)<->WAO*
COH_H2O*<->BuE_H2O_op*
DEE(g)+op*<->DEEOP*
E*+Acet(g)<->EtOHAcet*
AOL*+W(g)<->AOLOP*
AOLOP*<->CA2W*
W(g)+*<->W*
COH*+W(g)<->COH_H2O*
AOL(g)+op*<->AOLOP*
E*+W(g)<->EtOHwater*
AOL*<->AOL_MS*
AOL*<->AOL(g)+*
Acet*+W(g)<->AcetW*
En*+Acet(g)<->EnA*
AOOP*<->CA_H2OOP*
AOL_MS*<->CrotonOP*
CrotonOP*+E(g)<->CA_Ex*+W(g)

BuE_op*+W(g)<->BuE_H2O_op*
Acet(g)+COx*<->Acet_COx*
MYCROSOLVE REACTANT LIST
DEEOP*
E(g)
COx*
CA*
BuE_op*
EnA*
Acet*
AcetOP*
W(g)
Ex*
BuE(g)
op*
DEE(g)
COx_H2O*
EE*
CrotonOP*
CA(g)
COH*
Acet_COx*
COH_H2O*
Acet(g)
AcetAcet*
BuE_H2O_op*
CA_H2OOP*
AOL(g)
En*
AOLOP*
EnW*
CA2W*
AOOP*
AOL_MS*
AcetW*
AO*
*
COH(g)
EtOHwater*
WAO*
E*
EtOHAcet*
CA_Ex*
AOL*
W*

| 1 | 2Acet+Water+EtOH+* | <-> | Acet*+Acet+Water+EtOH |
|---|---|---|---|
| 2 | Acet*+Acet+Water+EtOH | <-> | (Acet+H2O)*+Acet+EtOH |
| 3 | (Acet+H2O)*+Acet+EtOH | <-> | (En+H2O)*+Acet+EtOH |
| 4 | (En+H2O)*+Acet+EtOH | <-> | En*+H2O+Acet+EtOH |
| 5 | En*+H2O+Acet+EtOH | <-> | EnA*+H2O+EtOH |
| 6 | EnA*+H2O+EtOH | <-> | AOL*+H2O+EtOH |
| 7 | AOL*+H2O+EtOH | <-> | AOLMS*+H2O+EtOH |
| 8 | AOLMS*+H2O+EtOH | <-> | CA#+H2O+EtOH |
| 9 | CA#+H2O+EtOH | <-> | #+H2O+EtOH+CA |
| 10 | #+H2O+EtOH+CA | <-> | *+2H2O+EtOH+CA |
| 11 | *+2H2O+EtOH+CA | <-> | EtOH*+2H2O+CA |
| 12 | EtOH*+2H2O+CA | <-> | Ex*+2H2O+CA |
| 13 | Ex*+2H2O+CA | <-> | ExCA*+2H2O |
| 14 | ExCA*+2H2O | <-> | AcetCOx*+2H2O |
| 15 | AcetCOx*+2H2O | <-> | COx* +2H2O + Acet |
| 16 | COx* +2H2O + Acet | <-> | COxH2O*+H2O+Acet |
| 17 | COxH2O*+H2O+Acet | <-> | (COH+H2O)*+H2O+Acet |
| 18 | (COH+H2O)*+H2O+Acet | <-> | (Bu+H2O)#+2H2O+Acet |
| 19 | (Bu+H2O)#+2H2O+Acet | <-> | Bu#+3H2O+Acet |
| 20 | Bu#+3H2O+Acet | <-> | #+Bu+3H2O+Acet |
| 21 | E*+E | <-> | EE* |
| 22 | EE* | <-> | D# |
| 23 | D# | <-> | D+# |
| 24 | E* | <-> | EY# |
| 25 | EY# | <-> | EY+# |
| 26 | COH* | <-> | COH+* |
| 27 | (COH+H2O)*+H2O+Acet | <-> | COH*+2H2O+Acet |

Table D1 binding energies of defected sites

|  | A* | Enx* |
|---|---|---|
| Large defect site | -0.89 | 0.28 |
| Reduced defect site | -0.78 | 0.28 |
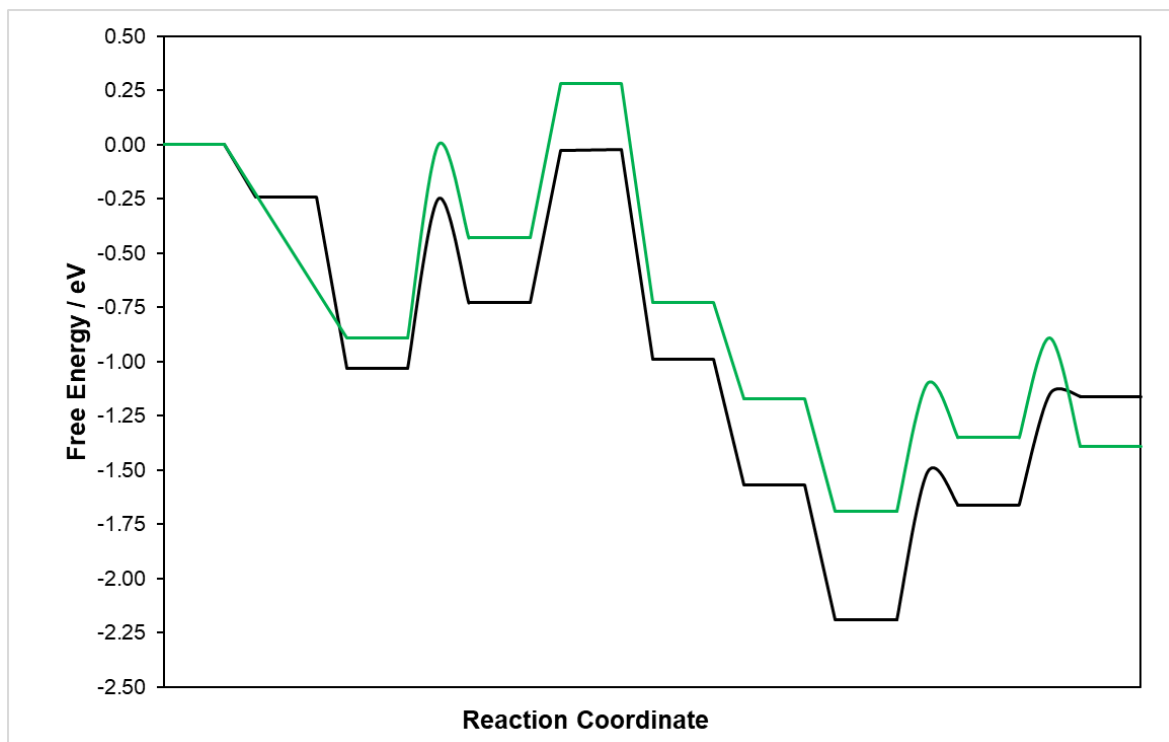
Figure E1 aldol condensation at defect open sites (green) versus internal closed Beta sites (black)
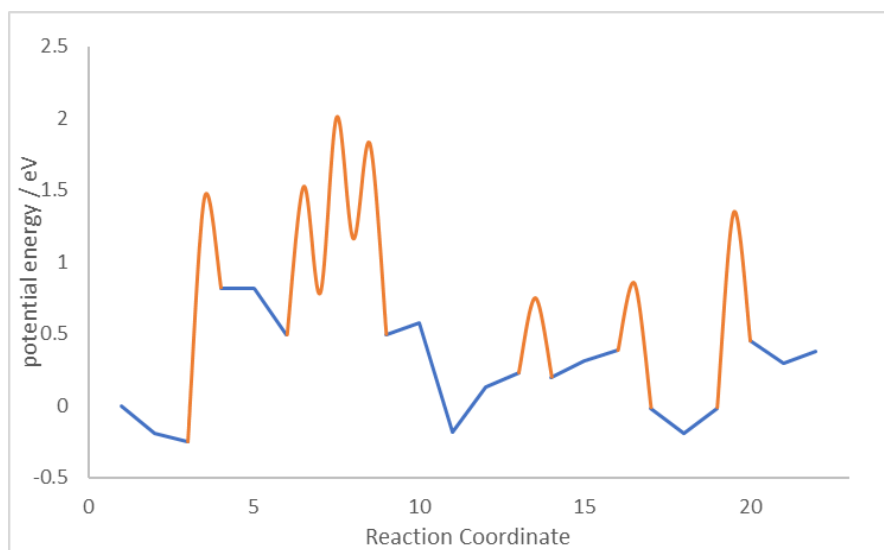


Figure E2 alternate enolate formation
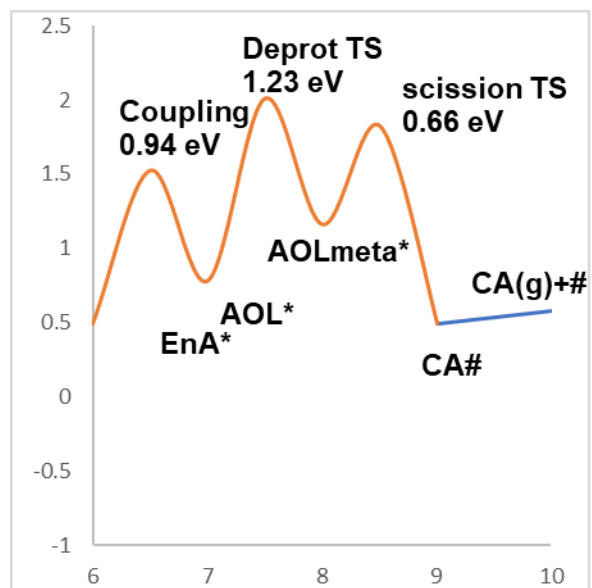
Figure E3 alternate aldol dehydration mechanism with sequential dehydration

# APPENDIX E SUPPLEMENTARY INFORMATION FOR  CHAPTER 6
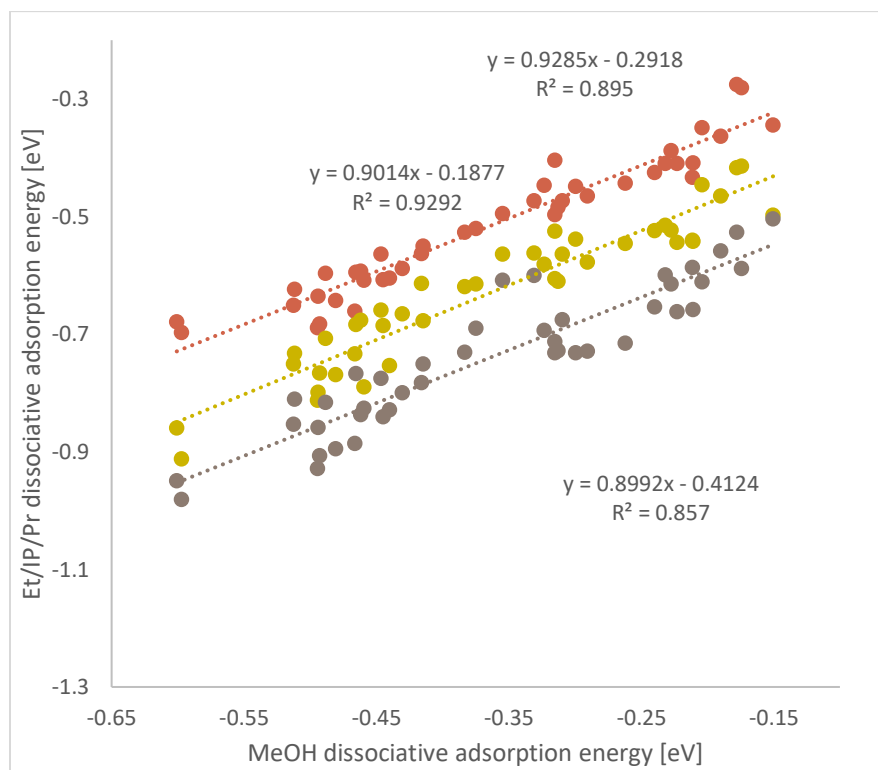


Figure E1 correlated binding energy of alkanols across the span of framework-heteroatom pairs

# APPENDIX F SUPPLEMENTARY INFORMATION FOR CHAPTER 7
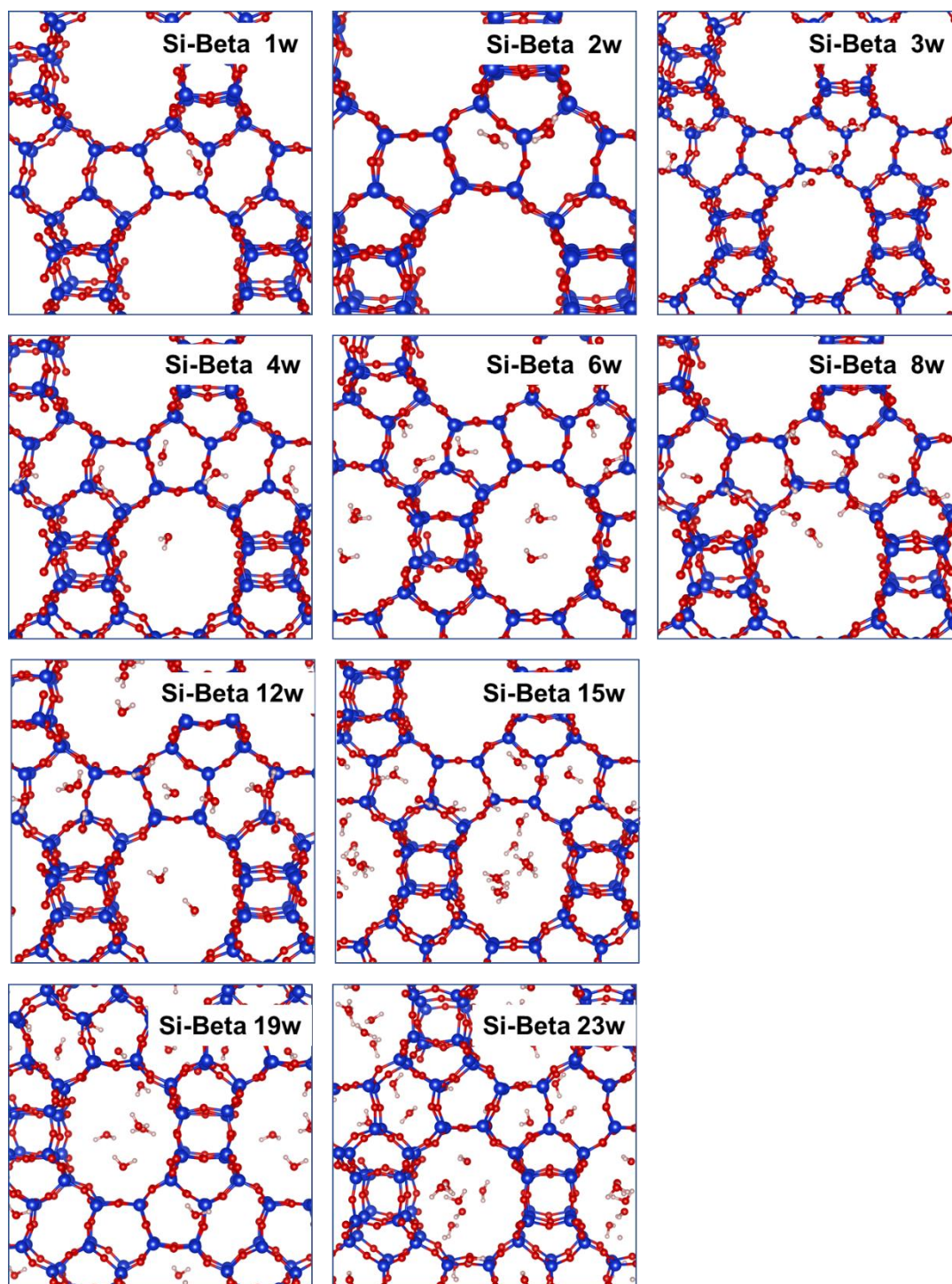


Figure F1 Representative snapshots of water structures obtained during production runs at varying density in Si-Beta
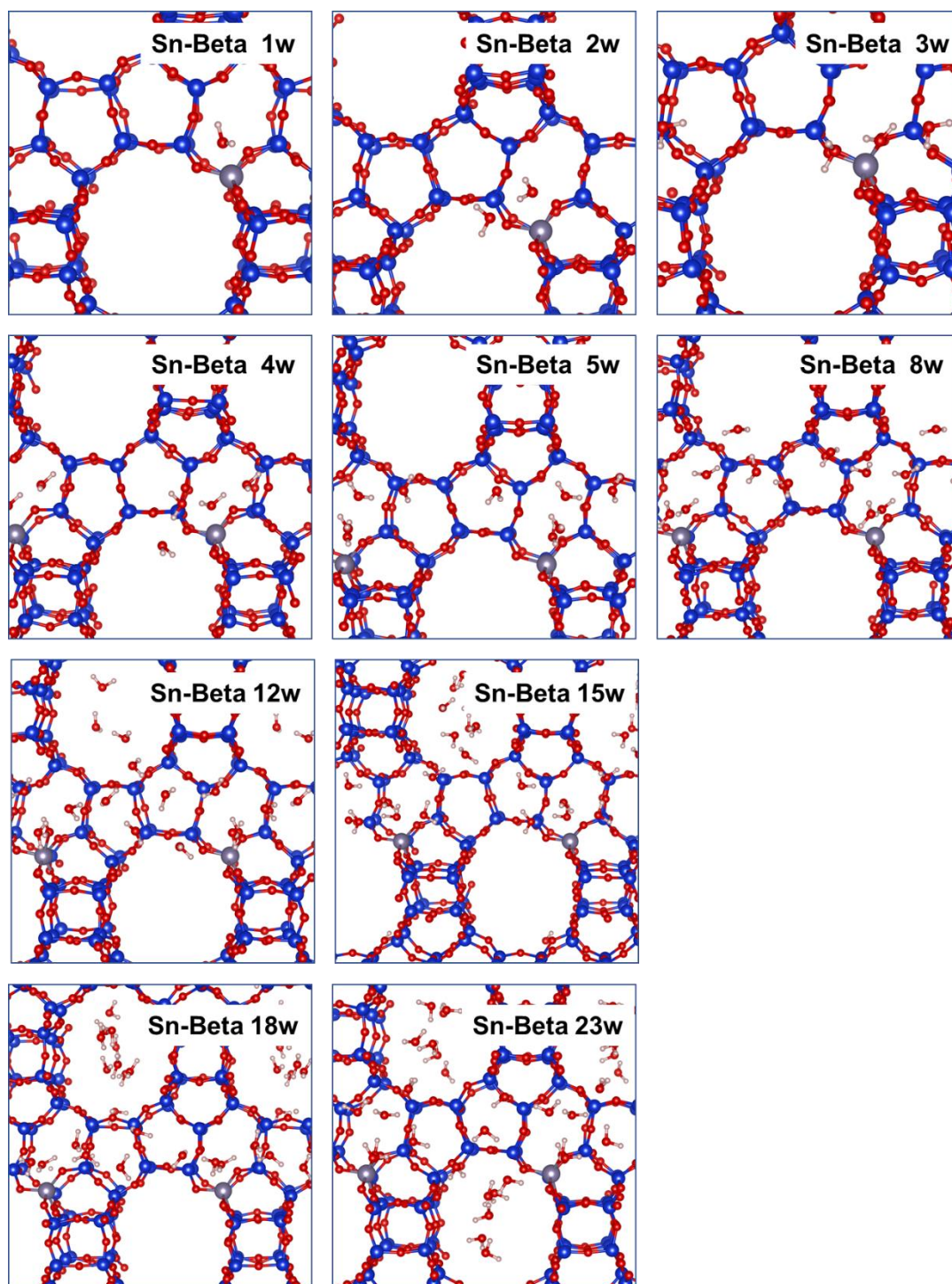
Figure F2 Representative snapshots of water structures obtained during production runs at varying density in Sn-Beta.
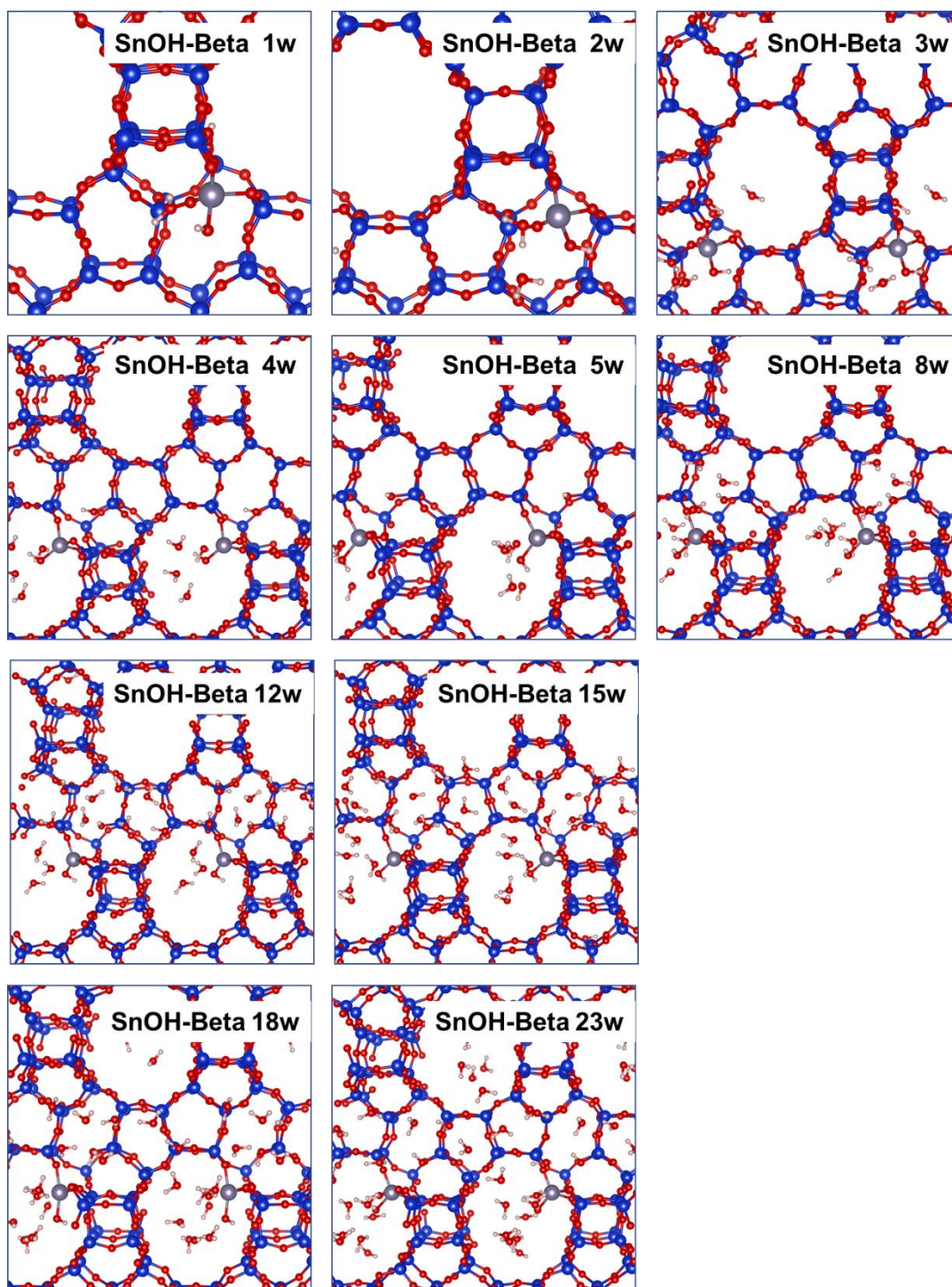
Figure F3 Representative snapshots of water structures obtained during production runs at varying density in SnOH-Beta.
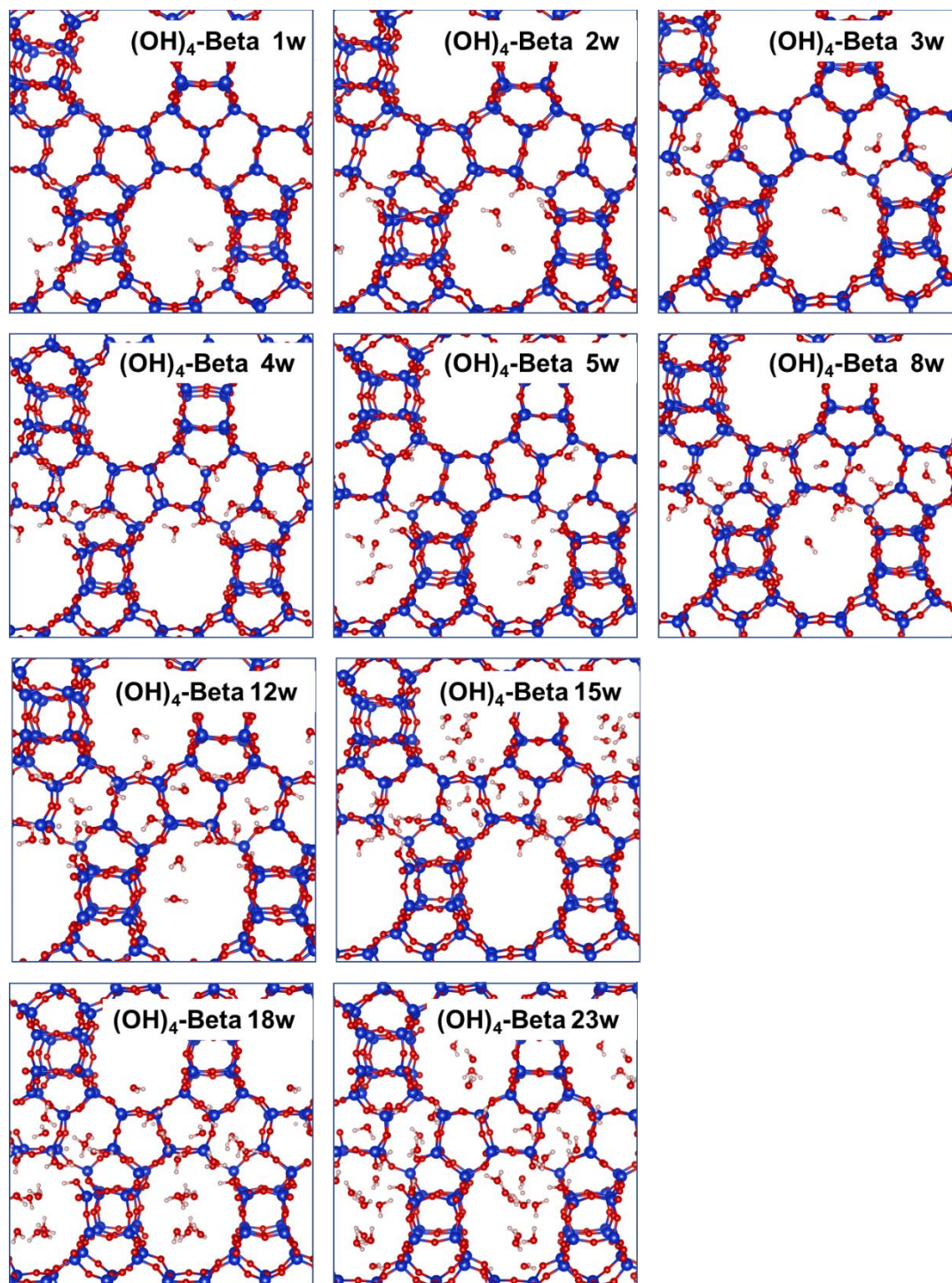
Figure F4. Representative snapshots of water structures obtained during production runs at varying density in (OH)$_4$-Beta.

*8 water unit cell⁻¹*
*2.08 10⁻³ mol g⁻¹*

*23 water unit cell⁻¹*
*5.98 10⁻³ mol g⁻¹*
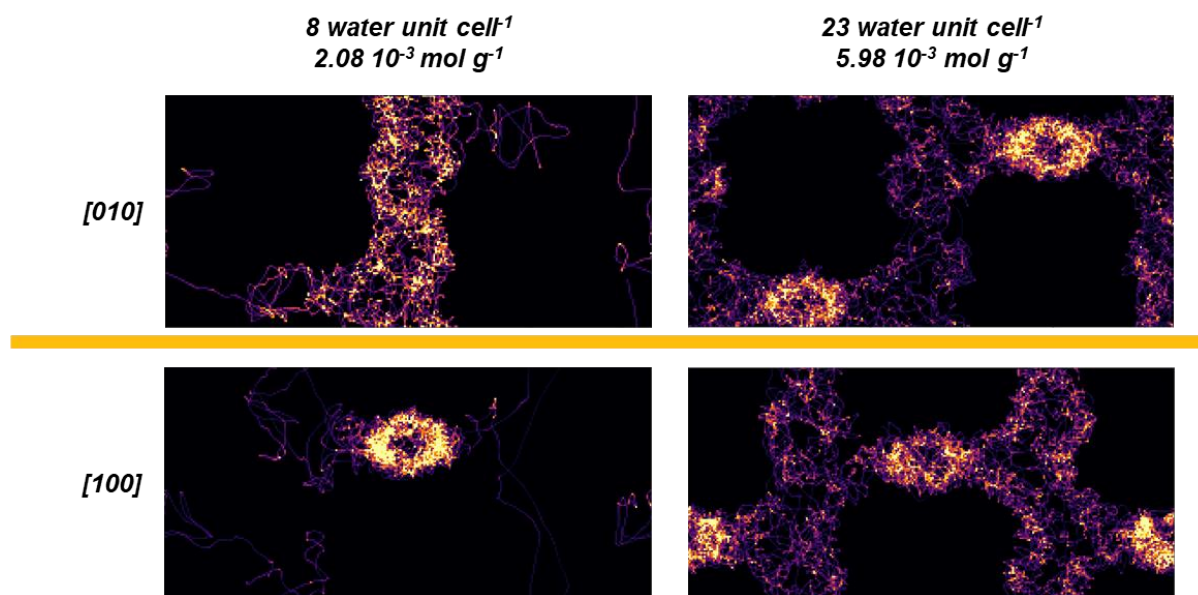
Figure F5. Time averaged density plot for Si-Beta along the [010] and [100] planes at low (8) and high (23) water densities (water unit cell$^{-1}$).
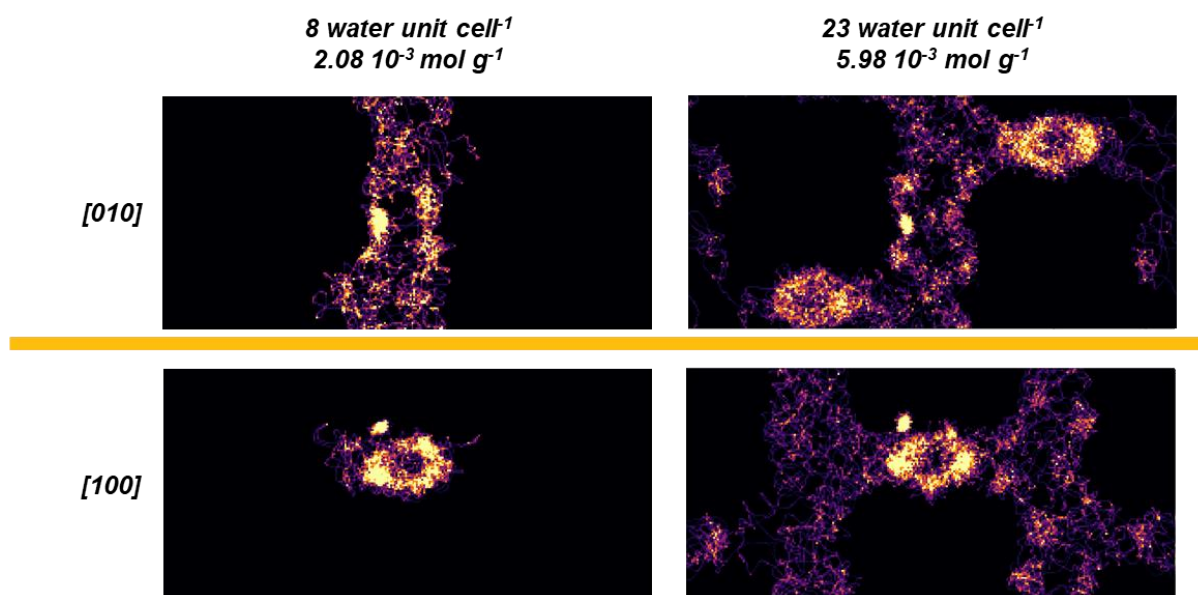


Figure F6. Time averaged density plot for Sn-Beta along the [010] and [100] planes at low (8) and high (23) water densities (water unit cell$^{-1}$).
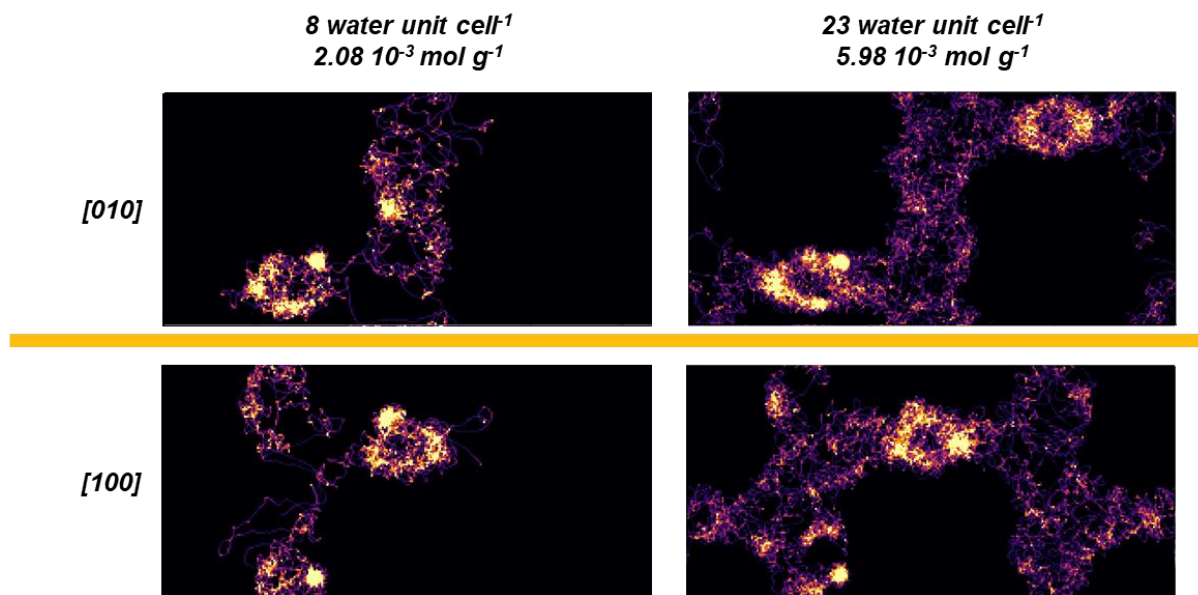
Figure F7. Time averaged density plot for SnOH-Beta along the [010] and [100] planes at low (8) and high (23) water densities (water unit cell$^{-1}$).
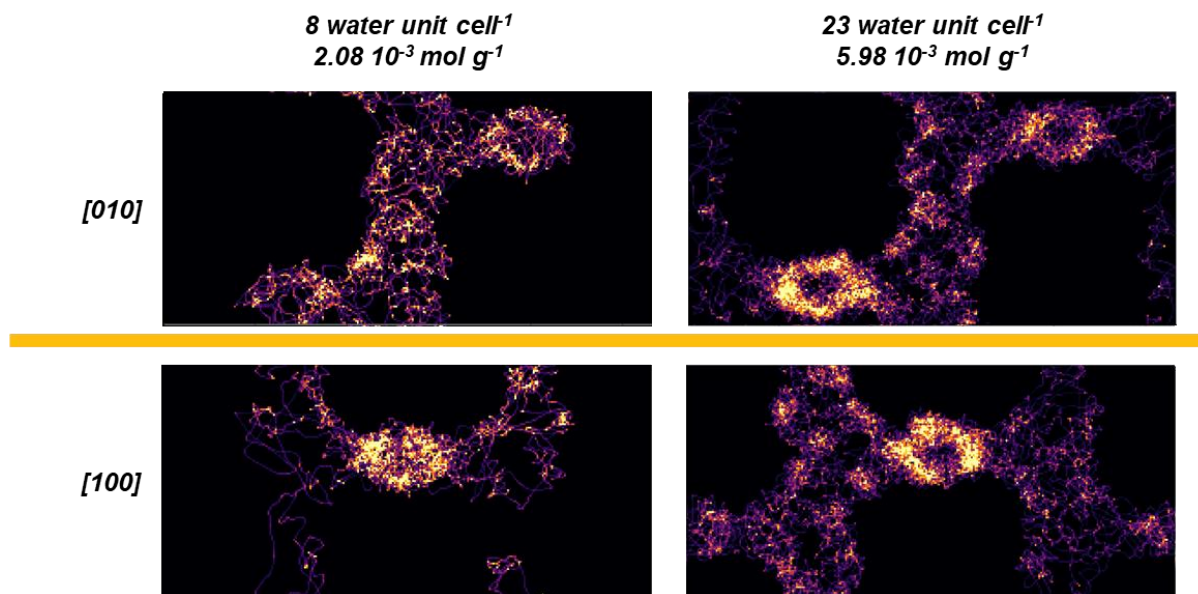


Figure F8. Time averaged density plot for (OH)$_4$-Beta along the [010] and [100] planes at low (8) and high (23) water densities (water unit cell$^{-1}$).
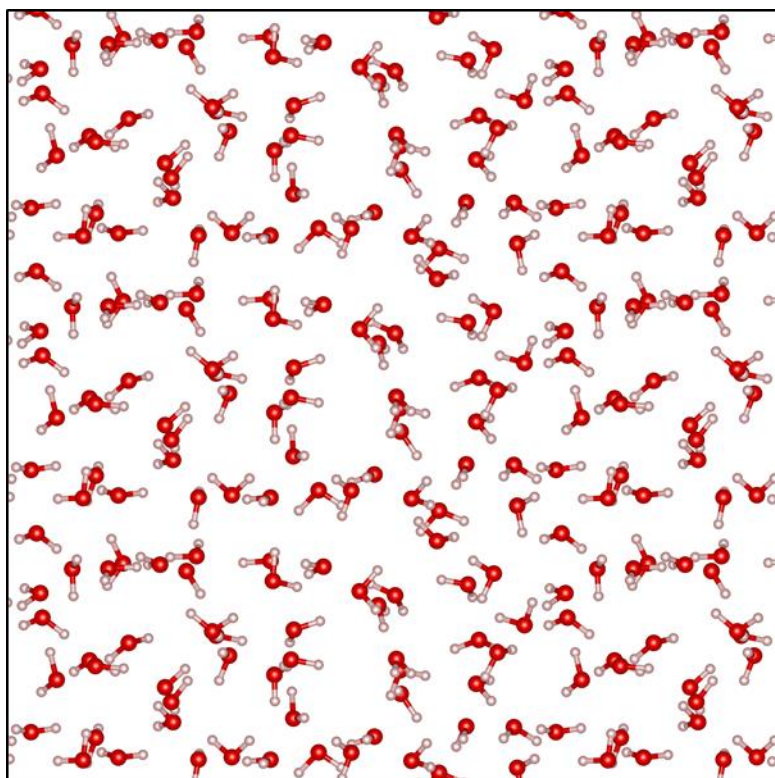
Figure F9. Supercell of bulk water simulated as a reference state.
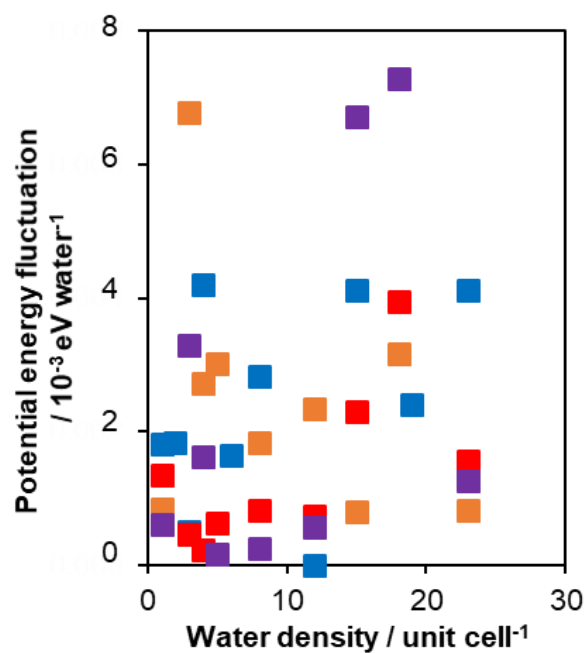
Figure F10. Fluctuations in the potential energy predicted per water molecule for Si-beta (blue), Sn-Beta (red), SnOH-Beta (orange), and $(OH)_4$-Beta (purple) at 19 ps and 20 ps.
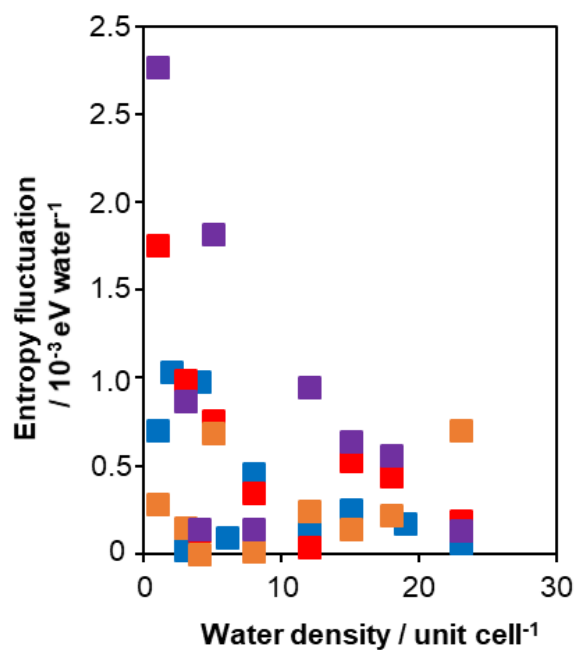


Figure F11. Fluctuations in the entropy predicted per water molecule for Si-beta (blue), Sn-Beta (red), SnOH-Beta (orange), and $(OH)_4$-Beta (purple) at 19 ps and 20 ps.
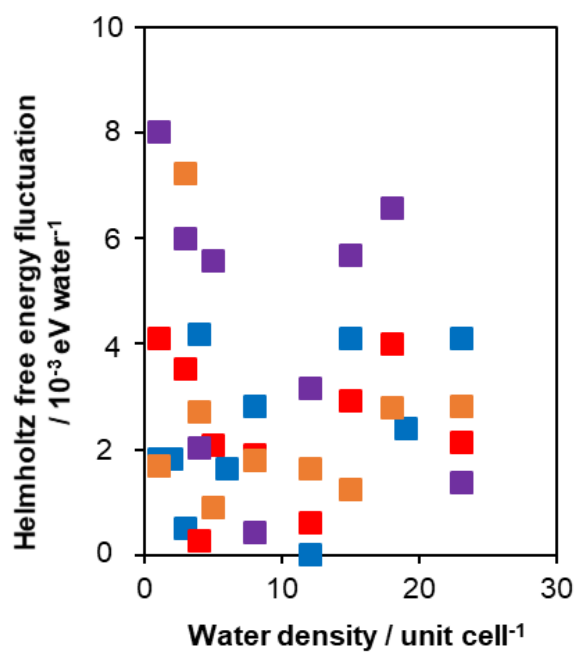
Figure F12. Fluctuations in the potential energy predicted per water molecule for Si-beta (blue), Sn-Beta (red), SnOH-Beta (orange), and $(OH)_4$-Beta (purple) at 19 ps and 20 ps.
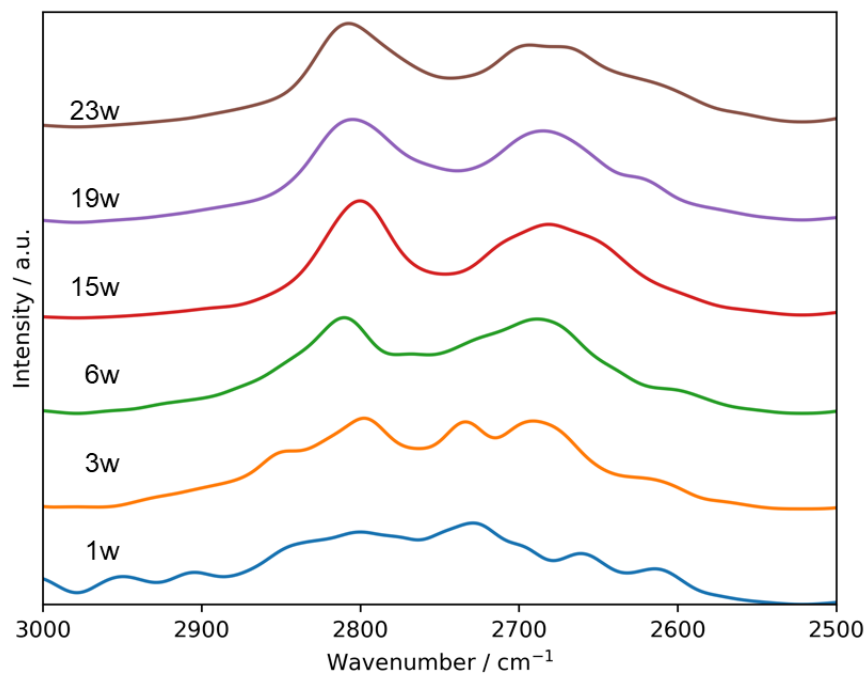
Figure F13. Calculated OD stretching peaks in Si-Beta. Spectra have been offset and normalized for clarity.
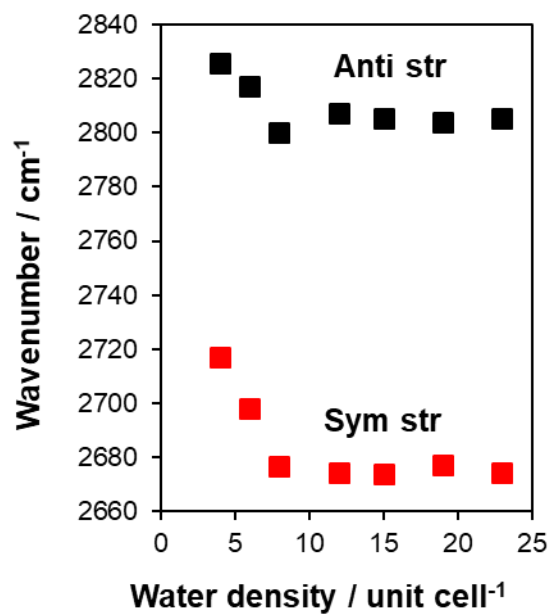


Figure F14. Calculated peak centers in Si-Beta.
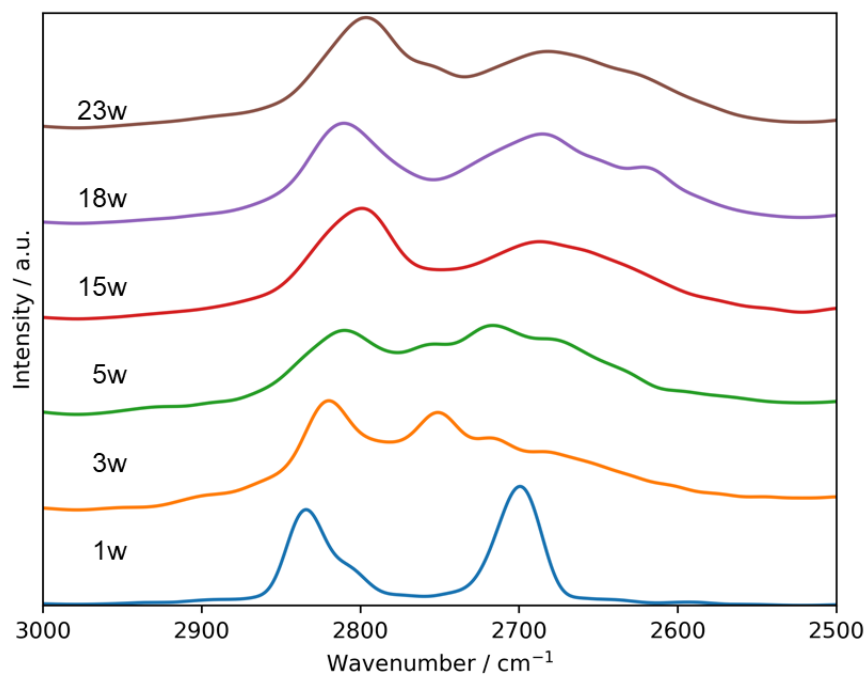
Figure F15. Calculated OD stretching peaks in Sn-Beta. Spectra have been offset and normalized for clarity.
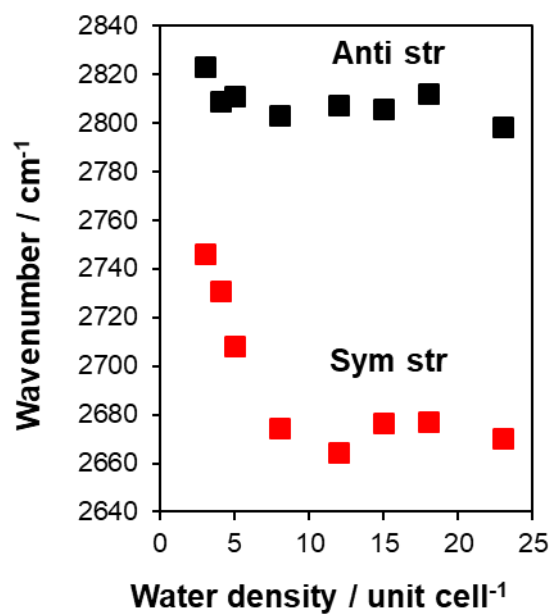


Figure F16. Calculated peak centers in Sn-Beta.
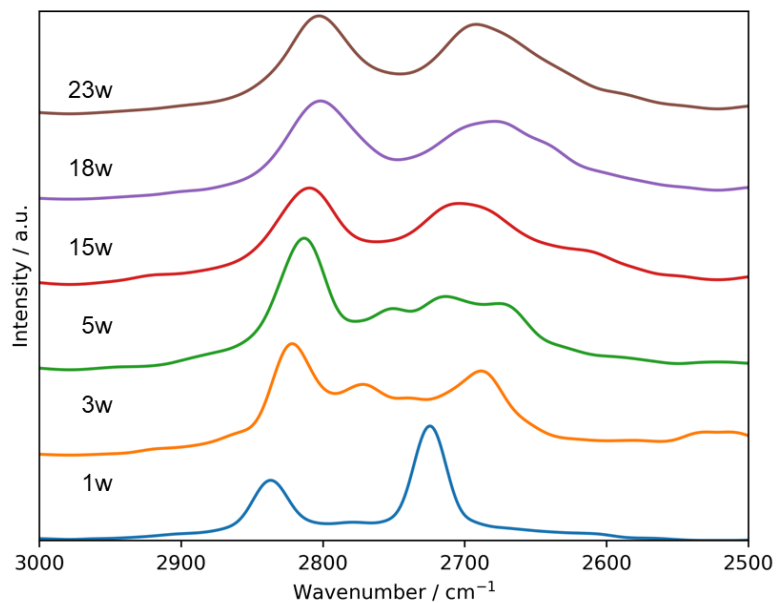
Figure F17. Calculated OD stretching peaks in SnOH-Beta. Spectra have been offset and normalized for clarity.
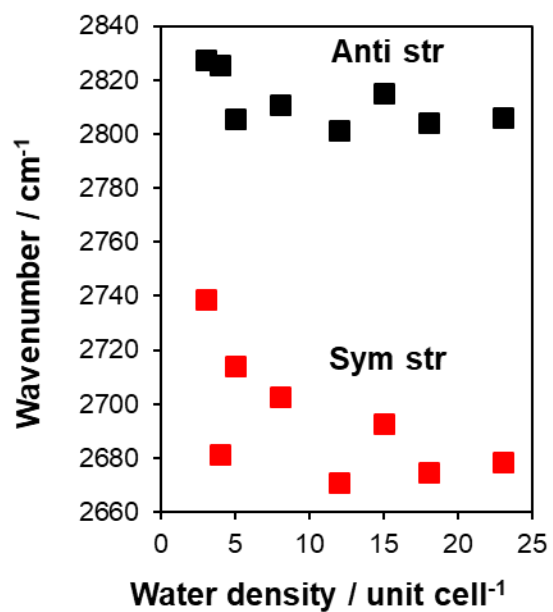


Figure F18. Calculated peak centers in SnOH-Beta.
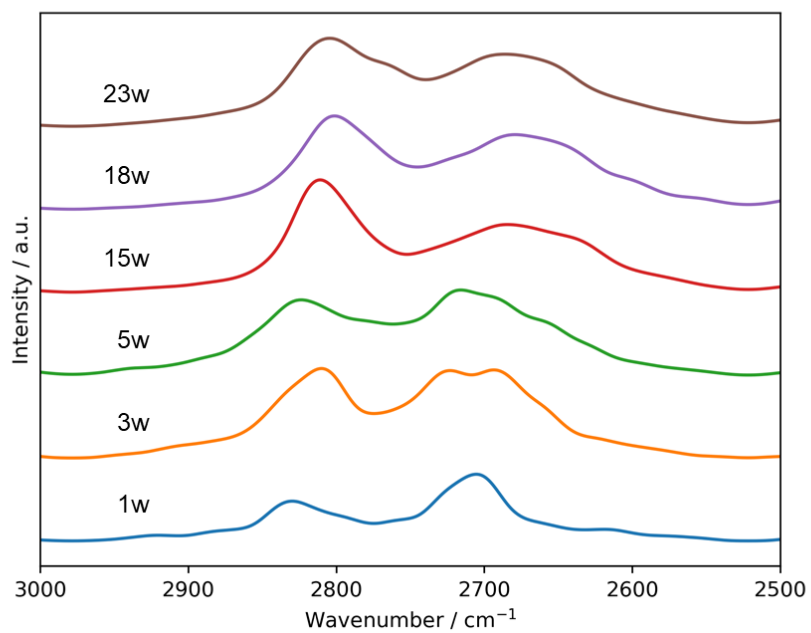
Figure F19. Calculated OD stretching peaks in $(OH)_4$-Beta. Spectra have been offset and normalized for clarity.
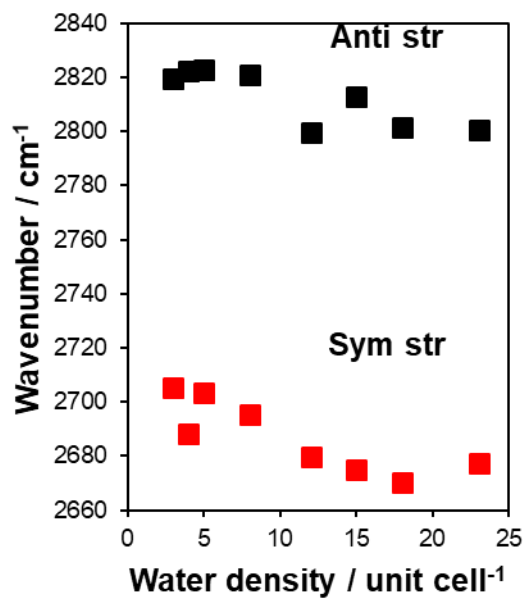


Figure F20. Calculated peak centers in SnOH-Beta.
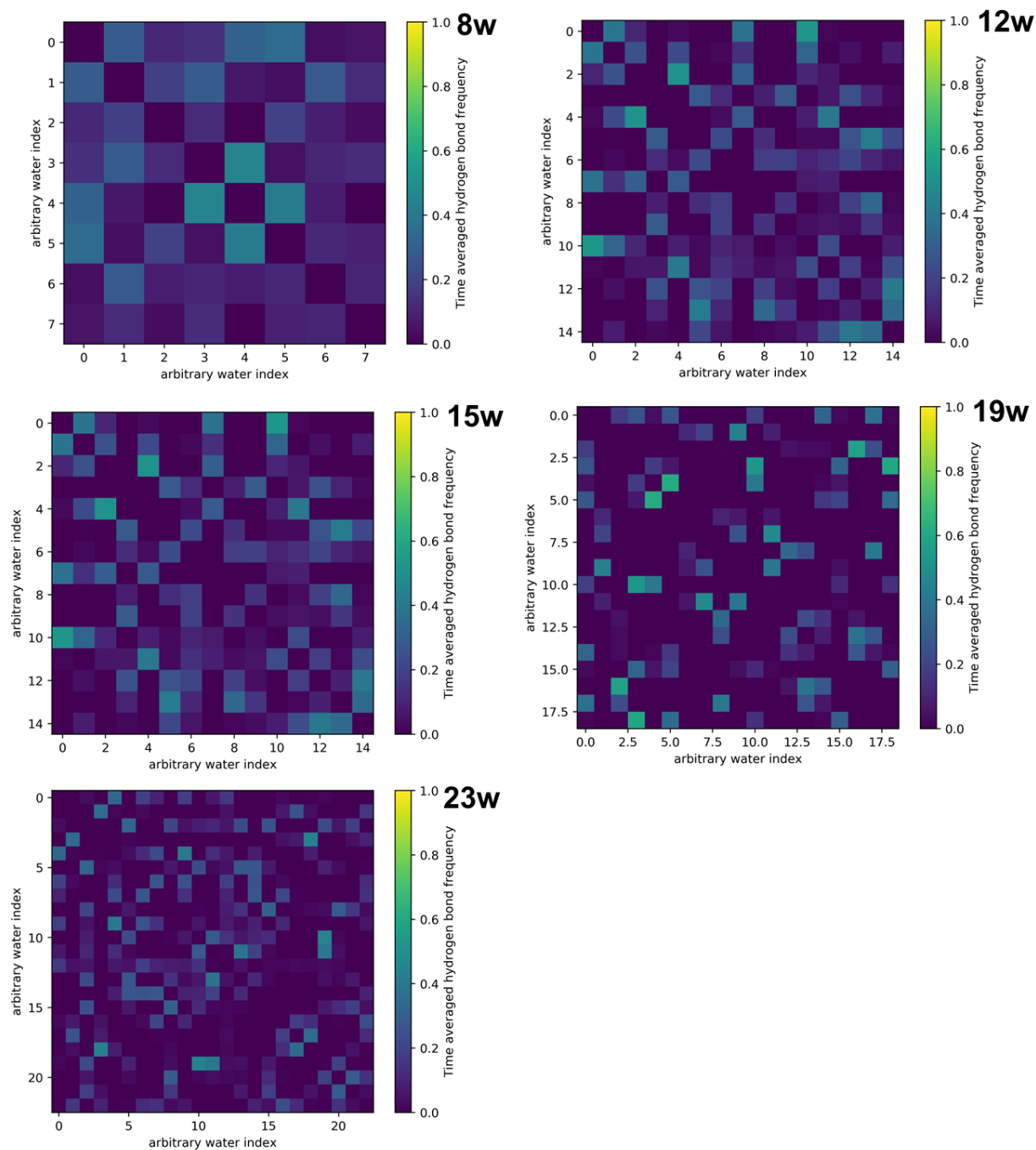
Figure F21. Hydrogen bonding graphs showing time averaged hydrogen bond frequency between water pairs in Si-Beta.
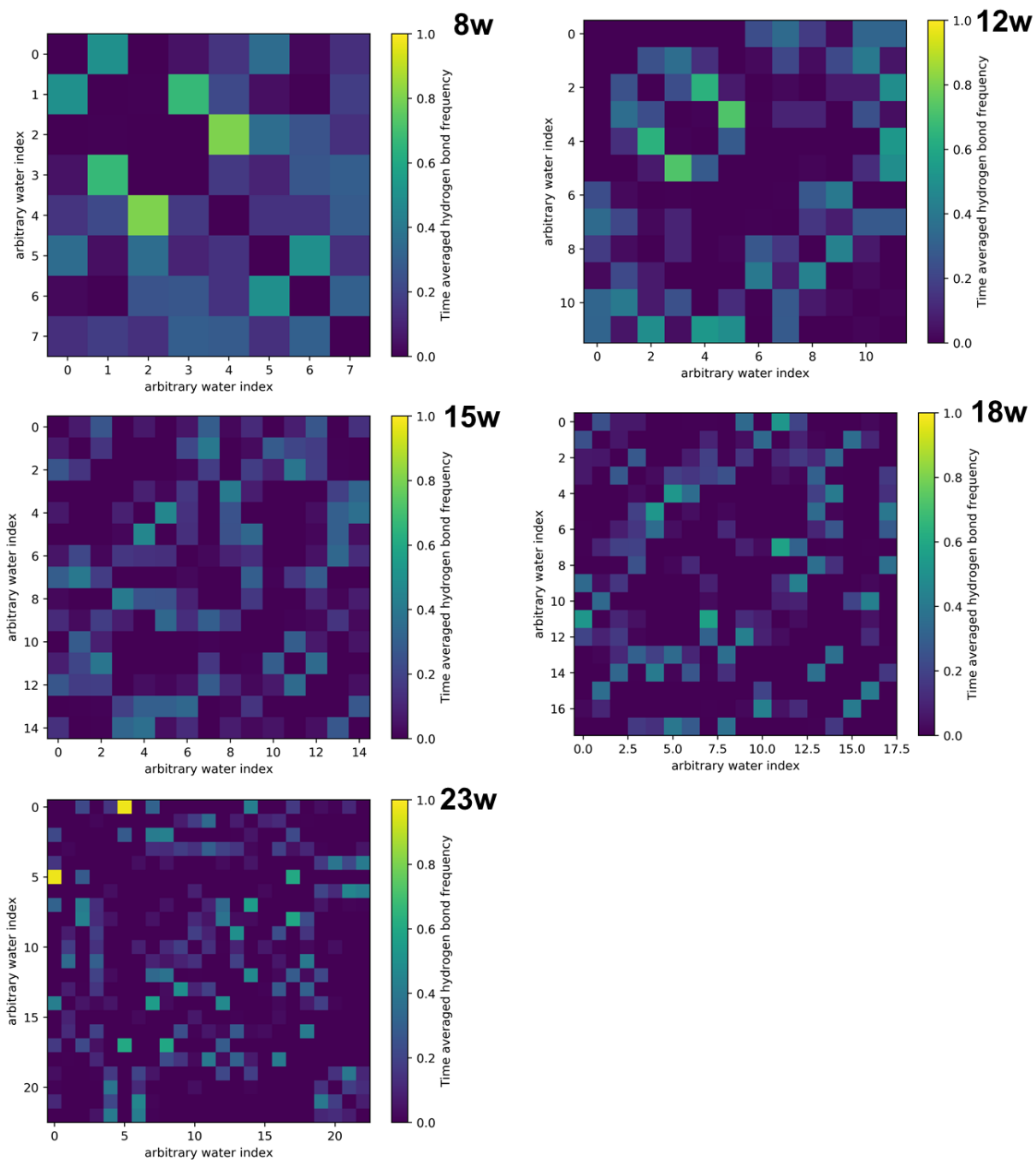
Figure F22. Hydrogen bonding graphs showing time averaged hydrogen bond frequency between water pairs in Sn-Beta.
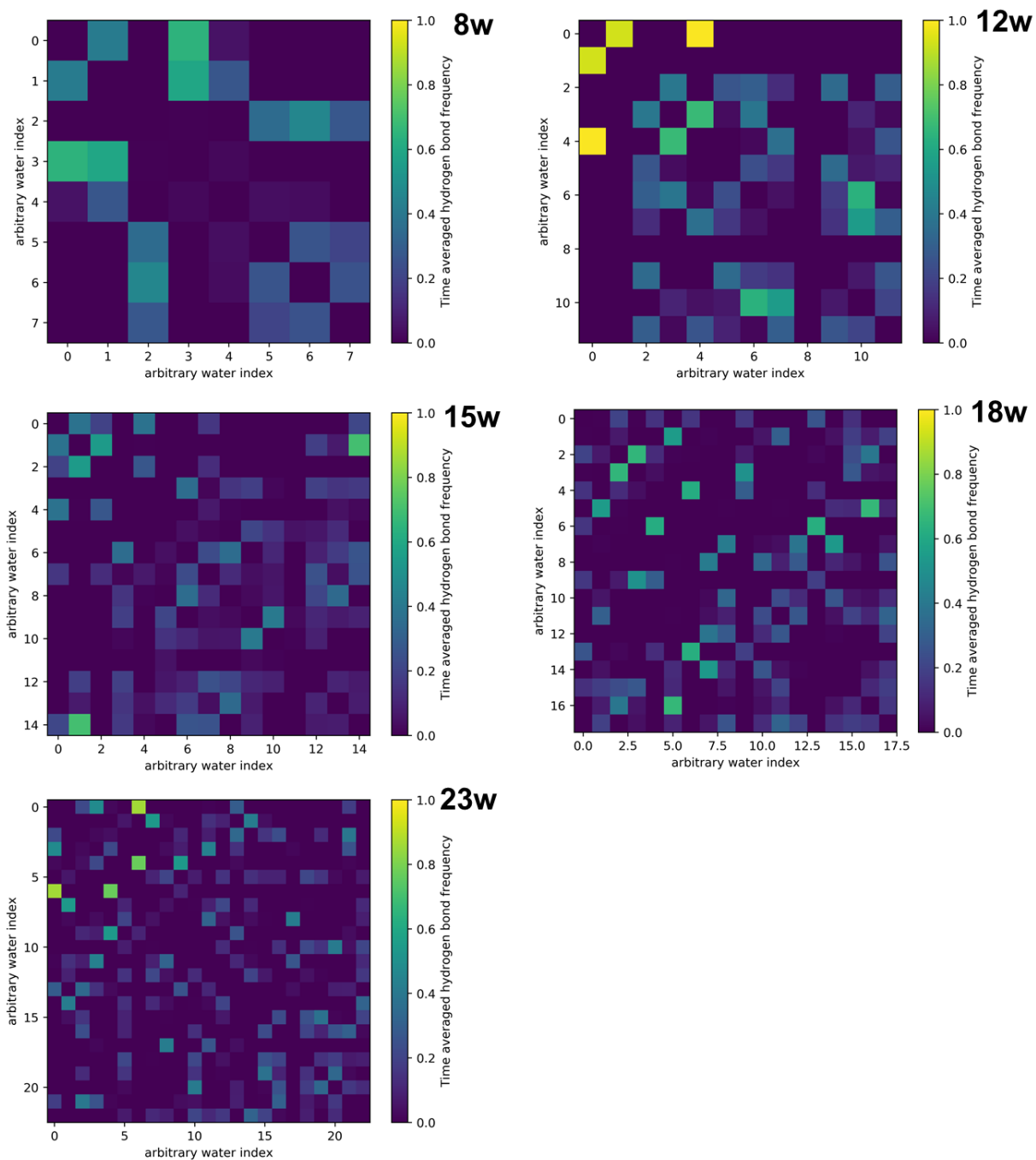
Figure F23. Hydrogen bonding graphs showing time averaged hydrogen bond frequency between water pairs in SnOH-Beta.
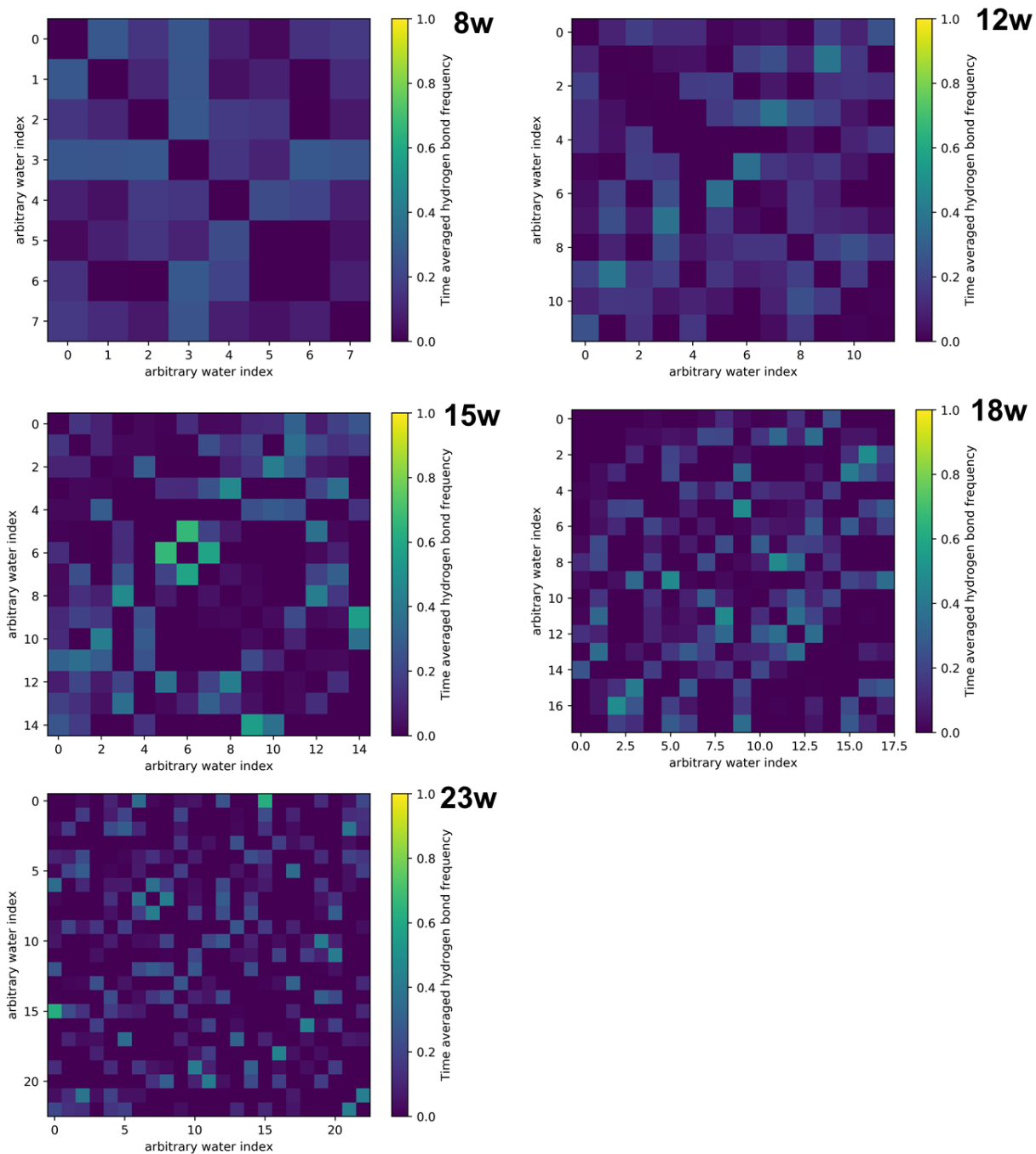
Figure F24. Hydrogen bonding graphs showing time averaged hydrogen bond frequency between water pairs in $(OH)_4$-Beta.
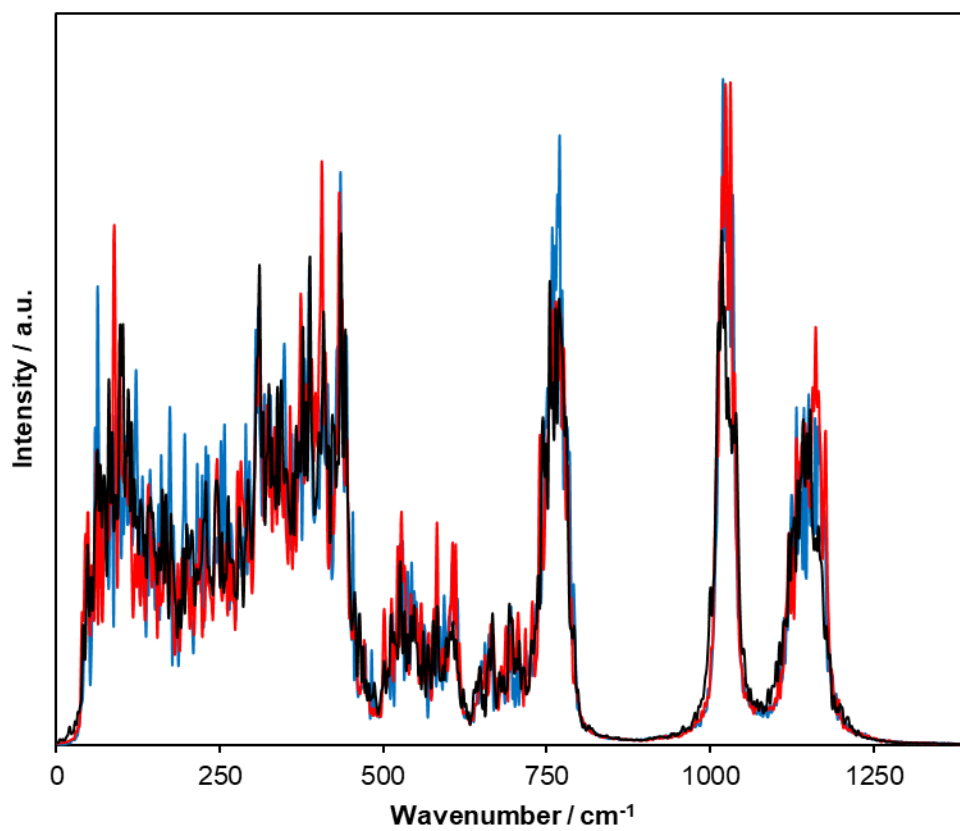
Figure F25. VDOS spectra of the Si-Beta framework at water densities of 0 (blue), 12 (red), and 45 (black) waters per unit cell.
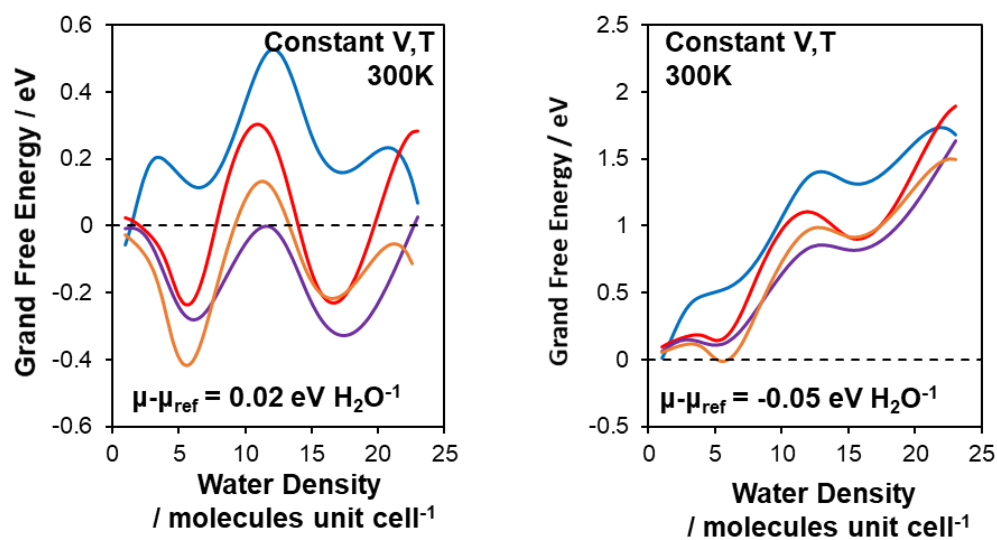
Figure F26. Grand potential energies referenced to P/P° = 0.05 for each defect; blue, Si-Beta; red, Sn-Beta; purple, SnOH; orange, (OH)$_4$-Beta .

# APPENDIX G SUPPLEMENTARY INFORMATION FOR CHAPTER 9

Table G1 binding energies of ethanol on H-Beta for each oxygen site

| T site index | proton location | Ethanol binding energy / eV |
|---|---|---|
| T0 | C0 | -0.98 |
| | C1 | -0.91 |
| | C2 | -0.86 |
| | C3 | -0.97 |
| T1 | C0 | -0.97 |
| | C1 | -0.99 |
| | C2 | -0.88 |
| | C3 | -0.78 |
| T2 | C0 | -0.91 |
| | C1 | -0.99 |
| | C2 | -0.91 |
| | C3 | -0.94 |
| T3 | C0 | -0.91 |
| | C1 | -0.91 |
| | C2 | -0.96 |
| | C3 | -0.91 |
| T4 | C0 | -0.96 |
| | C1 | -0.97 |
| | C2 | -0.95 |
| | C3 | - |
| T5 | C0 | -0.94 |
| | C1 | -0.99 |
| | C2 | -0.92 |
| | C3 | - |
| T6 | C0 | - |
| | C1 | -0.91 |
| | C2 | -1.00 |
| | C3 | - |
| T7 | C0 | -0.85 |
| | C1 | -0.92 |
| | C2 | -0.80 |
| | C3 | -0.92 |
| T8 | C0 | -0.90 |
| | C1 | -0.96 |
| | C2 | -1.00 |
| | C3 | -0.86 |
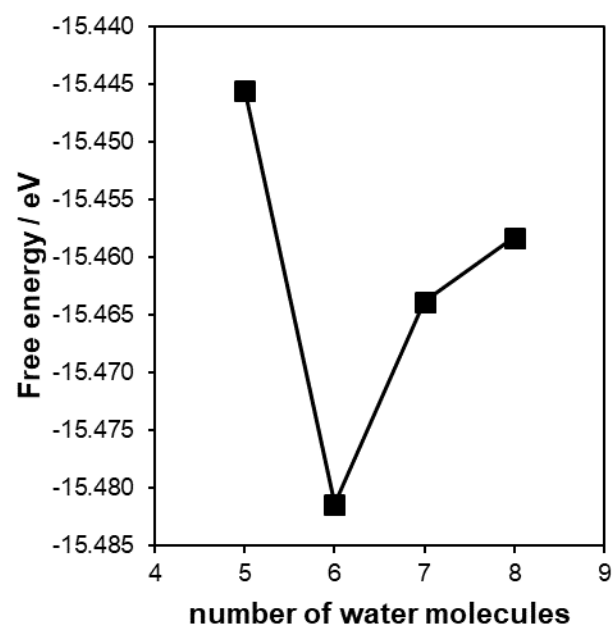
Figure G1 Local free energy of water physiosorbed in H-Beta

# APPENDIX H SUPPLEMENTARY INFORMATION FOR CHAPTER 10
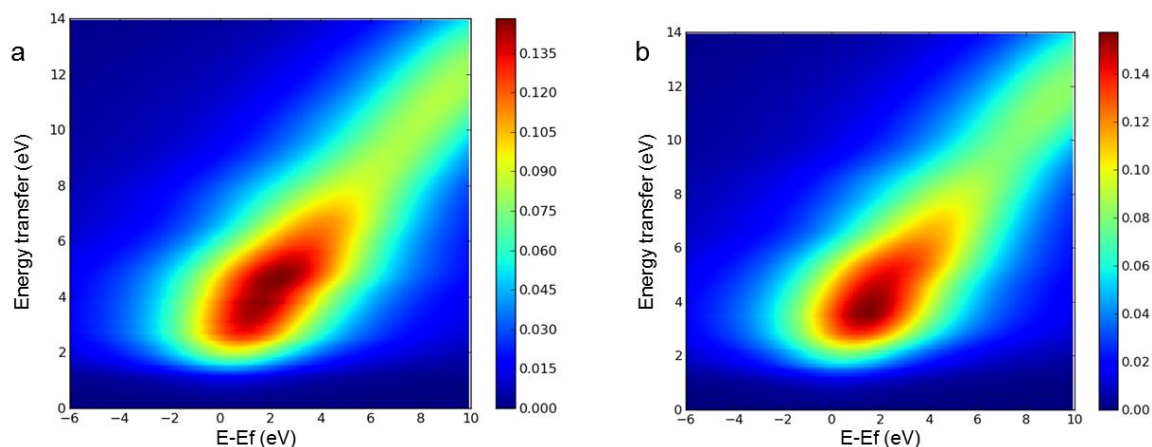


Figure H1. RIXS energy maps for the: (a) $Pt_1Zn_1(110)$ surface termination, and (b) $Pt_1Zn_1(101)$ surface termination.
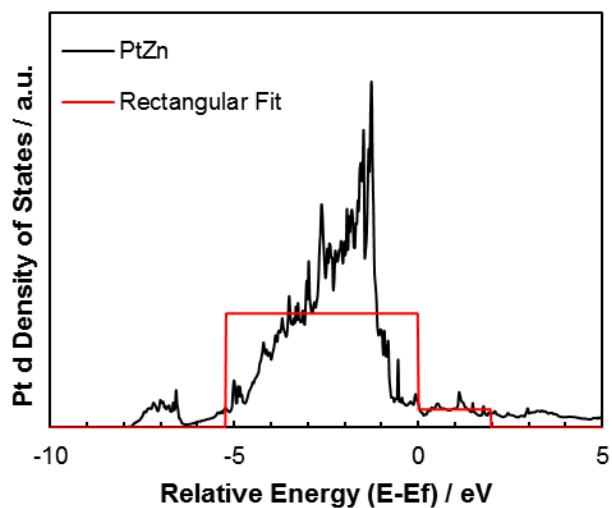


Figure H2. PtZn $d$-DOS and rectangular fitting for the simplified RIXS analysis. The center of each rectangle is the band center of the occupied and unoccupied states. The width of each rectangle is twice the band center. The height of the rectangle is fixed by the constraint that the total number of electrons in the band is constant.
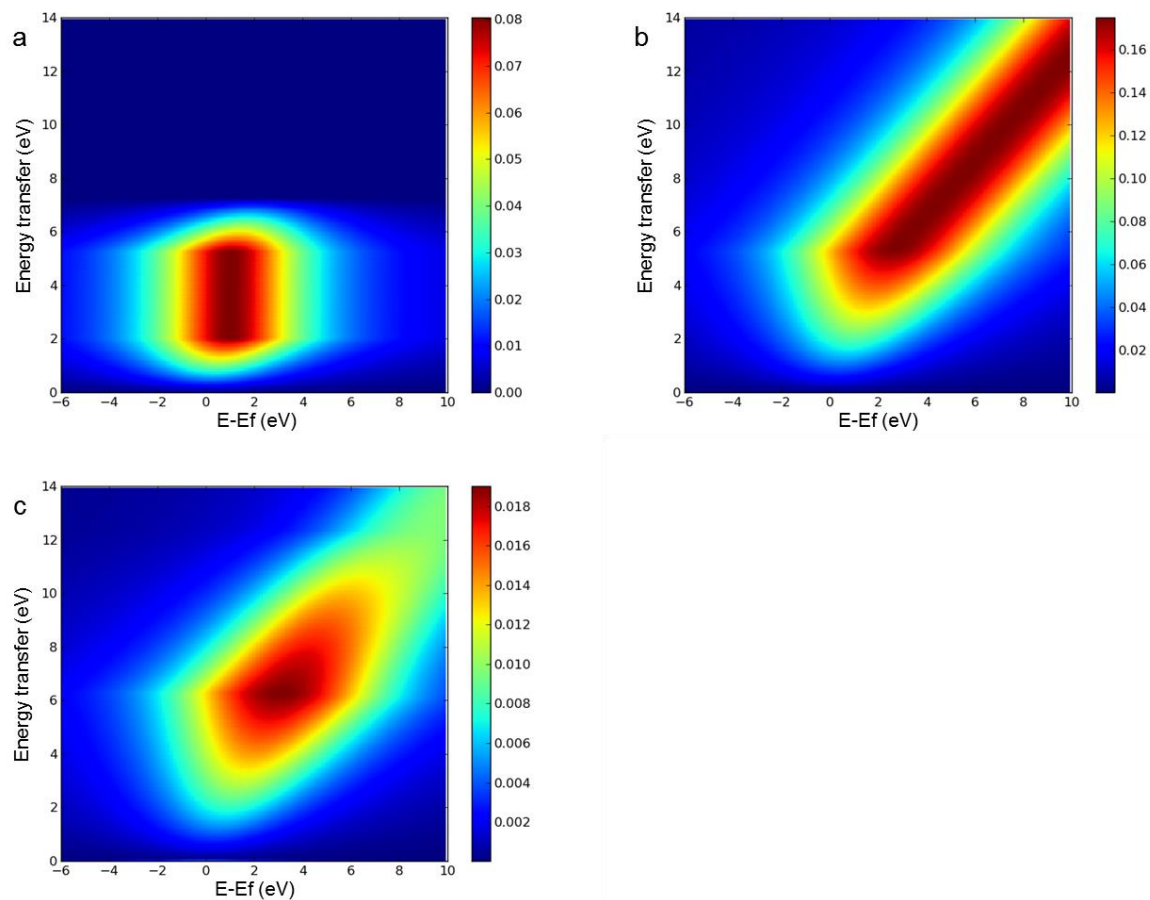
Figure H3. Simulated PtZn RIXS spectra for simplified rectangular DOS analysis. The small-width of unoccupied states in (a) shows a localized peak with no tail. The long, uniform width of unoccupied states in (b) shows a hypothetical long tail distribution with constant high intensity along the tail. In (c), an additional rectangle of lesser height is appended to the unoccupied DOS, leading to the formation of a tail of decaying intensity.
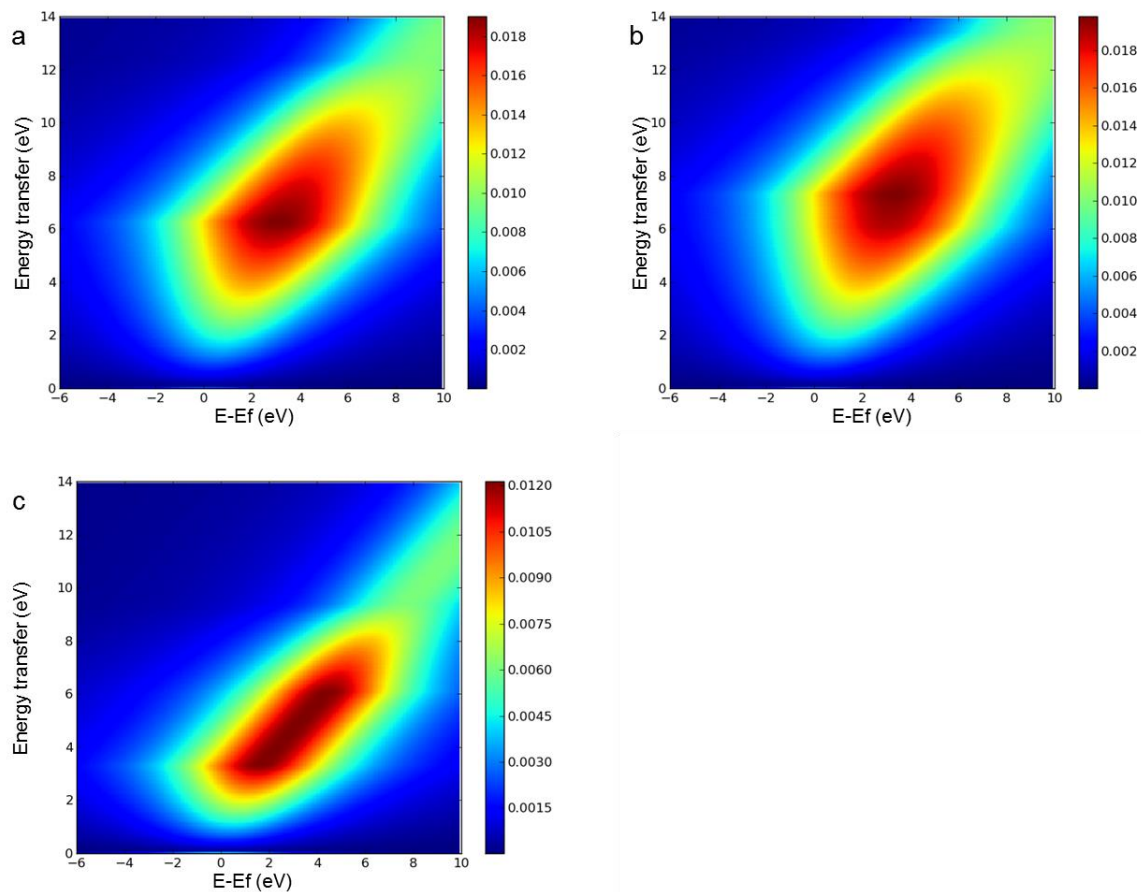
Figure H4. Adjusted PtZn RIXS spectra for the simplified rectangular DOS analysis. In (a), the unoccupied DOS is split into a second rectangular identical to Fig. S9(c). In (b), the width of the band is adjusted to be 2 eV longer than (a) by adding additional states at the edge below the Fermi energy ($E_f$). In (c), the width of the band is decreased such that the DOS is 2 eV narrower than (a) by removing states at the edge below $E_f$.

# APPENDIX I SUPPLEMENTARY INFORMATION FOR CHAPTER 11

Table I5 Binding energies of H, CO and CH₃ on different model surfaces. For H and CO, the gas phase references are $H_2$ and CO, whereas CH₃ binding is evaluated as the reaction energy of $CH_4(g)+* \leftrightarrow CH_3*+1/2H_2(g)$

| Model Surface * | DFT ΔE (eV) | | |
|---|---|---|---|
| | $\Delta E_H$ | $\Delta E_{CO}$ | $\Delta E_{CH3}$ |
| Pt (111) | -0.48 | -1.77 | 0.43 |
| Pt₃Mn-1s(111) | -0.54 | -1.76 | 0.42 |
| Pt₃Mn-1s(111)* | -0.54 | -1.71 | 0.42 |
| Pt₃Mn-2s(111) | -0.46 | -1.70 | 0.52 |
| Pt₃Mn-2s(111)* | -0.47 | -1.67 | 0.52 |
| Pt₃Mn(111) | -0.40 | -1.60 | 0.61 |
| Pt (211) | - | -2.07 | - |
| Pt₃Mn-2s(211) | - | -1.83 | - |
| Pt₃Mn (211) | - | -1.81 | - |

* 1s and 2s means 1 and 2 layers of Pt₃Mn phase on top of Pt, respectively. The "*" in the name of the model surface denotes that the model is constrained at the lattice constant of Pt₃Mn instead of Pt for that without a * in the name.
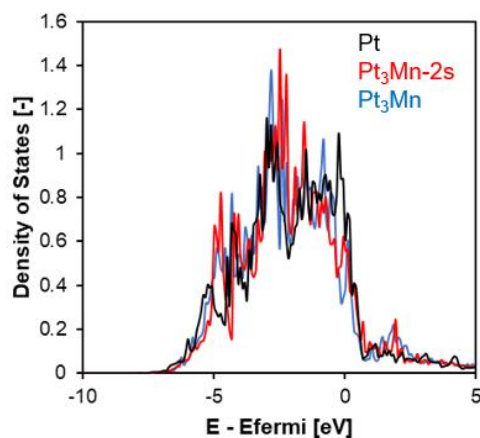


Figure. I1 Density of *d* states for (111) surface Pt atoms in each sample used for calculation of *d*-band centers with fixed Pt lattice constants (i.e. Pt₃Mn-2s(111)).

# APPENDIX J SUPPLEMENTARY INFORMATION FOR CHAPTER 12
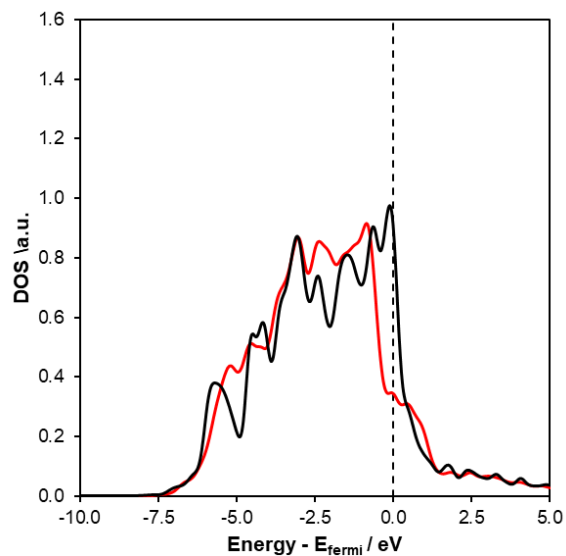


Figure J2. Pt $d$-DOS for $Pt_3Fe$ (red) and pure Pt at the same lattice strain (-3.14%) as $Pt_3Fe$ (black) for Pt surface atoms.
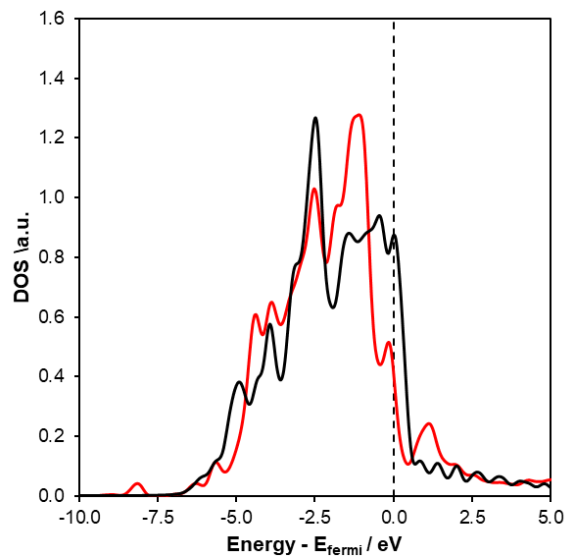


Figure J3. Pt $d$-DOS for $Pt_3Sn$ (red) and pure Pt at the same lattice strain (+2.15%) as $Pt_3Sn$ (black) for Pt surface atoms.

promoter strain effect on DOS
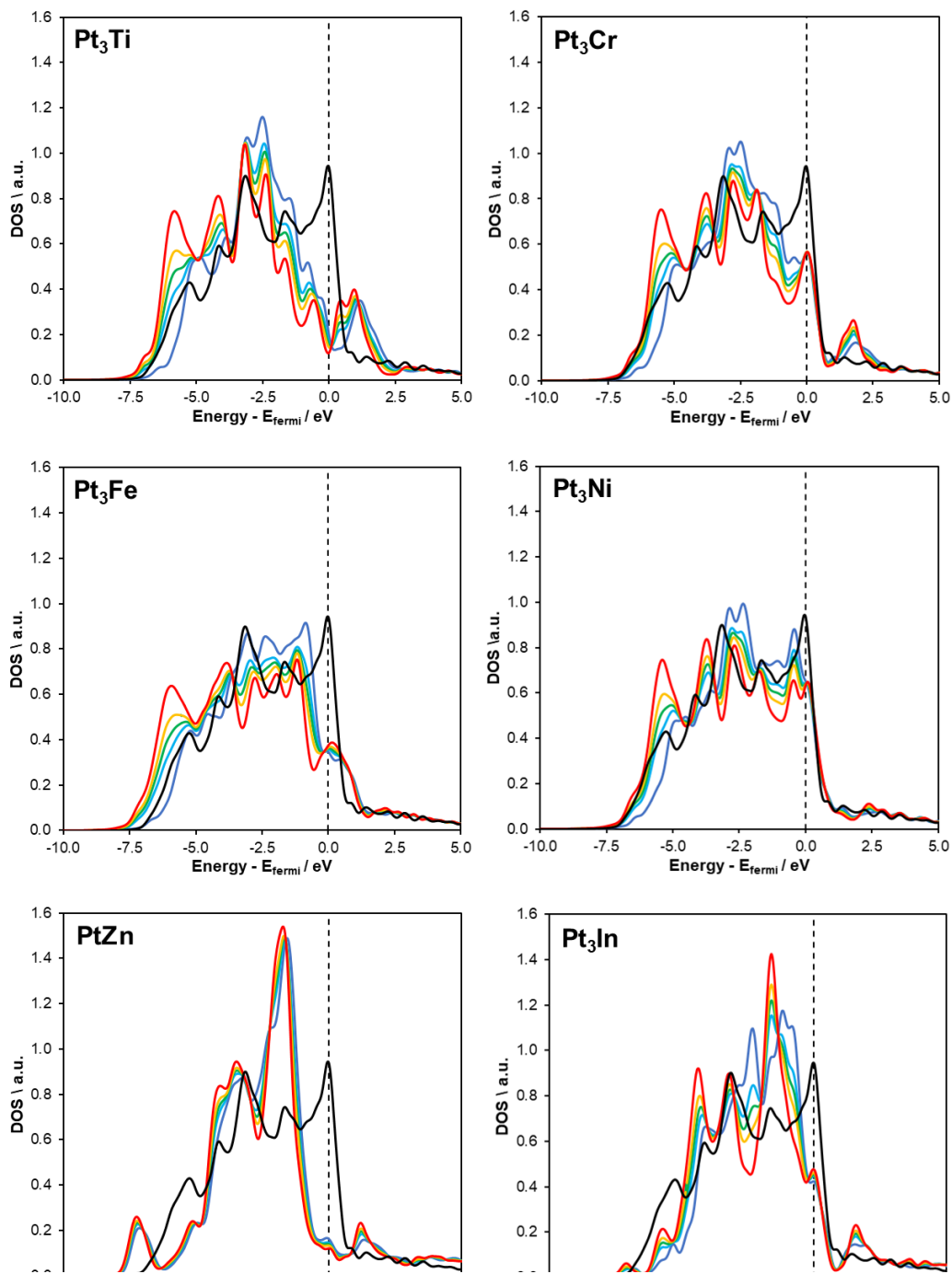


Figure J1 Pt DOS remaining alloys not in Figure 1. The DOS are plotted for increasing dispersion from 0% (red), 30% (yellow), 45% (green), 60% (cyan), and 100% (blue). Pure Pt with a 45% dispersion is plotted in black.

Simulated intermetallic RIXS
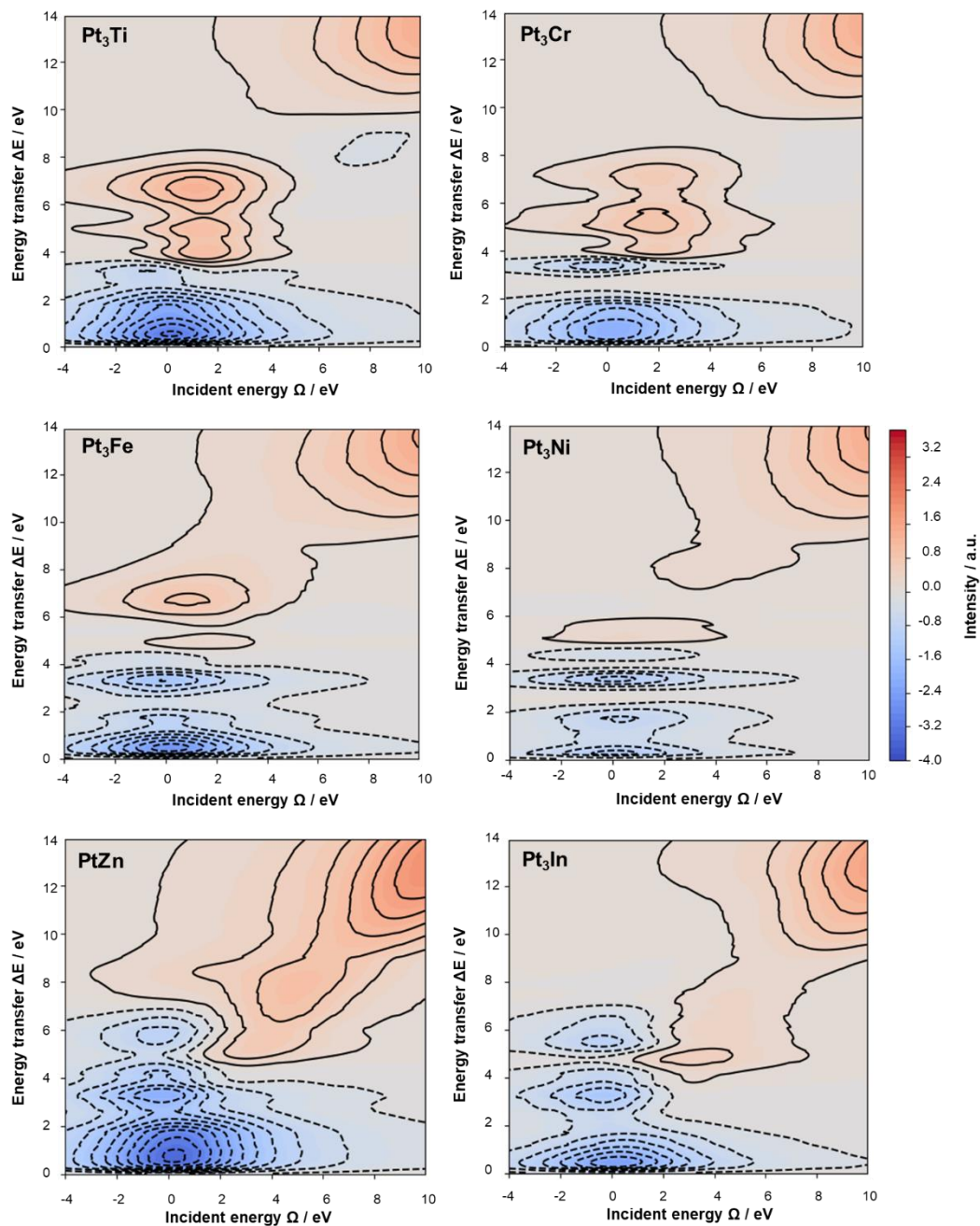


Figure J4. Pt DOS remaining alloys not in Figure 1. The DOS are plotted for increasing dispersion from 0% (red), 30% (yellow), 45% (green), 60% (cyan), and 100% (blue).

Modified *d* descriptor versus RIXS emission ω
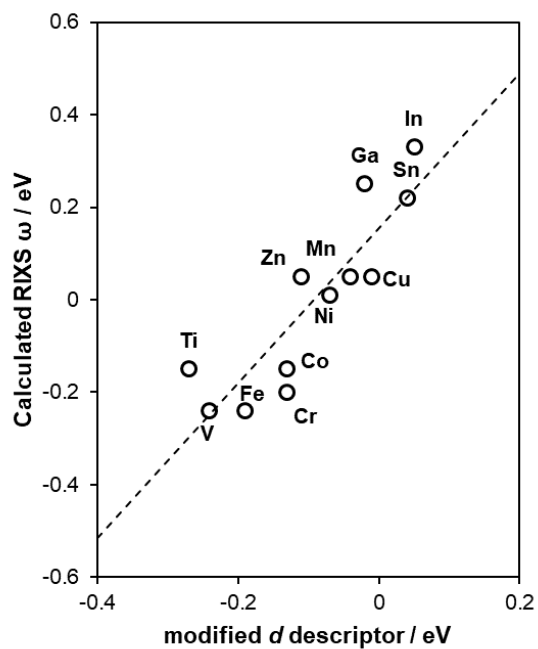


Figure J5 modified D band descriptor versus RIXS emission energy

Representative adsorbate structures
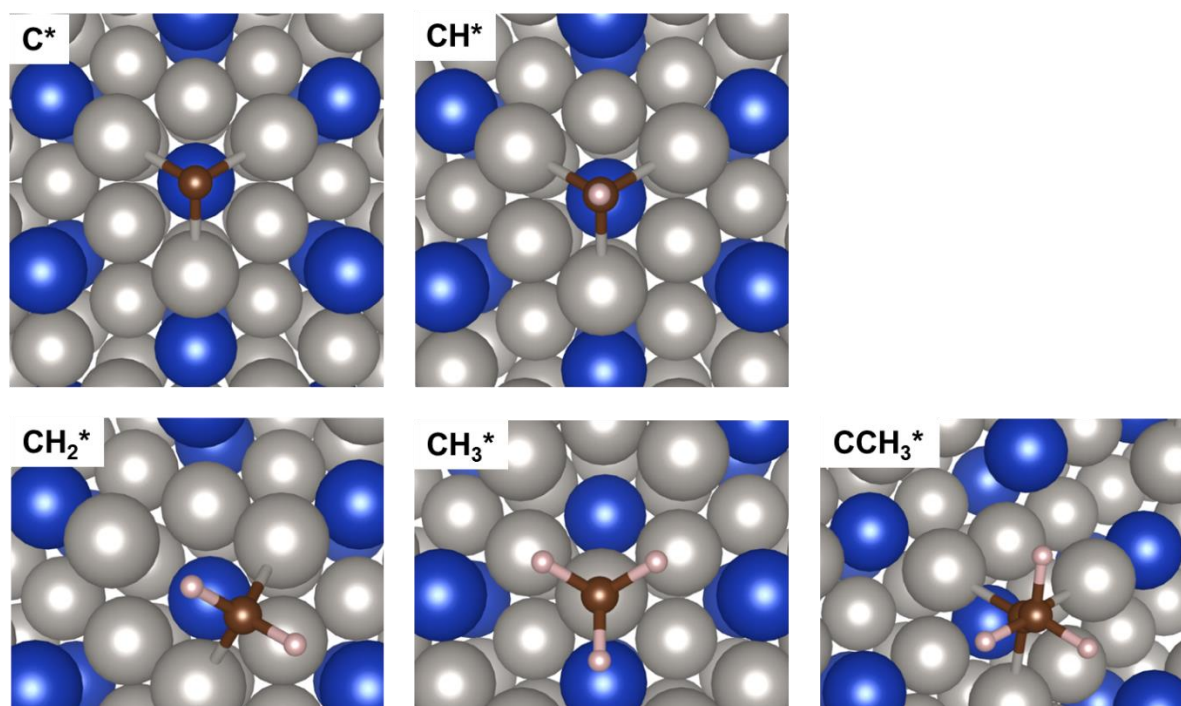


Figure J6. COHP of energies below the Fermi level for orbital interactions between C in CH and surface promoter metals (or Pt at the same lattice position for pure PT). Pure Pt is shown in black dashes, Cu (blue), Co (green), V (red) and Ti (purple).
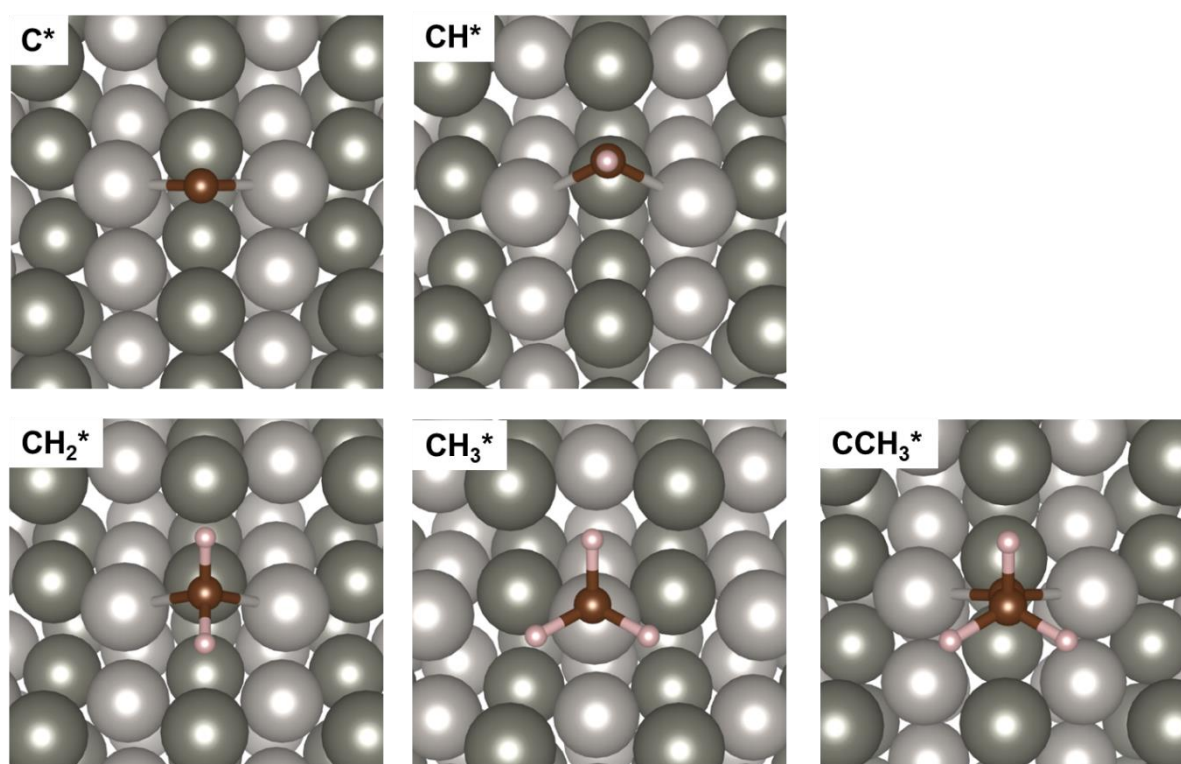
Figure J7. COHP of energies below the Fermi level for orbital interactions between C in CH and surface promoter metals (or Pt at the same lattice position for pure PT). Pure Pt is shown in black dashes, Cu (blue), Co (green), V (red) and Ti (purple).

Comparison of alternative descriptors
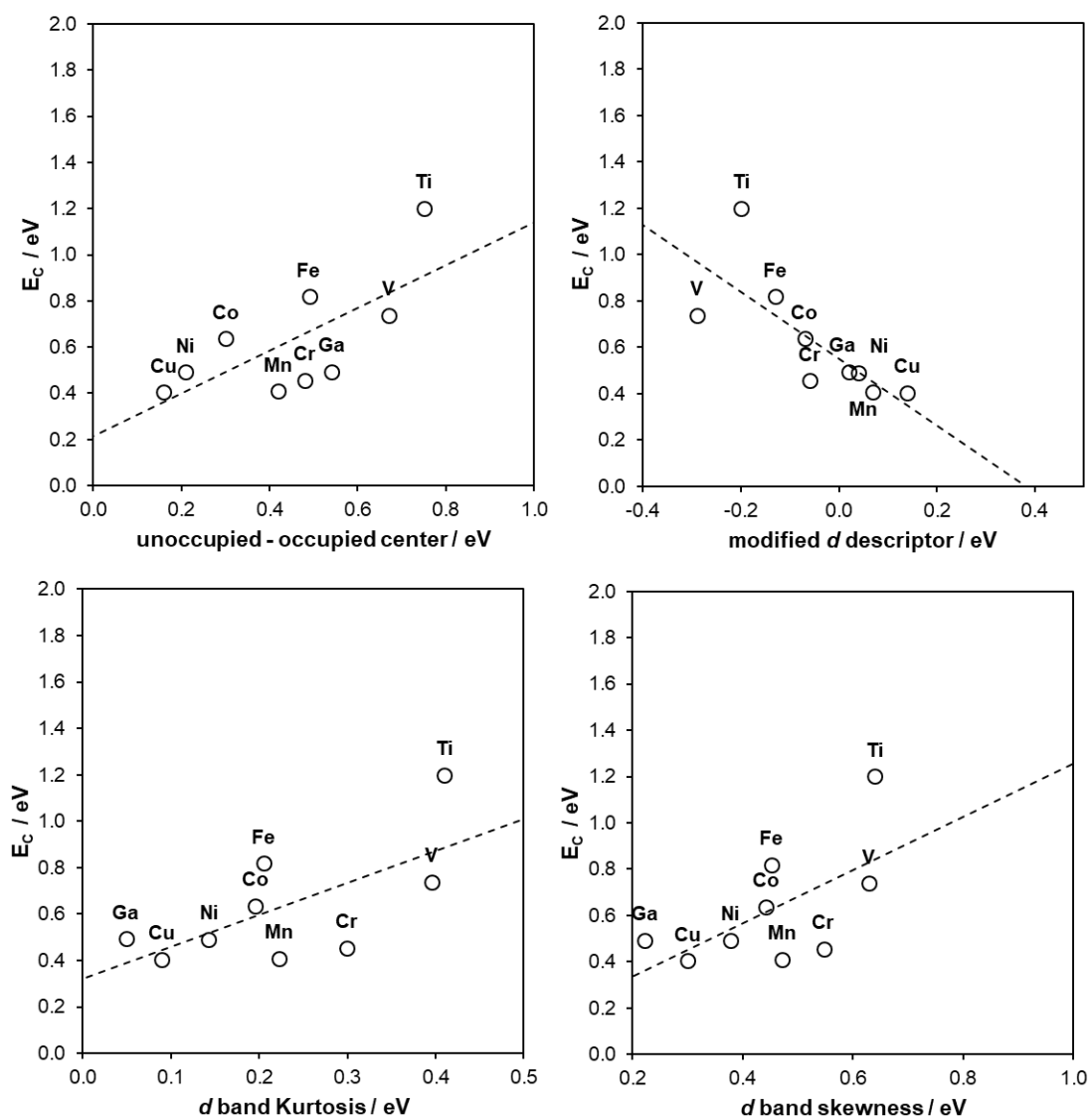


Figure J8. Alternative descriptors considered against CH binding energy.

S.2.8
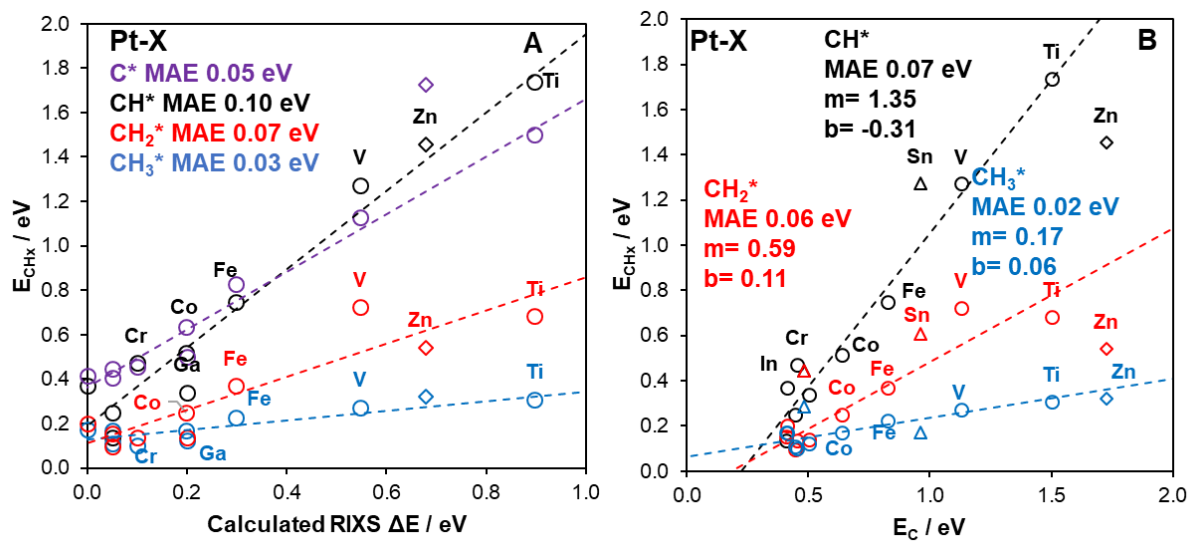


Figure J9. Strain corrected scaling relations at fixed lattice positions away from promoter metals.

# REFERENCES

[1]  P. Mehta *et al.*, "Overcoming ammonia synthesis scaling relations with plasma-enabled catalysis," *Nature Catalysis*, vol. 1, no. 4, p. 269, Apr. 2018.

[2]  L. Zhang *et al.*, "Electrochemical Ammonia Synthesis via Nitrogen Reduction Reaction on a MoS2 Catalyst: Theoretical and Experimental Studies," *Advanced Materials*, vol. 30, no. 28, p. 1800191, 2018.

[3]  T. P. Hughes, "Technological Momentum in History: Hydrogenation in Germany 1898-1933," *Past & Present*, no. 44, pp. 106–132, 1969.

[4]  "Vladimir Ipatieff." [Online]. Available: http://www.nasonline.org/member-directory/deceased-members/20001120.html. [Accessed: 23-May-2019].

[5]  C. Nolan *et al.*, "Past and future global transformation of terrestrial ecosystems under climate change," *Science*, vol. 361, no. 6405, pp. 920–923, Aug. 2018.

[6]  B. A. Swinburn *et al.*, "The Global Syndemic of Obesity, Undernutrition, and Climate Change: The Lancet Commission report," *The Lancet*, vol. 393, no. 10173, pp. 791–846, Feb. 2019.

[7]  "Monthly Energy Review," U.S. Energy Information Administration, May 2019.

[8]  P. Beiter, M. Elchinger, and T. Tian, "2016 Renewable Energy Data Book," NREL, 2017.

[9]  A. Al-Douri, D. Sengupta, and M. M. El-Halwagi, "Shale gas monetization – A review of downstream processing to chemicals and fuels," *Journal of Natural Gas Science and Engineering*, vol. 45, pp. 436–455, Sep. 2017.

[10]  J. J. Siirola, "The impact of shale gas in the chemical industry," *AIChE Journal*, vol. 60, no. 3, pp. 810–819, 2014.

[11]  J. C. Bricker, "Advanced Catalytic Dehydrogenation Technologies for Production of Olefins," *Top Catal*, vol. 55, no. 19, pp. 1309–1314, Dec. 2012.

[12]  E. M. Rubin, "Genomics of cellulosic biofuels," *Nature*, vol. 454, no. 7206, pp. 841–845, Aug. 2008.

[13]  F. Chen and R. A. Dixon, "Lignin modification improves fermentable sugar yields for biofuel production," *Nature Biotechnology*, vol. 25, no. 7, pp. 759–761, Jul. 2007.

[14]  E. Mizrachi *et al.*, "Network-based integration of systems genetics data reveals pathways associated with lignocellulosic biomass accumulation and processing," *Proc Natl Acad Sci USA*, vol. 114, no. 5, pp. 1195–1200, Jan. 2017.

[15]  T. Werpy and G. Petersen, "Top Value Added Chemicals from Biomass: Volume I -- Results of Screening for Potential Candidates from Sugars and Synthesis Gas," National Renewable Energy Lab., Golden, CO (US), DOE/GO-102004-1992, Aug. 2004.

[16]  A. J. Ragauskas *et al.*, "The Path Forward for Biofuels and Biomaterials," *Science*, vol. 311, no. 5760, pp. 484–489, Jan. 2006.

[17]  Y. Román-Leshkov and M. E. Davis, "Activation of Carbonyl-Containing Molecules with Solid Lewis Acids in Aqueous Media," *ACS Catalysis*, vol. 1, no. 11, pp. 1566–1580, Nov. 2011.

[18]  A. Corma, S. Iborra, and A. Velty, "Chemical Routes for the Transformation of Biomass into Chemicals," *Chem. Rev.*, vol. 107, no. 6, pp. 2411–2502, Jun. 2007.

[19]  P. Beiter, "2016 Renewable Energy Data Book," p. 132.

[20] C. Angelici, B. M. Weckhuysen, and P. C. A. Bruijnincx, "Chemocatalytic Conversion of Ethanol into Butadiene and Other Bulk Chemicals," *ChemSusChem*, vol. 6, no. 9, pp. 1595–1614, 2013.

[21] S. J. Khatib and S. T. Oyama, "Direct Oxidation of Propylene to Propylene Oxide with Molecular Oxygen: A Review," *Catalysis Reviews*, vol. 57, no. 3, pp. 306–344, Jul. 2015.

[22] T. A. Nijhuis, M. Makkee, J. A. Moulijn, and B. M. Weckhuysen, "The Production of Propene Oxide: Catalytic Processes and Recent Developments," *Ind. Eng. Chem. Res.*, vol. 45, no. 10, pp. 3447–3459, May 2006.

[23] J. E. Baggott, *The quantum story: a history in 40 moments*, Pbk. Oxford [England]: Oxford University Press, 2013.

[24] J. M. Thijssen, *Computational physics*, Reprint. with corr. Cambridge: Cambridge Univ. Press, 2003.

[25] A. Szabo and N. S. Ostlund, *Modern quantum chemistry: introduction to advanced electronic structure theory*. Mineola, N.Y: Dover Publications, 1996.

[26] J. Korringa, "On the calculation of the energy of a Bloch wave in a metal," *Physica*, vol. 13, no. 6–7, pp. 392–400, Aug. 1947.

[27] R. M. Martin, *Electronic structure: basic theory and practical methods*, 1st pbk. ed. with corrections. Cambridge, UK ; New York: Cambridge University Press, 2008.

[28] P. Hohenberg and W. Kohn, "Inhomogeneous Electron Gas," *Phys. Rev.*, vol. 136, no. 3B, pp. B864–B871, Nov. 1964.

[29] W. Kohn and L. J. Sham, "Self-Consistent Equations Including Exchange and Correlation Effects," *Phys. Rev.*, vol. 140, no. 4A, pp. A1133–A1138, Nov. 1965.

[30] J. Sun, A. Ruzsinszky, and J. P. Perdew, "Strongly Constrained and Appropriately Normed Semilocal Density Functional," *Phys. Rev. Lett.*, vol. 115, no. 3, p. 036402, Jul. 2015.

[31] J. Wellendorff *et al.*, "Density functionals for surface science: Exchange-correlation model development with Bayesian error estimation," *Physical Review B*, vol. 85, no. 23, Jun. 2012.

[32] J. Heyd and G. E. Scuseria, "Efficient hybrid density functional calculations in solids: Assessment of the Heyd–Scuseria–Ernzerhof screened Coulomb hybrid functional," *The Journal of Chemical Physics*, vol. 121, no. 3, p. 1187, 2004.

[33] J. Heyd, G. E. Scuseria, and M. Ernzerhof, "Hybrid functionals based on a screened Coulomb potential," *The Journal of Chemical Physics*, vol. 118, no. 18, p. 8207, 2003.

[34] W. M. C. Foulkes, L. Mitas, R. J. Needs, and G. Rajagopal, "Quantum Monte Carlo simulations of solids," *Rev. Mod. Phys.*, vol. 73, no. 1, pp. 33–83, Jan. 2001.

[35] A. A. Gokhale, S. Kandoi, J. P. Greeley, M. Mavrikakis, and J. A. Dumesic, "Molecular-level descriptions of surface chemistry in kinetic models using density functional theory," *Chemical Engineering Science*, vol. 59, no. 22–23, pp. 4679–4691, Nov. 2004.

[36] A. Bhan, S.-H. Hsu, G. Blau, J. M. Caruthers, V. Venkatasubramanian, and W. N. Delgass, "Microkinetic modeling of propane aromatization over HZSM-5," *Journal of Catalysis*, vol. 235, no. 1, pp. 35–51, Oct. 2005.

[37] X. Zhou *et al.*, "Computational Framework for the Identification of Bioprivileged Molecules," *ACS Sustainable Chem. Eng.*, vol. 7, no. 2, pp. 2414–2428, Jan. 2019.

[38] M. H. Hansen, J. K. Nørskov, and T. Bligaard, "First principles micro-kinetic model of catalytic non-oxidative dehydrogenation of ethane over close-packed metallic facets," *Journal of Catalysis*, vol. 374, pp. 161–170, Jun. 2019.

[39] M. Besora and F. Maseras, "Microkinetic modeling in homogeneous catalysis," *Wiley Interdisciplinary Reviews: Computational Molecular Science*, vol. 8, no. 6, p. e1372, 2018.

[40] B. Hammer and J. K. Nørskov, "Electronic factors determining the reactivity of metal surfaces," *Surface Science*, vol. 343, no. 3, pp. 211–220, Dec. 1995.

[41] B. Hammer and J. K. Norskov, "Why gold is the noblest of all the metals," *Nature*, vol. 376, no. 6537, p. 238, Jul. 1995.

[42] J. K. Nørskov *et al.*, "Universality in Heterogeneous Catalysis," *Journal of Catalysis*, vol. 209, no. 2, pp. 275–278, Jul. 2002.

[43] D. M. Newns, "Self-Consistent Model of Hydrogen Chemisorption," *Physical Review*, vol. 178, no. 3, pp. 1123–1135, Feb. 1969.

[44] P. W. Anderson, "Localized Magnetic States in Metals," *Physical Review*, vol. 124, no. 1, pp. 41–53, Oct. 1961.

[45] F. Abild-Pedersen *et al.*, "Scaling Properties of Adsorption Energies for Hydrogen-Containing Molecules on Transition-Metal Surfaces," *Phys. Rev. Lett.*, vol. 99, no. 1, p. 016105, Jul. 2007.

[46] A. S. Rosen, J. M. Notestein, and R. Q. Snurr, "Structure−Activity Relationships that Identify Metal−Organic Framework Catalysts for Methane Activation," *ACS Catal.*, Mar. 2019.

[47] A. J. Chowdhury, W. Yang, E. Walker, O. Mamun, A. Heyden, and G. A. Terejanu, "Prediction of Adsorption Energies for Chemical Species on Metal Catalyst Surfaces Using Machine Learning," *J. Phys. Chem. C*, vol. 122, no. 49, pp. 28142–28150, Dec. 2018.

[48] M. G. Medvedev, I. S. Bushmarinov, J. Sun, J. P. Perdew, and K. A. Lyssenko, "Density functional theory is straying from the path toward the exact functional," *Science*, vol. 355, no. 6320, pp. 49–52, Jan. 2017.

[49] J. Vieten *et al.*, "Materials design of perovskite solid solutions for thermochemical applications," *Energy & Environmental Science*, vol. 12, no. 4, pp. 1369–1384, 2019.

[50] R. Xu, W. Pang, J. Yu, Q. Huo, and J. Chen, *Chemistry of Zeolites and Related Porous Materials: Synthesis and Structure*. John Wiley & Sons, 2009.

[51] A. Corma, "Inorganic solid acids and their use in acid-catalyzed hydrocarbon reactions," *Chemical Reviews*, vol. 95, no. 3, pp. 559–614, 1995.

[52] M. Boronat and A. Corma, "Factors Controlling the Acidity of Zeolites," *Catalysis Letters*, vol. 145, no. 1, pp. 162–172, Jan. 2015.

[53] N. Y. Chen, *Shape Selective Catalysis in Industrial Applications, Second Edition,*. CRC Press, 1996.

[54] R. Gounder and E. Iglesia, "Catalytic Consequences of Spatial Constraints and Acid Site Location for Monomolecular Alkane Activation on Zeolites," *Journal of the American Chemical Society*, vol. 131, no. 5, pp. 1958–1971, Feb. 2009.

[55] J. Macht, R. T. Carr, and E. Iglesia, "Functional assessment of the strength of solid acid catalysts," *Journal of Catalysis*, vol. 264, no. 1, pp. 54–66, May 2009.

[56] M. Hartmann and L. Kevan, "Transition-Metal Ions in Aluminophosphate and Silicoaluminophosphate Molecular Sieves:  Location, Interaction with Adsorbates and Catalytic Properties," *Chem. Rev.*, vol. 99, no. 3, pp. 635–664, Mar. 1999.

[57] G. Busca, "Spectroscopic characterization of the acid properties of metal oxide catalysts," *Catalysis Today*, vol. 41, no. 1–3, pp. 191–206, May 1998.

[58] A. Corma, M. T. Navarro, and M. Renz, "Lewis acidic Sn(IV) centers—grafted onto MCM-41—as catalytic sites for the Baeyer–Villiger oxidation with hydrogen peroxide," *Journal of Catalysis*, vol. 219, no. 1, pp. 242–246, Oct. 2003.

[59] M. Moliner, C. Martínez, and A. Corma, "Multipore Zeolites: Synthesis and Catalytic Applications," *Angew. Chem. Int. Ed.*, vol. 54, no. 12, pp. 3560–3579, Mar. 2015.

[60] B. A. De Moor, M.-F. Reyniers, M. Sierka, J. Sauer, and G. B. Marin, "Physisorption and Chemisorption of Hydrocarbons in H-FAU Using QM-Pot(MP2//B3LYP) Calculations," *The Journal of Physical Chemistry C*, vol. 112, no. 31, pp. 11796–11812, Aug. 2008.

[61] L. Cheng, L. A. Curtiss, R. S. Assary, J. Greeley, T. Kerber, and J. Sauer, "Adsorption and Diffusion of Fructose in Zeolite HZSM-5: Selection of Models and Methods for Computational Studies," *The Journal of Physical Chemistry C*, vol. 115, no. 44, pp. 21785–21790, Nov. 2011.

[62] C. Tuma, T. Kerber, and J. Sauer, "The tert-Butyl Cation in H-Zeolites: Deprotonation to Isobutene and Conversion into Surface Alkoxides," *Angewandte Chemie International Edition*, vol. 49, no. 27, pp. 4678–4680, Jun. 2010.

[63] R. Y. Brogaard, C.-M. Wang, and F. Studt, "Methanol–Alkene Reactions in Zeotype Acid Catalysts: Insights from a Descriptor-Based Approach and Microkinetic Modeling," *ACS Catalysis*, vol. 4, no. 12, pp. 4504–4509, Dec. 2014.

[64] C.-M. Wang, R. Y. Brogaard, Z.-K. Xie, and F. Studt, "Transition-state scaling relations in zeolite catalysis: influence of framework topology and acid-site reactivity," *Catal. Sci. Technol.*, vol. 5, no. 5, pp. 2814–2820, 2015.

[65] C.-M. Wang, R. Y. Brogaard, B. M. Weckhuysen, J. K. Nørskov, and F. Studt, "Reactivity Descriptor in Solid Acid Catalysis: Predicting Turnover Frequencies for Propene Methylation in Zeotypes," *The Journal of Physical Chemistry Letters*, vol. 5, no. 9, pp. 1516–1521, May 2014.

[66] U. Olsbye *et al.*, "Conversion of Methanol to Hydrocarbons: How Zeolite Cavity and Pore Size Controls Product Selectivity," *Angewandte Chemie International Edition*, vol. 51, no. 24, pp. 5810–5831, Jun. 2012.

[67] J. B. Nicholas, "Density functional theory studies of zeolite structure, acidity, and reactivity," *Top. Catal.*, vol. 4, no. 1–2, pp. 157–171, 1997.

[68] M. Brändle and J. Sauer, "Combining ab initio techniques with analytical potential functions. A study of zeolite-adsorbate interactions for NH3 on H-faujasite," *Journal of Molecular Catalysis A: Chemical*, vol. 119, no. 1–3, pp. 19–33, May 1997.

[69] M. Boronat, P. Concepcion, A. Corma, M. Renz, and S. Valencia, "Determination of the catalytically active oxidation Lewis acid sites in Sn-beta zeolites, and their optimisation by the combination of theoretical and experimental studies," *Journal of Catalysis*, vol. 234, no. 1, pp. 111–118, Aug. 2005.

[70] C. Tuma and J. Sauer, "Treating dispersion effects in extended systems by hybrid MP2:DFT calculations?protonation of isobutene in zeolite ferrierite," *Physical Chemistry Chemical Physics*, vol. 8, no. 34, p. 3955, 2006.

[71] S. Grimme, J. Antony, S. Ehrlich, and H. Krieg, "A consistent and accurate ab initio parametrization of density functional dispersion correction (DFT-D) for the 94 elements H-Pu," *The Journal of Chemical Physics*, vol. 132, no. 15, p. 154104, Apr. 2010.

[72] "Database of Zeolite Structures." [Online]. Available: http://www.iza-structure.org/databases/. [Accessed: 23-Aug-2015].

[73] F. Abild-Pedersen *et al.*, "Scaling Properties of Adsorption Energies for Hydrogen-Containing Molecules on Transition-Metal Surfaces," *Phys. Rev. Lett.*, vol. 99, no. 1, p. 016105, Jul. 2007.

[74] M. M. Montemore and J. W. Medlin, "Scaling relations between adsorption energies for computational screening and design of catalysts," *Catal. Sci. Technol.*, vol. 4, no. 11, pp. 3748–3761, May 2014.

[75] T. Bligaard, J. K. Nørskov, S. Dahl, J. Matthiesen, C. H. Christensen, and J. Sehested, "The Brønsted–Evans–Polanyi relation and the volcano curve in heterogeneous catalysis," *Journal of Catalysis*, vol. 224, no. 1, pp. 206–217, May 2004.

[76] E. M. Fernández *et al.*, "Scaling Relationships for Adsorption Energies on Transition Metal Oxide, Sulfide, and Nitride Surfaces," *Angewandte Chemie International Edition*, vol. 47, no. 25, pp. 4683–4686, Jun. 2008.

[77] F. Calle-Vallejo, D. Loffreda, M. T. M. Koper, and P. Sautet, "Introducing structural sensitivity into adsorption–energy scaling relations by means of coordination numbers," *Nat Chem*, vol. 7, no. 5, pp. 403–410, May 2015.

[78] Z. Liu and S. I. Woo, "Recent Advances in Catalytic DeNOX Science and Technology," *Catalysis Reviews*, vol. 48, no. 1, pp. 43–89, Jan. 2006.

[79] C. Paolucci *et al.*, "Isolation of the Copper Redox Steps in the Standard Selective Catalytic Reduction on Cu-SSZ-13," *Angew. Chem.*, vol. 126, no. 44, pp. 12022–12027, Oct. 2014.

[80] Y. Mao, H.-F. Wang, and P. Hu, "Theoretical investigation of NH3-SCR processes over zeolites: A review," *Int. J. Quantum Chem.*, vol. 115, no. 10, pp. 618–630, May 2015.

[81] G. Kresse and J. Hafner, "\textit{Ab initio} molecular dynamics for liquid metals," *Phys. Rev. B*, vol. 47, no. 1, pp. 558–561, Jan. 1993.

[82] G. Kresse and J. Hafner, "\textit{Ab initio} molecular-dynamics simulation of the liquid-metal\char21{}amorphous-semiconductor transition in germanium," *Phys. Rev. B*, vol. 49, no. 20, pp. 14251–14269, May 1994.

[83] G. Kresse and J. Furthmüller, "Efficiency of ab-initio total energy calculations for metals and semiconductors using a plane-wave basis set," *Computational Materials Science*, vol. 6, no. 1, pp. 15–50, Jul. 1996.

[84] G. Kresse and J. Furthmüller, "Efficient iterative schemes for \textit{ab initio} total-energy calculations using a plane-wave basis set," *Phys. Rev. B*, vol. 54, no. 16, pp. 11169–11186, Oct. 1996.

[85] A. V. Krukau, O. A. Vydrov, A. F. Izmaylov, and G. E. Scuseria, "Influence of the exchange screening parameter on the performance of screened hybrid functionals," *The Journal of Chemical Physics*, vol. 125, no. 22, p. 224106, Dec. 2006.

[86] P. E. Blöchl, "Projector augmented-wave method," *Phys. Rev. B*, vol. 50, no. 24, pp. 17953–17979, Dec. 1994.

[87] G. Kresse and D. Joubert, "From ultrasoft pseudopotentials to the projector augmented-wave method," *Phys. Rev. B*, vol. 59, no. 3, pp. 1758–1775, Jan. 1999.

[88] J. P. Perdew, K. Burke, and M. Ernzerhof, "Generalized Gradient Approximation Made Simple," *Phys. Rev. Lett.*, vol. 77, no. 18, pp. 3865–3868, Oct. 1996.

[89] S. Nosé, "A unified formulation of the constant temperature molecular dynamics methods," *The Journal of Chemical Physics*, vol. 81, no. 1, pp. 511–519, Jul. 1984.

[90] X. Solans-Monfort, M. Sodupe, V. Branchadell, J. Sauer, R. Orlando, and P. Ugliengo, "Adsorption of NH3 and H2O in Acidic Chabazite. Comparison of ONIOM Approach with Periodic Calculations," *J. Phys. Chem. B*, vol. 109, no. 8, pp. 3539–3545, Mar. 2005.

[91] G. Deo and I. E. Wachs, "Reactivity of Supported Vanadium Oxide Catalysts: The Partial Oxidation of Methanol," *Journal of Catalysis*, vol. 146, no. 2, pp. 323–334, Apr. 1994.

[92] T. Waters, R. A. J. O'Hair, and A. G. Wedd, "Catalytic Gas Phase Oxidation of Methanol to Formaldehyde," *J. Am. Chem. Soc.*, vol. 125, no. 11, pp. 3384–3396, Mar. 2003.

[93] K. Routray, W. Zhou, C. J. Kiely, and I. E. Wachs, "Catalysis Science of Methanol Oxidation over Iron Vanadate Catalysts: Nature of the Catalytic Active Sites," *ACS Catal.*, vol. 1, no. 1, pp. 54–66, Jan. 2011.

[94] J. N. Allison and W. A. Goddard III, "Oxidative dehydrogenation of methanol to formaldehyde," *Journal of Catalysis*, vol. 92, no. 1, pp. 127–135, Mar. 1985.

[95] T. D. Courtney, C.-C. Chang, R. J. Gorte, R. F. Lobo, W. Fan, and V. Nikolakis, "Effect of water treatment on Sn-BEA zeolite: Origin of 960 cm−1 FTIR peak," *Microporous and Mesoporous Materials*, vol. 210, pp. 69–76, Jul. 2015.

[96] Y. Román-Leshkov and M. E. Davis, "Activation of Carbonyl-Containing Molecules with Solid Lewis Acids in Aqueous Media," *ACS Catalysis*, vol. 1, no. 11, pp. 1566–1580, Nov. 2011.

[97] A. Corma, L. T. Nemeth, M. Renz, and S. Valencia, "Sn-zeolite beta as a heterogeneous chemoselective catalyst for Baeyer–Villiger oxidations," *Nature*, vol. 412, no. 6845, pp. 423–425, Jul. 2001.

[98] A. Corma, M. E. Domine, L. Nemeth, and S. Valencia, "Al-Free Sn-Beta Zeolite as a Catalyst for the Selective Reduction of Carbonyl Compounds (Meerwein−Ponndorf−Verley Reaction)," *J. Am. Chem. Soc.*, vol. 124, no. 13, pp. 3194–3195, Apr. 2002.

[99] M. Moliner, Y. Román-Leshkov, and M. E. Davis, "Tin-containing zeolites are highly active catalysts for the isomerization of glucose in water," *PNAS*, vol. 107, no. 14, pp. 6164–6168, Apr. 2010.

[100] J. W. Harris, M. J. Cordon, J. R. Di Iorio, J. C. Vega-Vila, F. H. Ribeiro, and R. Gounder, "Titration and quantification of open and closed Lewis acid sites in Sn-Beta zeolites that catalyze glucose isomerization," *Journal of Catalysis*, vol. 335, pp. 141–154, Mar. 2016.

[101] Y.-P. Li, M. Head-Gordon, and A. T. Bell, "Analysis of the Reaction Mechanism and Catalytic Activity of Metal-Substituted Beta Zeolite for the Isomerization of Glucose to Fructose," *ACS Catal.*, vol. 4, no. 5, pp. 1537–1545, May 2014.

[102] M. Boronat, A. Corma, M. Renz, and P. M. Viruela, "Predicting the Activity of Single Isolated Lewis Acid Sites in Solid Catalysts," *Chemistry - A European Journal*, vol. 12, no. 27, pp. 7067–7077, Sep. 2006.

[103] H. Y. Luo, D. F. Consoli, W. R. Gunther, and Y. Román-Leshkov, "Investigation of the reaction kinetics of isolated Lewis acid sites in Beta zeolites for the Meerwein–Ponndorf–Verley reduction of methyl levulinate to γ-valerolactone," *Journal of Catalysis*, vol. 320, pp. 198–207, Dec. 2014.

[104] J. D. Lewis, "Cooperative activation of biomass-derived oxygenates with Lewis acid zeolites," Thesis, Massachussets Institute of Technology, 2017.

[105] R. Bermejo-Deval, M. Orazov, R. Gounder, S.-J. Hwang, and M. E. Davis, "Active Sites in Sn-Beta for Glucose Isomerization to Fructose and Epimerization to Mannose," *ACS Catal.*, vol. 4, no. 7, pp. 2288–2297, Jul. 2014.

[106] R. Bermejo-Deval *et al.*, "Metalloenzyme-like catalyzed isomerizations of sugars by Lewis acid zeolites," *PNAS*, vol. 109, no. 25, pp. 9727–9732, Jun. 2012.

[107] P. Wolf *et al.*, "Identifying Sn Site Heterogeneities Prevalent Among Sn-Beta Zeolites," *Helv. Chim. Acta*, vol. 99, no. 12, pp. 916–927, Dec. 2016.

[108]  S. R. Bare *et al.*, "Uniform Catalytic Site in Sn-β-Zeolite Determined Using X-ray Absorption Fine Structure," *Journal of the American Chemical Society*, vol. 127, no. 37, pp. 12924–12932, Sep. 2005.

[109]  C. M. Osmundsen, M. S. Holm, S. Dahl, and E. Taarning, "Tin-containing silicates: structure–activity relations," *Proc. R. Soc. A*, vol. 468, no. 2143, pp. 2000–2016, Jul. 2012.

[110]  P. Wolf *et al.*, "Correlating Synthetic Methods, Morphology, Atomic-Level Structure, and Catalytic Activity of Sn-β Catalysts," *ACS Catal.*, vol. 6, no. 7, pp. 4047–4063, Jul. 2016.

[111]  N. Rai, S. Caratzoulas, and D. G. Vlachos, "Role of Silanol Group in Sn-Beta Zeolite for Glucose Isomerization and Epimerization Reactions," *ACS Catal.*, vol. 3, no. 10, pp. 2294–2298, Oct. 2013.

[112]  P. Wolf *et al.*, "NMR Signatures of the Active Sites in Sn-β Zeolite," *Angew. Chem. Int. Ed.*, vol. 53, no. 38, pp. 10179–10183, Sep. 2014.

[113]  B. C. Bukowski and J. Greeley, "Scaling Relationships for Molecular Adsorption and Dissociation in Lewis Acid Zeolites," *J. Phys. Chem. C*, vol. 120, no. 12, pp. 6714–6722, Mar. 2016.

[114]  J. W. Harris *et al.*, "Molecular Structure and Confining Environment of Sn Sites in Single-Site Chabazite Zeolites," *Chem. Mater.*, Sep. 2017.

[115]  R. E. Skyner, J. L. McDonagh, C. R. Groom, T. van Mourik, and J. B. O. Mitchell, "A review of methods for the calculation of solution free energies and the modelling of systems in solution," *Phys. Chem. Chem. Phys.*, vol. 17, no. 9, pp. 6174–6191, Feb. 2015.

[116]  G. M. Lari, P. Y. Dapsens, D. Scholz, S. Mitchell, C. Mondelli, and J. Pérez-Ramírez, "Deactivation mechanisms of tin-zeolites in biomass conversions," *Green Chem.*, vol. 18, no. 5, pp. 1249–1260, Feb. 2016.

[117]  D. Padovan, C. Parsons, M. S. Grasina, and C. Hammond, "Intensification and deactivation of Sn-beta investigated in the continuous regime," *Green Chem.*, vol. 18, no. 18, pp. 5041–5049, Sep. 2016.

[118]  H. Knözinger, "Dehydration of Alcohols on Aluminum Oxide," *Angew. Chem. Int. Ed. Engl.*, vol. 7, no. 10, pp. 791–805, Oct. 1968.

[119]  S. Roy, G. Mpourmpakis, D.-Y. Hong, D. G. Vlachos, A. Bhan, and R. J. Gorte, "Mechanistic Study of Alcohol Dehydration on γ-Al $_2$ O $_3$," *ACS Catalysis*, vol. 2, no. 9, pp. 1846–1853, Sep. 2012.

[120]  J. F. DeWilde, H. Chiang, D. A. Hickman, C. R. Ho, and A. Bhan, "Kinetics and Mechanism of Ethanol Dehydration on γ-Al2O3: The Critical Role of Dimer Inhibition," *ACS Catal.*, vol. 3, no. 4, pp. 798–807, 2013.

[121]  C. Stegelmann, A. Andreasen, and C. T. Campbell, "Degree of Rate Control: How Much the Energies of Intermediates and Transition States Control Rates," *J. Am. Chem. Soc.*, vol. 131, no. 23, pp. 8077–8082, Jun. 2009.

[122]  F. Göltl and J. Hafner, "Structure and properties of metal-exchanged zeolites studied using gradient-corrected and hybrid functionals. I. Structure and energetics," *The Journal of Chemical Physics*, vol. 136, no. 6, p. 064501, Feb. 2012.

[123]  F. Göltl and J. Hafner, "Structure and properties of metal-exchanged zeolites studied using gradient-corrected and hybrid functionals. II. Electronic structure and photoluminescence spectra," *The Journal of Chemical Physics*, vol. 136, no. 6, p. 064502, Feb. 2012.

[124]  F. Göltl and J. Hafner, "Structure and properties of metal-exchanged zeolites studied using gradient-corrected and hybrid functionals. III. Energetics and vibrational spectroscopy of adsorbates," *The Journal of Chemical Physics*, vol. 136, no. 6, p. 064503, Feb. 2012.

[125]  G. Piccini and J. Sauer, "Effect of Anharmonicity on Adsorption Thermodynamics," *J. Chem. Theory Comput.*, vol. 10, no. 6, pp. 2479–2487, Jun. 2014.

[126]  G. Piccini, M. Alessio, and J. Sauer, "Ab Initio Calculation of Rate Constants for Molecule–Surface Reactions with Chemical Accuracy," *Angew. Chem. Int. Ed.*, vol. 55, no. 17, pp. 5235–5237, Apr. 2016.

[127]  G. M. Torrie and J. P. Valleau, "Nonphysical sampling distributions in Monte Carlo free-energy estimation: Umbrella sampling," *Journal of Computational Physics*, vol. 23, no. 2, pp. 187–199, Feb. 1977.

[128]  K. Alexopoulos *et al.*, "Anharmonicity and Confinement in Zeolites: Structure, Spectroscopy and Adsorption Free Energy of Ethanol in H-ZSM-5," *J. Phys. Chem. C*, Mar. 2016.

[129]  R. Y. Brogaard *et al.*, "Methanol-to-hydrocarbons conversion: The alkene methylation pathway," *Journal of Catalysis*, vol. 314, pp. 159–169, May 2014.

[130]  M. Jørgensen and H. Grönbeck, "Adsorbate Entropies with Complete Potential Energy Sampling in Microkinetic Modeling," *J. Phys. Chem. C*, vol. 121, no. 13, pp. 7199–7207, Apr. 2017.

[131]  A. Beste, "One-dimensional anharmonic oscillator: Quantum versus classical vibrational partition functions," *Chemical Physics Letters*, vol. 493, no. 1–3, pp. 200–205, Jun. 2010.

[132]  C. T. Campbell, "The Degree of Rate Control: A Powerful Tool for Catalysis Research," *ACS Catal.*, vol. 7, no. 4, pp. 2770–2779, Apr. 2017.

[133]  S. Grimme, "Semiempirical GGA-type density functional constructed with a long-range dispersion correction," *J. Comput. Chem.*, vol. 27, no. 15, pp. 1787–1799, Nov. 2006.

[134]  G. Henkelman and H. Jónsson, "Improved tangent estimate in the nudged elastic band method for finding minimum energy paths and saddle points," *The Journal of Chemical Physics*, vol. 113, no. 22, pp. 9978–9985, Dec. 2000.

[135]  G. Henkelman, B. P. Uberuaga, and H. Jónsson, "A climbing image nudged elastic band method for finding saddle points and minimum energy paths," *The Journal of Chemical Physics*, vol. 113, no. 22, pp. 9901–9904, Dec. 2000.

[136]  S. Smidstrup, A. Pedersen, K. Stokbro, and H. Jónsson, "Improved initial guess for minimum energy path calculations," *The Journal of Chemical Physics*, vol. 140, no. 21, p. 214106, Jun. 2014.

[137]  R. A. Olsen, G. J. Kroes, G. Henkelman, A. Arnaldsson, and H. Jónsson, "Comparison of methods for finding saddle points without knowledge of the final states," *The Journal of Chemical Physics*, vol. 121, no. 20, pp. 9776–9792, Nov. 2004.

[138]  A. A. Gokhale, S. Kandoi, J. P. Greeley, M. Mavrikakis, and J. A. Dumesic, "Molecular-level descriptions of surface chemistry in kinetic models using density functional theory," *Chemical Engineering Science*, vol. 59, no. 22–23, pp. 4679–4691, Nov. 2004.

[139]  T. Choksi and J. Greeley, "Partial Oxidation of Methanol on MoO3 (010): A DFT and Microkinetic Study," *ACS Catal.*, vol. 6, no. 11, pp. 7260–7277, Nov. 2016.

[140]  S. Maintz, V. L. Deringer, A. L. Tchougréeff, and R. Dronskowski, "LOBSTER: A tool to extract chemical bonding from plane-wave based DFT," *J. Comput. Chem.*, vol. 37, no. 11, pp. 1030–1035, Apr. 2016.

[141]   W. Tang, E. Sanville, and G. Henkelman, "A grid-based Bader analysis algorithm without lattice bias," *J. Phys.: Condens. Matter*, vol. 21, no. 8, p. 084204, 2009.

[142]   T. R. Josephson, G. R. Jenness, D. G. Vlachos, and S. Caratzoulas, "Distribution of open sites in Sn-Beta zeolite," *Microporous and Mesoporous Materials*.

[143]   A. V. Yakimov, Y. G. Kolyagin, S. Tolborg, P. N. R. Vennestrøm, and I. I. Ivanova, "119Sn MAS NMR Study of the Interaction of Probe Molecules with Sn-BEA: The Origin of Penta- and Hexacoordinated Tin Formation," *J. Phys. Chem. C*, vol. 120, no. 49, pp. 28083–28092, Dec. 2016.

[144]   M. A. Christiansen, G. Mpourmpakis, and D. G. Vlachos, "Density Functional Theory-Computed Mechanisms of Ethylene and Diethyl Ether Formation from Ethanol on γ-Al $_2$ O $_3$ (100)," *ACS Catalysis*, vol. 3, no. 9, pp. 1965–1975, Sep. 2013.

[145]   W. A. Cowdrey, E. D. Hughes, C. K. Ingold, S. Masterman, and A. D. Scott, "257. Reaction kinetics and the Walden inversion. Part VI. Relation of steric orientation to mechanism in substitutions involving halogen atoms and simple or substituted hydroxyl groups," *J. Chem. Soc.*, no. 0, pp. 1252–1271, Jan. 1937.

[146]   S. S. Lee, S. Y. Hong, J. C. Errey, A. Izumi, G. J. Davies, and B. G. Davis, "Mechanistic evidence for a front-side, SNi-type reaction in a retaining glycosyltransferase," *Nat Chem Biol*, vol. 7, no. 9, pp. 631–638, Sep. 2011.

[147]   W. Knaeble and E. Iglesia, "Kinetic and Theoretical Insights into the Mechanism of Alkanol Dehydration on Solid Brønsted Acid Catalysts," *J. Phys. Chem. C*, vol. 120, no. 6, pp. 3371–3389, Feb. 2016.

[148]   R. T. Carr, M. Neurock, and E. Iglesia, "Catalytic consequences of acid strength in the conversion of methanol to dimethyl ether," *Journal of Catalysis*, vol. 278, no. 1, pp. 78–93, Feb. 2011.

[149]   R. Gounder and E. Iglesia, "The catalytic diversity of zeolites: confinement and solvation effects within voids of molecular dimensions," *Chemical Communications*, vol. 49, no. 34, p. 3491, 2013.

[150]   Z.-J. Zhao *et al.*, "Importance of metal-oxide interfaces in heterogeneous catalysis: A combined DFT, microkinetic, and experimental study of water-gas shift on Au/MgO," *Journal of Catalysis*, vol. 345, no. Supplement C, pp. 157–169, Jan. 2017.

[151]   A. Plauck, E. E. Stangland, J. A. Dumesic, and M. Mavrikakis, "Active sites and mechanisms for H2O2 decomposition over Pd catalysts," *PNAS*, vol. 113, no. 14, pp. E1973–E1982, Apr. 2016.

[152]   S.-T. Lin, P. K. Maiti, and W. A. Goddard, "Two-Phase Thermodynamic Model for Efficient and Accurate Absolute Entropy of Water from Molecular Dynamics Simulations," *J. Phys. Chem. B*, vol. 114, no. 24, pp. 8191–8198, Jun. 2010.

[153]   S.-T. Lin, M. Blanco, and W. A. G. Iii, "The two-phase model for calculating thermodynamic properties of liquids from molecular dynamics: Validation for the phase diagram of Lennard-Jones fluids," *The Journal of Chemical Physics*, vol. 119, no. 22, pp. 11792–11805, Dec. 2003.

[154]   C. T. Campbell and J. R. V. Sellers, "The Entropies of Adsorbed Molecules," *J. Am. Chem. Soc.*, vol. 134, no. 43, pp. 18109–18115, Oct. 2012.

[155]   Z.-J. Zhao, A. Kulkarni, L. Vilella, J. K. Norskov, and F. Studt, "Theoretical insights into the selective oxidation of methane to methanol in copper-exchanged mordenite," *ACS Catal.*, May 2016.

[156]   J. S. Bates, B. C. Bukowski, J. W. Harris, J. P. Greeley, and R. Gounder, "Distinct Catalytic Reactivity of Sn Substituted in Framework Locations and at Defect Grain Boundaries in Sn-Zeolites," *ACS Catal.*, p. acscatal.9b01123, May 2019.

[157]   B. C. Bukowski, J. S. Bates, R. Gounder, and J. Greeley, "First principles, microkinetic, and experimental analysis of Lewis acid site speciation during ethanol dehydration on Sn-Beta zeolites," *Journal of Catalysis*, vol. 365, pp. 261–276, Sep. 2018.

[158]   G. Kresse and J. Hafner, "\textit{Ab initio}   molecular-dynamics simulation of the liquid-metal\char21{}amorphous-semiconductor transition in germanium," *Phys. Rev. B*, vol. 49, no. 20, pp. 14251–14269, May 1994.

[159]   G. Kresse and J. Furthmüller, "Efficient iterative schemes for    \textit{ab initio}   total-energy calculations using a plane-wave basis set," *Phys. Rev. B*, vol. 54, no. 16, pp. 11169–11186, Oct. 1996.

[160]   G. Kresse and J. Furthmüller, "Efficiency of ab-initio total energy calculations for metals and semiconductors using a plane-wave basis set," *Computational Materials Science*, vol. 6, no. 1, pp. 15–50, Jul. 1996.

[161]   J. Wellendorff *et al.*, "Density functionals for surface science: Exchange-correlation model development with Bayesian error estimation," *Physical Review B*, vol. 85, no. 23, Jun. 2012.

[162]   P. E. Blöchl, "Projector augmented-wave method," *Phys. Rev. B*, vol. 50, no. 24, pp. 17953–17979, Dec. 1994.

[163]   G. Kresse and D. Joubert, "From ultrasoft pseudopotentials to the projector augmented-wave method," *Phys. Rev. B*, vol. 59, no. 3, pp. 1758–1775, Jan. 1999.

[164]   P. A. Wright, W. Zhou, J. Pérez-Pariente, and M. Arranz, "Direct Observation of Growth Defects in Zeolite Beta," *J. Am. Chem. Soc.*, vol. 127, no. 2, pp. 494–495, Jan. 2005.

[165]   J. M. Newsam, M. M. J. Treacy, W. T. Koetsier, and C. B. D. Gruyter, "Structural Characterization of Zeolite Beta," *Proceedings of the Royal Society of London A: Mathematical, Physical and Engineering Sciences*, vol. 420, no. 1859, pp. 375–405, Dec. 1988.

[166]   G. Henkelman and H. Jónsson, "Improved tangent estimate in the nudged elastic band method for finding minimum energy paths and saddle points," *The Journal of Chemical Physics*, vol. 113, no. 22, pp. 9978–9985, Dec. 2000.

[167]   G. Henkelman, B. P. Uberuaga, and H. Jónsson, "A climbing image nudged elastic band method for finding saddle points and minimum energy paths," *The Journal of Chemical Physics*, vol. 113, no. 22, pp. 9901–9904, Dec. 2000.

[168]   G. Piccini and J. Sauer, "Effect of Anharmonicity on Adsorption Thermodynamics," *J. Chem. Theory Comput.*, vol. 10, no. 6, pp. 2479–2487, Jun. 2014.

[169]   P. Wolf *et al.*, "Correlating Synthetic Methods, Morphology, Atomic-Level Structure, and Catalytic Activity of Sn-β Catalysts," *ACS Catal.*, vol. 6, no. 7, pp. 4047–4063, Jul. 2016.

[170]   M. Boronat, P. Concepción, A. Corma, M. Renz, and S. Valencia, "Determination of the catalytically active oxidation Lewis acid sites in Sn-beta zeolites, and their optimisation by the combination of theoretical and experimental studies," *Journal of Catalysis*, vol. 234, no. 1, pp. 111–118, Aug. 2005.

[171]   M. Boronat, A. Corma, and M. Renz, "Mechanism of the Meerwein−Ponndorf−Verley−Oppenauer (MPVO) Redox Equilibrium on Sn− and Zr−Beta Zeolite Catalysts," *J. Phys. Chem. B*, vol. 110, no. 42, pp. 21168–21174, 2006.

[172]  S. Grimme, "Semiempirical GGA-type density functional constructed with a long-range dispersion correction," *Journal of Computational Chemistry*, vol. 27, no. 15, pp. 1787–1799, Nov. 2006.

[173]  G. Li, E. A. Pidko, and E. J. M. Hensen, "Synergy between Lewis acid sites and hydroxyl groups for the isomerization of glucose to fructose over Sn-containing zeolites: a theoretical perspective," *Catal. Sci. Technol.*, vol. 4, no. 8, pp. 2241–2250, Jul. 2014.

[174]  N. Rai, S. Caratzoulas, and D. G. Vlachos, "Role of Silanol Group in Sn-Beta Zeolite for Glucose Isomerization and Epimerization Reactions," *ACS Catal.*, vol. 3, no. 10, pp. 2294–2298, Oct. 2013.

[175]  J. D. Lewis, M. Ha, H. Luo, A. Faucher, V. K. Michaelis, and Y. Román-Leshkov, "Distinguishing Active Site Identity in Sn-Beta Zeolites Using 31P MAS NMR of Adsorbed Trimethylphosphine Oxide," *ACS Catal.*, vol. 8, no. 4, pp. 3076–3086, Feb. 2018.

[176]  M. Boronat, P. Concepción, A. Corma, and M. Renz, "Peculiarities of Sn-Beta and potential industrial applications," *Catalysis Today*, vol. 121, no. 1–2, pp. 39–44, Mar. 2007.

[177]  Y. Román-Leshkov and M. E. Davis, "Activation of Carbonyl-Containing Molecules with Solid Lewis Acids in Aqueous Media," *ACS Catal.*, vol. 1, no. 11, pp. 1566–1580, 2011.

[178]  J. D. Lewis, S. Van de Vyver, and Y. Román-Leshkov, "Acid–Base Pairs in Lewis Acidic Zeolites Promote Direct Aldol Reactions by Soft Enolization," *Angewandte Chemie International Edition*, vol. 54, no. 34, pp. 9835–9838, 2015.

[179]  L. B. Young, "Preparing phenylalkanes," US4301316A, 17-Nov-1981.

[180]  R. B. LaPierre, R. D. Partridge, N. Y. Chen, and S. S. Wong, "Catalytic dewaxing process," US4419220A, 06-Dec-1983.

[181]  R. B. LaPierre, R. D. Partridge, N. Y. Chen, and S. S. Wong, "Hydrotreating/isomerization process to produce low pour point distillate fuels and lubricating oil stocks," US4518485A, 21-May-1985.

[182]  N. Y. Chen and T. J. Huang, "Hydroprocessing catalyst," US4672049A, 09-Jun-1987.

[183]  M. Boudart, "Turnover Rates in Heterogeneous Catalysis," *Chem. Rev.*, vol. 95, no. 3, pp. 661–666, May 1995.

[184]  R. Davis, "Turnover rates on complex heterogeneous catalysts," *AIChE Journal*, vol. 64, no. 11, pp. 3778–3785, 2018.

[185]  M. Moliner, Y. Román-Leshkov, and M. E. Davis, "Tin-containing zeolites are highly active catalysts for the isomerization of glucose in water," *PNAS*, vol. 107, no. 14, pp. 6164–6168, Apr. 2010.

[186]  A. Corma, L. T. Nemeth, M. Renz, and S. Valencia, "Sn-zeolite beta as a heterogeneous chemoselective catalyst for Baeyer–Villiger oxidations," *Nature*, vol. 412, no. 6845, pp. 423–425, Jul. 2001.

[187]  J. D. Lewis, S. Van de Vyver, and Y. Román-Leshkov, "Acid–Base Pairs in Lewis Acidic Zeolites Promote Direct Aldol Reactions by Soft Enolization," *Angew. Chem. Int. Ed.*, vol. 54, no. 34, pp. 9835–9838, Aug. 2015.

[188]  H. Y. Luo, J. D. Lewis, and Y. Román-Leshkov, "Lewis Acid Zeolites for Biomass Conversion: Perspectives and Challenges on Reactivity, Synthesis, and Stability," *Annu. Rev. Chem. Biomol. Eng.*, Aug. 2015.

[189]   W. M. Quattlebaum, W. J. Toussaint, and J. T. Dunn, "Deoxygenation of Certain Aldehydes and Ketones: Preparation of Butadiene and Styrene [1]," *J. Am. Chem. Soc.*, vol. 69, no. 3, pp. 593–599, Mar. 1947.

[190]   P. Müller, S. P. Burt, A. M. Love, W. P. McDermott, P. Wolf, and I. Hermans, "Mechanistic Study on the Lewis Acid Catalyzed Synthesis of 1,3-Butadiene over Ta-BEA Using Modulated Operando DRIFTS-MS," *ACS Catal.*, vol. 6, no. 10, pp. 6823–6832, Oct. 2016.

[191]   V. L. Sushkevich, D. Palagin, and I. I. Ivanova, "With Open Arms: Open Sites of ZrBEA Zeolite Facilitate Selective Synthesis of Butadiene from Ethanol," *ACS Catal.*, vol. 5, no. 8, pp. 4833–4836, Aug. 2015.

[192]   V. L. Sushkevich, I. I. Ivanova, V. V. Ordomsky, and E. Taarning, "Design of a Metal-Promoted Oxide Catalyst for the Selective Synthesis of Butadiene from Ethanol," *ChemSusChem*, vol. 7, no. 9, pp. 2527–2536, Sep. 2014.

[193]   V. L. Sushkevich and I. I. Ivanova, "Mechanistic study of ethanol conversion into butadiene over silver promoted zirconia catalysts," *Applied Catalysis B: Environmental*, vol. 215, pp. 36–49, Oct. 2017.

[194]   C. R. Ho, S. Shylesh, and A. T. Bell, "Mechanism and Kinetics of Ethanol Coupling to Butanol over Hydroxyapatite," *ACS Catal.*, vol. 6, no. 2, pp. 939–948, Feb. 2016.

[195]   C. Yang and Z. Y. Meng, "Bimolecular Condensation of Ethanol to 1-Butanol Catalyzed by Alkali Cation Zeolites," *Journal of Catalysis*, vol. 142, no. 1, pp. 37–44, Jul. 1993.

[196]   M. Boronat, P. Concepción, A. Corma, M. Renz, and S. Valencia, "Determination of the catalytically active oxidation Lewis acid sites in Sn-beta zeolites, and their optimisation by the combination of theoretical and experimental studies," *Journal of Catalysis*, vol. 234, no. 1, pp. 111–118, Aug. 2005.

[197]   T. R. Josephson, G. R. Jenness, D. G. Vlachos, and S. Caratzoulas, "Distribution of open sites in Sn-Beta zeolite," *Microporous and Mesoporous Materials*, vol. 245, pp. 45–50, Jun. 2017.

[198]   B. C. Bukowski, J. S. Bates, R. Gounder, and J. Greeley, "First principles, microkinetic, and experimental analysis of Lewis acid site speciation during ethanol dehydration on Sn-Beta zeolites," *Journal of Catalysis*, vol. 365, pp. 261–276, Sep. 2018.

[199]   T. R. Josephson *et al.*, "Cooperative Catalysis by Surface Lewis Acid/Silanol for Selective Fructose Etherification on Sn-SPP Zeolite," *ACS Catal.*, Aug. 2018.

[200]   D. Palagin, V. L. Sushkevich, and I. I. Ivanova, "C–C Coupling Catalyzed by Zeolites: Is Enolization the Only Possible Pathway for Aldol Condensation?," *J. Phys. Chem. C*, vol. 120, no. 41, pp. 23566–23575, Oct. 2016.

[201]   J. M. Newsam, M. M. J. Treacy, W. T. Koetsier, and C. B. D. Gruyter, "Structural Characterization of Zeolite Beta," *Proceedings of the Royal Society A: Mathematical, Physical and Engineering Sciences*, vol. 420, no. 1859, pp. 375–405, Dec. 1988.

[202]   F. Liebau, "Ordered microporous and mesoporous materials with inorganic hosts: definitions of terms, formula notation, and systematic classification," *Microporous and Mesoporous Materials*, vol. 58, no. 1, pp. 15–72, Feb. 2003.

[203]   L. B. McCusker, F. Liebau, and G. Engelhardt, "Nomenclature of structural and compositional characteristics of ordered microporous and mesoporous materials with inorganic hosts(IUPAC Recommendations 2001)," *Pure and Applied Chemistry*, vol. 73, no. 2, pp. 381–394, Jan. 2001.

[204]  V. A. Blatov, O. Delgado-Friedrichs, M. O'Keeffe, and D. M. Proserpio, "Three-periodic nets and tilings: natural tilings for nets," *Acta Cryst A*, vol. 63, no. 5, pp. 418–425, Sep. 2007.

[205]  R. B. Laughlin and J. D. Joannopoulos, "Theory of surface phonons in amorphous silica," *Phys. Rev. B*, vol. 17, no. 12, pp. 4922–4930, Jun. 1978.

[206]  R. B. Laughlin, J. D. Joannopoulos, C. A. Murray, K. J. Hartnett, and T. J. Greytak, "Intrinsic Surface Phonons in Porous Glass," *Phys. Rev. Lett.*, vol. 40, no. 7, pp. 461–465, Feb. 1978.

[207]  M. Wilson and T. R. Walsh, "Hydrolysis of the amorphous silica surface. I. Structure and dynamics of the dry surface," *The Journal of Chemical Physics*, vol. 113, no. 20, pp. 9180–9190, Nov. 2000.

[208]  A. Roder, W. Kob, and K. Binder, "Structure and dynamics of amorphous silica surfaces," *J. Chem. Phys.*, vol. 114, no. 17, pp. 7602–7614, Apr. 2001.

[209]  Y. Yu, B. Wang, M. Wang, G. Sant, and M. Bauchy, "Revisiting silica with ReaxFF: Towards improved predictions of glass structure and properties via reactive molecular dynamics," *Journal of Non-Crystalline Solids*, vol. 443, pp. 148–154, Jul. 2016.

[210]  I. A. Koppel, P. Burk, I. Koppel, I. Leito, T. Sonoda, and M. Mishima, "Gas-Phase Acidities of Some Neutral Brønsted Superacids: A DFT and ab Initio Study," *J. Am. Chem. Soc.*, vol. 122, no. 21, pp. 5114–5124, May 2000.

[211]  M. Brändle and J. Sauer, "Acidity Differences between Inorganic Solids Induced by Their Framework Structure. A Combined Quantum Mechanics/Molecular Mechanics ab Initio Study on Zeolites," *J. Am. Chem. Soc.*, vol. 120, no. 7, pp. 1556–1570, Feb. 1998.

[212]  A. J. Jones and E. Iglesia, "The Strength of Brønsted Acid Sites in Microporous Aluminosilicates," *ACS Catal.*, vol. 5, no. 10, pp. 5741–5755, Oct. 2015.

[213]  D. P. Estes *et al.*, "C–H Activation on Co,O Sites: Isolated Surface Sites versus Molecular Analogs," *J. Am. Chem. Soc.*, vol. 138, no. 45, pp. 14987–14997, Nov. 2016.

[214]  M. F. Delley *et al.*, "Proton transfers are key elementary steps in ethylene polymerization on isolated chromium(III) silicates," *PNAS*, vol. 111, no. 32, pp. 11624–11629, Aug. 2014.

[215]  N. M. Schweitzer *et al.*, "Propylene Hydrogenation and Propane Dehydrogenation by a Single-Site Zn2+ on Silica Catalyst," *ACS Catal.*, vol. 4, no. 4, pp. 1091–1098, Apr. 2014.

[216]  A. H. Larsen *et al.*, "The atomic simulation environment—a Python library for working with atoms," *J. Phys.: Condens. Matter*, vol. 29, no. 27, p. 273002, Jun. 2017.

[217]  K. Robinson, G. V. Gibbs, and P. H. Ribbe, "Quadratic Elongation: A Quantitative Measure of Distortion in Coordination Polyhedra," *Science*, vol. 172, no. 3983, pp. 567–570, 1971.

[218]  M. E. Fleet, "Distortion parameters for coordination polyhedra," *Mineralogical Magazine*, vol. 40, no. 313, pp. 531–533, Mar. 1976.

[219]  W. Kabsch, "A solution for the best rotation to relate two sets of vectors," *Acta Cryst A*, vol. 32, no. 5, pp. 922–923, Sep. 1976.

[220]  M. W. Walker, L. Shao, and R. A. Volz, "Estimating 3-D location parameters using dual number quaternions," *CVGIP: Image Understanding*, vol. 54, no. 3, pp. 358–367, Nov. 1991.

[221]  J. C. Kromann, *Calculate Root-mean-square deviation (RMSD) of two molecules, using rotation, in xyz or pdb format: charnley/rmsd*. 2019.

[222]  P. H. Mott, A. S. Argon, and U. W. Suter, "The atomic strain tensor," *Journal of Computational Physics*, vol. 101, no. 1, pp. 140–150, Jul. 1992.

[223]  P. M. Gullett, M. F. Horstemeyer, M. I. Baskes, and H. Fang, "A deformation gradient tensor and strain tensors for atomistic simulations," *Modelling Simul. Mater. Sci. Eng.*, vol. 16, no. 1, p. 015001, 2008.

[224]  M. Wang *et al.*, "Genesis and Stability of Hydronium Ions in Zeolite Channels," *Journal of the American Chemical Society*, Jan. 2019.

[225]  A. Vjunov *et al.*, "Following Solid-Acid-Catalyzed Reactions by MAS NMR Spectroscopy in Liquid Phase—Zeolite-Catalyzed Conversion of Cyclohexanol in Water," *Angewandte Chemie International Edition*, vol. 53, no. 2, pp. 479–482, 2014.

[226]  C.-D. Wu and W. Lin, "Highly Porous, Homochiral Metal–Organic Frameworks: Solvent-Exchange-Induced Single-Crystal to Single-Crystal Transformations," *Angewandte Chemie International Edition*, vol. 44, no. 13, pp. 1958–1961, Mar. 2005.

[227]  K. Koga, G. T. Gao, H. Tanaka, and X. C. Zeng, "Formation of ordered ice nanotubes inside carbon nanotubes," *Nature*, vol. 412, no. 6849, pp. 802–805, Aug. 2001.

[228]  N. Nakashima, Y. Tomonari, and H. Murakami, "Water-Soluble Single-Walled Carbon Nanotubes via Noncovalent Sidewall-Functionalization with a Pyrene-Carrying Ammonium Ion," *Chem. Lett.*, vol. 31, no. 6, pp. 638–639, Jun. 2002.

[229]  G. Hummer, J. C. Rasaiah, and J. P. Noworyta, "Water conduction through the hydrophobic channel of a carbon nanotube," *Nature*, vol. 414, no. 6860, pp. 188–190, Nov. 2001.

[230]  K. K. S. Lau *et al.*, "Superhydrophobic Carbon Nanotube Forests," *Nano Lett.*, vol. 3, no. 12, pp. 1701–1705, Dec. 2003.

[231]  J. C. Vega-Vila, J. W. Harris, and R. Gounder, "Controlled insertion of tin atoms into zeolite framework vacancies and consequences for glucose isomerization catalysis," *Journal of Catalysis*, vol. 344, pp. 108–120, Dec. 2016.

[232]  R. Bermejo-Deval, M. Orazov, R. Gounder, S.-J. Hwang, and M. E. Davis, "Active Sites in Sn-Beta for Glucose Isomerization to Fructose and Epimerization to Mannose," *ACS Catal.*, vol. 4, no. 7, pp. 2288–2297, Jul. 2014.

[233]  J. W. Harris, M. J. Cordon, J. R. Di Iorio, J. C. Vega-Vila, F. H. Ribeiro, and R. Gounder, "Titration and quantification of open and closed Lewis acid sites in Sn-Beta zeolites that catalyze glucose isomerization," *Journal of Catalysis*, vol. 335, pp. 141–154, Mar. 2016.

[234]  J. Dijkmans, J. Demol, K. Houthoofd, S. Huang, Y. Pontikes, and B. Sels, "Post-synthesis Snβ: An exploration of synthesis parameters and catalysis," *Journal of Catalysis*, vol. 330, pp. 545–557, Oct. 2015.

[235]  M. Trzpit *et al.*, "The Effect of Local Defects on Water Adsorption in Silicalite-1 Zeolite:  A Joint Experimental and Molecular Simulation Study," *Langmuir*, vol. 23, no. 20, pp. 10131–10139, Sep. 2007.

[236]  P. Demontis, G. Stara, and G. B. Suffritti, "Behavior of Water in the Hydrophobic Zeolite Silicalite at Different Temperatures. A Molecular Dynamics Study," *J. Phys. Chem. B*, vol. 107, no. 18, pp. 4426–4436, May 2003.

[237]  P. Demontis, J. Gulín-González, M. Masia, and G. B. Suffritti, "The behaviour of water confined in zeolites: molecular dynamics simulations versus experiment," *J. Phys.: Condens. Matter*, vol. 22, no. 28, p. 284106, 2010.

[238]  "Dynamical behavior of one-dimensional water molecule chains in zeolites: Nanosecond time-scale molecular dynamics simulations of bikitaite," *The Journal of Chemical Physics*, vol. 120, no. 19, pp. 9233–9244, Apr. 2004.

[239]   D. T. Bregante *et al.*, "Cooperative Effects between Hydrophilic Pores and Solvents: Catalytic Consequences of Hydrogen Bonding on Alkene Epoxidation in Zeolites," *J. Am. Chem. Soc.*, Jan. 2019.

[240]   H. W. Horn *et al.*, "Development of an improved four-site water model for biomolecular simulations: TIP4P-Ew," *J. Chem. Phys.*, vol. 120, no. 20, pp. 9665–9678, May 2004.

[241]   H. J. C. Berendsen, J. R. Grigera, and T. P. Straatsma, "The missing term in effective pair potentials," *The Journal of Physical Chemistry*, vol. 91, no. 24, pp. 6269–6271, Nov. 1987.

[242]   "The Nose–Hoover thermostat," *The Journal of Chemical Physics*, vol. 83, no. 8, pp. 4069–4074, Oct. 1985.

[243]   W. M. Haynes and D. R. Lide, Eds., *CRC handbook of chemistry and physics: a ready-reference book of chemical and physical data*, 93. ed., 2012–2013. Boca Raton, Fla.: CRC Press, 2012.

[244]   S.-T. Lin, P. K. Maiti, and W. A. Goddard, "Two-Phase Thermodynamic Model for Efficient and Accurate Absolute Entropy of Water from Molecular Dynamics Simulations," *J. Phys. Chem. B*, vol. 114, no. 24, pp. 8191–8198, Jun. 2010.

[245]   T. A. Pascal, S.-T. Lin, and W. A. Goddard III, "Thermodynamics of liquids: standard molar entropies and heat capacities of common solvents from 2PT molecular dynamics," *Phys. Chem. Chem. Phys.*, vol. 13, no. 1, pp. 169–181, 2011.

[246]   M. Brehm and B. Kirchner, "TRAVIS - A Free Analyzer and Visualizer for Monte Carlo and Molecular Dynamics Trajectories," *J. Chem. Inf. Model.*, vol. 51, no. 8, pp. 2007–2023, Aug. 2011.

[247]   A. Barrat, M. Barthélemy, R. Pastor-Satorras, and A. Vespignani, "The architecture of complex weighted networks," *PNAS*, vol. 101, no. 11, pp. 3747–3752, Mar. 2004.

[248]   J. D. Durrant and J. A. McCammon, "HBonanza: A computer algorithm for molecular-dynamics-trajectory hydrogen-bond analysis," *Journal of Molecular Graphics and Modelling*, vol. 31, pp. 5–9, Nov. 2011.

[249]   C.-H. Wang, P. Bai, J. I. Siepmann, and A. E. Clark, "Deconstructing Hydrogen-Bond Networks in Confined Nanoporous Materials: Implications for Alcohol–Water Separation," *J. Phys. Chem. C*, vol. 118, no. 34, pp. 19723–19732, Aug. 2014.

[250]   T. Zhou, P. Bai, J. I. Siepmann, and A. E. Clark, "Deconstructing the Confinement Effect upon the Organization and Dynamics of Water in Hydrophobic Nanoporous Materials: Lessons Learned from Zeolites," *J. Phys. Chem. C*, vol. 121, no. 40, pp. 22015–22024, Oct. 2017.

[251]   F. Dehne and H. Noltemeier, "Voronoi trees and clustering problems," *Information Systems*, vol. 12, no. 2, pp. 171–175, Jan. 1987.

[252]   W. Brostow, M. Chybicki, R. Laskowski, and J. Rybicki, "Voronoi polyhedra and Delaunay simplexes in the structural analysis of molecular-dynamics-simulated materials," *Phys. Rev. B*, vol. 57, no. 21, pp. 13448–13458, Jun. 1998.

[253]   S. Dalla Bernardina *et al.*, "Water in Carbon Nanotubes: The Peculiar Hydrogen Bond Network Revealed by Infrared Spectroscopy," *J. Am. Chem. Soc.*, vol. 138, no. 33, pp. 10437–10443, Aug. 2016.

[254]   S. E. Denmark and G. L. Beutner, "Lewis base catalysis in organic synthesis," *Angewandte Chemie International Edition*, vol. 47, no. 9, pp. 1560–1638, 2008.

[255]   J. M. Hogg, L. C. Brown, K. Matuszek, P. Latos, A. Chrobok, and M. Swadźba-Kwaśny, "Liquid coordination complexes of Lewis acidic metal chlorides: Lewis acidity and insights into speciation," *Dalton Trans.*, vol. 46, no. 35, pp. 11561–11574, Sep. 2017.

[256]   B. C. Gates, H. Knoezinger, and F. C. Jentoft, *Advances in Catalysis*, vol. 54. Academic Press, 2011.

[257]   E. V. Anslyn and D. A. Dougherty, *Modern Physical Organic Chemistry*. University Science, 2005.

[258]   M. J. Gilkey and B. Xu, "Heterogeneous Catalytic Transfer Hydrogenation as an Effective Pathway in Biomass Upgrading," *ACS Catal.*, vol. 6, no. 3, pp. 1420–1436, Mar. 2016.

[259]   J. Sun and Y. Wang, "Recent Advances in Catalytic Conversion of Ethanol to Chemicals," *ACS Catal.*, vol. 4, no. 4, pp. 1078–1090, Apr. 2014.

[260]   J. F. DeWilde, H. Chiang, D. A. Hickman, C. R. Ho, and A. Bhan, "Kinetics and Mechanism of Ethanol Dehydration on $\gamma$-Al$_2$O$_3$: The Critical Role of Dimer Inhibition," *ACS Catalysis*, vol. 3, no. 4, pp. 798–807, Apr. 2013.

[261]   M. A. Christiansen, G. Mpourmpakis, and D. G. Vlachos, "Density Functional Theory-Computed Mechanisms of Ethylene and Diethyl Ether Formation from Ethanol on $\gamma$-Al2O3(100)," *ACS Catal.*, vol. 3, no. 9, pp. 1965–1975, 2013.

[262]   E. G. Derouane *et al.*, "Elucidation of the mechanism of conversion of methanol and ethanol to hydrocarbons on a new type of synthetic zeolite," *Journal of Catalysis*, vol. 53, no. 1, pp. 40–55, Jun. 1978.

[263]   C. B. Phillips and R. Datta, "Production of Ethylene from Hydrous Ethanol on H-ZSM-5 under Mild Conditions," *Ind. Eng. Chem. Res.*, vol. 36, no. 11, pp. 4466–4475, Nov. 1997.

[264]   D. Mei and J. A. Lercher, "Mechanistic insights into aqueous phase propanol dehydration in H-ZSM-5 zeolite," *AIChE Journal*, vol. 63, no. 1, pp. 172–184, 2017.

[265]   Y. Zhi *et al.*, "Dehydration Pathways of 1-Propanol on HZSM-5 in the Presence and Absence of Water," *Journal of the American Chemical Society*, vol. 137, no. 50, pp. 15781–15794, Dec. 2015.

[266]   C. T. Campbell and J. R. V. Sellers, "Enthalpies and Entropies of Adsorption on Well-Defined Oxide Surfaces: Experimental Measurements," *Chem. Rev.*, vol. 113, no. 6, pp. 4106–4135, Jun. 2013.

[267]   H. Chiang and A. Bhan, "Catalytic consequences of hydroxyl group location on the rate and mechanism of parallel dehydration reactions of ethanol over acidic zeolites," *Journal of Catalysis*, vol. 271, no. 2, pp. 251–261, May 2010.

[268]   A. Vjunov *et al.*, "Tracking the Chemical Transformations at the Brønsted Acid Site upon Water-Induced Deprotonation in a Zeolite Pore," *Chem. Mater.*, vol. 29, no. 21, pp. 9030–9042, Nov. 2017.

[269]   J. J. H. B. Sattler, J. Ruiz-Martinez, E. Santillan-Jimenez, and B. M. Weckhuysen, "Catalytic Dehydrogenation of Light Alkanes on Metals and Metal Oxides," *Chem. Rev.*, vol. 114, no. 20, pp. 10613–10653, Oct. 2014.

[270]   M. Guisnet and P. Magnoux, "Organic chemistry of coke formation," *Applied Catalysis A: General*, vol. 212, no. 1, pp. 83–96, Apr. 2001.

[271]   J. H. Sinfelt, "Catalysis by alloys and bimetallic clusters," *Acc. Chem. Res.*, vol. 10, no. 1, pp. 15–20, Jan. 1977.

[272]   J. H. Sinfelt, J. L. Carter, and D. J. C. Yates, "Catalytic hydrogenolysis and dehydrogenation over copper-nickel alloys," *Journal of Catalysis*, vol. 24, no. 2, pp. 283–296, Feb. 1972.

[273]   O. A. Bariås, A. Holmen, and E. A. Blekkan, "Propane Dehydrogenation over Supported Pt and Pt–Sn Catalysts: Catalyst Preparation, Characterization, and Activity Measurements," *Journal of Catalysis*, vol. 158, no. 1, pp. 1–12, Jan. 1996.

[274]   C. Kappenstein, M. Gueʹrin, K. Lázár, K. Matusek, and Z. Paál, "Characterisation and activity in n-hexane rearrangement reactions of metallic phases on Pt–Sn/Al2O3 catalysts of different preparations," *J. Chem. Soc., Faraday Trans.*, vol. 94, no. 16, pp. 2463–2473, Jan. 1998.

[275]   M. Santhosh Kumar, D. Chen, A. Holmen, and J. C. Walmsley, "Dehydrogenation of propane over Pt-SBA-15 and Pt-Sn-SBA-15: Effect of Sn on the dispersion of Pt and catalytic behavior," *Catalysis Today*, vol. 142, no. 1, pp. 17–23, Apr. 2009.

[276]   L. Nykänen and K. Honkala, "Selectivity in Propene Dehydrogenation on Pt and Pt$_3$Sn Surfaces from First Principles," *ACS Catalysis*, vol. 3, no. 12, pp. 3026–3030, Dec. 2013.

[277]   L. Nykänen and K. Honkala, "Density Functional Theory Study on Propane and Propene Adsorption on Pt(111) and PtSn Alloy Surfaces," *The Journal of Physical Chemistry C*, vol. 115, no. 19, pp. 9578–9586, May 2011.

[278]   J. R. Kitchin, J. K. Nørskov, M. A. Barteau, and J. G. Chen, "Modification of the surface electronic and chemical properties of Pt(111) by subsurface 3d transition metals," *J. Chem. Phys.*, vol. 120, no. 21, pp. 10240–10246, May 2004.

[279]   V. R. Stamenkovic *et al.*, "Trends in electrocatalysis on extended and nanoscale Pt-bimetallic alloy surfaces," *Nature Materials*, vol. 6, no. 3, pp. 241–247, Mar. 2007.

[280]   G. Sun *et al.*, "Breaking the scaling relationship via thermally stable Pt/Cu single atom alloys for catalytic dehydrogenation," *Nature Communications*, vol. 9, no. 1, Dec. 2018.

[281]   B. S. Mun, M. Watanabe, M. Rossi, V. Stamenkovic, N. M. Markovic, and P. N. Ross, "A study of electronic structures of Pt3M (M=Ti,V,Cr,Fe,Co,Ni) polycrystalline alloys with valence-band photoemission spectroscopy," *The Journal of Chemical Physics*, vol. 123, no. 20, p. 204717, Nov. 2005.

[282]   Y. Xiong *et al.*, "Revealing the atomic ordering of binary intermetallics using in situ heating techniques at multilength scales," *PNAS*, vol. 116, no. 6, pp. 1974–1983, Feb. 2019.

[283]   T. Ghosh, B. M. Leonard, Q. Zhou, and F. J. DiSalvo, "Pt Alloy and Intermetallic Phases with V, Cr, Mn, Ni, and Cu: Synthesis As Nanomaterials and Possible Applications As Fuel Cell Catalysts," *Chemistry of Materials*, vol. 22, no. 7, pp. 2190–2202, Apr. 2010.

[284]   M. Armbrüster, R. Schlögl, and Y. Grin, "Intermetallic compounds in heterogeneous catalysis—a quickly developing field," *Science and Technology of Advanced Materials*, vol. 15, no. 3, p. 034803, Jun. 2014.

[285]   Z. Cui *et al.*, "Synthesis of Structurally Ordered Pt$_3$Ti and Pt$_3$V Nanoparticles as Methanol Oxidation Catalysts," *Journal of the American Chemical Society*, vol. 136, no. 29, pp. 10206–10209, Jul. 2014.

[286]   N. J. LiBretto, C. Yang, Y. Ren, G. Zhang, and J. T. Miller, "Identification of Surface Structures in Pt3Cr Intermetallic Nanocatalysts," *Chem. Mater.*, vol. 31, no. 5, pp. 1597–1609, Mar. 2019.

[287]   Z. Wu *et al.*, "Changes in Catalytic and Adsorptive Properties of 2 nm Pt$_3$Mn Nanoparticles by Subsurface Atoms," *Journal of the American Chemical Society*, vol. 140, no. 44, pp. 14870–14877, Nov. 2018.

[288]   Z. Yu, J. A. Sawada, W. An, and S. M. Kuznicki, "PtZn-ETS-2: A novel catalyst for ethane dehydrogenation," *AIChE Journal*, vol. 61, no. 12, pp. 4367–4376, 2015.

[289]   V. J. Cybulskis *et al.*, "Zinc Promotion of Platinum for Catalytic Light Alkane Dehydrogenation: Insights into Geometric and Electronic Effects," *ACS Catal.*, vol. 7, no. 6, pp. 4173–4181, Jun. 2017.

[290]   B. Hammer and J. K. Nørskov, "Theoretical surface science and catalysis—calculations and concepts," in *Advances in Catalysis*, vol. 45, Elsevier, 2000, pp. 71–129.

[291]   H. Xin, A. Vojvodic, J. Voss, J. K. Nørskov, and F. Abild-Pedersen, "Effects of $d$-band shape on the surface reactivity of transition-metal alloys," *Phys. Rev. B*, vol. 89, no. 11, p. 115114, Mar. 2014.

[292]   H. Höchst, S. Hüfner, and A. Goldmann, "XPS-valence bands of iron, cobalt, palladium and platinum," *Physics Letters A*, vol. 57, no. 3, pp. 265–266, Jun. 1976.

[293]   A. Kotani and S. Shin, "Resonant inelastic x-ray scattering spectra for electrons in solids," *Rev. Mod. Phys.*, vol. 73, no. 1, pp. 203–246, Feb. 2001.

[294]   L. J. P. Ament, M. van Veenendaal, T. P. Devereaux, J. P. Hill, and J. van den Brink, "Resonant inelastic x-ray scattering studies of elementary excitations," *Rev. Mod. Phys.*, vol. 83, no. 2, pp. 705–767, Jun. 2011.

[295]   J. Singh, C. Lamberti, and J. A. van Bokhoven, "Advanced X-ray absorption and emission spectroscopy: in situ catalytic studies," *Chem. Soc. Rev.*, vol. 39, no. 12, pp. 4754–4766, Nov. 2010.

[296]   P. Glatzel, J. Singh, K. O. Kvashnina, and J. A. van Bokhoven, "In Situ Characterization of the 5d Density of States of Pt Nanoparticles upon Adsorption of CO," *J. Am. Chem. Soc.*, vol. 132, no. 8, pp. 2555–2557, Mar. 2010.

[297]   J. Singh, R. C. Nelson, B. C. Vicente, S. L. Scott, and J. A. van Bokhoven, "Electronic structure of alumina-supported monometallic Pt and bimetallic PtSn catalysts under hydrogen and carbon monoxide environment," *Phys. Chem. Chem. Phys.*, vol. 12, no. 21, pp. 5668–5677, May 2010.

[298]   E. Suljoti *et al.*, "Direct Observation of Molecular Orbital Mixing in a Solvated Organometallic Complex," *Angew. Chem. Int. Ed.*, vol. 52, no. 37, pp. 9841–9844, Sep. 2013.

[299]   J. J. Yan *et al.*, "Resonant inelastic X-ray scattering determination of the electronic structure of oxyhemoglobin and its model complex," *PNAS*, p. 201815981, Jan. 2019.

[300]   S. Saerens, M. K. Sabbe, V. V. Galvita, E. A. Redekop, M.-F. Reyniers, and G. B. Marin, "The Positive Role of Hydrogen on the Dehydrogenation of Propane on Pt(111)," *ACS Catal.*, vol. 7, no. 11, pp. 7495–7508, Nov. 2017.

[301]   M. Boudart, *Kinetics of heterogeneous catalytic reactions.* Place of publication not identified: Princeton Univ Press, 2014.

[302]   L. G. Cesar, C. Yang, Z. Lu, Y. Ren, G. Zhang, and J. T. Miller, "Identification of a $Pt_3$ Co Surface Intermetallic Alloy in Pt–Co Propane Dehydrogenation Catalysts," *ACS Catal.*, pp. 5231–5244, May 2019.

[303]   E. C. Wegener *et al.*, "Structure and reactivity of Pt–In intermetallic alloy nanoparticles: Highly selective catalysts for ethane dehydrogenation," *Catalysis Today*, vol. 299, pp. 146–153, Jan. 2018.

[304]   P. Strasser *et al.*, "Lattice-strain control of the activity in dealloyed core–shell fuel cell catalysts," *Nature Chemistry*, vol. 2, no. 6, pp. 454–460, Jun. 2010.

[305]   J. Greeley, W. P. Krekelberg, and M. Mavrikakis, "Strain-Induced Formation of Subsurface Species in Transition Metals," *Angewandte Chemie*, vol. 116, no. 33, pp. 4396–4400, 2004.

[306]   F. Abild-Pedersen, J. Greeley, and J. K. Nørskov, "Understanding the Effect of Steps, Strain, Poisons, and Alloying: Methane Activation on Ni Surfaces," *Catal Lett*, vol. 105, no. 1, pp. 9–13, Nov. 2005.

[307]   A. Vojvodic, J. K. Nørskov, and F. Abild-Pedersen, "Electronic Structure Effects in Transition Metal Surface Chemistry," *Top Catal*, vol. 57, no. 1, pp. 25–32, Feb. 2014.

[308]   J. Greeley, "Theoretical Heterogeneous Catalysis: Scaling Relationships and Computational Catalyst Design," *Annual Review of Chemical and Biomolecular Engineering*, vol. 7, no. 1, p. null, 2016.

[309]   R. Michalsky, Y.-J. Zhang, A. J. Medford, and A. A. Peterson, "Departures from the Adsorption Energy Scaling Relations for Metal Carbide Catalysts," *J. Phys. Chem. C*, vol. 118, no. 24, pp. 13026–13034, Jun. 2014.

[310]   T. Choksi, P. Majumdar, and J. P. Greeley, "Electrostatic Origins of Linear Scaling Relationships at Bifunctional Metal/Oxide Interfaces: A Case Study of Au Nanoparticles on Doped MgO Substrates," *Angewandte Chemie International Edition*, vol. 57, no. 47, pp. 15410–15414, 2018.

[311]   M. Taramasso, G. Perego, and B. Notari, "Preparation of porous crystalline synthetic material comprised of silicon and titanium oxides," US4410501A, 18-Oct-1983.

[312]   M. Haruta, "Size- and support-dependency in the catalysis of gold," *Catalysis Today*, vol. 36, no. 1, pp. 153–166, Apr. 1997.

[313]   T. Hayashi, K. Tanaka, and M. Haruta, "Selective Vapor-Phase Epoxidation of Propylene over Au/TiO2Catalysts in the Presence of Oxygen and Hydrogen," *Journal of Catalysis*, vol. 178, no. 2, pp. 566–575, Sep. 1998.

[314]   M. Shekhar *et al.*, "Size and Support Effects for the Water–Gas Shift Catalysis over Gold Nanoparticles Supported on Model Al2O3 and TiO2," *J. Am. Chem. Soc.*, vol. 134, no. 10, pp. 4700–4708, Mar. 2012.

[315]   B. Taylor, J. Lauterbach, and W. N. Delgass, "Gas-phase epoxidation of propylene over small gold ensembles on TS-1," *Applied Catalysis A: General*, vol. 291, no. 1, pp. 188–198, Sep. 2005.

[316]   J. Huang, T. Takei, T. Akita, H. Ohashi, and M. Haruta, "Gold clusters supported on alkaline treated TS-1 for highly efficient propene epoxidation with O2 and H2," *Applied Catalysis B: Environmental*, vol. 95, no. 3, pp. 430–438, Apr. 2010.

[317]   T. A. Nijhuis, B. J. Huizinga, M. Makkee, and J. A. Moulijn, "Direct Epoxidation of Propene Using Gold Dispersed on TS-1 and Other Titanium-Containing Supports," *Ind. Eng. Chem. Res.*, vol. 38, no. 3, pp. 884–891, Mar. 1999.

[318]   W.-S. Lee, L.-C. Lai, M. Cem Akatay, E. A. Stach, F. H. Ribeiro, and W. N. Delgass, "Probing the gold active sites in Au/TS-1 for gas-phase epoxidation of propylene in the presence of hydrogen and oxygen," *Journal of Catalysis*, vol. 296, pp. 31–42, Dec. 2012.

[319]   A. M. Joshi, W. N. Delgass, and K. T. Thomson, "Partial Oxidation of Propylene to Propylene Oxide over a Neutral Gold Trimer in the Gas Phase:  A Density Functional Theory Study," *J. Phys. Chem. B*, vol. 110, no. 6, pp. 2572–2581, Feb. 2006.

[320]   D. H. Wells, A. M. Joshi, W. N. Delgass, and K. T. Thomson, "A Quantum Chemical Study of Comparison of Various Propylene Epoxidation Mechanisms Using H2O2 and TS-1 Catalyst," *J. Phys. Chem. B*, vol. 110, no. 30, pp. 14627–14639, Aug. 2006.

[321]   T. Otto, S. I. Zones, and E. Iglesia, "Challenges and strategies in the encapsulation and stabilization of monodisperse Au clusters within zeolites," *Journal of Catalysis*, vol. 339, pp. 195–208, Jul. 2016.

[322]  M. Moliner, J. E. Gabay, C. E. Kliewer, P. Serna, and A. Corma, "Trapping of Metal Atoms and Metal Clusters by Chabazite under Se-vere REDOX Stress," *ACS Catal.*, Aug. 2018.

[323]  A. Hoffman, M. DeLuca, and D. Hibbitts, "Restructuring of MFI Framework Zeolite Models and Their Associated Artifacts in Density Functional Theory Calculations," *J. Phys. Chem. C*, vol. 123, no. 11, pp. 6572–6585, Mar. 2019.

[324]  C. Lamberti, S. Bordiga, A. Zecchina, G. Artioli, G. Marra, and G. Spanò, "Ti Location in the MFI Framework of Ti−Silicalite-1: A Neutron Powder Diffraction Study," *J. Am. Chem. Soc.*, vol. 123, no. 10, pp. 2204–2212, Mar. 2001.

[325]  B. Assadollahzadeh and P. Schwerdtfeger, "A systematic search for minimum structures of small gold clusters Aun (n=2–20) and their electronic properties," *The Journal of Chemical Physics*, vol. 131, no. 6, p. 064306, Aug. 2009.

[326]  B. Silvi and A. Savin, "Classification of chemical bonds based on topological analysis of electron localization functions," *Nature*, vol. 371, no. 6499, p. 683, Oct. 1994.

[327]  R. Dronskowski and P. E. Bloechl, "Crystal orbital Hamilton populations (COHP): energy-resolved visualization of chemical bonding in solids based on density-functional calculations," *J. Phys. Chem.*, vol. 97, no. 33, pp. 8617–8624, Aug. 1993.

[328]  M. Thomas, M. Brehm, R. Fligg, P. Vöhringer, and B. Kirchner, "Computing vibrational spectra from ab initio molecular dynamics," *Phys. Chem. Chem. Phys.*, vol. 15, no. 18, pp. 6608–6622, Apr. 2013.

# VITA

Brandon Christopher Bukowski was born in New Haven Connecticut on 13$^{th}$ April 1992 to Christopher and Theresa Bukowski. He earned his Bachelor of Chemical Engineering degree from Worcester Polytechnical Institute (WPI) in May of 2014. At WPI, he worked with Prof. N. Aaron Deskins as an undergraduate researcher where he performed density functional theory calculations of carbon, both nanotubes and graphene sheets with defects for electrochemistry and photocatalysis. He started as a graduate student at the Charles D. Davidson School of Chemical Engineering at Purdue University. Here he conducted research under Prof. Jeffrey Greeley where he used density functional theory and molecular dynamics to understand catalysis and solvent structuring in microporous materials as well as simulating x-ray spectra for metal nanoparticles. He married Yunxin Chen in Lafayette Indiana on 12$^{th}$ July, 2017. He will begin work as a postdoctoral research associate for Prof. Randall Q. Snurr at Northwestern University where he will continue to study microporous materials for catalysis. He plans to pursue a career in academia after his postdoc.

# PUBLICATIONS

Bates, J. S.; Bukowski, B. C.; Harris, J. W.; Greeley, J. P.; Gounder, R. Distinct Catalytic Reactivity of Sn Substituted in Framework Locations and at Defect Grain Boundaries in Sn-Zeolites. *ACS Catal.* **2019**, acscatal.9b01123. https://doi.org/10.1021/acscatal.9b01123.

Bregante, D. T.; Johnson, A. M.; Patel, A. Y.; Ayla, E. Z.; Cordon, M. J.; Bukowski, B. C.; Greeley, J.; Gounder, R.; Flaherty, D. W. Cooperative Effects between Hydrophilic Pores and Solvents: Catalytic Consequences of Hydrogen Bonding on Alkene Epoxidation in Zeolites. *J. Am. Chem. Soc.* **2019**. https://doi.org/10.1021/jacs.8b12861.

Wu, Z.; Bukowski, B. C.; Li, Z.; Milligan, C.; Zhou, L.; Ma, T.; Wu, Y.; Ren, Y.; Ribeiro, F. H.; Delgass, W. N.; et al. Changes in Catalytic and Adsorptive Properties of 2 Nm $Pt_3$ Mn Nanoparticles by Subsurface Atoms. *Journal of the American Chemical Society* **2018**, *140* (44), 14870–14877. https://doi.org/10.1021/jacs.8b08162.

Bukowski, B. C.; Bates, J. S.; Gounder, R.; Greeley, J. First Principles, Microkinetic, and Experimental Analysis of Lewis Acid Site Speciation during Ethanol Dehydration on Sn-Beta Zeolites. *Journal of Catalysis* **2018**, *365*, 261–276. https://doi.org/10.1016/j.jcat.2018.07.012.

Cybulskis, V. J.; Bukowski, B. C.; Tseng, H.-T.; Gallagher, J. R.; Wu, Z.; Wegener, E.; Kropf, A. J.; Ravel, B.; Ribeiro, F. H.; Greeley, J.; et al. Zinc Promotion of Platinum for Catalytic Light Alkane Dehydrogenation: Insights into Geometric and Electronic Effects. *ACS Catal.* **2017**, *7* (6), 4173–4181. https://doi.org/10.1021/acscatal.6b03603.

Bukowski, B. C.; Greeley, J. Scaling Relationships for Molecular Adsorption and Dissociation in Lewis Acid Zeolites. *J. Phys. Chem. C* **2016**, *120* (12), 6714–6722. https://doi.org/10.1021/acs.jpcc.6b01157.

Zhu, Z.; Bukowski, B.; Deskins, N. A.; Zhou, H. S. Bamboo Shaped Carbon Nanotube Supported Platinum Electrocatalyst Synthesized by High Power Ultrasonic-Assisted Impregnation Method for Methanol Electrooxidation and Related Density Functional Theory Calculations. *International Journal of Hydrogen Energy* **2015**, *40* (5), 2216–2224. https://doi.org/10.1016/j.ijhydene.2014.12.039.

Bukowski, B.; Deskins, N. A. The Interactions between TiO2 and Graphene with Surface Inhomogeneity Determined Using Density Functional Theory. *Phys. Chem. Chem. Phys.* **2015**, *17* (44), 29734–29746. https://doi.org/10.1039/C5CP04073F.